AFRL-ML-WP-TR-2004-4283

LIFE PREDICTION METHODOLOGIES FOR AEROSPACE MATERIALS ANNUAL REPORT, 2003

N.E. Ashbaugh, R.A. Brockman, D.J. Buchanan, G.A. Hartman, A.L. Hutson, K. Li, and W.J. Porter

University of Dayton Research Institute
Structural Integrity Division
300 College Park
Dayton, OH 45469-0128

JUNE 2003

Interim Report for 25 May 2002 – 24 May 2003

STINFO INTERIM REPORT

MATERIALS AND MANUFACTURING DIRECTORATE
AIR FORCE RESEARCH LABORATORY
AIR FORCE MATERIEL COMMAND
WRIGHT-PATTERSON AIR FORCE BASE, OH 45433-7750

NOTICE

Using government drawings, specifications, or other data included in this document for any purpose other than government procurement does not in any way obligate the U.S. Government. The fact that the government formulated or supplied the drawings, specifications, or other data does not license the holder or any other person or corporation; or convey and rights or permission to manufacture, use, or sell any patented invention that may relate to them.

This report has been reviewed by the Air Force Research Laboratory Wright Site Office of Public Affairs (AFRL/WS/PA) and is releasable to the National Technical Information Service (NTIS). At NTIS, it will be available to the general public, including foreign nationals.

This technical report has been reviewed and is approved for publication.

/s/

_____
JAY R JIRA, Project Engineer
Life Prediction Branch
Metals, Ceramics & NDE Division

/s/

_____
ROLLIE DUTTON, Chief
Metals Branch
Metals, Ceramics and NDE Division

/s/

_____
GERALD J. PETRAK, Assistant Chief
Metals, Ceramics & NDE Division
Materials & Manufacturing Directorate

Copies of this report should not be returned unless return is required by security considerations, contractual obligations, or notice on a specific document.

REPORT DOCUMENTATION PAGE

Form Approved
OMB No. 0704-0188

1. REPORT DATE *(DD-MM-YY)*	2. REPORT TYPE	3. DATES COVERED *(From - To)*
June 2003	Interim	05/25/2002 – 05/24/2003

4. TITLE AND SUBTITLE

LIFE PREDICTION METHODOLOGIES FOR AEROSPACE MATERIALS ANNUAL REPORT, 2003

5a. CONTRACT NUMBER
F33615-98-C-5214

5b. GRANT NUMBER

5c. PROGRAM ELEMENT NUMBER
62102F

6. AUTHOR(S)

N.E. Ashbaugh, R.A. Brockman, D.J. Buchanan, G.A. Hartman, A.L. Hutson, K. Li, and W.J. Porter

5d. PROJECT NUMBER
4347

5e. TASK NUMBER
52

5f. WORK UNIT NUMBER
01

7. PERFORMING ORGANIZATION NAME(S) AND ADDRESS(ES)

University of Dayton Research Institute
Structural Integrity Division
300 College Park
Dayton, OH 45469-0128

8. PERFORMING ORGANIZATION REPORT NUMBER

9. SPONSORING/MONITORING AGENCY NAME(S) AND ADDRESS(ES)

Materials and Manufacturing Directorate
Air Force Research Laboratory
Air Force Materiel Command
Wright-Patterson AFB, OH 45433-7750

10. SPONSORING/MONITORING AGENCY ACRONYM(S)
AFRL/MLLMN

11. SPONSORING/MONITORING AGENCY REPORT NUMBER(S)
AFRL-ML-WP-TR-2004-4283

12. DISTRIBUTION/AVAILABILITY STATEMENT
Approved for public release; release is unlimited.

13. SUPPLEMENTARY NOTES
Report contains color. This work is the result of Department of Air Force contract number F33615-98-C-5214. The appendix contains numerous preprints. If published, the various publishers may assert copyright. If so, the United States has for itself and others acting on its behalf an unlimited, nonexclusive, irrevocable, paid-up royalty-free worldwide license to use for its purposes.

14. ABSTRACT

The ability to predict turbine-engine-materials behavior under operating conditions is an important facet of Phase 0 DARPA Prognostics programs. Studies of nickel-based superalloys – René 88DT, IN-100, and Waspaloy -- have been undertaken to assess: (a) baseline mechanical props. of material extracted from retired turbine disks, (b) microstructures of each alloy using optical microscopy and SEM, including OIM, (c) environment and load-history effects on FCG props., and (d) capability of fracture surface marking for crack-front location during spin-pit testing. Studies of retained residual stresses from surface treatments such as shot peening and material processing and service, i.e., bulk residual stresses, have been undertaken to incorporate residual stresses into future damage-tolerance based life management programs. Capabilities directed at integration of experiment and analysis are new test software, enhanced thermal imaging system at elevated temperature, and improved crack length measurement techniques.

Analytical models have been developed for the relaxation of shot peening-induced residual stresses as a result of thermal exposure, and for simulating the shot peening process in detail to estimate both residual stress and plastic strain distributions in processed parts. Using statistically based data for the size, shape and spacing of typical defects, Monte Carlo simulations were performed to determine probability distributions for localized stress amplification factors in bulk samples of IN100. Anisotropic elastic and the elastic-plastic

Abstract continued on back

15. SUBJECT TERMS Titanium aluminides, ceramic matrix composites, nickel-base superalloys, turbine blade materials, high-cycle fatigue, fatigue crack growth, elevated temperatures, creep, thermal fatigue, thermomechanical fatigue, fretting fatigue, load interactions, mixed-mode, stress intensity factors, finite element analysis, nondestructive evaluation

16. SECURITY CLASSIFICATION OF:

a. REPORT	b. ABSTRACT	c. THIS PAGE
Unclassified	Unclassified	Unclassified

17. LIMITATION OF ABSTRACT:
SAR

18. NUMBER OF PAGES
316

19a. NAME OF RESPONSIBLE PERSON (Monitor)
Jay R. Jira

19b. TELEPHONE NUMBER *(Include Area Code)*
(937) 255-1358

Standard Form 298 (Rev. 8-98)
Prescribed by ANSI Std. Z39-18

14. ABSTRACT (concluded)

behaviors of γ-TiAl have been characterized through novel experiments and used to define a suitable crystal plasticity model for the material. A probabilistic model for the yield strength variations in this material also has been defined, to simulate the highly localized slip behavior observed in laboratory experiments.

In other areas, fretting fatigue studies included experimental and analytical investigations of fretting fatigue crack propagation, contact material effect on fretting fatigue strength, and characterization of laboratory and service generated fretting fatigue damage. A deformation mapping system was used to monitor changes on the surface of γ-TiAl tensile specimens at prescribed stress levels at the grain boundaries and adjoining grains. An experimental approach employing γ-TiAl specimens fabricated using focused ion beams (FIB) in an SEM was initiated. Fracture, fatigue and creep rupture behavior of melt-infiltrated SiC/SiC ceramic matrix composite (CMC) with effusion holes were studied. A creep and damage accumulation model for an oxide/oxide CMC has been developed that accounts for the anisotropy of the creep response in off-axis orientations.

TABLE OF CONTENTS

FOREWORD

The work described in this report was performed at the Behavior/Life Prediction Section of the Metals Branch in the Metals, Ceramics & Nondestructive Evaluation Division of the Materials & Manufacturing Directorate, Air Force Research Laboratory (AFRL/MLLMN) under Contract No. F33615-98-C-5214, "Life Prediction Methodologies for Aerospace Materials." Mr. Jay Jira of AFRL administers the contract. The Structural Integrity Division, University of Dayton Research Institute, Dayton, Ohio conducts the program with Dr. Noel E. Ashbaugh and Mr. Robert J. Andrews acting as the Principal Investigator and Program Manager, respectively. This report is an interim report on the progress of the 6-year contractual effort.

In the fifth year of the contract, the investigations were developed and directed by Drs., Robert Brockman, Geoffrey Frank, and Kezhong Li and Messrs. Phil Blosser, Dennis Buchanan, George Hartman, and W. John Porter III, and Mrs. Alisha Hutson. Mrs. Jacqui Hawkins was responsible for coordinating the input and typing of this document. This interim report covers the work performed during the period of 25 May 2002 to 24 May 2003.

1.0   EXECUTIVE SUMMARY

1.1   COMPONENT DAMAGE ASSESSMENT PREDICTION

Over the last year, significant efforts in support of the DARPA-sponsored Materials Prognostics program have continued. Studies focusing on understanding microstructural/mechanical behavior relationships, environmental and load spectra effects on fatigue crack growth, the development of advanced damage monitoring techniques, and component modeling have been the cornerstones of this endeavor. To date, the metals under investigation include the nickel-base superalloys René 88DT, IN-100, and Waspaloy. The sources of these materials are retired gas turbine engine disks that are being considered in Air Force programs aimed at service life extension. Careful evaluation of the microstructures of each alloy have been undertaken using optical microscopy and scanning electron microscopy, including orientation imaging microscopy. Baseline mechanical properties have been determined for these alloys to aid test planning and comparison to data reported in the literature. A significant amount of testing to determine the effects of environmental conditions and load history has been performed. Both the environment and load history have been shown to significantly effect fatigue crack growth properties. Efforts to 'mark' fracture surfaces at known intervals to determine crack shape and growth rates were very successful. The success in fracture surface marking was culminated by General Electric Aircraft Engines applying an MLLMN-designed loading scheme during the spin-pit test of a René 88DT disk. The fracture surfaces were clearly marked and growth rates and crack shapes readily determined in post-test fracture analysis.

Exceptional efforts at developing three-dimensional finite element models of components and turbine engine assemblies to aid in spin-pit performance and damage progression predictions were undertaken. Also, important advances were achieved in refining a nondestructive evaluation technique based on the use of non-linear acoustics and in determining of the beta parameter for various levels of damage. Finally, methods for understanding and interpreting variability in fatigue performance through high cycle fatigue testing and fractographic analysis were advanced.

1.2   LIFE PREDICTION WITH RESIDUAL STRESS

A life prediction methodology that incorporates residual stresses is critical to safely extending the useful life of shot peened components such as turbine engine disks. Current damage-tolerance based life management concepts do not incorporate the beneficial effects of surface residual stresses. Characterizing the relaxation of residual stresses due to temperature, exposure time and mechanical loading is essential to development of a physically-based life prediction

model. Shot peening typically imparts a compressive residual stress to a depth of approximately 100-150 µm. Therefore, fatigue initiation and short fatigue crack growth behavior will be strongly influenced by the presence of surface residual stresses. Characterizing crack growth behavior of corner cracks in subelement geometries under engine operating spectrums will provide pertinent data to support the extension of life limiting components.

Bulk residual stresses are also present in turbine engine disks. Bulk stresses develop from nonuniform cooling rates during oil quenching of the disk after a solution heat treatment cycle. The magnitude of these bulk stresses can be a large fraction of the material yield strength. X-ray residual stress measurement techniques are not preferred for measuring bulk residual stresses. Determination of bulk residual stresses and strains was achieved with measured angular displacements of a split disk and an analytical model to described the deformation. The angular displacements were imposed boundary conditions for the elasticity (closed form) and finite element models. The predicted bulk strains from the models were in excellent agreement with measured strain gage and Moiré data.

Shot peening simulations are in progress to predict the retained residual stress depth profile. Models from the literature and FEA simulations show reasonable comparisons to x-ray diffraction results. However, current simulations are based on material behavior at strain rates not representative of shot peening processes. Material behavior data at high strain rates could improve the predicted residual stress profiles.

1.3   PHYSICALLY-BASED CONSTITUTIVE MODELING

Improving our ability to predict component life and to extend the useful life of fielded components requires that we reduce or eliminate sources of uncertainty in analytical life prediction. Toward this end, we are developing more accurate mathematical models of material behavior that can clarify the role of stress gradients, environmental factors, residual stresses and other factors in determining fatigue life.

In support of the DARPA materials prognosis program, UDRI has performed numerous studies of crack propagation using new finite element-based analytical tools developed at AFRL/MLLMN. Problem areas in the analytical tools were identified and improvements suggested. Additional experiments and analytical simulations have been performed to identify the magnitude and distribution of bulk residual stresses in complex engine components.

We have conducted analytical studies of the relaxation of shot peening-induced residual stresses as a result of thermal exposure, and verified these models by direct measurements.

Analytical methods have been developed for simulating the shot peening process in detail, for the purpose of estimating both residual stress and plastic strain distributions in processed parts.

UDRI has developed analytical models for stress fields in the neighborhood of defects in nickel-based superalloys. Using statistically based data, measured at AFRL/MLLMN, for the size, shape and spacing of typical defects, we have performed Monte Carlo simulations to determine probability distributions for localized stress amplification factors in bulk samples of IN100.

We also have made significant advances in our development of physically-based models of the behavior of gamma titanium aluminide intermetallics. Both the anisotropic elastic behavior and the elastic-plastic behavior of this class of materials has been characterized through novel experiments, and used to define a suitable crystal plasticity model for the inelastic behavior of gamma. A probabilistic model for the yield strength variations in this material also has been defined, to model the highly localized slip behavior observed in AFRL experiments.

1.4   INTEGRATION OF EXPERIMENTAL PROCEDURES AND ANALYSES

Physically-based models of material behavior depend on integration of experimental and analytical results. Performing experiments that produce data more directly usable in modeling efforts is one of the components of this integration effort. Targeting experimental work at the same scale at which the models are to be developed is a second component. Making direct measurements of physically-based parameters in the models, rather than calculating the parameters from related measurements, is a third component. The UDRI has continued to refine several experimental methods and systems and has developed new capabilities directed at the experiment/analysis integration goal. These methods and capabilities include new software, enhanced thermal imaging systems, and improved crack length measurement techniques.

1.5   HIGH CYCLE FATIGUE AND FRETTING

Efforts to understand the behavior of titanium alloys subject to fretting fatigue conditions continue to be the focus of studies aimed at improving damage tolerant design and reducing maintenance costs of military aircraft. Both analytical and experimental studies designed to simulate the fretting fatigue damage that occurs in turbine engine blade attachments have been undertaken. The focus of these studies included experimental and analytical investigation of fretting fatigue crack propagation, effect of contact material on fretting fatigue strength, and characterization of laboratory and service generated fretting fatigue damage.

Results of an evaluation of a fracture mechanics approach for determining propagation or non-propagation of fretting fatigue nucleated cracks suggest that this approach is better than a stress

analysis approach due to the poor understanding of crack initiation criteria in a gradient stress field. Success of the fracture mechanics approach was linked to accurate knowledge of the coefficient of friction, μ, which has a profound influence on the calculated stress field used in the K analysis. Fretting fatigue strength was determined to be insensitive to contact material composition beyond its influence on μ, which will differ for different material pairs.

A study designed to assess the effect of fretting fatigue damage in the form of wear and cracking indicated that cracks with a surface length of 100 μm or greater are required to measurably reduce material fatigue strength. The threshold behavior of those cracks was similar to the behavior of naturally initiated cracks. No correlation was observed with measured surface roughness, a common criterion for retirement of service components.

A related study was developed to attempt to identify the regions on fretted specimens where crack nucleation was imminent, based on a range of characterization techniques. Characterization of fretted samples, compared with specimens from other test fixtures, revealed the presence of fatigue and wear mechanisms. Comparison with fretted regions from retired engine components indicated more aggressive wear damage in the engine components than in the laboratory specimens.

1.6 γ-TiAl-BASE ALUMINIDES

In order to facilitate the introduction of gamma titanium aluminide (γ-TiAl) alloys into gas turbine engine application, models that accurately represent material behavior under extreme loading and environmental conditions are needed. To address this need, we have continued to pursue an approach closely linking a carefully planned experimental and analytical program. A project investigating the tensile behavior of specimens with very large γ-TiAl grains in the gage section was expanded to include single grain boundaries (2 grains) and grain boundary triple points (3 grains). A deformation mapping system was used to monitor changes on the surface of the tensile specimens at prescribed stress levels at the grain boundaries and within the adjoining grains. From the deformation mapping information, it is possible to back out local or far-field strains as a function of applied stress. Very good agreement was found between the far-field deformation mapping results and the strain gage results over the entire stress-strain curve. A comparison of the elastic results from 3-dimensional finite element (3-D FE) model, the deformation mapping data and the strain gage measurements produced favorable agreement. Substantial efforts are planned to further fine-tune a crystal plasticity model based on slip system activation during loading. Additionally, a 3-D FE model of a simulated turbine engine blade leading edge was created to demonstrate a potential USAF application of advanced intermetallic materials. Randomly oriented

grains were used to highlight the anisostropic nature of γ-TiAl under possible service load conditions.

Finally, an experimental approach employing specimens fabricated using focused ion beams (FIB) in a scanning electron microscope was initiated. The FIB-produced specimens were then subjected to compressive loading via a nanoindentor. The diameters of the compression specimens were approximately 20 μm. This approach will allow for the determination of constituent-level properties ideally suited for use in model development.

1.7   CERAMIC MATRIX COMPOSITES

Damage tolerant ceramic matrix composites (CMC) that exhibit relatively little degradation in mechanical properties at elevated temperature are being evaluated for high temperature aerospace applications. Many of these complex components have fillets, corners, holes and other structural features that develop multiaxial stress states under thermal and mechanical loading. Room and elevated temperature tests on ±45° Nextel™720/AS were used to characterize the off-axis tensile and creep behavior. This off-axis material behavior will provide guidance in the development of new CMC materials and redesign of existing components. Fracture, fatigue and creep rupture behavior of melt-infiltrated (MI) SiC/SiC CMC with effusion holes were also studied. Fracture and sustained load (creep) experiments on effusion hole specimens were used to determine how damage initiates and propagates with exposure time. A NASA program to develop a nondestructive assessment method of damage in CMC was supported by completing several interrupted fatigue tests on MI and chemical vapor infiltration (CVI) C/SiC CMC.

Several of the experimental programs provided mechanical behavior data to support the analytic modeling efforts on oxide/oxide CMC. A creep and damage accumulation model has been developed that accounts for the anisotropy of the creep response in off-axis orientations. This model will be employed to improve the prediction of the stress state around holes and notches.

HCF tests at room and elevated temperature were performed on CVI and MI SiC/SiC CMC. Software and hardware modifications were also completed to improve data acquisition and control.

2.0   INTRODUCTION

2.1   BACKGROUND

The U.S. Air Force (USAF) has various programs in place directed toward the advancement of new gas turbine engines and aerospace vehicle technology and the support of current gas turbine engines. These programs include Integrated High-Performance Turbine Engine Technology (IHPTET), National Turbine Engine Durability (NTED), and Engine Rotor Life Extension (ERLE). The primary goals are (1) extend safely the life of current/legacy rotors, (2) improve performance, i.e., maintain properties at higher service temperatures, and (3) reduction in weight, i.e., use of lightweight materials with high-temperature capability. The need to extend the life of a wide range of current aerospace components has resulted in programs such as ERLE, HCF initiative, Aging Aircraft, Propulsion Life, and DARPA Prognosis. These programs are directed toward conventional materials, such as Ni-base superalloys, titanium (Ti) alloys (near α and $\alpha+\beta$), and aluminum alloys. To apply the advanced materials effectively or to consider further applications of conventional materials that have experienced service conditions, a thorough understanding of the material behavior must be obtained and a methodology of life prediction for these materials must be developed or refined. Advanced materials such as gamma titanium aluminide (γ-TiAl) alloys, high-temperature intermetallics, and CMC are leading candidates to satisfy these needs for various engine components.

2.2   PROGRAM OBJECTIVES

The primary objectives of this program are to:

    (a) evaluate the performance of advanced and conventional materials under simulated service conditions

    (b) develop and/or adapt experimental techniques for characterization of deformation, damage evolution, and failure of advanced and conventional materials under typical service conditions

    (c) develop an understanding of the mechanisms leading to deformation, damage accumulation, and failure of advanced and conventional materials under a variety of test conditions, including simulated mission cycles

(d) develop physically based deformation and life prediction models necessary to ensure in-service reliability and maintainability of advanced and conventional materials subjected to aerospace usage loading conditions

(e) transition the new technology to USAF suppliers and customers

(f) use and update the data for various aerospace materials in the current archival system and enhance the materials data archival procedure.

2.3 REPORT ORGANIZATION

This fifth interim report presents the research conducted on the material behavior and modeling of aerospace materials within the Behavior/Life Prediction Section (MLLMN) of the Metals Branch (MLLM) in the Metals, Ceramics & Nondestructive Evaluation Division of the Materials and Manufacturing Directorate at Wright-Patterson Air Force Base, OH. This effort was conducted over the period from 25 May 2002 to 24 May 2003. The investigations that have been completed and were in progress during the fifth year of the contract will be discussed in this report.

The investigations for Component Damage Assessment Prediction, Life Prediction with Residual Stresses, Physically Based Constitutive Modeling, Integration of Experimental Procedures and Analysis, High Cycle Fatigue and Fretting, Damage Tolerance Studies of γ-TiAl-Based Titanium Aluminides, and Damage Accumulation and Failure of Ceramic Matrix Composites are discussed in Sections 3, 4, 5, 6, 7, 8, and 9, respectively. The first four investigations are associated with ERLE and DARPA Prognosis Programs. Ancillary laboratory activities are presented in Section 10. Extended discussions of the work-in-progress are presented to provide as much information as possible about the current investigations. Copies of the manuscripts, which have been written on the completed efforts, are provided in an appendix, Compilation of Manuscripts, for the convenience of readers who wish to have more detailed information of the investigations readily available.

3.0   COMPONENT DAMAGE ASSESSMENT PREDICTION

3.1   MATERIAL STUDIES OF NICKEL-BASE SUPERALLOYS

3.1.1   Waspaloy

Waspaloy is a widely used nickel-base superalloy in Air Force gas turbine propulsion systems. Components fabricated using Waspaloy are candidates for current efforts at extending their useful life in Air Force propulsion systems. To aid in this endeavor, an understanding of the role played by the microstructure on the mechanical behavior of wrought Waspaloy is required. Hence, detailed investigations using metallography, scanning electron-based orientation imaging microscopy (OIM) and image analysis techniques of the microstructures in retired components were undertaken. Material was excised from three retired compressor disks at various locations for this investigation. The service lives of the interrogated parts were not appreciably different.

The microstructural investigations centered on the determination of average grain size, grain size and defect distribution, and crystallographic orientation. Material from radial and circumferential orientations of the rim, web and bore was evaluated. In two cases, the grain size was found to decrease slightly from the bore to the rim with no distinct crystallographic texture apparent. However, one disk was found to have a duplex grain structure with regions of fine grains 3-5µm in diameter surrounded by grains approaching 50-80µm in diameter. The fine-grained areas exhibited no pronounced crystallographic texture.

Upon presentation of these microstructural findings to representatives from Pratt & Whitney (P&W), it was learned that our results are consistent with P&W's expectations and that all of these microstructures are acceptable for Waspaloy compressor disks.

3.1.2   René 88DT

René 88DT is a nickel-base superalloy developed by General Electric (GE) for various gas turbine engine applications. This effort has focused on the characterization of René 88DT microstructures from a gas turbine engine disk. The component was manufactured using powder metallurgy processes in concert with forging. A supertransus heat treatment is used with René 88DT.

Cross-sections of the disk were removed using electric discharge machining (EDM) and metallographic samples representing locations within the bore, web and rim were prepared. For optical microscopy, the samples were etched using etchant and studied using bright-field

techniques. On the scanning electron microscope, backscattered electron techniques were used and the samples were viewed in their as-polished state.

In all locations, the microstructure consisted of fine (~200 nm diameter) gamma prime particles in a gamma matrix. The average grain size was approximately 20 μm with some coarsening evident from the rim to the bore. Minimal porosity and non-metallic inclusions were present. According to representatives of GE Aircraft Engines (GEAE), the microstructures encountered in this investigation were within GEAE's acceptability limits.

3.1.3 IN-100

The nickel-base superalloy IN-100 has been used for gas turbine applications for the past 25 years. Originally introduced as an ingot metallurgy alloy, IN-100 has gained wide application in turbine engine systems as a powder metallurgy (P/M) product. Various compressor disks manufactured using P/M IN-100 have been identified by the Air Force as candidates for life extension. By life extension it is meant that the part is believed to reliably and safely perform longer than it's original design life. The challenge is to understand how much longer the part can perform through investigating the processes that lead to part failure and how to predict and/or abate their occurrence.

A key to understanding how metals will perform in service is to understand the microstructure of the metal in question. In this case, cross-sections of a gas turbine engine disk made of IN-100 were excised via EDM, the cross-section was then cut into smaller pieces and mounted into metallographic mounts and polished. Optical and scanning electron microscopy techniques were used to evaluate the microstructures.

The compressor disk materials used in this study were subjected to a subtransus heat treatment. The microstructure was composed of two types of gamma prime particles. The larger or subsolvus gamma prime found primarily in the grain boundaries and the finer or aging gamma prime dispersed throughout the grains. The diameters of each are approximately 1 μm and 100 nm, respectively. The average grain size was approximately 5 μm. The microstructure was consistent throughout the disk cross-sections. Orientation imaging microscropy revealed a random crystallographic orientation irrespective of location in the disk cross-sections.

3.1.4 Fatigue Crack Initiation Mechanism in Nickel-Base Superalloys [C1]

It is well established that fatigue crack initiation of Ni-base superalloys occurs at intrinsic defects. An IN100 forging produced using a powder metallurgy technique contained contrasting populations of pre-existing pores and nonmetallic inclusions (NMI). The purpose of this

investigation was to examine the effects of the defect type, shape and size on the low cycle fatigue crack initiation behavior. Both void- and NMI-related origins were almost equally observed on the fracture surfaces using scanning electron microscopy (SEM). The void-related origins were located on the sample surfaces and NMI-related origins tended to locate subsurface or internal. Critical sizes for void- and NMI-related defect origins appear to exist with the critical NMI area greater than an order of magnitude larger than the void area. The statistical 2-D distribution of defect size and shape in the cross section of a forging indicate that the results excluded the large NMI particles that had a low sampling probability due to low volume percentage.

3.2 BASIC MECHANICAL PROPERTIES - BASELINE/QUALIFICATION AND USAGE

In order to determine appropriate stress levels for low and high cycle fatigue testing, creep testing, etc… and for comparison against data from the literature, it is occasionally necessary to perform standard tensile tests at various loading rates and temperatures. These efforts continued over the last year using René 88DT, IN-100 and Waspaloy samples extracted from retired turbine and compressor disks.

Additionally, hardness testing was performed throughout a cross-section of a René 88DT turbine disk to determine location-to-location variability. Some variability was found and tended to trend with the microstructural differences discussed in Section 3.1.2, but the results were determined to be normal for the part in question.

Finally, chemistries for many of the René 88DT, In-100 and Waspaloy disk have been analyzed and a database with this information maintained.

3.3 ENVIRONMENTAL EFFECTS ON FATIGUE CRACK GROWTH IN TURBINE ENGINE MATERIALS

3.3.1 The Role of Air in Fatigue Load Interaction [C2]

Natural fatigue crack formation and growth were studied in notched Al-Cu alloy coupons through high-resolution SEM fractography. The experiments were conducted under programmed loading conditions designed to induce microscopic marking of the crack formation and growth process under varying stress ratio and closure-free crack tip conditions. Control experiments were performed by switching between an air and vacuum environment. In air, varying the stress ratio from 0.74 down to 0.64 retards crack growth by up to a factor of five. This 'closure-free' stress ratio history effect totally disappears in vacuum, suggesting a significant environmental

influence on stress ratio and its history. Crack-tip stress state appears to moderate environmental action, revealing a potential mechanism sensitive to residual stress. Consequently, crack closure, residual stress and crack front and plane orientation are identified as major load interaction mechanisms whose synergistic action controls fatigue under variable amplitude loading. The study also appears to suggest that as a consequence of the crack seeking the path of least resistance, load-sequence-sensitive-crack plane and front orientation may only induce retardation effects.

3.3.2 Environment-Related Load History in Elevated Temperature Fatigue of a Nickel-Base Superalloy [C3]

Near-threshold elevated temperature fatigue crack growth rates in nickel-base superalloy IN-100 are sensitive to load history effects that cannot be attributed to crack closure. The effects disappear in vacuum, suggesting operative mechanisms that are environment related. Experiments on compact-tension coupons under low amplitude loading show that programmed step-wise reduction in stress ratio causes noticeably retarded crack growth that cannot be explained from crack closure considerations. The effect rapidly diminishes with increasing stress-intensity range, indicating a near-threshold phenomenon. This effect is altogether absent in vacuum tests at elevated temperature. The experiments also indicate crack growth retardation when fatigue loading is mixed with hold-time. This appears to be caused by incompatible macro- and micro-crack front orientation associated with differences between the nature of sustained load and fatigue cracking.

3.3.3 Fatigue by Diffusion-Induced Brittle Micro-Fracture [C4]

Where there is potential for gas-metal diffusion, fatigue crack formation and extension can proceed by brittle micro-fracture (BMF). As slip is internal to the material and insensitive to hydrostatic stress, it may not be affected by either environment or mean (residual) stress. During the rising half of a fatigue load cycle, increasing notch root and crack-tip hydrostatic stress further enhanced by local constraint, can cause almost instantaneous crack front cyclic diffusion embrittlement (CFCDE). As a consequence, BMF component of fatigue crack extension by tensile de-cohesion or shear failure will be promoted in addition to Mode II by irreversible cyclic slip. The BMF component will be sensitive to crack-tip stress state as well as stress history in variable amplitude fatigue and therefore, will diminish or vanish altogether in vacuum. The CFCDE-BMF model explains accelerated transgranular fatigue by environmental action. It also appears to explain a variety of other phenomena including residual stress effect in metal fatigue.

3.4 LOAD SPECTRA EFFECTS ON FATIGUE CRACK GROWTH

3.4.1 IN-100 (PWA1100)

Limited efforts were undertaken to understand the crack growth behavior of IN-100 at elevated temperature. The material of interest in this work was PWA1100, which is a sub-transus heat treated version of IN-100 commonly used in P&W commercial turbine disk applications. Tests were performed to determine the effect of stress ratio, frequency and constant K_{max} conditions on fatigue crack growth behavior. Results from these fatigue crack growth results are being incorporated into local fatigue crack growth modeling efforts supporting activities such as the P&W mini-disk spin pit program (Section 3.6).

3.4.2 Waspaloy

To aid in understanding the variability in fatigue crack growth behavior of Waspaloy brought upon by differences in local microstructure and use in service, a test program using material from retired F-100 12th stage disks was initiated. Fatigue crack growth specimens were extracted from bore, web and rim locations of three retired 12th stage disks. Tests were conducted at 650°C using a variety of loading spectra with varying stress ratios, constant K_{max} levels and frequencies. The effect of dwell cycles was also investigated. The tests were performed using the recently-developed WinMate fatigue crack growth module and crack growth was monitored via a refined direct-current-potential-difference (DCPD) technique. Significant location-to-location microstructural variability and fatigue crack growth response were observed between the three disks investigated with fatigue crack growth rates differing by up to five times under particular conditions. Investigations with the goal of understanding the mechanisms behind these differences in behavior are ongoing.

3.4.3 A Synergistic Multi-Mechanism Model for Fatigue Crack Growth under Service Conditions [C5]

Crack-tip advance under given applied cyclic load conditions is moderated by several mechanisms including crack closure, residual stress, crack front incompatibility and blunting. Experiments were designed to isolate the action of individual mechanisms using programmed variable amplitude load sequences. Fractographic observations from studies on three different materials indicate the synergistic action of at least three significant mechanisms. A model is proposed incorporating these mechanisms to describe variable amplitude fatigue crack growth. Model response appears to be consistent with fractographic observations.

3.4.4 A Mission-Element Approach for Crack Growth Under Turbine Engine Spectra [C6]

The U.S. Air Force is embarking on a technology development initiative to extend the useful lifetime of major, fracture-critical components in currently fielded gas turbine engines. A key element of this program is the development of improved methods for prediction of fatigue crack growth. Current approaches for life management of engine components tend to ignore potential benefits in crack propagation lifetime that may occur as the result of load interaction phenomena that occurs under variable amplitude spectrum loading. The objective of the project was to assess the role of load-interaction effects in an advanced Ni-base superalloy when subjected to loading events representative of turbine engine usage.

3.5 FRACTOGRAPHY ASSESSMENTS OF CRACK GROWTH AND LOAD INTERACTION (Spin Pit Simulation)

In support of the spin pit testing programs being performed by General Electric and Pratt & Whitney for DARPA, experiments utilizing specimens fabricated from nickel-base superalloys IN-100, Waspaloy and René 88DT and simulated spin pit loading and environments were conducted. The goal of these experiments was to determine the conditions necessary to sufficiently "mark" fracture surfaces at known intervals in an effort to track crack shape and growth rate through a compact tension specimen. Changes in the applied load ratios and/or loading frequency for short periods during a loading sequence have been the most effective means for introducing marker bands. Alloys that have been successfully "marked" in the lab include powder metallurgy IN-100 and René 88DT in a supertransus heat treated condition and wrought Waspaloy. Findings from our experiments were applied in an actual spin pit test of a René 88DT F404 turbine disk assembly and resulted in a clearly marked fracture surface through the complex cross section of the disk.

3.6 CRACK PROPAGATION SIMULATION

Crack propagation simulations corresponding to spin pit cyclic tests performed at Patuxent River have been performed for a notional disk design produced by Pratt and Whitney under the AIM program, and for a General Electric low-pressure turbine disk from the F404 engine. These simulations exercise numerous capabilities and options of the Zencrack software currently being developed by Zentech, Inc. under Air Force Small Business Innovation Research (SBIR) funding.

A sector finite element model of the AIM disk test assembly has been created and analyzed for the spin pit conditions used to test minidisks #1 (12,000-25,000 RPM, 90°F temperature gradient bore to rim) and #2 (12,000-26,000 RPM, 90°F temperature gradient). Several idealizations of the disk-arbor interface conditions have been analyzed to assess the sensitivity of the predictions to the model assumptions. However, the press-fit interface provides no alternate load path and therefore proves to be quite insensitive to the idealization of this region.

Several crack propagation analyses have been attempted for cracks in the rim area, inboard of the cut-away area representing the blade roots. The rim cracks are corner cracks that leave a relatively small ligament of material along one edge of the crack before becoming a through crack. Zencrack was not effective for analyzing this crack geometry, and essentially no useful results were obtained from this exercise.

Successful crack propagation simulations have been performed for edge cracks in the bore of the disk, oriented in a plane containing the axis of symmetry and the radial axis of the disk. All of these crack growth simulations use ABAQUS submodels, driven by the "global" solution for the entire test assembly. For both test conditions, cracks have been propagated numerically up to a length (measured along either surface) of more than six millimeters, beginning with a crack length of 0.44831 mm. In disk #1, this corresponds to approximately 7,400 cycles, with the mid-crack K values ranging between 19-62 MPa-√m. For disk #2, the same crack growth is observed in just over 1,500 cycles, with K = 20-67 MPa-√m. The crack shapes predicted by Zencrack agree very well with crack profiles obtained using marker blocks in the spin pit tests.

Both Zencrack method 1 (analyze one load case and apply appropriate scale factors for the minimum loading condition) and method 2 (analyze separate loading conditions for min and max loading) were used for the crack propagation simulations. Because the rotational loading is clearly the dominant loading condition, the agreement between the two methods is quite good in this particular problem. Method 2 is recommended in general for non-proportional loading conditions since it is not difficult to apply and involves fewer analytical assumptions.

Initial crack growth analyses for the bore crack were performed using multiple crack blocks, mapped onto the actual (curved) geometry of the bore edge. To continue the analysis over significant crack lengths, the original crack blocks were replaced by Zencrack's "large crack blocks", which allow crack propagation nearly all the way across the block. The shortcoming of the large crack block approach is that the curved edge of the bore cannot be included in the model, because the crack block is defined by a single 20-node element. Crack areas from the

initial crack growth model were used to define an initial crack size on the large-crack-block model with the same area.

While the crack growth predictions obtained from these models are reasonably good, significant numerical problems were observed in nearly all of the Zencrack simulations using large crack blocks. In particular, as the ABAQUS meshing changes, the constraints that tie the crack block mesh to the surrounding mesh are applied at spatial intervals that are determined by the current mesh spacing. As a result, "hot spots" tend to occur at locations where the coarser of the two meshes is tied to the finer one. There is no effective way to adjust the mesh spacing in the original model to avoid this problem since the spacing on the Zencrack-generated side of the mesh changes dramatically as the solution progresses. To make matters worse, some tying constraints invariably are missed and these are often difficult to isolate; in most cases, we have had to confirm node-by-node that the proper constraints have been applied and patch in the additional constraints by hand in the original ABAQUS input deck. (This requires first running Zencrack to determine the node numbers that need to be constrained.) This pair of problems underscores the basic difficulty of using an external data generation program (like Zencrack, or FRANC) to manipulate a model from a third-party analysis program – the number of possible input options that must be recognized and adapted to in the crack front mesh are virtually unlimited.

Stress and crack propagation analyses of the GE F404 LPT disk also have been performed using ABAQUS and Zencrack. Models of the disk only and of the complete spin pit test assembly have been prepared and analyzed. The disk geometry was modeled using Catia, to allow for adjustments in the number of features in certain areas of the model. The Catia model has been reconstructed from paper drawings since geometry data in electronic form was not available for the part. Details of the modifications made for spin pit testing were obtained from the test group at Pax River. Sector models of the disk and of the complete assembly have been based on an 11.25-degree sector with reflective symmetry (1/32 of the complete system). The sector models include two blade slots, two TV holes, and two holes for each of the forward and rear cooling plate connections. The number of forward and rear shaft bolts (actually 36 each) and rear shaft holes (actually 26) were modified to 32 instances for the sector models. Densities of the fasteners for which a modified number of instances are used have been modified to obtain the correct inertial forces. The sector model of the spin test assembly is similar to the model analyzed by GE, except that the UDRI model includes the complete forward and rear shafts, arbor, and spindle; the GE model truncates some features at each end of the assembly for simplicity.

Interferences at the part interfaces and bolted connections in the assembly model have been adjusted to obtain the correct preload forces as specified in the assembly drawings. All interferences are resolved at room temperature, so the actual preloads at operating temperature will be slightly different.

Stress analysis of the disk assembly model requires several ABAQUS analysis steps: (1) resolution of interference and contact conditions; (2) temperature rise; (3) spin-up to minimum RPM, for use in Zencrack analysis; and (4) spin-up to maximum RPM. When plasticity is included in the model, additional cycles are added between minimum and maximum RPM until the cyclic plastic strains disappear.

Stress results for the spin test conditions have been compared rather extensively with linear elastic predictions made by GE. Detailed comparisons have been made in several key regions, including: disk bore; forward and aft flanges; blade slot bottoms; selected locations in the lower (inner) disk; and forward cooling plate arms. In general both the displacement and stress results agree very well, with the maximum differences being on the order of 7-8 percent. The difference in assumed boundary conditions in the GE ANSYS model from the actual support conditions (as modeled in the UDRI model) seem to be the primary cause of the differences observed in the two analyses.

Based upon analytical estimates of the residual stresses in the disk (section 4.4.4), and upon observations from the spin tests, crack propagation analyses for the TV hole area, which was initially considered an area of high interest, have not been attempted. We have constructed ABAQUS submodels for crack studies in this area.

Crack propagation submodels have been prepared for cracks in the disk bore and the blade slot bottom of the disk. These models are based on estimates of the initial crack shape from the spin tests. In the case of the bore crack, initial crack models have been prepared using "normal" Zencrack crack blocks, whose main value is the prediction of stress intensity factors and initial crack growth rates. Based on additional information received subsequently from the spin tests, a large crack block-based Zencrack model is being prepared for analysis.

3.7   F100 DISK MODELING

Finite element models of the Pratt and Whitney F100 12th stage compressor disk have been created for use in modeling both the spin pit test conditions and residual stresses in the disk. Initially, geometry information for these models was based on drawings for part number 4022612, which is different from most of the test data (part number 4068812). Recently,

geometry data for the correct part number has been supplied by Pratt and Whitney, and the model predictions have been revised based on the correct geometry.

Most of the analysis performed on the F100 disk models has been for purposes of estimating bulk residual stresses in serviced disks, as described in section 4.4.4. A limited number of crack propagation simulations have been performed, to study the behavior of cracks in the neighborhood of the anti-rotation tangs on the disk surface. Because of the recess adjacent to each tang, a significant stress concentration exists at the tang root, producing hoop stresses of approximately 130 ksi. Actually, the peak stresses are inclined approximately 10 degrees from the axial direction and involve a combination of the hoop and axial stresses. The seeded flaws in the Pax River spin tests of this disk have been placed in this location, at 10 degrees off normal, on the outer corner of the tang recess.

Zencrack analyses of the initial seeded crack have been performed to obtain stress intensity factors and estimate initial crack growth rates. Only a small amount of crack growth could be obtained from the initial flaw model since the corner crack comes very close to the far side of the tang recess and quickly becomes a through crack. Two additional models of the tang crack area have been created and analyzed, in which an initial through-crack is assumed. In the first model, the dimensions of the through crack were based on the initial crack growth estimates obtained from the corner crack model. Estimates of crack growth directions have been obtained from this model, indicating a possible tendency of the crack to turn into the plane of the disk as observed in the spin tests. Later, observations of the spin pit tests were used to update the crack geometry and obtain improved estimates of the crack growth directions through the snap ring thickness. Several key observations can be made from the resulting solutions. First, the stress intensity factor appears to vary significantly across the width of the snap ring, producing highly nonuniform crack growth rates. Secondly, the crack propagation directions predicted by Zencrack do suggest the sort of crack turning observed in the test, although crack growth beyond about 0.020 in could not be obtained regardless of the size controls and tolerances selected in Zencrack. Finally, it seems clear that, even if the initial crack turning observed in the tests were to be predicted correctly using Zencrack, the subsequent change in direction of the crack toward the blade post region definitely would not be predicted since factors other than K-controlled crack growth obviously are important in this problem. The blade post area toward which the crack turns is a highly stressed area but the stress concentration does not extend inward to the radial position where the propagating crack lies, which is immediately adjacent to the snap ring.

All of these analyses have been performed on ABAQUS submodels, driven by results from a sector model of the F100 disk. As with the Zencrack models described in the previous

17

section, numerous problems were observed in establishing the proper constraints between the Zencrack-generated mesh and the existing ABAQUS mesh, necessitating by-hand patches to the ABAQUS data.

In the process of analyzing the second large-crack model above, an additional problem in the Zencrack input was identified. Zencrack allows the specification of initial crack surface dimensions using either edge ratios (i.e., fraction of edge length) or actual dimensions. In the Zencrack examples we have seen and in the analyses we have performed with Zencrack, typically the edge ratios have been used. These ratios (or the corresponding dimensions) describe the surface length of the crack either on adjacent faces of the crack block (for corner cracks) or on opposing edges (for through cracks). In the F100 large crack model, a series of through-crack blocks has been used with corner-crack blocks at each end. In adjacent-crack blocks, the edge ratios or dimensions of mating surfaces must be identical since the crack is continuous. Zencrack generates errors when through-crack blocks are joined to corner-crack blocks because the through-crack block logic appears to use the wrong edges to define the crack lengths. By trial and error, we have found that the edge lengths used in the crack length calculations for through-crack blocks actually are adjacent edges (as they should be for a corner crack), rather than the opposing edges. This error exists in Zencrack 7.0; we have not tested for the same error in Zencrack 7.1.

3.8   NON-LINEAR ACOUSTICS

Several studies of nonlinear acoustic properties in metallic materials in recent years have shown promise as a new nondestructive evaluation technique for early detection and tracking of fatigue damage as a precursor to crack initiation. Majority of these studies has been conducted on laboratory specimens with optically flat surfaces using a capacitive detector with air as the dielectric medium. The aim of this investigation is to develop methodology to improve the sensitivity of the capacitive detector and to utilize it to evaluate the accumulated fatigue damage of nickel-base superalloy specimens with less than ideal surface preparation.

The preparation of specimens has begun. A group of machined flat dogbone specimens were initially electropolished to remove prior residual stresses due to machining. They are being cycled under a constant amplitude load at 650°C to various fractions of failure life from zero to one. The tests will be interrupted periodically to allow evaluation of the specimens. The nonlinear acoustic parameter, beta, proportional to the amplitude of the second harmonic frequency of the transmitted wave packet will be determined in the gage length of these specimens.

3.9 VARIABILITY STUDIES IN FATIGUE LIFE OF TI-6AL-2SN-4ZR-6MO

3.9.1 Microstructure Based Variability in Fatigue Life of Ti-6Al-2Sn-4Zr-6Mo [C7]

The variability in fatigue life of a Ti-6Al-2Sn-4Zr-6Mo alloy was studied. The cumulative life distribution plot was found to be composed of two distinct failure mechanisms, designated as Type-I and Type-II. The likelihood of Type-I vs. Type-II failure shifted with respect to the stress level such that at lower stress levels there was increased probability of Type-II failure. It was also found that the variability in life was introduced primarily at the crack nucleation stage, specifically, formation of a stage-I crack across an equiaxed primary-α particle.

3.9.2 Dual Fatigue Failure Modes in Ti-6Al-2Sn-4Zr-6Mo and Consequences on Probabilistic Life Prediction [C8]

The variability in fatigue life of the Ti-6Al-2Sn-4Zr-6Mo (Ti-6-2-4-6) alloy was investigated. Cumulative life distribution plots were found to be composed of two failure mechanisms. The data could be closely represented by a cumulative distribution function (CDF) resulting from the superposition of the CDFs of the individual mechanisms. An approach for life prediction based on the data due to the worst-case mechanism was suggested.

3.9.3 Variability in Fatigue Life of Ti-6Al-2Sn-4Zr-6Mo [C9]

Variability in fatigue life of the Ti-6Al-2Sn-4Zr-6Mo (Ti-6-2-4-6) alloy was investigated. It was found that the variability in life was introduced at the crack nucleation stage, i.e., formation of the stage-I crack across an equiaxed primary-α particle. Cumulative life distribution plots were found to be composed of two failure mechanisms. The mean lives of the two types of failure differed by two orders of magnitude. Also, the likelihood of failure by the "higher-life" mechanism increased with decreasing stress amplitude. It was also found that the variability in life of Ti-6-2-4-6 could not be tracked through the variability in the size of the relevant microstructural unit. Rather, the life variability can be accounted for through the variability in deformation accumulation in a given α_p as influenced by the orientation of the surrounding α particles.

4.0 LIFE PREDICTION WITH RESIDUAL STRESSES

4.1 RELAXATION IN PM IN100 DUE TO TEMPERATURE AND EXPOSURE TIME

4.1.1 Determination of X-Ray Cold Work Calibration Curve

The determination of the X-ray cold work calibration curve for powder metal (PM) IN100 was subcontracted to Lambda Research Incorporated of Cincinnati, OH. Ten samples were machined from a PM IN100 turbine engine disk into cylindrical compression specimens with nominal diameter of 12.7 mm and height of 19 mm. The samples were compressed to varying levels, up to approximately 30% true plastic strain (cold work). The compressed samples were sectioned for X-ray diffraction (XRD) measurement to determine the diffraction peak width. It is important to note that although the true plastic strain is a tensor quantity, the XRD technique cannot determine the components of the tensor, only a scalar representation of the true plastic deformation tensor. An empirical relationship between the diffraction peak half-width and an effective true plastic strain was established. The empirical equation used by Lambda to relate the peak half-width to the effective true plastic strain is shown,

$$W_{1/2} = A[1 - \exp(-B * \varepsilon_p)] + C * \varepsilon_p + D \quad,$$

where (A, B, C, D) are fitting parameters, $W_{1/2}$ is the peak half-width and ε_p is the true plastic strain.

4.1.2 Residual Stress Relaxation Modeling

Measurements of residual stress relaxation in PM IN100 under thermal exposure, made by Lambda Research, Inc., have been studied analytically to determine the nature of the residual stress relaxation observed in the tests. The Lambda measurements include both surface stresses and residual stress profiles into the depth.

The analytical studies have been performed using models representing rectangular parallelepipeds, with the models extending several millimeters into the depth to the region in which the residual stresses associated with surface enhancement processes are negligible. X-ray diffraction measurements on baseline specimens not subjected to high temperature after shot peening have been used to supply the initial conditions for the analytical models. The direct stress components are initialized to the stress distributions obtained from the corrected X-ray diffraction measurements; plastic strains are initialized to values obtained from the cold work

values measured experimentally. The initial conditions are introduced into the model via ABAQUS user subroutines SIGINI and HARDINI, respectively.

Note that the initial stresses satisfy the equilibrium conditions trivially, since their derivatives (e.g., $\dfrac{\partial \sigma_{xx}}{\partial z}$ and $\dfrac{\partial \sigma_{yy}}{\partial z}$, if z is the depth direction) do not appear in the equilibrium equations. However, when the stresses at all depths are used to define lumped internal nodal forces in the finite element model, slight redistributions of the stresses may occur as a result of the discretization errors. In all of the models used, the element spacing is much less than the spacing of the experimental measurements, and this redistribution is minimal. Nonetheless, we allow an initial analysis step under no mechanical or thermal load to ensure that the discrete model is properly in equilibrium.

The analytical model is subjected to the temperature condition corresponding to the specific specimen being modeled, using the temperature-dependent stress-strain characteristics of the PM IN100 alloy. We have found that the residual stress relaxation observed at low exposure times (on the order of 30 minutes or less), for which creep strains are likely to be relatively small, is primarily caused by the tendency of the metal to flow, at elevated temperature, at stress levels lower than the existing residual stress. Therefore, after cooling, the residual stress at any depth is reduced to the flow stress at the exposure temperature and the level of plastic strain existing at that depth.

Because additional stress relaxation is observed for longer exposure times, time-dependent creep deformation also plays a role in the observed stress relaxation. Additional experiments have been conducted to determine the creep characteristics of PM IN100 as a function of stress level and prior prestrain. Analysis of additional models that include the creep deformation effect are in progress.

4.2 CRACK INITIATION AND GROWTH IN FEATURE SPECIMENS

4.2.1 Characterization of Corner Crack Growth in Subelement Geometries

Several specimen geometries for corner crack growth analysis were designed and machined from forgings and retired turbine engine disks for fatigue crack growth (FCG) testing. All geometries were designed to investigate corner crack growth from features in turbine engine disks. An emphasis was placed on collecting corner crack growth data for small cracks, near the NDE detection limit of approximately 100 μm. Electric discharge machining (EDM) starter notches were machined into features to initiate crack growth at a specific location.

The first geometry was a thin (B = 1.2 – 2 mm) double-edge notch tension (DEN(T)) geometry. This geometry was particularly suited for extracting specimens from thin sections of the disks. Unfortunately, the 1.2 mm thickness of this specimen limited the range of corner crack growth data. A thick DEN(T) geometry was designed where the gage section of the specimen was machined from a thick portion of the disk. The slugs were inertia welded to IN718 bar stock and machined to the final dimensions. The thick DEN(T) geometry provided sufficient corner crack growth data at the expense of increased specimen machining cost. All tests were instrumented with Direct Current Potential Difference (DCPD) hardware to continuously measure crack growth. Optical crack length measurements were made with a traveling microscope at elevated temperature. The optical crack length data were used to correct the continuously recorded DCPD data. Periodically, tests were interrupted to perform acetate replica measurements of crack lengths at room temperature. SEM analysis of specimen fracture surfaces were completed to determine the precrack profile at the interior of the sample and to identify and measure marker blocks.

4.2.2   Finite Element Analysis of Corner Crack Growth Analysis under Spectrum Loading Conditions

Finite element models of the feature specimens described in the previous section were developed for fatigue crack growth predictions. The crack growth predictions were accomplished using a program called Zencrack, which was developed by Zentech under an Air Force contract. The original uncracked FE mesh was modified to replace a large single element with a special crack block that contained the crack front and a predefined number of elements. The Zencrack program called a finite element program, such as ABAQUS, ANSYS, or MARC, to solve for the displacements and stresses in the model at each increment in crack length. Zencrack calculated the increment in crack length and modified the mesh inside the crack block for the new crack length. Crack growth predictions with block loading spectrums and constant amplitude spectrums were completed. Fatigue crack growth predictions for several feature specimens, using three different geometries with corner cracks, were completed.

4.3   CYCLIC RELAXATION OF SHOT PEENED RESIDUAL STRESSES IN Ti-6Al-2Sn-4Zr-6Mo

Dogbone specimens, extracted from a pancake forging, were used to characterize residual stress relaxation under cyclic loading in Ti-6Al-2Sn-4Zr-6Mo. The specimen gage section was 20 mm long by 7.5 mm wide and 2 mm thick. The specimens were shot peened to an Almen intensity of 4A with a MI-110-R shot specification. Residual stress measurements were made at

the surface and at nominal depths of 12, 25, 50, 75, 125, 175, 250 and 350 μm in the gage section of the specimens. Residual stress measurements were subcontracted to Lambda Research Incorporated of Cincinnati, OH. The size of the region irradiated by X-ray was 8 mm by 5 mm centered in the gage section of the sample. All residual stress measurements were made in the direction of the applied mechanical load. Six samples were used to characterize the residual stress relaxation as a function of maximum applied cyclic stress. One sample was used as a baseline to characterize the as shot peened residual stress depth profile. The residual stress at the surface and to a depth of 60 μm was constant and equal in magnitude to the yield strength measured from monotonic tensile data, approximately 1100 MPa. Maximum stresses for the five cyclic tests were chosen to be 1100 MPa and below. Stress-strain data was acquired using extensometry during cyclic loading. Ten fatigue cycles were applied to the samples to acquire stabilized hysteresis loops and to capture any cyclic relaxation. Specimens cycled at stresses below 1100 MPa exhibited linear elastic stress-strain behavior and residual stress depth profiles similar to the as shot peened profile. A specimen cycled at 1100 MPa exhibited hysteresis in the stress-strain loops and a decrease in the surface residual stress. The largest change in the residual stress depth profile occurred at the surface.

4.4 CRACK INITIATION AND GROWTH IN FEATURE SPECIMENS

4.4.1 Measurement of Bulk Residual Stresses in René 88DT HPT Disks

Residual stress measurements were made at the surface and at selected depths of a 1/6 section HPT disk. A total of six measurement locations were chosen from a set of potential fracture critical locations. Four of the measurement locations were at slot bottoms and two measurements were located at aft upper bolt holes. All residual stress measurements were in the circumferential orientation. Residual stress measurements were made at the surface and at nominal depths of 12, 25, 50, 75, 125, 175, 250 and 350 μm. Blade posts were EDM from the disk to provide a clear path for the x-ray diffraction measurements. Prior to removing the blade posts a strain gage was applied at the location of x-ray depth measurements to measure relaxation strain. The change in strain caused by the removal of the blade post was used to calculate a sectioning stress. This sectioning stress correction as applied to the surface and all depth measurements equally. Sectioning stresses at the slot bottoms were negligible, less than 2 MPa.

Residual stress depth measurements at the aft upper bolt hole were made in the circumferential direction as a function of radial depth on one hole and as a function of axial depth on another hole. The axial depth measurements were made at a hole on the interior of the section, away from the free surface. The radial depth measurements were made on a small sectioned

piece that was liberated from the disk. A sectioning stress for the liberated piece was calculated base on a strain gage measurement at the x-ray location. The sectioning stress correction was 210 MPa. The residual stress depth profiles at both aft bolt holes were completely compressive. Typically, a component that has been shot peened will have compressive stresses on the surface and to a depth of approximately 150 μm. Deeper into depth the stresses will become tensile. However, since the depth profiles for these locations were compressive to a depth of 350 μm, it can be concluded that a bulk compressive residual stress was present at this location in the disk. The residual stress depth profile of the aft bolt hole near the edge was lower in magnitude to the profile at the midsection of the disk, consistent with the Poisson effect. Residual stress measurements were made at four different slot bottom locations. All slot bottom measurements of residual stress oscillated between tensile and compressive values.

4.4.2 Characterization of Residual Stress and Strain Fields in Waspaloy Compressor Disk

Residual stresses and strains in a 12th stage Waspaloy disk were determined using several complementary analytical and experimental techniques. Experimental measurements include X-ray diffraction, Moiré-interference gages, and strain gages. X-ray and Moiré data were collected before and after splitting the disk. Strain gage data were collected as the disk was split using EDM. Displacement of fiducial marks spanning the EDM cut were used as imposed boundary conditions to drive the closed form elasticity solution and the finite element predictions described in sections 4.4.3 and 4.4.4, respectively. The elasticity and FE predictions were in excellent agreement with measured strain gage data and the strains deduced from Moiré measurements.

4.4.3 Elasticity (Closed Form) Solution for Bulk Residual Stresses

Processing of the material for a rotor, machining the excess material from the processed shape and imposing service conditions on the rotor are the predominate factors creating bulk residual stresses (BRS) in an engine rotor. Since serviced rotors must be cut, usually several times, to excise material for characterization, a procedure has been developed to evaluate BRS in these rotors. In the procedure, the circumferential displacement that occurs across a radial cut between the outer rim and the inner bore is measured. If the rotor closes across the cut, enough material must be removed between the cut surfaces so that the surfaces are stress free, i.e., the surfaces do not contact, and the measured circumferential displacement is considered to be

24

negative. Currently, a number of these rotors have been cut not only to obtain test specimens but also just the BRS.

The BRS distribution in the rotor is assumed to be axisymetric. Prior to splitting, the BRS in the rotor is assumed to be given by the first-order, closed-form, elasticity solution [Timoshenko & Goodier, 1951]:

$$\sigma_{rr} = B_i (1 + 2 \ln r) + 2C_i + A_i / r^2,$$
$$\sigma_{\theta\theta} = B_i (3 + 2 \ln r) + 2C_i - A_i / r^2,$$
$$\sigma_{r\theta} = 0,$$

for the radial, circumferential, and shear stress, respectively, and where A_i, B_i, and C_i are constants and r is the radial coordinate. The solution applies ideally to a uniform thickness rotor. For a cut rotor, the circumferential displacement under generalized plane stress conditions across the cut is given by the linear function in r, $2\pi B_i r / E$, where E is Young's modulus. The constant, B_i, is determined from the measured displacements as a function of r across the cut. The other two constants, A_i and C_i, are determined so that the radial stress on the inner and outer boundaries is zero.

This stress solution has been extended to rotors of variable thickness. For this case, the rotor is likened to a series of concentric rings. A radial cross-section of the rotor would be composed of a series of rectangular cross-sections of the rings where the height of each rectangular cross-section of a ring corresponds to the average thickness of the rotor cross-section between the inner and outer radii of the ring. Internal features or voids of the rotor such as bolt holes that do not have circumferential continuity are not considered to contribute to the cross-sectional area of the rotor on average. The constants -- A_i, B_i, and C_i -- apply to the ith ring of a series of concentric rings that comprise the rotor. Let n represent the number of concentric rings. The n-sets of constants -- A_i, B_i, and C_i -- for each ring are solved by imposing the measured displacement across the cut as a proportional function of r, the continuity of the radial displacement and radial force at the interface between adjacent rings, and the radial stress on the inner boundary of the inner ring and on the outer boundary of the outer ring to be zero. This approximate solution has been found on average to compare favorably with a 3-dimensional finite-element solution that involves geometric details of the rotor.

The circumferential displacements across a cut have been evaluated for rotors that are thin with a ratio of maximum thickness to difference between outer and inner radii < 0.2 and thick with a ratio > 0.4. For a thin disk the circumferential displacements across a cut are

generally proportional to the radial coordinate. For a thick disk they may not be proportional to the radial coordinate especially in the vicinity of a thick inner bore. Prediction of bulk residual strains from the circumferential displacement across a cut of a thin rotor has been generally in good agreement with measurements of changes in strain at a variety of locations on the rotor obtained from strain gages and Moiré interferometry techniques. Also, predicted BRS have yielded results in agreement with changes in stresses measured by X-ray diffraction techniques. However, these measured stresses have a great deal of scatter associated with them.

4.4.4 Finite Element Solution for Bulk Residual Stresses

Finite element model estimates of the bulk residual stresses in all of the turbine engine disks mentioned in sections 3.6 and 3.7 (Pratt & Whitney AIM mini-disk, GEAE F404 LPT disk, and Pratt & Whitney F100 12th stage compressor disk) have been obtained based on analyses driven by measured relative displacement data from disks cut in the laboratory. Additional estimates for the Pratt & Whitney compressor disk have been calculated based on models in which an imposed temperature field is used as a potential function for the residual stress field. Analyses based on the cut-disk displacement data have been performed using both sector models and half-disk models. Calculations using the temperature potential method have been performed using half-disk models only.

Only one of the Pratt & Whitney AIM mini-disks has been split and measured. For all of the disks, the displacement measurements are essentially circumferential components, based on the location of fiducial marks on the surfaces of the disk. The location of the marks after splitting the disk has been determined to within approximately 0.00010 inch using a coordinate measuring machine (CMM) on the University of Dayton campus.

In the case of the mini-disk, the coordinate data are best represented by separate linear displacement variations in the bore and the rim, joined by a cubic spline. This special measure is needed because of the relatively large area and moment of inertia in the bore, due to the large flange there. A single, purely linear displacement fit underestimates the angular displacement in both the bore and the rim, causing the stresses to be underestimated as well. The residual hoop stresses predicted from the ABAQUS sector model of the disk agree quite well with Pratt & Whitney's forging simulations, which predict tensile stress of about 4.5 ksi in the bore and 10 ksi compression in the neighborhood of the rim. In this model, the peak stresses near the rim are somewhat lower (7.0 ksi), since the disk is split in the rim area to simulate the presence of blade slots.

The GE F404 disk has been analyzed for several sets of cut-disk displacement data, averaging an angular displacement of about five milliradians. The half-disk models show considerable stress variations in the area immediately adjacent to the cut, with relatively uniform stress in the remainder of the disk. In the sector models, the stresses are more evenly distributed because of the periodic boundary conditions on the hoop displacements. In our initial models, the details of the blade slot are not included due to a lack of geometry data. However, residual stresses in the neighborhood of 30 ksi (compression) have been estimated from these models, and later confirmed by more detailed models including the blade slot geometry.

For the Pratt & Whitney 12th stage disk, extensive comparisons have been made between the finite element model predictions and various measured data. Using solutions based on the measured cut-disk displacement data, the models have been used to predict strain variations in the cut disks as measured by both strain gauges and a Moiré fringe technique. Agreement of the predictions with both sets of measured data is excellent. The finite element predictions of residual stress also are in excellent agreement with analytical estimates based on closed-form elasticity solutions (section 4.4.3).

4.5   SHOT PEENING PROCESS SIMULATION

UDRI has prepared analytical models for the purpose of simulating the shot peening process, and the resulting residual stress and strain distributions. The primary purpose of this analysis is to characterize the details of the stress distribution in a way that x-ray diffraction measurements cannot duplicate, and to better understand the meaning of the "cold work" measurements typically obtained as part of the residual stress field data from x-ray diffraction studies.

Our analysis of the shot peening process uses LS-DYNA to predict the response of a sample of material to repeated impacts in a specified pattern on the surface. For simplicity, the impacting shot is idealized as being perfectly rigid. Initial estimates of the shot velocity and other peening parameters are obtained using a simplified model [Cao, et al.]. The solutions ultimately will need to be fine-tuned by simulating the response of the Almen strip used as an indicator in the actual process.

Shot peening simulations have been performed by specifying a sequence of impacts in an overlapping pattern on the surface of the specimen. The number of shots required to provide a reasonable simulation can be quite large, since the size of the contact area for a given impact is on the order of 0.1 mm. Thickness distributions of the predicted residual stresses are in excellent qualitative agreement with the X-ray diffraction data. The predicted peak subsurface stresses are

within 10-15 percent of the measured values. Simulations using a greater number of impacts over a larger area are planned. It should be noted that additional factors that may be important to the comparison have not been resolved, such as achieving the intended Almen intensity in the simulation.

5.0 PHYSICALLY-BASED CONSTITUTIVE MODELING

5.1 MODELING OF DEFECTS IN Ni-BASED SUPERALLOYS

In PM IN100, we have focused thus far on the characterization of voids, which are the primary defects of interest. Parametric, finite element-based modeling techniques are being investigated. However, the analyses that we have performed are based on closed-form elasticity solutions [Moschovidis] for the stress field in the neighborhood of a void or pair of voids. While the analysis is an elasticity solution, it is complicated enough that computer software is required to do the actual evaluation of the solution for specific parameters. Our software implementation of this model is capable of analyzing the stress field in the neighborhood of pairs of ellipsoidal voids (or inclusions), and defining stress concentration factors based on their spacing, aspect ratios, relative orientations, and properties. The analytical predictions have been corroborated by detailed finite element solutions for selected check cases. The advantage of the closed-form solution is clear since many cases can be evaluated very quickly without meshing problems or discretization errors.

5.2 PROBABILISTIC MODELING

A probabilistic model has been created to characterize stress concentrations caused by voids in PM IN100. The model uses Monte Carlo simulation to compute probability distributions of stress components in a material with known defect distribution statistics, including defect size, shape (aspect ratios), and spacing. The relative orientations of the defects, as well as the loading direction used, are assumed to be uniformly random. Thus far, the model has been used in conjunction with the elasticity model described in section 5.1 to compute probabilistic stress field data in PM IN100. Measured data for defect size, shape, and spacing have been obtained from measurements in various regions (rim, web, and bore) of serviced IN100 disks.

6.0 INTEGRATION OF EXPERIMENTAL PROCEDURES AND ANALYSES

A close relationship between experiments and analysis and modeling efforts is a primary goal of The UDRI on-site activity. This relationship is a consideration in every technical activity The UDRI has engaged in during the past year. The following paragraphs contain information on the specifics of these efforts to maintain a close experimental/analytical relationship and the results we have achieved.

6.1 TEST AUTOMATION SOFTWARE DEVELOPMENT

One of the hallmarks of contemporary material characterization testing is automation of the test control and data acquisition functions. The UDRI has been in the forefront of material mechanical test automation software for over two decades, having developed various automation software packages leading up to the current WinMATE implementation. In the past year, much of this effort has been shifted to a separate contract; however, a number of the key elements of the development were still performed as part of the on-site effort. Specifically, these elements include laboratory debugging, user feedback, and certain enhancements done in situ.

A significant part of developing automation software is ensuring that the functions and interface meet the needs of the end users. In the case of the on-site contract, the end users are both the technical staff charged with performing the tests on a day-to-day basis as well as the project engineers and scientists who determine the test conditions and data to be acquired. The initial software design is done, of course, with these needs in mind. Nevertheless, it is rarely possible to capture all the essential elements required by the end users without their direct feedback after using a working version of the software. The on-site UDRI staff has participated on a regular basis in both using the code, providing suggestions for enhancements, and reporting errors. This feedback has resulted in over 300 specific changes to the code, making it a substantially more usable research tool.

6.2 INFRARED DAMAGE DETECTION SYSTEM (IDDS) ENHANCEMENTS

One of the ways in which we integrate experiments and analytical modeling is by providing experimental tools that can measure physical parameters corresponding to specific elements of the models. As we extend material models from the continuum mechanics to the microstructural realm, we require tools that allow us to experimentally study material response at the same reduced scale. The UDRI has therefore been developing an enhanced infrared damage

detection system (IDDS) to detect highly localized damage regions on the scale of the microstructure.

6.2.1   Improved IDDS Resolution [C10]

In the base IDDS, a sensitive microscope system is used to monitor infrared radiation emitted by a specimen subjected to service loading. Small changes in radiation due to bulk volume dilatation, local work (plasticity, slip, etc.), cavity radiation, modified surface morphology, and other phenomena can be detected and precisely located on the specimen surface. Intensive material science studies can then be directed at the specific local region of the radiation anomaly. Cracks with surface lengths of 15 to 20 µm have been routinely detected in titanium and nickel-base alloys. Additional detection events show no observable surface-connected crack and may be evidence of pre-crack damage evolution.

The UDRI has enhanced the basic IDDS by integrating a new camera with improved resolution. This camera was installed to detect pre-crack damage evolution events on a regular basis. Studies of the localized damage phenomena at these sites will eventually produce a more thorough understanding of the damage mechanisms under realistic service loading.

6.2.2   IDDS at Elevated Temperature

The enhanced IDDS includes capability to operate at elevated temperatures. This work is being spearheaded by Dr. Richard Greene in conjunction with UDRI staff members. As the temperature is increased, infrared radiation levels also increase as the fourth power of the temperature in Kelvins. Thus, a method of reducing the intensity of the radiation is needed to avoid overloading the camera detector. To address this problem, a neutral density filter has been added to the IDDS camera/microscope system. The filter has specific band block characteristics which match the 3 to 5 µm wavelength band, where the camera collects photons. To date, data has been collected at temperatures up to 650ºC. This elevated temperature IDDS capability is essential if we are to obtain data directly related to the analytical efforts to model material behavior under actual service conditions.

7.0 HIGH CYCLE FATIGUE AND FRETTING

7.1 FRETTING FATIGUE UNDER HIGH CYCLE FATIGUE

7.1.1 A Fracture Mechanics Methodology Assessment for Fretting Fatigue [C11]

A fracture mechanics methodology was evaluated for a fretting fatigue geometry in which one end of a specimen clamped between fretting pads was loaded in axial fatigue. In previous work, results from experiments on Ti-6Al-4V pads and specimens were evaluated using finite element analyses where stress intensity factors were calculated assuming a single-edge tension, Mode I crack to form. In the present work, mixed-mode behavior was considered and a more realistic crack geometry was incorporated. K_I and K_{II} were calculated from stress fields determined from the finite element analysis using a weight function method and assuming a single-edge Mode I / Mode II inclined crack. A correction was then applied based on empirical crack aspect ratio data. K_I and K_{II} were analyzed for several experimentally determined combinations of contact pad geometry, specimen thickness, and loading conditions used to obtain a range of normal and shear forces, each corresponding to a fatigue life of 10^7 cycles. The fracture mechanics methodology was used to determine the conditions for propagation or non-propagation of cracks that initiate in the edge-of-contact region based on a mixed-mode driving force and a short crack corrected threshold. The coefficient of friction was also varied in the analyses. The fracture mechanics approach appears to be a better method for determining the threshold for fretting fatigue than a stress analysis because thresholds for K are better known than criteria for crack initiation in a gradient stress field.

7.1.2 Fretting Fatigue Crack Progression Study

A study was conducted to quantify fretting fatigue damage and to evaluate the residual fatigue strength of specimens subjected to select fretting fatigue test conditions. Flat Ti-6Al-4V specimens were tested against flat Ti-6Al-4V fretting pads with blending radii at the edges of contact. Fretting fatigue damage was investigated for 10% of total life for two combinations of static average clamping stress and applied axial stress, identified from prior work [Hutson, et al.]. Accumulated damage on some samples was characterized using full field surface roughness evaluation to assess the accuracy of surface roughness as a measure of fretting fatigue damage. All samples were inspected using SEM to identify and measure fretting fatigue cracks, and were heat-tinted to mark the crack front location of those cracks. The effect of fretting fatigue on uniaxial fatigue strength was quantified by step-loading the fretting-damaged specimens under

uniaxial fatigue loading at R=0.5 and 300 Hz. Results from the residual fatigue strength tests were correlated with characterization results. Crack aspect ratios were measured via optical fractography and the results used with the fatigue limit stress, identified during the uniaxial testing, to evaluate the threshold behavior for cracks of various size.

Surface roughness measurements, quantified in terms of asperity height, indicated no measurable difference with unfretted specimen surfaces. When quantified in terms of asperity spacing, the roughness measurements did reflect changes in the specimen surfaces as a result of fretting fatigue cycling, but those changes did not correspond to the presence of previously identified fretting fatigue cracks or to decreases in residual fatigue strength. Fretting fatigue cracks with surface lengths, 2c, of 100 μm or greater, which were only identified on specimens tested at the higher stress condition, were required before measurable decreases in residual fatigue strength were recorded. Aspect ratios measured for cracks that propagated to fracture during uniaxial fatigue cycling were very near unity for crack surface lengths below 150 μm, but tended to decrease with increasing crack surface length. Threshold stress intensity factors calculated for these cracks indicated threshold behavior consistent with naturally initiated cracks that were stress relieved to remove load history effects.

7.1.3 Effect of Contact Material on Fretting Fatigue Behavior of Ti-6Al-4V

An experimental study was conducted to explore fretting fatigue behavior of Ti-6Al-4V in contact with varying pad surface compositions. Four conditions were selected to provide a range of compositions and hardnesses: Ti-6Al-4V, 7075-T6 Al, IN100, and Cu-Ni plasma spray-coated Ti-6Al-4V. Mechanical behavior against each of the pad types was characterized through S-N fatigue testing and through evaluation of fretting fatigue strength for 10^7 cycles via step testing. Coefficient of friction, μ, was quantified for the experimental configuration and loading conditions used here. Pad surfaces were characterized through visual assessment via SEM, hardness and composition evaluation, and surface profile measurements. Results from the Cu-Ni coated pads were compared to results obtained from a cross-section of a retired compressor blade bearing similar base alloy and coating composition and structure.

Limited difference in fretting fatigue strength was associated with contact material. A modest increase in strength was observed for specimens tested against IN 100 and coated pads as compared to those tested against Ti-6Al-4V pads; however, pad roughness was identified as primary factor in the increased capability. Another factor was determined to be μ, which was identified as ~0.7 for Ti-6Al-4V, ~0.4 for IN100, ~0.3 for coated pads and ~0.2 for Al pads. Fretting wear was minimal for all cases. IN 100 pads produced the greatest amount of debris on

the specimen, in which a considerable amount of oxygen was identified during spectral analysis. Some of the oxidized material on the specimens was identified as being TiO_2 or alumina and resulted in some wear of the harder material in the dissimilar material pairs.

Spectral analysis was also used to compare the coated pads to a retired blade root section. The composition and structure of the base metals were similar, identified as titanium alloys with an equiaxed primary α and $\alpha_2+\beta$ lamellar duplex structure. Both coatings were composed of copper and nickel in solid solution and exhibited evidence of extensive porosity from the plasma spray process used in coating application. The substrate/coating interfaces were both characterized by the presence of alumina particles, presumably from the surface preparation process used prior to coating application. The blade coating did show evidence of a layered coating structure, suggesting the use of different spray parameters. The primary difference between the test pad and the blade root was in wear characteristics. While the test pad indicated only plastic deformation of asperity tips and negligible wear, the blade root bore evidence of extensive wear and degradation or removal of the coating in certain regions.

7.1.4 Fretting Fatigue Damage Characterization

Each of the specimens tested in the fretting fatigue test fixture used for AFRL/MLLMN by UDRI has several locations where cracks may nucleate. However, not all of those locations will bear cracks when subjected to nominally identical fretting fatigue conditions, due to local variations in surface topography and microstructure. Many specimens subjected to the fretting fatigue conditions described in section 7.1.2 either bore no quantifiable damage (i.e. no cracks) or only bore one or two cracks out of the eight possible crack locations. These results indicate no measurable reduction in strength in the absence of a measurable crack, but some damage would be expected to accumulate even if cracking had not yet commenced. An investigation to quantify this damage has been developed and is intended to help identify those regions where crack nucleation was imminent as well as investigate what differences make one region more resistant to fretting fatigue cracking than others.

Several specimens from section 7.1.2 and from prior investigations have been identified for further characterization, and additional testing is planned to allow comparison of specimens with and without the residual stress field that results from the specimen manufacturing process. A characterization matrix has been developed and includes residual stress measurement, non-linear acoustic evaluation, SEM, TEM, metallographic analysis, eddy current and thermography assessment.

7.1.5 HCFF Technical Support

UDRI has provided technical support for testing programs being conducted by AFRL/MLLMN personnel, including development of a 300 Hz fretting fatigue fixture similar to the one currently used at Purdue University, ongoing investigation of fretting fatigue under conditions of variable contact loading, and assessment of fretting nucleated crack behavior via bend testing of C-shaped specimens. This support has been provided in the form of recommendations on various hardware requirements to fit the fretting fatigue fixtures onto the previously assembled HCF test systems. Also, UDRI has provided the necessary changes to the data acquisition software to accommodate the requirements of the newly developed fretting fatigue apparatuses.

7.1.6 Shear Wave Crack Detection Feasibility In Fretting Fatigue

In the 1999-2000 contract year, UDRI conducted experiments to evaluate the viability of using ultrasonic shear wave crack detection to locate fretting fatigue cracks *in situ* as part of a larger fretting fatigue investigation. This year (2002-2003), this work has been expanded to confirm prior results and to provide an adequate material for documentation of the work in a journal. Testing of a specimen, with EDM notches located at the edges of contact, was tested to evaluate the response of the ultrasonic crack detection hardware for notches of different size and placement along the edge of contact and to determine the sensitivity of the technique in the presence of components in contact. Since the transducers used in the study were designed to detect damage occurring in the middle of the specimen, two center notches of different size (250 and 500 μm wide) were manufactured to allow for comparison of the ultrasonic response. Also, the 500 μm center notch was compared with 500 μm notches that were placed off-center to determine how much ultrasonic signal might be lost when interrogating a fretting-fatigue nucleated crack, which would tend to nucleate near the specimen edge. The sample was also inspected post-test using ultrasonic c-scanning for correlation with the shear wave results. Autocorrelation of the shear wave responses is planned in addition to the comparison with the c-scan results.

7.2 20 kHz TEST SYSTEM DEVELOPMENT

During the past year, UDRI has been involved in continuing the development of a test system to run at ultra-high frequency. The system was installed in the lab approximately two years ago, but loads in the test specimens had not been verified and test control software had not been developed. UDRI has completed development of LabView® based software, which features

a graphical user interface and is designed to control essential test parameters and perform data acquisition functions for S-N and step-load testing. In addition, the loads conveyed to the test specimen have been verified for positive stress ratios. The system will be deemed fully operational as soon as the specimen loads have been verified for R=-1.

8.0 DAMAGE TOLERANCE STUDIES OF γ-TiAl-BASE TITANIUM ALUMINIDES

8.1 MODELING EFFORTS OF STRESS STATES LEADING TO CRACK INITIATION

8.1.1 Determination of Young's Modulus of Grains in a Gamma Titanium Aluminide Alloy [C12]

As efforts continue to mature gamma titanium aluminide alloys from the laboratory into industrial application, significant work remains to accurately model the behavior of these intermetallic materials under service load conditions. The development of accurate models is dependent upon the input of reliable material properties that, in the case of gamma alloys, reflect the anisotropy intrinsic to their make-up. Of particular interest is development of models to predict elastic and plastic behavior as a precursor to fatigue initiation and crack growth. In a review of information pertaining to Young's modulus measurements for γ-TiAl alloys, primarily those for polysynthetically-twinned (PST) materials, the reported data showed significant differences based on alloy chemistry and lamellar spacing, as well as lamellar orientation. The lack of information regarding the elastic behavior of these alloys is in contrast to the well-understood effects of lamellar orientation on plastic deformation and fracture. From this review it was concluded that development of a consistent set of Young's modulus measurements was requisite to develop an accurate, finite element-based model. Therefore, an experimental and analytical process for determining the elastic response of grains in a gamma titanium aluminide alloy was developed. Three-dimensional finite element models were employed to deduce the transversely isotropic properties. The results were compared with those reported for PST materials.

8.1.2 Measurement and Modeling of Orthotropic Elastic Behavior of Grains in a Gamma Titanium Aluminide Alloy [C13]

Gamma titanium aluminide (γ-TiAl) alloys have been under development for use in rotating components for gas turbine engines. Detailed 3-dimensional (3D) grain-level finite element models are being developed to predict damage initiation and accumulation in γ-TiAl during service loading. These models require knowledge of the orthotropic nature of the elastic and plastic deformation of individual grains. While the elastic properties of gamma and alpha-2 single-phase materials have been extensively studied, the elastic response of fully lamellar two-phase materials has not received the same degree of attention. This study employed an integrated experimental and analytical approach to deduce the elastic grain properties in a γ-TiAl.

37

Specimens with gage sections composed of specifically-oriented individual lamellar grains were tested in tension. 3D finite element analyses were used to deduce the elastic grain properties. These grain properties were used to accurately predict the elastic properties of PST and polycrystalline γ-TiAl.

8.1.3 Numerical Models of Orthotropic and Lamellar Grain Structures [C14]

In this study, a method for numerically estimating localized stress concentrations that arise in materials with anisotropic crystalline grains was utilized. This method is used to quantify stress variations within polycrystals of γ.TiAl, a material system composed of two phases of orthotropic material – lamellar colonies of TiAl/Ti3Al interspersed with small grains of pure TiAl. Effective elastic properties for the lamellar colonies are calculated from the constituent properties using a procedure developed for laminated orthotropic materials. It was postulated that the local anisotropy and differing orientations of adjacent grains of material can lead to microyielding at stresses below the mean yield strength of the material. The effects of local elastic anisotropy on stresses are presented as statistical variations in the stress distributions under simple states of loading. Three-dimensional and two-dimensional models were investigated.

8.1.4 Compression Testing of Micro-Specimens Machined via FIB

In collaboration with researchers from MLLM, compression testing of micro-specimens machined from large grain K5 material was undertaken. The cylindrical micro-specimens were fabricated using a FEI DB235® dual electron beam/ focused ion beam microscope. The specimens were approximately 20 mm in diameter and 50 mm in height. One end of the micro-specimen remained attached to the base metal, i.e., the sample had only one free end. To perform the compression tests, the unconstrained end of the specimens was loaded using a MTS Nano Indentor® XP with a flat-tipped diamond indentor. Loads were monitored via a piezo-based load cell. Specimens with two different lamellar orientations were fabricated and tested. As expected, the anisotropic nature of the gamma TiAl material was exhibited by the distinctly different elastic and plastic response of each orientation. Post-test microscopy revealed the presence of significant slip plane activation over the length of each specimen. The use of micro-specimen test methods will eventually allow for the timely generation of grain-based properties that will greatly aid in the development of accurate material property prediction models.

8.2   SMART CONCEPT DEMO]

With many different material systems and at many size scales, our ability to develop models of material behavior has advanced well beyond our ability to efficiently evaluate and calibrate these models. Evaluation and calibration of sophisticated, physically-based models are hampered by the relative paucity of data that are available through traditional test techniques. One very promising area for efficiently acquiring large amounts of good-quality data is through full-field deformation mapping accomplished with machine vision. With full-field deformation mapping, it is possible to study material behavior under a wide variety of conditions and at a wide variety of spatial scales. It is also possible to efficiently calibrate and evaluate probabilistic models through automated and extensive sampling. A prototype system was developed for integrating modeling and experimentation, enabling very efficient evaluation and calibration of candidate material-behavior models.

9.0 DAMAGE ACCUMULATION AND FAILURE OF CERAMIC MATRIX COMPOSITES (CMC)

9.1 CHARACTERIZATION OF OXIDE/OXIDE, SiC/SiC AND C/SiC CMC

9.1.1 Creep Rupture Behavior of ±45° Oxide/Oxide Nextel™720/AS Composite [C15]

Oxide/Oxide Ceramic Matrix Composites (CMC) are currently being demonstrated in high-temperature aerospace applications where their beneficial resistance to oxidation is critical to a successful design. Typical applications include engine components that are axis-symmetric in shape and subjected to axis-symmetric thermal and mechanical loadings. Traditional woven CMC materials used in these components are typically made from rectangular 0°/90° fiber architectures. In many cases the highest stresses are not coincident with the orientation of the reinforcing fibers. Hence, these components could produce stress states that approach the off-axis tensile and creep strengths of the CMC. The CMC investigated was composed of an Alumina-Silica matrix reinforced with an eight-harness satin weave (8HSW) of Nextel™720 fibers. Tensile and creeps tests on ±45° Nextel™720/AS were performed to characterize the off-axis material behavior. All elevated temperature tests were performed at 1100°C. The data show that the ultimate strength and the 100 hour creep strength ratio of ±45° to 0°/90° are 0.6 and 0.3, respectively. Results of creep tests show that the secondary creep strain rate of the ±45° orientation can be as high as 5000X that of the 0°/90° orientation at 1100°C and 90MPa.

9.1.2 Durability of MI SiC/SiC Composites with Effusion Holes

Melt-infiltrated (MI) SiC/SiC CMC are targeted for high-temperature aerospace applications such as combustor liners. These components may include effusion holes that are used to lay down a film of cooling air on the hot wall. During service, these locations are subjected to long-term exposures, cyclic mechanical loading and thermal stresses. A study was initiated to assess the durability of MI SiC/SiC with effusion holes. MI Sylramic/SiC and High-Nicalon-S/SiC straight-sided specimens with 0.5 mm diameter holes laser machined at a 20° angle to the specimen surface were evaluated under sustained-load (creep) and cyclic fatigue test conditions. Test results show that cyclic fatigue loading has a lower rupture life than sustained loading.

9.1.3   Interrupted Fatigue Testing of MI and CVI C/SiC CMC

Experimental support was provided to Dr. Shankar Mall for interrupted fatigue testing of MI C/SiC. These tests support a program with NASA to develop a non-destructive assessment method for material damage in CMC. A total of thirty-six test specimens are in the test matrix. The effect of frequency, stress ratio, maximum stress and temperature are under investigation. The test matrix has four interruptions during the life of the specimen for non-destructive measurements by NASA. Two of the non-destructive measurements have been completed. The first set consisted of running 5 cycles on each specimen. The second set was ten thousand cycles at 10 Hertz on each specimen. Numerous slip tests in the gripping fixture were completed to determine the best chose of tab material and grip pressure to minimize grip failures and specimen slipping.

9.2   ELASTICITY/DAMAGE/CREEP MODEL FOR OXIDE/OXIDE NEXTEL™720/AS CMC

Creep behavior of the N720/AS material system has been the main area of investigation in the current reporting period. The creep behavior is fiber-dominated, so determining the fraction of the nominal stress actually sustained by the fibers is a critical issue for creep modeling. A second important characteristic, also related to the relative stiffness and creep resistance of fiber and matrix, is the highly anisotropic nature of the creep response of the composite.

Creep characteristics of the Nextel 720 fiber have been defined using single fiber creep data [Wilson, et al.]. A two-level Mori-Tanaka model [Mori and Tanaka] has been used to define the effective properties of the CMC and, in the process, define stress amplification factors relating the fiber stress to the nominal stress components. The first level of Mori-Tanaka analysis is used to define effective properties of the matrix since the matrix material cannot be manufactured and tested directly. The effective properties for the matrix are obtained using handbook properties for the alumina and silica components together with measured volume fractions of alumina, silica, and voids. The second-level analysis combines the effective matrix properties with the fiber properties to define effective elastic properties of the CMC as well as stress and strain concentration factors for the fiber and matrix regions. It should be noted that, when the composite is loaded and sustains damage that degrades the elastic properties, the corresponding effective properties and stress concentration factors also change. The code we have written for effective property calculation takes this effect into account. Accordingly, the stress concentration factors used to determine fiber stresses for creep analysis are stress dependent. In all of the creep

analyses performed with this model, we have assumed strictly monotonic loading up to the stress level of interest prior to analyzing the creep behavior.

Several blind predictions have been made of the 0-degree and 90-degree CMC creep behavior at 1000-1200°C, including data from AFRL and NASA Glenn. All of these analyses predict the steady creep rate of the CMC within a factor of two, which is considered excellent agreement.

In-house experimental studies of the off-axis creep behavior of N720/AS have been performed primarily using notched specimens, taken from a weave CMC and instrumented to record off-axis data in areas of stress concentration. During the present reporting period, basic off-axis data for the creep behavior were not available; however, analyses of the notched specimens have been performed for a series of assumed off-axis properties. In particular, we employ the creep rate potential

$$f(\sigma) = \sqrt{\sigma_{11}^2 - \sigma_{11}\sigma_{22} + \sigma_{22}^2 + \frac{3}{k^2}\sigma_{12}^2}$$

leading to the creep strain rate components

$$\dot{\varepsilon}_{ij} = \dot{\varepsilon}\frac{\partial f}{\partial \sigma_{ij}}$$

in which the effective creep rate is determined from the stress level, temperature, and damage state at a point. Here 'k' is a factor characterizing the anisotropy of the creep behavior; $k = 1$ implies isotropic creep response, and $k < 1$ gives more flexible off-axis creep behavior. Predictions of the notch mouth opening displacement (NMOD) of notched specimens tested at AFRL suggests that k is between 0.25 and 0.5. A value of $k = 0.25$ implies that the creep rate for a 45-degree orientation for a given stress is about 20 times as great as the corresponding fiber direction creep rate.

Analyses of notched specimens for 70 hours at 100 MPa nominal stress and 1100°C have been performed for several k values between zero and one. The results reveal that for sufficiently anisotropic properties, relaxation of the net section stresses in a notched tension specimen may not occur as it would in a similar, isotropic specimen, and in fact the peak stress might even increase. The reason for this behavior is that, in an anisotropic material, the most significant creep rates can occur in areas that do not have the highest stresses, but merely have high principal stresses aligned with the ±45-degree material directions. Such areas shed load to other regions in

which the material is more favorably oriented for resisting the loads, but actually have higher principal stresses.

9.3 HIGH CYCLE FATIGUE OF CVI C/SiC COMPOSITE

Experimental support was provided for high-frequency (500 Hz) HCF testing of chemical vapor infiltrated (CVI) and melt-infiltrated (MI) SiC/SiC CMC at elevated and room temperature, respectively. Dynamic load calibrations were completed with this study and were shown to be consistent with previous calibrations. An extensive study of load train alignment, specimen gripping and tab material were completed to reduce the number of grip failures and specimen slipping of these higher strength CMC materials. Hardware modifications included the upgrade of a DC power supply for reduction of noise into the data signals and improved test system control.

10.0 Ancillary Test Facility Activities

10.1 MATERIAL BEHAVIOR

10.1.1 Tensile Testing of Gamma Titanium Aluminide Specimens

Thirty-seven gamma titanium aluminide specimens were tensile tested at temperatures ranging from room temperature to 980°C. These specimens included numerous compositions and heat treatments. References for the publication of these test results for the specific materials are given in Table 1 below.

Material Composition (at %)	Designation	Number of Tests	Reference
Ti-46Al-1.75Cr-3Nb-.17W-.18B	K5A	3 ET Tests	[Kim and Dimiduk]
Ti-45Al-1.2Cr-2.2Nb-.3Mo-.3C		4 ET Tests	[Y-W. Kim et al.,1]
Ti-46Al-1.2Cr-.3Mo-.3C		4 ET Tests	[Y-W. Kim et al.,1]
Ti-46.2Al-2Cr-3Nb-0.2W-0.2Zr-0.2B-0.1Si-0.2C	99C	6 RT Tests	[Y-W. Kim et al.,2]
Ti-46Al-1Cr-3Nb-0.3W-0.2B-0.5C-0.2Si	02K5B1	4 RT & 4 ET Tests	ib.
Ti-45Al-1Mn-6Nb-0.5W-0.15B-0.6C-0.2Si	02DB1	4 RT & 4 ET Tests	ib.
Ti-46Al-1Cr-3Nb-0.3W-0.2B-0.5C-0.2Si	02K5B2	2 RT Tests	ib.
Ti-45Al-1Mn-6Nb-0.5W-0.15B-0.6C-0.2Si	02DB3	6 RT Tests	ib.

10.1.2 Torsion and Tension Fatigue Testing of Turbine Blade Material (Ti-6-4), with Quantified Impact Damage

This test program required the design of a torsion fatigue test fixture and the development of a torsion test method for turbine blade material (Ti-6-4) test specimens. The specimen was planar with ends having a rectangular cross-section and with a center test section having a cross-section similar to the cross-section of a turbine blade with simulated foreign object damage (FOD). Since the specimen cross-section would warp under an applied torque, axial deformation parallel to the torsion axis was not restricted in the grips.

The center test sections were impacted with a 1/8" diameter chrome steel sphere at velocities of 200 and 300 m/s to simulate FOD. Some of the specimens were vacuum stress relieved after impact. Baseline torsion fatigue tests at applied torque ratios of 0 and –1 were conducted on specimens that had not been impacted.   Torsion fatigue tests were conducted on specimens in the as-impacted condition at applied torque ratios of 0 and –1 and in the stress-relieved condition at an applied torque ratio of 0. These specimens were fatigued until visible cracks appeared in the test section.

The torsion tests were performed on a horizontal test frame with a rotary actuator in torque control. The waveform for the applied torque was sinusoidal at 10 Hz and the amplitude was controlled with a PC using the MATE test software.

Tension fatigue tests were conducted on the impacted specimens having the same geometry as the torsion specimens in both the as-impacted condition and stress-relieved condition at an applied stress ratio of 0.1. The tension fatigue tests were conducted on a standard fatigue test frame with a sinusoidal waveform at a frequency of 30 Hz until fracture.

All tests were conducted using an increasing stress-step method where the tests were started at a stress level below the expected failure stress for 10^6 cycles and was increased 10% after each 10^6 cycles block until failure occurred. All tests were conducted in laboratory air at a temperature of 23°C.

10.2 LABORATORY ENHANCEMENTS

10.2.1 Upgrade Of Laboratory Test Automation Hardware and Instrumentation

About two-thirds of the servo-hydraulic test systems (eighteen out of 27) have been updated using the Windows-based WinMATE DCPD software and seventeen of those systems use the large console for expanded instrumentation usage. In addition, a roll-around WinMATE system is used for load-train alignment and two Mate roll-around systems are available for test control of the remaining systems that have not been updated.

10.2.2 HCF Laboratory LabView Software and Hardware Implementation

A new field supply was installed on the large Unholtz-Dickie shaker system. A new DC power supply was researched, purchased, and implemented into the lab to replace the previous 3-phase power supply. The new power supply eliminated unnecessary electrical noise from the older power supply, improved the safety of the test system, and allowed for greater flexibility in the test system.

An eddy current sensor was needed for the resonance test system to allow for the determination of loads applied to test coupons at these high frequencies. The previous sensor had a bandwidth of only 10 kHz. This bandwidth was unacceptable for use in this system. The new sensor and electronics are currently being used to conduct tests at 20,000 Hz at a stress ratio of -1.0 to determine if bending of the specimen has been playing any role in the previous tests that were conducted at stress ratios >0.

The HCF software for resonance system was modified to incorporate two A/D boards and to increase the loop time for better system control. The need for faster data acquisition on the

resonance system required that we introduce a second National Instruments board into the system to allow for collection of feedback signals to more effectively control the command signal. This change will be unique to this test system. The HCF software was also changed to determine load transfer for fretting tests and to include interlocks to stop data acquisition.

Modifications to a utility software package were made to allow for a direct comparison of applied axial load and the load transferred through a fretting rig. This package will eventually be incorporated into the main HCF software library. An interlock system was also incorporated to stop the software upon completion of the tests to reduce the excess data collection and the time required to manipulate the data.

A new digital filter was coded to remove noise from signals without significant delay in loop time. Usually, digital filtering of signals is discouraged because of the increased software loop time and sluggish control obtained from this loss of speed. However, the unique requirements of this test system required that we handle the feedback signals in a manner that would allow for more accurate data manipulation. This filter performed better than the previous analog filters used and allowed for the signals to be more effectively monitored during the system design/checkout procedure. While originally designed to be used in the resonance system, this filter has proven to be very useful in other applications and is being installed in various software packages used in the HCF lab as time becomes available.

Created new software to allow monitoring of accelerometers for determining system maintenance requirements. This software package contains a 3 dimensional graph that allows for a graphical representation of the actual armature movement of the various shaker systems. By occasionally using this software, the actual displacements of the armature can be seen and any repair work can be implemented to assure system life and alignment.

10.2.3 Improvement in Load Frame Alignment Equipment and Procedures

Process optimization of load frame alignment procedures was the focus of the past year. Equipment modifications to increase measurement sensitivity were implemented. Alignment specimens were uniquely configured to match loading and dimensional requirements of test coupons thus insuring precise frame alignment within the boundaries of the actual test. In-house preparation of alignment specimens has greatly reduced cost and lead-time for obtaining new geometries.

46

10.2.4 Improvements to the Laboratory Water Cooling System

The laboratory water-cooling system was flushed and cleaned after many machine shutdowns due to internal corrosion and algae issues. The reservoir tank was cleaned out and the aluminum block manifolds (the corrosion source) were reamed out. Steel plugs in the manifolds were replaced with aluminum plugs. Loops were added to the end of each branch to keep water flowing and prevent the water from becoming stagnant when test systems on a branch were not used. Two different types of corrosion inhibitors and an algaecide were added to the system and are being monitored to keep the system stable.

10.3 DATA ARCHIVAL SYSTEM

The Data Archive is a central computer on which test data generated by MLLMN is stored and indexed. Its purpose is to prevent the loss of valuable test data and provide independent user access within MLLMN. UDRI provides continued support for local server administration of file access privileges and works with MLOC on global system administration. A large volume of test data for coupons was added to the archive to the archive this year and the documentation provided to the users was maintained.

Plans are being developed to address issues of archive education for new and existing users, as needed. UDRI has also begun developing instructions for data transfer from the physically isolated networks (PINs) to the data archive, which will be incorporated into the archive standard operating procedures documentation. Instructions will be provided for users with and without network access authorization.

11.0 REFERENCES

Cao, W., R. Fathalloh, J. Barralis, and L. Castex, "Residual Stresses in Shot Peened Metal Components. SHOTPEEN: An Interactive Prediction Software," Shot Peening (ICRS4), Society for Experimental Mechanics, Baltimore, Maryland, 1994.

Hutson, A.L., C. Neslen, and T. Nicholas, "Characterization of Fretting Fatigue Crack Initiation Processes in Ti-6Al-4V," Tribology International, 2002, pp. 133-143.

Mori, T. and K. Tanaka, "Average Stress in Matrix and Average Elastic Energy of Materials with Misfitting Inclusions," Acta Metallurgica, Vol. 21, 1973, pp. 571-574.

Mosschovidis, Z.A., "Two Ellipsoidal Inhomogeneities and Related Problems Treated by the Equivalent Inclusion Method," Doctoral Dissertation, Northwestern University, 1975.

Timoshenko, S. and J.N. Goodier, , Theory of Elasticity, 2nd ed. McGraw-Hill Book Co., Inc., 1951, pp. 66-69.

Wilson, D.M., S.L. Lieder, and D.C. Lueneburg, "Microstructure and High Temperature Properties of Nextel 720 Fibers," Ceramic Engineering Science Proceedings, Vol. 16, No. 5, 1995, pp. 1005-1014.

LIST OF SYMBOLS, ABBREVIATIONS, AND ACRONYMS

ABBREVIATION	DEFINITION
3D	Three-dimensional
3-DFE	Three-dimensional finite element
8HSW	Eight harness satin weave
γ-TiAl	Gamma titanium aluminide
A/D	Analog-to-digital
BMF	Brittle micro fracture
BRS	Bulk residual stress
CDF	Cumulative distribution function
CFCDE	Crack front cyclic diffusion embrittlement
CMC	Ceramic matrix composites
CMM	Coordinate measuring machine
CVI	Chemical vapor infiltrated
DCPD	Direct current potential difference
DEN(T)	Double edge notch tension specimen
EDM	Electric discharge machining
ERLE	Engine Rotor Life Extension
FCG	Fatigue crack growth
FIB	Focused ion beams
FOD	Foreign object damage
GE	General Electric
GEAE	GE Aircraft Engines
HCF	High Cycle Fatigue
IDDS	Infrared Damage Detection System
IHPTET	Integrated High Performance Turbine Engine Technology
MI	Melt infiltrated
MLLM	Metals Branch
MLLMN	Behavior/Life Prediction Section
MLOC	Government Computer Support
NDE	Nondestructive evaluation
NMI	Nonmetallic inclusion
NMOD	Notch mouth opening displacement
NTED	National Turbine Engine Durability
OIM	Orientation imaging microscopy
PIN	Physically isolated networks
PM	Powder metal
P/M	Powder metallurgy
PST	Polysynthetically twinned
SBIR	Small Business Innovation Research
SEM	Scanning electron microscopy
Ti	Titanium
USAF	United States Air Force
XRD	X-ray diffraction

APPENDIX
COMPILATION OF MANUSCRIPTS

LIST OF MANUSCRIPTS

EFFECTS OF DEFECTS ON CRACK INITIATION OF IN100 (P/M) UNDER LOW CYCLE FATIGUE CONDITIONS

K. Li[†], N. E. Ashbaugh[†] and A. H. Rosenberger[*]

It is well established that fatigue crack initiation of Ni-base superalloys occurs at intrinsic defects. IN100 produced by powder metallurgy technique contained contrasting populations of pre-existing pores and nonmetallic inclusions (NMI). The purpose of this investigation was to examine the effects of the defect type, shape and size on the low cycle fatigue crack initiation behavior. Both void and NMI related origins were almost equally observed on the fracture surfaces using SEM. The void-related origins were located on the sample surface and NMI related origins tended to locate subsurface or internal. Critical sizes for void and NMI related defect origins appear to exist with the critical NMI area greater than an order of magnitude larger than the void area. The statistical 2-D distribution of defect size and shape in the cross section of a forging, indicated that the results excluded the large NMI particles, which had a low sampling probability due to low volume percentage.

INTRODUCTION

IN100, a nickel-base superalloy, is currently employed for US Air Force gas turbine engine applications. The potential causes of these component failures are mainly due to low cycle fatigue (LCF). It has been well established that fatigue cracks in nickelbase superalloys nucleate from defects [1-3]. Very small voids and NMI are common in IN100, which was manufactured via powder metallurgy (P/M). The objective of this study is to evaluate fatigue crack initiation under LCF conditions, since the LCF life of nickelbase superalloys is always dominated by crack nucleation [1]. The fatigue crack initiation sites on the fracture surfaces were identified, the defect types were characterized, and the defect shapes and sizes were measured. A comparison was made between defect size and shape of the crack nucleation site observed in the fracture surface and the defect size and shape distribution on a cross section of a forging.

[*]Air Force Research Laboratory, Materials & Manufacturing Directorate, AFRL/MLLMN, 2230 Tenth St, Wright-Patterson AFB, OH 45433-7817 USA

[†] University of Dayton Research Institute, 300 College Park, Dayton, OH 45469-0128, USA

MATERIAL AND EXPERIMENTAL PROCEDURE

The structure of IN100 was produced via gas atomization, extrusion and isothermal forging, followed by supersolvus solution heat treatment and aging. Figure 1 shows the microstructure composed of γ' particles and annealing twins in the γ matrix. The average grain size is about 20-25 μm. Cylindrical specimens having a nominal diameter of 6.35 mm were machined and specimen surfaces were low stress ground. The fatigue test was conducted in air at 538°C and frequency 0.5 Hz, under loading control with a stress ratio, R, of 0.05. Nine specimens were tested. Four of the nine specimens were machined from a scrap forging (labeled virgin material) and the other five from a used component (labeled serviced material). The axes of all the cylindrical specimens are parallel to the circumferential direction of each respective component.

An analysis of the defect in a cross section of the virgin material was performed. Generally two kinds defects were observed in this material: voids and non-metallic inclusions (NMI). Voids generally have an elliptical shape and are often found in interconnected clusters, Figure 2(a). Figure 2(b) shows two NMI particles. Energy dispersive x-ray spectrum (EDS) indicated that the NMI was composed of mainly aluminum oxide and some silicon oxides. To obtain a defect size and shape distribution of the material an entire cross section was cut into eleven pieces followed by mounting and mechanical polishing. Twenty optical images at 200x magnification were randomly taken for each specimen. The defect size, shape and distribution were analyzed from the images using computer software. Fractographic examination was conducted on the samples to characterize both the location and source of crack origins. Geometric details of the crack-causing defect were also measured in the SEM.

RESULTS AND DISCUSSION

Fatigue crack initiation sites: number, location & feature

Due to test temperature of 538 °C, each crack initiation region is colorfully heat tinted and can be easily recognized. The shapes of the tinted regions are dependent on the location of the initiation site – surface or slightly subsurface origins have a thumbnail shape and the internal origins are circular. Using scanning electron microscopy, the fatigue crack initiation site(s) of each tested specimen (total nine) could be pinpointed. SEM images clearly revealed that the fatigue crack nucleation was induced by a defect, either a void, see Figure 3 (b,d), or a NMI, see Figure 3(a,c). The fatigue crack of sample #760, Figure 3(a), originated from internal NMI and sample #763 from 100um subsurface NMI, Figure 3(c). In both cases twinning was involved in micro-crack propagation. The cracks of sample #491 and #761,

both originated from void clusters on the surface. On the fracture surfaces the main voids looked very deep with interconnection of several of the voids. The initiation sites of all nine specimens are transgranular cleavage and the cleavage planes are perpendicular to the loading axis. This indicates a mode II initiation; that is, fracture stress governs the initiation process instead of yield strength.

The majority of the tested specimens had only one fatigue crack. Multiple fatigue initiation was observed on two specimens: #762 and #491. Two cracks were initiated on #762 and propagated independently until they finally joined together. For #491 six cracks were initiated and propagated but only one developed into a dominant crack and that was responsible for the final fracture. It is believed that this was due to a two-step loading, that is 8,437 cycle were applied 1000MPa followed by 2,224 more cycle at 1140 MPa (R=0.05) which lead to failure. It is believed that the minor cracks initiated when the load increased to 1140 MPa but the major crack initiated at the lower stress level.

Figure 4 shows projections of the initiation sites traced from SEM images of the fracture surfaces. Based on this figure, the values of area, aspect ratio, length and width of the initiation cracks were determined using image analysis software. Table 1 summarizes the results of the fatigue testing and measurement of initiation defects. The fatigue test results in Table 1 show that there was no significant difference in the LCF strength observed between the virgin and serviced material.

TABLE 1   Results of LCF Test (540 $^{\circ}$C in air, R = 0.05 & 0.5Hz) and Fatigue Crack Initiation Size Measurements

ID	Stress σ_{max} (MPa)	Nf	Initiation site location, feature (numbers of site)	Initiation site			
				area (μm^2)	aspect ratio	length (μm)	width (μm)
486V[1]	1000 /1140	10,661	Surface void (1)	237.8	1.38	19.6	15.7
491V	1140	10,919	Surface void (6)	273.0	1.50	23.5	16.4
493V	1140	11,633	Surface void (1)	248.2	2.30	28.9	15.7
761S	1140	9,989	Surface void (1)	321.1	1.30	30.0	14.4
762S	1140	12,069	Surface void (2)	295.0 256.5	1.60 3.10	27.5 38.6	18.1 12.4
759S	1000	37,238	Surface NMI (1)	3,579.0	1.63	89.0	56.0
760S	1000	353,639	Internal NMI (1)	4,345.0	6.79	179.9	33.2
481V[2]	1140	13,341	17μm NMI (1) subsurface	3,007.0	2.13	96.0	52.0
763S	1140	18,995	100 μm NMI subsurface (1)	5,275.0	2.00	120.4	58.5

V & S indicated as virgin material and serviced material, respectively
[1]N_f = 8,437 at 1000MPa and N_f = 2,224 at 1140MPa.
[2]Total six initiation sites were observed, but only one is dominant.

The two kinds of initiation sites, voids and non-metallic inclusions (NMI) show significant difference in morphology and dimension, see Figure 3 and Table 1. The defects seemed to play an equal role in crack initiation, since five of the nine specimens nucleated from voids, four specimens originated from NMI. Void clusters seemed to be more prone to crack initiation than a single void since in three of five specimens (#761, #493 & #491) fatigue cracks originated from void clusters, see Figure 3(b) & 3(d) as well as Table 1. The compositions of the NMI related initiation sites were determined using EDS, performed on the fracture surfaces of the four specimens (#481, 759, 763 &760). The x-ray spectra of the four samples were very similar and indicated that NMI was composed of dominant aluminum and silicon oxides with lesser amounts of magnesium, chromium and titanium oxides. Table 1 also showed that the initiation voids generally have rounder shape (aspect ratio 1.3 - 2.3), however, the NMI has very irregular shape (aspect ratio 1.6 - 6.8). More surprisingly, the critical size (area) of voids was 240 - 320 μm^2, however, the sizes of NMI were 3000 to 5300 μm^2. Thus, the area of NMI is more than one order of magnitude larger than of the voids. Figure 5 shows fatigue life data with respect to the defect area size based on the results in Table 1. The fatigue life is similar when the crack initiated from voids (with the exception of specimen #486 that saw the two different load levels), whereas the life is more variable if the initiation site is NMI. Also, under identical loading conditions, R = 0.05, σ_{max} = 1140 MPa, the specimens that failed from a void had a shorter fatigue life than those that failed from an inclusion. This indicates that smaller voids (or void clusters) are more potent at debiting life than larger NMI.

Although no annealing twins were observed in the fatigue crack initiation site, they were definitely involved in the crack propagation. Twinning was observed in the crack initiation region on fracture surfaces of specimen #760, Figure 3(a), #762 and #763, Figure 3(c). In Figure 3 (a) & (c), it seemed to imply that annealing twins assisted microcrack propagation. Two equally-weighted initiation cracks observed on #762 were propagated independently on different height of crystallographic planes. Subsequently, the two planes were joined together along twins due to macro propagation.

Defect distribution

It is well known that intrinsic defects, void and NMI, are common in powder metallurgied (P/M) superalloys [1-3]. The defects size, shape, volume fraction and distribution are related to the processing. The measured size of initiation defects including void and NMI from the fracture surface of the fatigued specimens under LCF conditions suggest that defect area is a critical parameter governing crack initiation. Since all the axes of the cylindrical fatigue specimens are parallel the circumferential direction of the forging, the defect size distribution of a cross section was determined. Specimens were prepared from a cross section by mechanically polishing. Twenty images of the cross section at eleven distributed locations were taken by optical microscope under 200x magnification. An area of

5.1 mm^2 per location was investigated. Each optical image, which is a grayscale image, showed gray defects on the bright matrix. The images were transformed into a binary image, black defects on the white matrix, by setting proper brightness threshold levels using image analysis software. The defects were characterized by: area, maximum and minimum length, maximum and minimum width as well as aspect ratio using the same software. Figure 6 is a histogram showing the distribution of the defect area. A total of 1288 defects were sampled from the 566 mm^2 of the cross section. Figure 6 indicates that small defects are dominant, that is, the areas of 96.6% of the defect population range from 0 to 200 μm^2. If a defect size 'd' is defined as the square root of its area, 96.6% defect population had sizes below 14.2 μm. Since the size of NMI is much large than voids this indicates that the majority of the defects are small voids. The critical area of the void related crack initiation ranges from 240 to 330 μm^2 or d = 15.5-18.2 μm, Table 1. This suggested that large defects (d > 14.2 μm), which have a population of 3.4%, actually govern the LCF life of the material. Figure 6 also shows that when d > 31.6 μm, there is only one defect (40 μm < d < 41.2 μm) present. This value is much smaller than the NMI-related crack nucleation sizes (d = 54.5-72.8 μm corresponding to area 3000-5300 μm^2), Table 1. Two ideas follow from these results. First, fatigue cracks initiate from the largest, (perpendicular to the loading axis) fractured NMI in its cross section – unless a sufficiently large void of cluster of voids exists. Second, the polished cross section of a forging, where the defect distribution was measured, rarely has the opportunity to sample the largest NMI section due to a very low NMI vol. %. This result strongly suggested that the 2-D defect distribution did not characterize the largest NMI due to its low vol. %. To establish a correlation between the defect size distribution and the initiation defect size, a 3-D model of the distribution is necessary.

CONCLUSION

Fatigue crack initiation sites of IN100 tested at 538°C were defect-related. Two distinguish defects were identified: void and NMI. Significant shape and size difference between void and NMI were concluded. The area of NMI, where fatigue crack initiated is one order larger than the area of void initiation site. No close correlation was deduced between the measured initiation crack size on the fracture surface and the 2-D defect size distribution of the cross section.

REFERENCE LIST

(1) Albrecht, J., *Mater Sci Engng*, Vol. A263, 1999, pp.176-186.

(2) Goto, M., Knowles, D.M., Engng Frac Mech, Vol. 60, No.1, 1998, pp. 1-18.

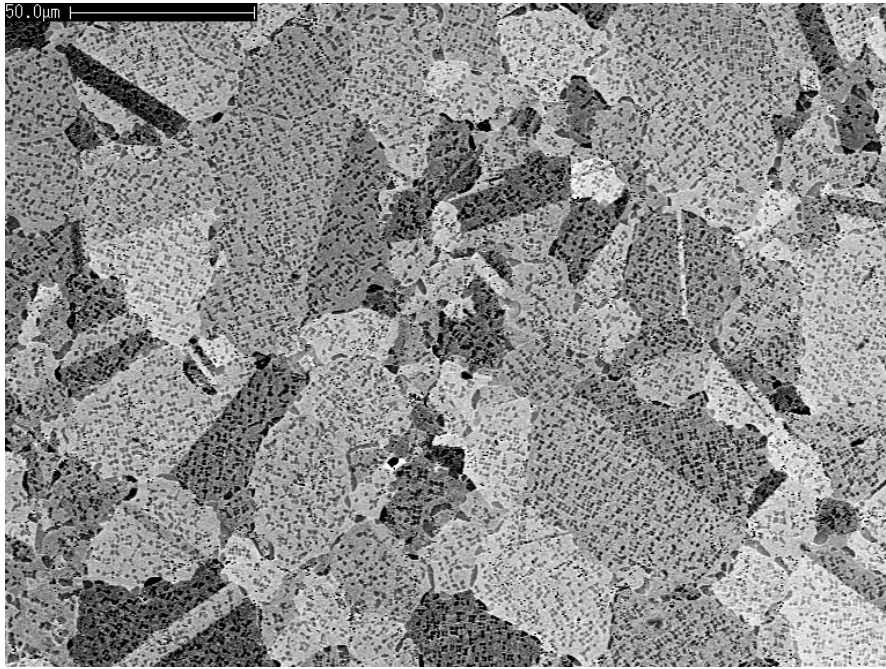(3) Hyzak, J.M., and Bernstein, I.M., *Metall Trans*, Vol.13A, 1982, pp. 33-43.

FIGURE 1 SEM back-scattered image showing that the microstructure of IN100 consists of γ' particles in the γ matrix. Annealing twins are also visible.
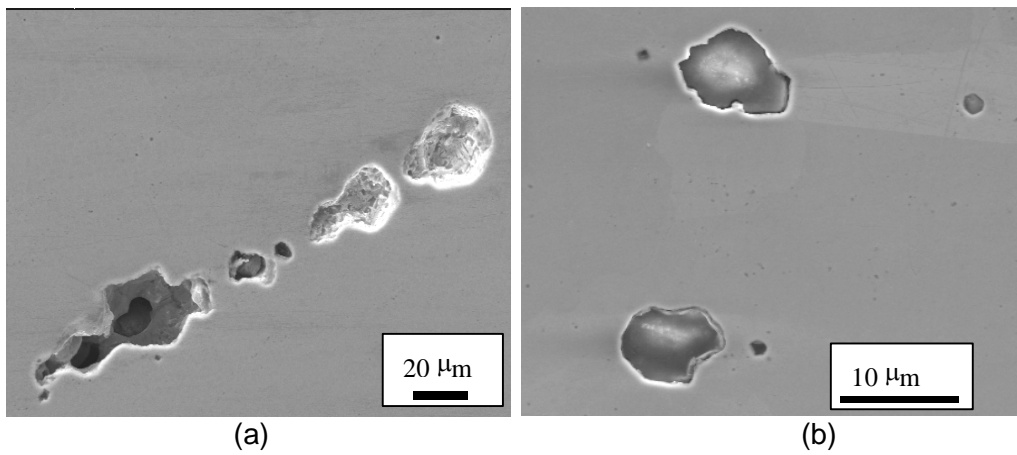

20 μm

10 μm

(a)

(b)

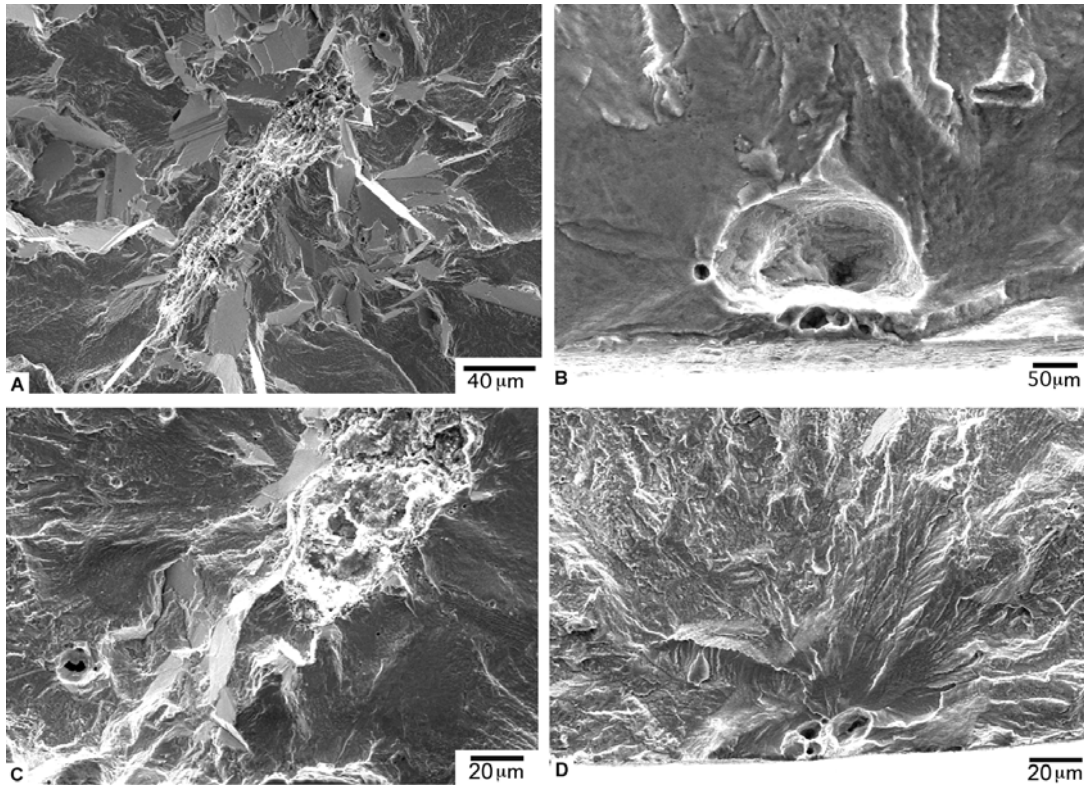FIGURE 2 Defects of IN100: voids (a) and NMI (b).

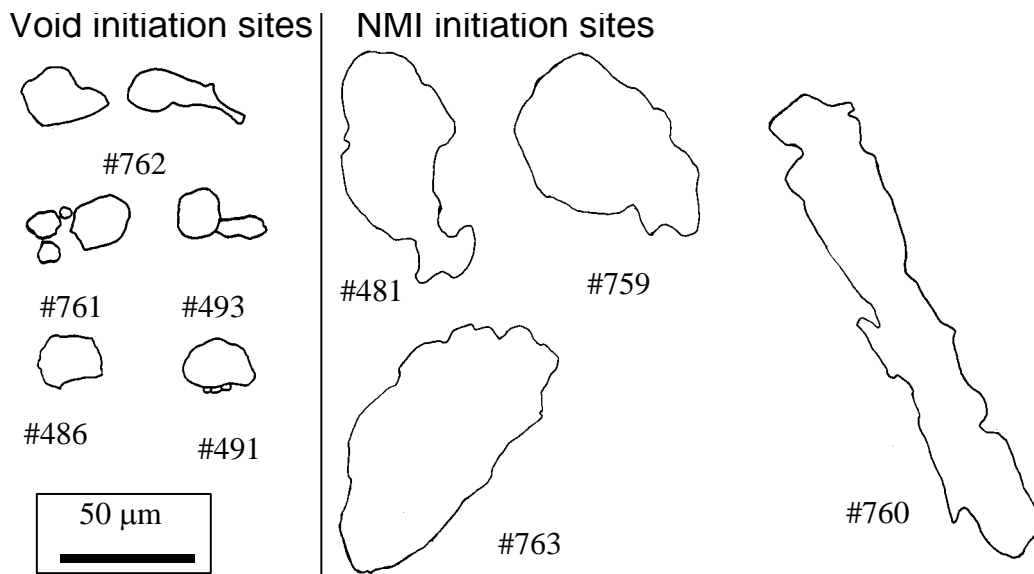FIGURE 3 SEM images showing the fatigue crack initiation sites in samples; a) #760, b) #491, c) #763, and d) #761

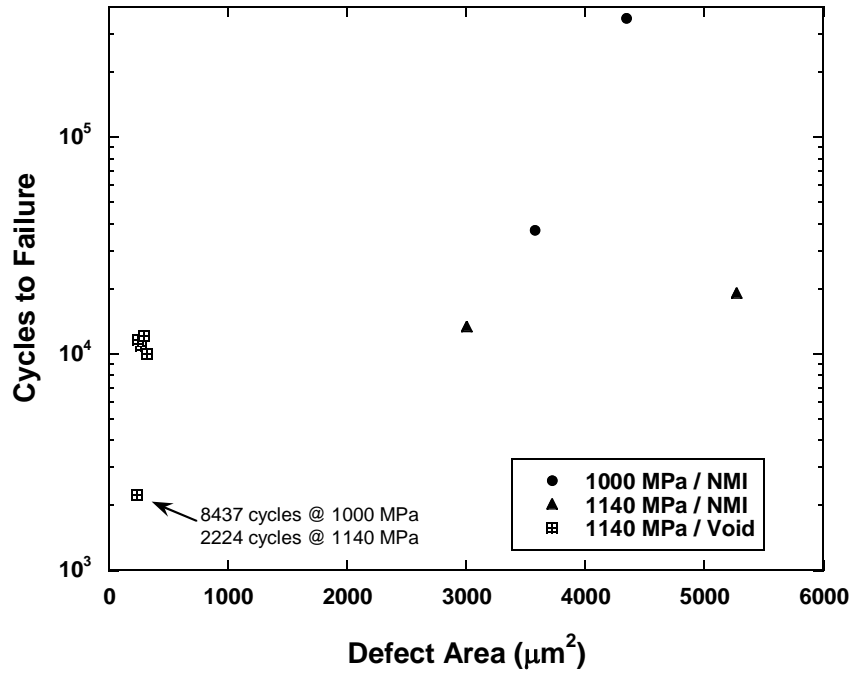FIGURE 4 Traced initiation site profiles (the number under each drawing indicating the specimen number).

FIGURE 5 Fatigue life with respect to defect area. Maximum stress levels indicated in figure, 538°C / R=0.1 / 0.5 Hz.
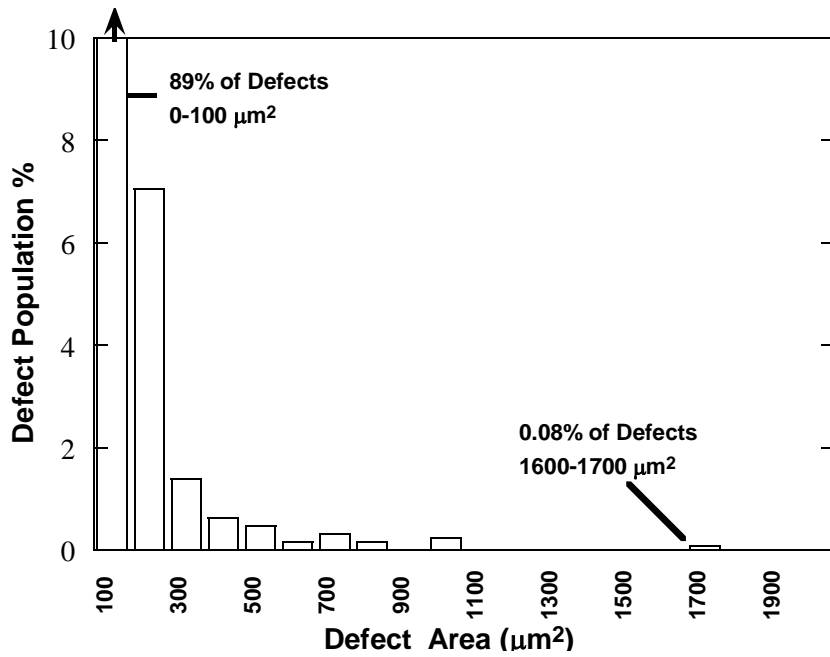
Figure 6   Defect size distribution of a cross section of IN100, showing defect population % (Y) with respect to area (X).

THE ROLE OF AIR IN FATIGUE LOAD INTERACTION

R. Sunder[1], W.J. Porter[2] and N.E. Ashbaugh[2]

[1]BiSS Research, 41A, AECS 2nd Stage, Bangalore 560 094, India

[2]University of Dayton Research Institute, 300, College Park, Dayton, OH 45469, USA

ABSTRACT

Natural fatigue crack formation and growth were studied in notched Al-Cu alloy coupons through high-resolution SEM fractography. The experiments were conducted under programmed loading conditions designed to induce microscopic marking of the crack formation and growth process under varying stress ratio and closure-free crack tip conditions. Control experiments were performed by switching between an air and vacuum environment. In air, varying the stress ratio from 0.74 down to 0.64 retards crack growth by up to a factor of five. This 'closure-free' stress ratio *history* effect totally disappears in vacuum, suggesting a significant environmental influence on stress ratio and its history. Crack-tip stress state appears to moderate environmental action, revealing a potential mechanism sensitive to residual stress. Consequently, crack closure, residual stress and crack front and plane orientation are identified as major load interaction mechanisms whose synergistic action controls fatigue under variable amplitude loading. The study also appears to suggest that as a consequence of the crack seeking the path of least resistance, load-sequence sensitive crack plane and front orientation may only induce retardation effects.

KEY WORDS: Fatigue crack growth, stress ratio, load interaction, air and vacuum, fractography, striations, markers.

INTRODUCTION

Advances in crack detection and tracking technology, combined with developments in fatigue crack growth prediction techniques have progressively diminished the proportion of crack growth life that is left unaccounted as 'life to crack formation'. A variety of prediction models[1-3] have been implemented for predictive analysis[4] of crack growth under service usage conditions. Success of crack growth modeling hinges on the ability to simulate load interaction effects[5]. While such effects are known to be many, the better-known models (e.g., ref. 1) appear to perform well using just one effect - crack closure[5].

Crack closure is a dominant load interaction effect as it directly controls the magnitude of the fatigue cycle[6]. Its effect on crack growth rate is overwhelming since da/dN is a power function of effective stress intensity range, K_{eff}.

Empirical approaches by nature can account for more than one load interaction effect and thereby improve prediction quality. A recent example of success using such an approach is the development of the so called K_{PR} parameter[7], that is said to account for both closure as well as residual stresses. K_{op} is defined as the stress intensity at which the crack is open, while K_{PR} is defined as the stress intensity above which variation in applied K will grow the crack. It would follow that fractographic crack closure estimates[8,9] are a microscopic equivalent of K_{PR} measurement. Both essentially characterize a certain 'effective' crack driving force, rather than attempting to define a certain deformation point such as 'opening' or 'closing'.

The K_{PR} approach is able to handle certain aspects of crack growth behavior that the closure approach does not seem to. Significant among these are load interaction effects at high stress ratio. These are levels at which there appears to be no sign of crack closure from crack-opening-displacement measurements. While the K_{PR} approach does handle effects that closure cannot, it does so by way of empirical correlation. The effect is attributed to compressive residual crack tip stresses. There is no quantification of these compressive stresses and their so-called 'accumulation' under repeated loading. Further, there is no explanation as to why and how these compressive stresses retard the fatigue process.

Another recent study also found that R-effects persist even when the crack is fully open[10]. These were attributed to a change in crack extension mechanism characterized by a change in 'micro-void density' as observed on the fracture surface.

In previous work, we reported the effect of (closure-free) high stress ratio and stress level on the growth of naturally forming notch root fatigue cracks[11, 12]. A correlation between the two was established. However, we were unable to *explain*

the noticeable effect of stress ratio and applied stress level on near-threshold crack growth rate.

Closure-related R-effects have been comprehensively covered in the literature. This work attempts to resolve closure-unrelated *R-history* effects. Our focus was on naturally-forming fatigue cracks at notches so as to cover the stage of crack formation and early growth. The experiments reached down to crack sizes of a few microns and growth rates as low as 10^{-11} m/cycle.

EXPERIMENTAL PROCEDURE

A schematic of the experimental procedure appears in Fig. 1. Notched coupons were tested under specially designed programmed loading. Under such conditions, cracks form at one or more sites. The procedure uses quantitative fractography to reconstruct crack kinetics from the point of natural crack formation. To study the kinetics of such cracks, the loading program is designed to include so called 'marker loads'. These loads are specially designed to meet two contradicting requirements: they should leave a discernible mark on the fracture surface, but by themselves, should cause negligible crack extension and negligible load interaction effects. The bulk of crack extension is caused by the loading pattern of interest in the experiment. It may be noted that this procedure does not rely on the formation of fatigue striations in individual cycles. The number of cycles between marker loads is controlled to effectively 'zoom' into the growth range of interest. Most of our experiments used a block size of 2000 cycles. This permitted observation of growth rates down to and below 10^{-10} m / cycle.

Experiments were performed on two Al-Cu alloys, 2014-T6511 rolled bar stock and 2024-T351 plate stock. The experiment on 2024-T351 was specifically designed to study material behavior cited in Ref. 10.

A variety of notched coupons were used in the study on 2014-T6511 (Fig. 3a-c). The 2024-T351 experiment was on a notched C(T) specimen shown in Fig. 3c. All the specimens were cut for loading along the L-T direction.

The load programs used in the experiments are schematically described in Fig.2. The programmed load sequences used in the experiments are built around two components: the so-called 'closure block' and the so-called '3R' block. The closure block permits fractographic estimate of crack opening stress[8,9]. The salient features of the load sequence design are: Application of programmed blocks of small amplitude, high stress ratio (Hi-R) cycles, interspersed with large amplitude, low stress ratio (Lo-R) marker cycles. The Hi-R cycles were designed to preclude fatigue crack closure. The three Hi-R blocks as well as the markers were of the same relative magnitude in all the experiments. The variation was by way of load level corresponding to 100% (max) reference. The reference load level was selected between 50-100% of yield point to cause high enough notch root stresses that facilitate reasonably early crack formation.

Most experiments were conducted with Hi-R block duration of 2000 cycles at each of three stress ratios. After each such block, 10 marker cycles were applied. These were intended to mark the crack front at the conclusion of each Hi-R block. It may be noted that the cycle parameters were selected following several iterations to enable quantitative electron fractography.

Crack growth rate is determined from marker spacing. All the experiments were conducted at crack growth rates typically below 10^{-8} m/cycle and crack sizes below a few hundred microns. The marker technique has been found to be effective, consistent and reproducible over these ranges of crack size and crack growth rate[11-13] to an extent that other known techniques are not capable of.

The Hi-R cycles were designed with R > 0.65. This was to reduce or eliminate crack closure altogether. Their number was large to ensure they caused the bulk of crack growth. The number of Lo-R markers (usually 10) was much smaller than the Hi-R cycles (usually 2000) to ensure that crack extension during markers was negligible (typically less than 5% of overall crack extension). As crack extension mode changes during the large Lo-R cycles, the instantaneous crack front is registered on the fracture surface as a discernible topographic feature.

In order to avoid overload effects, the markers were designed to have maximum stress similar to the Hi-R cycles at highest R. The marker cycles were designed to terminate at minimum stress. Thus, given the hysteretic nature of closure[14], the crack is even more likely to be fully open under the subsequent Hi-R cycles.

The steps of Hi-R cycles were selected to be close in magnitude (0.66, 0.69 and 0.73). Such a small R-variation was expected to have a marginal effect on da/dN. Under the lower stress ratio cycles the fatigue crack tip will see the effect of prior cycling at higher stress. However, the crack is expected to be fully open under all three stress ratios.

Most of the tests were performed in laboratory air. However, a few were performed with the environment cycled between air and vacuum.

Computer-controlled servo-hydraulic test systems were used for programmed loading at a frequency of about 15 Hz. The scheme of testing was to repeat the designated programmed load block until failure. The exception to this rule was the experiment involving air-vacuum-air cycling. In this particular experiment, the block duration and repeat count for vacuum was increased keeping in mind reduced crack growth rates in vacuum. The first sequence was in air to promote crack formation. The chamber was then evacuated to below 10^{-8} torr for the vacuum sequence. At the end of the vacuum sequence, air would be let into the chamber and the test continued in air. Such alternation continued to specimen failure. While vacuum-air transition takes only a few minutes, the air-vacuum transition can take 24-48 hours.

As very small, naturally-forming cracks were involved, no attempt was made to track the fatigue process during testing. The block count at failure was recorded. Post-failure quantitative scanning electron microscopy (SEM) was employed to re-construct the entire fatigue process and determine growth rates from striation (marker) bands radiating from the crack formation site(s).

Some of the air tests are reported in[11-13]. Relevant results are reproduced here to enable ready comparison and discussion. Typical fractures from the air sequence appear in Figs. 4-6.

Interpretation of results. The results are obtained exclusively from post-failure fractography. The different possibilities in striation band-width distribution during the 3R blocks are:

- No closure effect and no closure-unrelated R-effect as indicated by all three bands being equal.

- Closure-unrelated S_{max} or R-effect. First band exceeds second band, which in-turn, may or may not exceed third band.

- Partial crack closure at lowest R, with total absence of closure-unrelated stress-ratio effect. First two bands are equal and exceed third band.

- Crack closure plus closure-unrelated stress-ratio effect. No two bands are similar. Besides, difference in bandwidth due to two lower stress ratios are more dramatic than between the two higher stress ratios. This is because the lowest stress ratio sees the greatest extent of closure. In addition, it also sees closure-unrelated R-effect. The two combine to reduce striation bandwidth to vanishing proportions.

RESULTS AND DISCUSSION

Fig. 4 is typical of long crack growth rates as seen on a C(T) specimen. The sets of three bands representing the three Hi-R blocks are distinctly visible. However, there is no discernible variation in growth rates indicating little or no R-effect. This was expected given the fact that the stress ratios were specially designed to preclude closure. The excellent quantitative and qualitative reproducibility at the microscopic level of crack growth rate appears striking. Each band corresponds to 2000 cycles of loading. The so-called 'zoom-in' effect is self-evident, as striations from individual cycles are not visible. However, growth rate can be accurately determined by dividing bandwidth by number of cycles. As evident from the sharp

ridges, the 10-cycle marker loading caused negligible crack extension, but induced noticeable change in local crack front orientation to leave a discernible mark.

Figs. 5a-c show macros of crack formation sites from three different tests. As seen in Fig. 5a, crack growth rate across the three stress ratios is even at crack size approximately 0.4 mm and above. This is similar to long crack behavior as registered in Fig. 4. However, the same does not hold at smaller crack sizes within the white circle in Fig. 5a. This is the area surrounding the crack formation point and is highlighted in Fig. 6.

Fig. 5d shows a zoomed in region from the white circle in Fig. 5c. In this picture, crack growth rate at the highest R was about 5×10^{-9} m/cycle, which is near threshold. A strong R-effect is seen even though the change in stress ratio was marginal (0.733 down to 0.64). In the lowest R, reduction in crack growth rate is almost by a factor of three by comparison to the highest R. Note also that the difference in growth rates between the two lower stress ratios (0.69 and 0.64) is marginal.

Fig. 6 shows typical patterns of marker bands at different crack depth from crack formation site. All of these fractographs are from the encircled area around the crack formation site in Fig. 5a. Results of quantitative analysis of these pictures appear in Fig. 7. They cover crack size interval 0.02 to 0.15 mm over which da/dN at highest R varies from 2.7×10^{-10} to 2.8×10^{-9} m/cycle. This represents a substantial variation in da/dN in the near-threshold range that substantially controls total fatigue life. Fractographic data in Fig. 5 and 6 suggest excellent reproducibility and consistency of growth rate data. Also evident is the systematic and significant change in growth rates from marginal variation in R.

The data in Fig. 7 indicate highly non-linear reduction in crack growth rate with reducing R. While da/dN drops dramatically in the second block, the reduction in da/dN in the third block, if any, is marginal.

Fig. 8 shows crack growth rate variation observed in previous work on the same material over a programmed load block with five steps of decreasing stress ratio.

The first three of these are identical to the sequence used in the current tests. These data were obtained close to a keyhole notch on a C(T) specimen. It may be noted that the crack may have been partly closed in the fourth R-step and certainly was partly closed in the fifth step. This may explain the substantial (order of magnitude) retardation in growth rate over the fifth step by comparison to the first step.

The fracture morphology in Fig. 8 is typical of patterns we observed in numerous similar experiments. One may conclude that the shape of the crack front is extremely sensitive to the rate at which it progresses in each cycle. At near-threshold growth rate, the crack front is relatively straight both in the plane of loading as well as in the plane of fracture. As growth rate increases, microscopic arcing of the crack front is observed combined with out-of-plane growth, promoted by dual slip and multiple crack tip slip planes. The process appears to correlate with growth rate and is obviously reversible as evident from the pattern in Fig. 8. These may be the first signs of *load sequence-induced*, crack-extension front and mode incompatibility.

As crack growth rate increases, the fracture surface undergoes more violent transformation. Typical fractographs that reflect this behavior appear in Fig. 9. Shown are striation patterns obtained on long cracks in a C(T) specimen under 'closure-free' load interaction between Hi-R loading blocks and markers[11,12]. The low amplitude, Hi-R cycles 'try' to keep the fracture surface 'flat and smooth' (Fig. 9a). As growth rate during the markers progressively increases, a point is reached when the markers induce crack branching, which effectively enforces mixed-mode conditions[13]. This effect is highlighted in Fig. 9b,c,d. Obviously, features such as crack branching and highly distorted crack front are not what the Hi-R cycles would see under constant amplitude loading. Such incompatibility may be expected to induce substantial closure-unrelated crack retardation in any 'major-minor' type of cycling.

The evidence in Figs. 5-8 points to a significant effect of stress ratio variation on crack growth rate. The variation in stress ratio over successive steps was marginal (about 0.05). It would follow that stress-ratio history, rather than absolute values of

R, caused significant reduction in da/dN at lower stress ratio. Obviously, a load interaction effect other than crack closure was responsible for this retardation effect.

A recent study by Riddel and Piascik[10] on 2024-T351 Al-Cu alloy related closure-free R-effects to 'micro-void density' on the fatigue fracture surface. These data were obtained under constant ΔK with varying stress ratio. The crack growth rate data plateau between R = 0.4 and 0.6. The region below R = 0.4 is attributed to crack closure as determined from near-tip measurements. The measurements indicated that the crack would be fully open above R = 0.4, which would explain the plateau in da/dN beyond this R. Surprisingly, da/dN was found to increase once again beyond R = 0.6. Interestingly, over this same interval, there appears be a steady growth in 'micro-void' density, which may explain the authors' conclusion.

By comparison to the results reported by Riddel and Piascik, the data obtained in this study (e.g., Fig. 7) appear to show a substantially greater R-effect. While Riddel and Piascik established an increase in da/dN of about 15% over an increase in R from 0.7 to 0.8, the data in Fig. 7 indicate an increase of over 250%. To investigate this contrasting difference, an experiment was designed around a C(T) key hole-notched specimen cut from the same material as the one used in ref. 10.

The programmed load sequence used in the experiment is described in Fig. 2. The sequence consists of a crack closure block[13], followed by five repeats of the three Hi-R steps. Marker loads enable identification of crack extension from each segment of this load sequence. Thus, the number of equally spaced bands in the closure block determines crack opening stress level.

Typical fractographs from the study appear in Figs. 10-14. Fig. 10a is a macro of a notch root area showing two sets of striation bands corresponding to two repeats of the load sequence. Equally spaced marker bands corresponding to the closure block are visible at a distance of less than 30 μm from the notch surface at bottom left. The second set starts above and to the left, about 100 um from the notch root. This is followed by five sets of three Hi-R bands. Surprisingly, the first two bands are equally spaced, while the third is narrower. This may be explained by the crack being partially closed in the lowest of the Hi-R blocks. This is clearly visible in the

zoomed-in areas shown in Figs. 10c,d. The first two bands being similar, one would have to conclude the absence of closure-unrelated stress-ratio effect. The third band being narrow can only imply that the crack was partially closed. Even though the stress ratio was high, partial closure is made possible by the relatively sharp notch that must have induced compressive residual cycles after the first tensile load, thereby effectively reducing notch root (local) stress ratio and causing closure over initial crack growth.

As the crack progresses from left to right in Fig. 10c, we see the five sets of Hi-R blocks with the closure block in between. Judging from the 8 equally spaced bands, S_{op} was of the order of 50%. S_{min} in the lowest of the 3R blocks is 46.6% of maximum stress (of the spectrum), which explains why the third of the three Hi-R bands is narrower than the previous two. An enlarged fractograph showing four sets of Hi-R blocks appears in Fig. 10d.

In contrast to the 3R band width distribution in Figs. 10a,c,d, the one in Fig. 10b shows a distribution closer to what is observed in the tests on 2014-T6511 and summarized in Fig. 7. Interestingly, the crack growth rate seen in Fig. 10b (about 1.5×10^{-9} m/cycle) is in the same range as that covered by the data in Fig. 7. These data are several times lower than those seen in Fig. 10a,c,d.

The 3R bands in Figs. 10a,c,d all correspond to da/dN in excess of about 5×10^{-9} m/c. The highest R band in Fig. 10b corresponds to about 1.25×10^{-9}, which is about three times lower than in Figs. 10a,c,d.

The notch root results from 2014-T6511 and 2024-T351 show similar trends. At growth rates less than about 5×10^{-9} m/cycle, there is a noticeable, closure-unrelated R-effect. At higher growth rates, the effect is not seen. However, partial closure of the notch root crack in the C(T) keyhole specimen caused a corresponding reduction in da/dN.

As the crack front grows away from the notch root, closure stress drops to that expected of long cracks and crack growth rates equalize in all three Hi-R blocks.

This is seen in Fig. 11a. From this crack length on, the growth rate exceeds the range investigated on the 2014-T6511 notched coupons.

The fractographs from progressively larger crack size, shown in Figs. 11b-d, indicate a steady increase in the proportion of crack extension during the marker cycles. This was evident earlier in Fig. 12a, where the marker bands are no longer the fine line observed earlier. As da/dN in marker cycles exceeds about 10^{-6} m/c, individual striations become clearly visible. As seen earlier in Fig. 11 from 2014-T6511, the high growth rate during the markers is accompanied by distortion of the crack front as well as plane. It would appear this causes retardation in the Hi-R cycles that are now forced (at least initially) to extend the crack along a path that *may not be of least resistance*. This may explain why the proportion of marker cycles on the fractograph increases disproportionately. Given the crack growth rate in the Paris regime, the effect may not be attributed to change in slope of the da/dN versus ΔK curve.

Figs. 12a,b show typical fractographs at higher growth rates. At this point the flat portions associated with the Hi-R and closure block cycles appear as 'pockets' in an otherwise non-uniform, pockmarked surface with the 'micro-voids' reported in ref. 10. The macro view in Fig. 13a shows the predominance of high growth rate characteristics and only a marginal flat region. One may conclude that crack extension at this point was almost exclusively due to the marker cycles. The crack was effectively *arrested* during the low amplitude cycles even though it was fully open and even though the same cycles had grown the crack at smaller crack size.

Fig. 13b shows an unusual combination of fracture morphology. In the middle is a flat area associated with one of the Lo-R closure steps where load amplitude was sufficiently large to grow the crack, yet sufficiently small to occur on a flat plane. Preceding this region to the left is a void with the remains of the fractured (near-circular) particulate in the middle. Surrounding this void is a cluster of micro-voids whose coalescence is associated with the static fracture process. This picture suggests intermittent quasi-static cracking (perhaps during the markers) in the final stages of the fatigue process.

It would follow that the voids reported in ref. 10 are not micro-voids associated with the fracture process. A separate paper addresses the nature of these voids[15]. They are 'fatigue voids' associated with the separation from the matrix of non-coherent constituent particulates. Fatigue voids are about an order of magnitude larger than microvoids and take the near spherical shape of the particulates contained within. It would follow that 'fatigue' voids are merely a signature of crack growth path, just as striations are signatures of growth rate. Therefore, it may not be appropriate to conclude, as in ref. 10, that void density is sensitive to loading parameters such as stress ratio or K_{max}.

The evidence presented thus far appears to confirm significant closure-unrelated stress-ratio effects as well as 'stress-ratio history' effects. These were brought out by the closure-free programmed load sequence experiments. The experiments show much greater retardation in crack growth rate with reducing R than can be explained by the constant-amplitude results reported earlier[10]. As stress ratio variation caused only a marginal change in fracture morphology (e.g. see Fig. 8 C(T) 5R test) such retardation may not be attributed to mode incompatibility *either*.

Previous work attributed closure-unrelated R-effects to the magnitude of local notch root stresses[11-12]. While the significance of K_{max} tending to K_c is obvious by way of an increasing proportion of quasi-static fracture, S_{max} tending to S_{ult} may also enhance the probability of localized quasi-static rupture in the case of short cracks growing out of a highly stressed notch root. However, the fractographs in Fig. 6 show no sign of quasi-static rupture (fracture) by way of micro-void coalescence or ductile shear. Quite to the contrary, the consistently reproducible evidence of accelerated crack growth at Hi-R reaches down to near- and sub-threshold crack growth rates. It would appear that the effect of crack tip mean stress (enhanced by increasing stress level or stress ratio) manifests on a *cycle-by-cycle* basis. Considering that both these are accepted to be a consequence of crack tip single (Stage I) and duplex (Stage II) slip[16], one may assume that the effect in question renders these slip mechanisms irreversible. In earlier work, surface slip

irreversibility has been attributed to environmental action (oxidation in the case of Al-alloys tested in air)[20].

In an attempt to investigate the possible role of environment in explaining the effect of stress-ratio and R-history on Stage I / Stage II fatigue, we designed a new experiment imposing a change in environment. A notched 2014-T6511 coupon was tested under the 3R programmed load sequence alternately in air and vacuum. A pilot test was performed to optimize the loading program for vacuum. It revealed potential problems with experiments in vacuum. Crack growth in air is characterized by excellent striation formation at crack growth rates $> 5 \times 10^{-8}$ m/cycle. In contrast, vacuum does not seem conducive to striation formation even at 10^{-6} m/c (see Fig. 14). Environment appears to play a role in striation formation. Following Laird's mechanism of striation formation, it would appear that duplex slip reversal at the crack tip surface in vacuum is accompanied by near-total re-fusion of opposing slip surfaces leading to considerably reduced growth rate and a 'tacky' appearance of growth bands. Oxidation would not allow re-fusion to occur; thereby forming the contrasting undulations that appear as fatigue striations.

On the basis of pilot tests in vacuum, the load sequence for the vacuum portion of the test was modified to contain 5000 cycles instead of 2000 at each R. The number of marker loads was increased to 20. Also, the number of 3R blocks in each vacuum sequence was increased to 40, while in air, it was set to 10. These accounted for the order of magnitude reduction in crack growth rate expected in vacuum in order to assist quantitative fractography.

The test coupon was first cycled in air for 10 blocks. Then the chamber was evacuated to below 10^{-8} torr and the vacuum program applied for 40 blocks. At this point, the test was stopped and air admitted into the chamber before commencing the next air cycle. The coupon failed in the 8th sequence, which was the 4th vacuum sequence. In view of the slow process of evacuation, the air-vacuum transition time took about 50 hours.

Fig. 15a shows a macro of the notch area. The arrows point to two crack formation sites. Judging from differences in growth rates between the two sites, the top site

initiated first and grew into the dominant crack whose progress is charted in Fig. 15b with a zoomed-in view of early fatigue in Fig. 15c. The air sequences carry odd numbers, while the vacuum sequences are even. The two sequences are easily identifiable by shade of gray, by difference in band spacing as well as by the difference in block count.

A fatigue crack appears to have formed in the very first air sequence and grew to a depth of about 5 μm. This is followed by a narrow band of growth in vacuum. Overlapping this region and the following air sequence is a rectangular segment of approximately 10μm by 10μm in area, that appears to have been abrasively damaged, perhaps by fracture debris, leaving behind a surface with no discernible fatigue features. Aside from this area, the rest of the fracture area provides a wealth of information described below.

Marker bands in the air sequences 5 and 7 (see Fig. 15b,c) reproduce behavior observed in previous tests (Fig. 5-7). The closure-unrelated R-effect is consistent and reproducible. It was apparently insensitive to the vacuum-air-vacuum transitions.

Figs.16a-c show high magnification areas of vacuum crack growth in sequences 6 and 8. We were not successful in identifying any growth bands in areas 2 and 4, which cover crack size up to 30 μm. Areas 6 - 8 cover crack size exceeding about 80 μm and growth rates between 10^{-10} and 10^{-9} m/cycle. The fractographic evidence in Fig. 16 appears to suggest the total absence of stress ratio as well as R-history effects in vacuum. It would follow that in vacuum, over the observed interval of growth rate, crack closure is the only operating mechanism for R-effects. Conversely, this may be proof that closure-free stress ratio and R-history effects observed in conventional testing are a consequence of environmental action. Air appears to emerge as a major factor affecting load interaction effects. It may be noted that over the same range of crack growth rate *as well as* stress intensity, data for air show substantial R-effect.

Figs. 17a-c show zoomed in areas highlighting transition from air to vacuum and from vacuum to air. The marker bands immediately following transition from vacuum to air (6 to 7 in Figs.17a, c) and from air to vacuum (7 to 8 in Figs. 17 b, c) show that activation/deactivation of environmental action is instantaneous. It follows, that the effect is associated with the cycle-by-cycle fatigue loading process and is not associated with any sustained (time dependent) action of environment. In the event any time-dependent effect was involved, one would have observed a transient region of varying growth rates each time there was a vacuum-air-vacuum transition. This was not the case.

The evidence in Fig. 17 leads to the conclusion that the fatigue crack extension process is driven exclusively on a cycle-by-cycle basis and is relatively insensitive to any cumulative damage processes ahead of the crack tip. While the stress-strain field ahead and in the wake of the crack tip are significant, the history leading to them is less so. This in turn implies that the models of single and duplex slip[16] leading to cycle-by-cycle crack extension are, in fact, operative.

Fig. 18 summarizes the crack growth rates from the air-vac-air experiment. Crack growth in vacuum is retarded by over an order of magnitude by comparison to Hi-R air. The difference somewhat diminishes at air growth rates in excess of 10^{-6} m/cycle. This may be expected, considering that high fatigue crack growth rates may be attributed to coalescence of sheared particulates, and substantial duplex slip, which are internal to the material and therefore less susceptible to environmental action. Quite simply, increasing cyclic slip increases the required depth of environmental action.

While the significance of environmental action in stress-ratio and stress-ratio history effects appears to be ignored by prediction models reported in the literature, its isolation in the current study is not altogether unexpected. Consider the relationship of K_{th} versus stress ratio for a steel[19]. It is clearly analogous to the stress-ratio dependence of near-threshold da/dN observed on Al-alloys in this study. The model of oxygen-slip band interaction[20] explains the role of atmospheric air in accelerating Stage I fatigue crack formation and growth.

Stress ratio and R-history, in principle, translate to crack tip mean stress. While Stage I and II mechanisms are operative, K_{eff} determines the extent of reversed single or duplex slip. These in turn may be treated as Mode II components. The axial or Mode I component superposed on the Mode II component during a cyclic loading cycle will be controlled by crack tip mean stress. The Mode I component may be treated as insignificant if slip reversal alone drives the crack as per Laird[16, 17]. However, if we associate Mode I crack opening with superposed tensile stress *across* slip planes, ingress of oxygen will promote their Mode I separation by oxidation. The chemistry of the process is known to be accelerated by the tensile stress component. This may serve as the explanation for the 'closure-free' R-effects reported in this paper.

Given the role of environment, unusual crack growth retardation due to marginal reduction in stress ratio under programmed loading in air (Fig. 6, 7, 8) can be interpreted in a new light. A marginal reduction in R by 0.05 led to a factor of between 2.5-4x reduction in growth rate, possibly due to hysteretic reduction in near-tip mean stress. Further decrease in R by an equal amount caused only a marginal difference. This appears to suggest a highly non-linear relationship between the degree of 'unloading' and the shielding of the crack tip from environmental action. If one views the crack tip as a region of extreme inelasticity subject to local strain-controlled conditions, the associated stress-strain hysteresis loop would explain why marginal nominal unloading causes substantial reduction in local tensile stress.

The connection between stress-ratio history and environmental effect is indicative of vacuum crack growth rates representing an 'intrinsic' fatigue crack growth resistance of a material. Stress ratio and its history appear to *moderate* the role of environment in accelerating crack growth beyond intrinsic (vacuum) behavior.

SUMMARY

Three main operating mechanisms appear to synergistically control the kinetics of crack growth at a given applied stress intensity range:

Fatigue crack closure (Acceleration and Retardation). Crack opening stress is load and crack growth history sensitive. This directly affects K_{eff} - the primary driving force in fatigue. The crack closure effect prevails over the entire range of da/dN – from crack formation, right up to failure.

Environment (Acceleration and Retardation). Crack tip stress-state controls susceptibility to environmental action. R-history determines *instantaneous, crack-tip hysteresis-dependent* mean Mode I stress component, which in turn controls the extent of *cyclic* environmental action. Environment determines to what extent crack extension in a single fatigue cycle of given K_{eff} will be enhanced by comparison to (intrinsic) vacuum growth rate. This effect is seen on a cycle-by-cycle basis and is closely linked to the degree of crack tip cyclic slip *reversibility*. It is unrelated to sustained load effects (corrosion cracking), that are characterized by inter-granular, time-dependent cracking. Broadly speaking, residual stress effects in fatigue may be attributed to environmental action. Residual compressive stresses protect the crack tip from the environment, while residual tensile stresses *increase exposure*. This effect is cyclic by nature and *instantaneously* responds to change in environment or residual stress. This environmental effect is more pronounced at near-threshold growth rates and appears to diminish to vanishing proportions with increasing growth rate. The effect disappears in vacuum, suggesting that the vacuum fatigue process is insensitive to stress ratio, stress history and residual stresses, unless these manifest themselves through other operative mechanisms, such as crack closure.

The stress-state associated with a higher load level is established *instantaneously* with the conclusion of the tensile half of the cycle. However, transition to a stress-state corresponding to a lower load level requires the crack to grow *out of* a larger previous plastic zone. This renders acceleration effects momentary and prolongs retardation effects.

It must be noted, that the significance of crack tip stress state (residual stress) has been highlighted in recent work [23]. However, no *explanation* for the effect was available at the time. Comparative tests in air and vacuum including to and fro

transition. High-resolution quantitative electron fractography revealed the nature and extent of this effect. The specially designed load sequence precluded the effect of closure.

Crack front incompatibility (retardation only).   Crack extension in each cycle moderates crack front and crack plane shape and tortuosity. The cumulative effect of preceding cyclic crack extension (history) under variable amplitude loading results in a crack front and plane that need not be the same as crack front and plane resulting from constant amplitude loading of a given magnitude. This represents a deviation from path of least resistance, leading to proportionate retardation in crack. This effect is load history sensitive and typical of load spectra involving the combined action of high and low magnitude fatigue cycles. Examples are transport aircraft wing and gas turbine load spectra.

The three mechanisms listed above may explain why most empirical models appear to work for *some* cases. These include the Wheeler [2] and Willenborg [3] models that appeared before the closure phenomenon was understood. They also explain 'anomalies' in fatigue crack growth that cannot be addressed by existing models including closure [6] as well as the more recent K_{PR} approach [7]. Crack extension under multiple overloads[22] is an example that has eluded explanation thus far: considerably increased crack extension in first overload cycle followed by even crack extension in subsequent overloads in a multiple overload sequence may be explained by environmentally enhanced crack growth in the first cycle. This action is diminished by the newly enlarged plastic zone. Subsequent overloads thus shielded from the environment cause considerably reduced crack extension. One may expect that if these overloads were applied in vacuum, crack extension in the first overload cycle would not be significantly different from that in the subsequent overload cycles.

CONCLUSION

Crack growth behavior is sensitive to a number of variables. Major load interaction mechanisms include crack closure, crack tip stress state and enforced crack extension mode.

The crack cannot propagate unless it is open. This underscores the significance of fatigue crack closure.

Environmental action may be explained by inhibition of slip reversibility through oxidation. Vacuum crack growth rate is related to extreme (limit) crack-tip slip reversibility. Slip reversibility is decreased by crack face dis-bond promoted by oxidation, which in turn is controlled by local tensile stress component. As both Stage I & II cracking involve crack tip slip reversal, crack-tip residual stress will directly affect environmental action and therefore, crack growth rate. This is a cycle-by-cycle process and responds instantaneously to change in loading as well as environment. The effect appears to be totally absent in vacuum. In air, the effect is pronounced at near-threshold conditions and appears to diminish with increasing crack growth rate. By having a bearing on crack formation and early crack growth, this effect significantly affects total fatigue life.

The beneficial effect of residual stress is manifested through reduced crack tip environmental action. Crack tip residual stress is controlled by load history. In long cracks, such residual compressive stresses will be greater if estimated monotonic plastic zone size due to current load cycle is smaller than that of pre-existing monotonic plastic zone and vice versa. Fatigue resistance of crack formation sites and short cracks is enhanced by inhibiting environmental action. It would follow that the action of compressive residual stresses is similar to that of protective coatings – both inhibit ingress of aggressive agents.

High crack growth rates accompanied by fatigue void coalescence from internal shearing of secondary non-coherent particulates (strain localization as in ref. 21) and micro-void coalescence under localized quasi-static cracking (as K_{max} approaches K_{1c}) are unlikely to be affected by environment in the same manner as early crack growth. This may explain why the difference between air and vacuum crack growth rates diminishes at high growth rates. Fig. 23 schematically summarizes the R-ratio effect over the entire range of growth rates.

The transition in crack extension mode from Stage I to Stage II to quasi-static crack extension is a continuous process. This process is accompanied by a gradual

transition in crack front shape and plane. However, while the former is sensitive to individual load cycles, the latter is sensitive to cumulative crack extension. Therefore, under variable amplitude loading, preferred crack extension mode and prevailing crack front shape and plane may not be 'compatible'. As crack growth occurs along the path of least resistance, one may presume that incompatibility between current mode and prevailing crack front geometry can only cause retardation. A possible exception may be the tongue-shaped crack tunneling under enforced flat crack surface, which would appear highly accelerated by comparison to crack extension under similar loading given a slant fracture plane.

Unlike mode-incompatibility, crack closure and crack tip residual stress-induced environmental effect can cause retardation as well as acceleration. However, environment-induced acceleration will be evident only during the first cycle and may not be crack extension - dependent. All three effects will show crack extension dependent retardation. This may explain why crack acceleration effects are reported less often.

REFERENCES

1. Newman, J.C., A Crack Closure Model for Predicting Fatigue Crack Growth under Aircraft Spectrum Loading, Methods and Models for Predicting Fatigue Crack Growth under Random Loading, ASTM STP 748, J.B. Chang and C.M. Hudson, Eds., American Society for Testing and Materials, 1981, pp. 53-84.

2. Wheeler, O.E., Journal of Basic Engineering, Trans. ASME, March 1972, pp. 181-186.

3. Willenborg, J.D., Engle, R.M., and Wood, H.A., A Crack Growth Retardation Model Using an Effective Stress Concept, AFFDL-TM-FBR-71-1, Air Force Flight Dynamics Laboratory, 1971.

4. Forman, R.G., Shivakumar, V., Newman, J.C., Jr., Piotrowski, S.M., and Williams, L.C., Development of the NASA/FLAGRO Computer Program, Fracture Mechanics: Eighteenth Symposium, ASTM STP 945, D.T. Read and R.P. Reed, Eds., American Society for Testing and Materials, Philadelphia, 1988, pp. 781-803.

5. Schijve, J., Observations on the Prediction of Fatigue Crack Growth Propagation Under Variable Amplitude Loading, Fatigue Crack Growth Under Spectrum Loads, ASTM STP 595, American Society for Testing and Materials, 1976, pp. 3-23.

6. Elber, W., The Significance of Fatigue Crack Closure, Damage Tolerance in Aircraft Structures, ASTM STP 486, American Society for Testing and Materials, Philadelphia, 1971, pp. 230-242.

7. Lang, M. and Marci, G., Reflecting on the Mechanical Driving Force of Fatigue Crack Propagation, Fatigue and Fracture Mechanics: Twenty-Ninth Volume, ASTM STP 1332, T.L. Panontin and S.D. Sheppard, Eds., American Society for Testing and Materials, West Conshohocken, PA, 1999.

8. Sunder, R., and Dash, P.K., Int. J. Fatigue, Vol. 4, 1982, pp. 97-105.

9. Sunder, R., Prakash, R.V., and Mitchenko, E.I., Fractographic Study of Notch Fatigue Crack Closure and Growth Rates, Fractography of Modern Engineering Materials, Composites and Metals, Second Volume, ASTM STP 1203, J.E., Masters and L.N. Gilbertson, Eds., American Society for Testing and Materials, Philadelphia, 1993, pp. 113-131.

10. Riddel, W.T., and Piascik, R.S., Stress Ratio Effects on Crack Opening Loads and Crack Growth Rates in Aluminum Alloy 2024, Fatigue and Fracture Mechanics: Twenty-Ninth Volume, ASTM STP 1332, T.L. Panontin and S.D. Sheppard, Eds., American Society for Testing and Materials, West Conshohocken, PA, 1999.

11. Sunder, R., Porter, W.J., and Ashbaugh, N.E., The Effect of Stress Ratio on Fatigue Crack Growth Rate in the Absence of Closure, International J. Fatigue, Vol. 19, Supp. No. 1, 1997, pp. S211-S221.

12. Sunder, R., Porter, W.J., and Ashbaugh, N.E., Stress-Level Dependent Stress Ratio Effect on Fatigue Crack Growth, Fatigue and Fracture Mechanics: Twenty-Ninth Volume, ASTM STP 1332, T.L. Panontin and S.D. Sheppard, Eds., American Society for Testing and Materials, West Conshohocken, PA, 1999.

13. Ashbaugh, N.E., Porter, W.J., Prakash, R.V., and Sunder, R., A Fractographic Study of Load-Sequence – Induced Mixed-Mode Fatigue Crack Growth in an Al-Cu Alloy, Mixed-Mode Crack Behavior, ASTM STP 1359, K.J. Miller and D.L. McDowell, Eds., American Society for Testing and Materials, West Conshohocken, PA, 1999, pp. 258-278.

14. R. Sunder, Notch Root Crack Closure under Cyclic Inelasticity, FFEMS, vol. 16, No. 7, 1993, pp. 677-692.

15. Sunder, R., Porter, W.J., and Ashbaugh, N.E., Fatigue Voids And Their Significance, Manuscript submitted to FFEMS, 2001.

16. Laird, C, Mechanisms and Theories of Fatigue, Fatigue and Microstructure, ASM, Metals Park, 1978, pp. 149-204

17. Laird, C., The Influence of Metallurgical Structure on the Mechanism of Fatigue Crack Propagation, Fatigue Crack Propagation, ASTM STP 415, American Society of Testing and Materials, West Conshohocken, PA, 1967, p.131.

18. H. Shen, S.E. Podlaseck and I.R. Kramer, Acta Met, 14, 341 (1966).

19. R.J. Cooke, P.E. Irving, G.S. Booth and C.J. Beevers, Eng. Fract. Mech. 7, 69 (1975)

20. Duquette, D.J., Environmental Effects I: General Fatigue Resistance and Crack Nucleation in Metals and Alloys, Fatigue and Microstructure, ASM, Metals Park, 1978, pp. 335 –364

21. Starke, E.A., Jr., and Lutjering, G., Cyclic Plastic Deformation and Microstructure, Fatigue and Microstructure, ASM, Metals Park, 1978, pp. 205-244.

22. Lang, M. and Marci, G., The Influence of Single and Multiple Overloads on Fatigue Crack Propagation, FFEMS, vol. 22, 1999, pp. 257-271.

LIST OF FIGURES

crack size. This appears to suggest retardation under lower amplitude cycling, rather than acceleration under the marker loads. Keyhole notched 2024-T351 C(T).

Fig. 12 Markers begin to dominate at high crack growth rates. Flat region corresponding to low amplitude cycling is vastly reduced. Keyhole notched 2024-T351 C(T). Crack growth in low amplitude cycles appears to be effectively arrested at certain locations due to local crack plane orientation and roughness.

Fig. 13 Crack extension predominantly under high amplitude markers. Low amplitude crack growth down to vanishing proportions as shown by rare pockets of flat region in a) that is zoomed into in b). b) shows a mix of fatigue and quasi-static component in the form of ductile micro-void coalescence normally associated with static fracture. Keyhole notched 2024-T351 C(T).

Fig. 14 By contrast to air, vacuum is not conducive to fatigue striation formation - even at growth rate as high as 10^{-6} m/cycle. Note 'tacky' texture of striation bands. It would appear that crack-tip slip reversibility comes in the way of discernible striation formation. Notched 2014-T6511.

Fig. 15 Notch root crack formation and growth under periodic transition between air and vacuum. a-c show typical fractographs with progressive degree of zoom-in. Macro in a) shows two crack formation sites marked by arrows. Regions on the fracture surface are numbered 1 to 8 with odd numbers indicating Air and even numbers corresponding to Vacuum. Notched 2014-T6511.

Fig. 16 Typical fractographs from vacuum region of fatigue fracture. d) is zoomed in area encircled in c). Note even spacing, indicating total absence of stress ratio history effect. Notched 2014-T6511.

Fig. 17 Typical fractographs confirming the absence of any transition effect associated with environment change. Switching from air to vacuum or vice-versa causes an immediate change in crack growth behavior. This indicates absence of 'environment history' effect. Notched 2014-T6511.

Fig. 18 Summary of crack growth rates in air and vacuum as determined from quantitative fractography. Notched 2014-T6511.
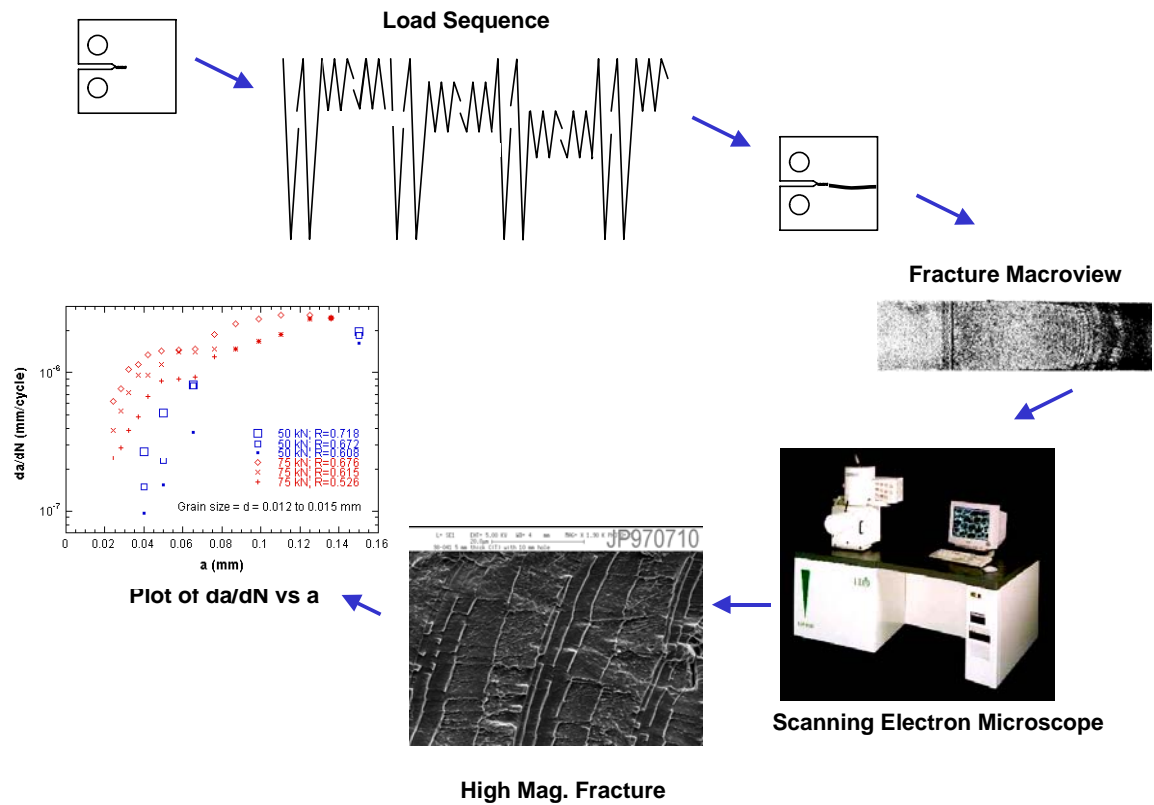
Load Sequence

Fracture Macroview

Scanning Electron Microscope

Plot of da/dN vs a

da/dN (mm/cycle)

10^{-6}

10^{-7}

50 kN; R=0.718
50 kN; R=0.872
50 kN; R=0.608
75 kN; R=0.676
75 kN; R=0.615
75 kN; R=0.526

Grain size = d = 0.012 to 0.015 mm

a (mm)

0   0.02 0.04 0.06 0.08 0.1 0.12 0.14 0.16

JP970710

High Mag. Fracture

Fig. 1   Schematic of experimental procedure. Notched coupons – programmed loading with markers – fatigue fractures – electron microscopy to reconstruct crack formation and growth process – da/dN vs a plot.
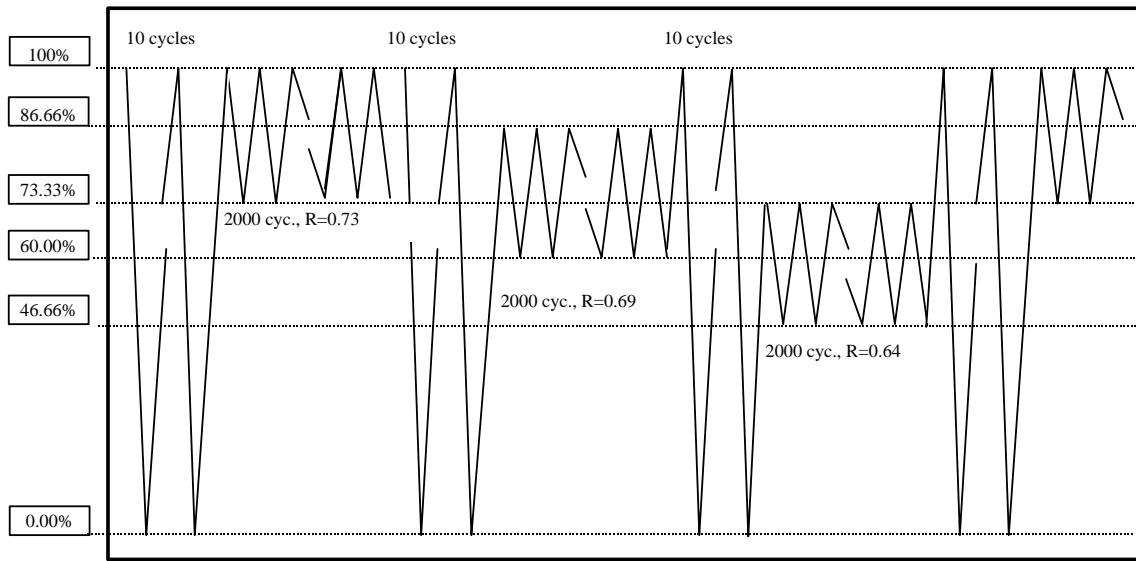
a)
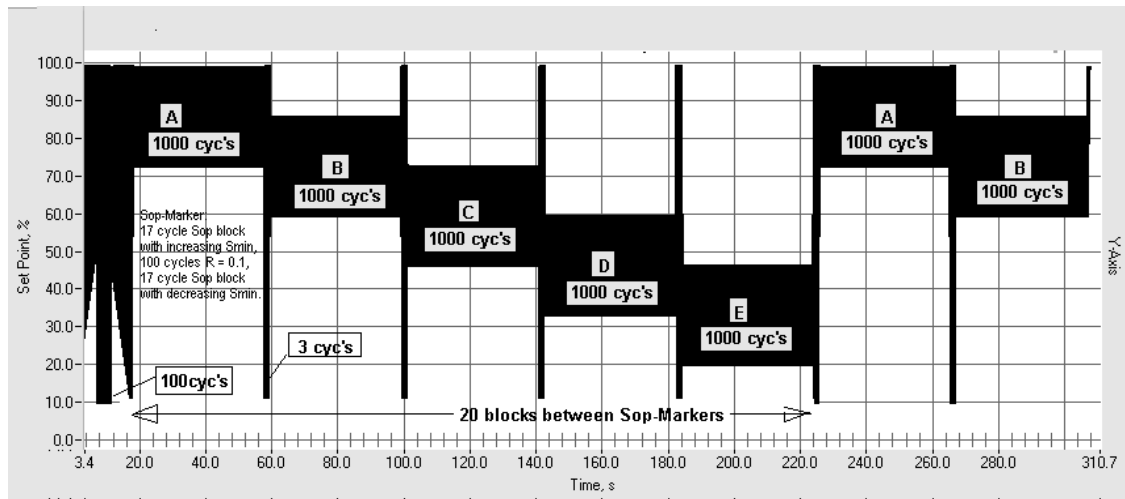
b)

Fig. 2   Load programs used in the study: a) 3R blocks and b) 5R with closure blocks [13].

NSE(T)

a)

NC(T)

b)

C(T)

c)
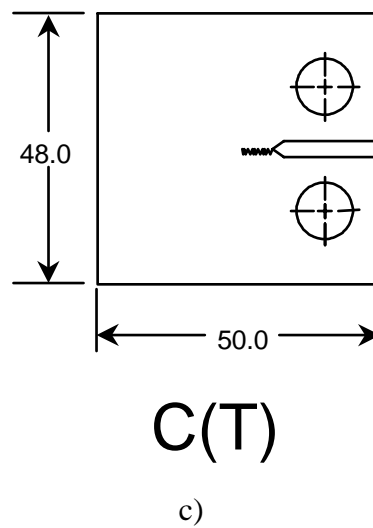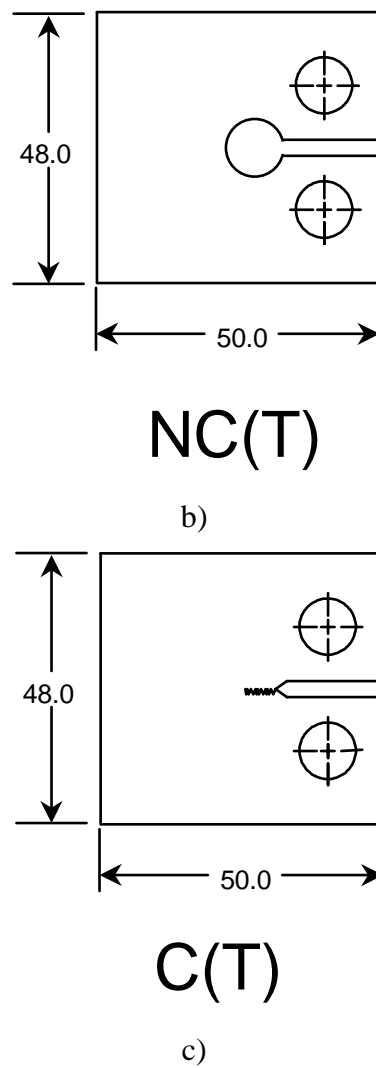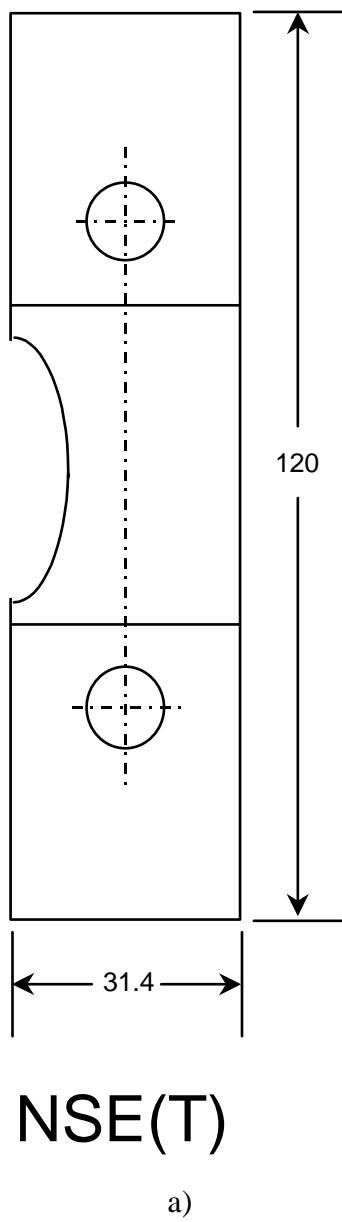
Fig. 3   Notched coupons used in the experiments: a) NSE(T), b) NC(T), and c) C(T).
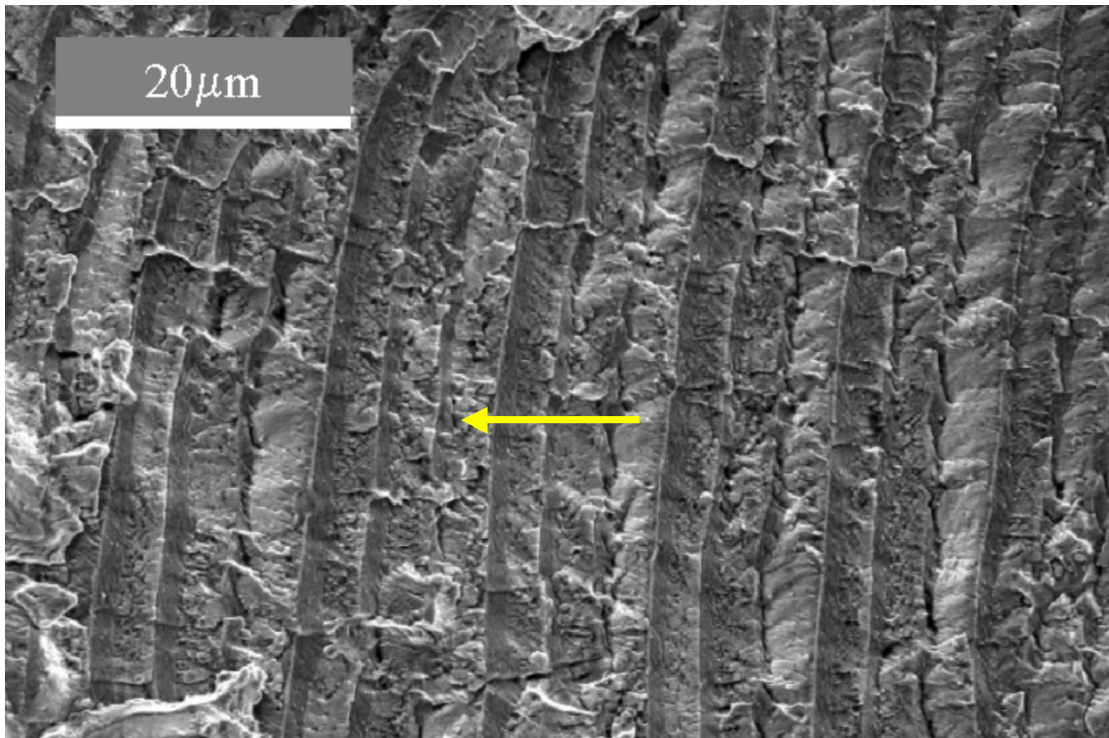
Fig. 4   Typical fractograph from long crack test on a C(T) specimen. Uniform striation bands indicate that at crack growth rate of about 2×10^{-9} m/cycle, the fatigue process was not sensitive to stress ratio variation. There appears to be no stress ratio effect in the absence of closure.
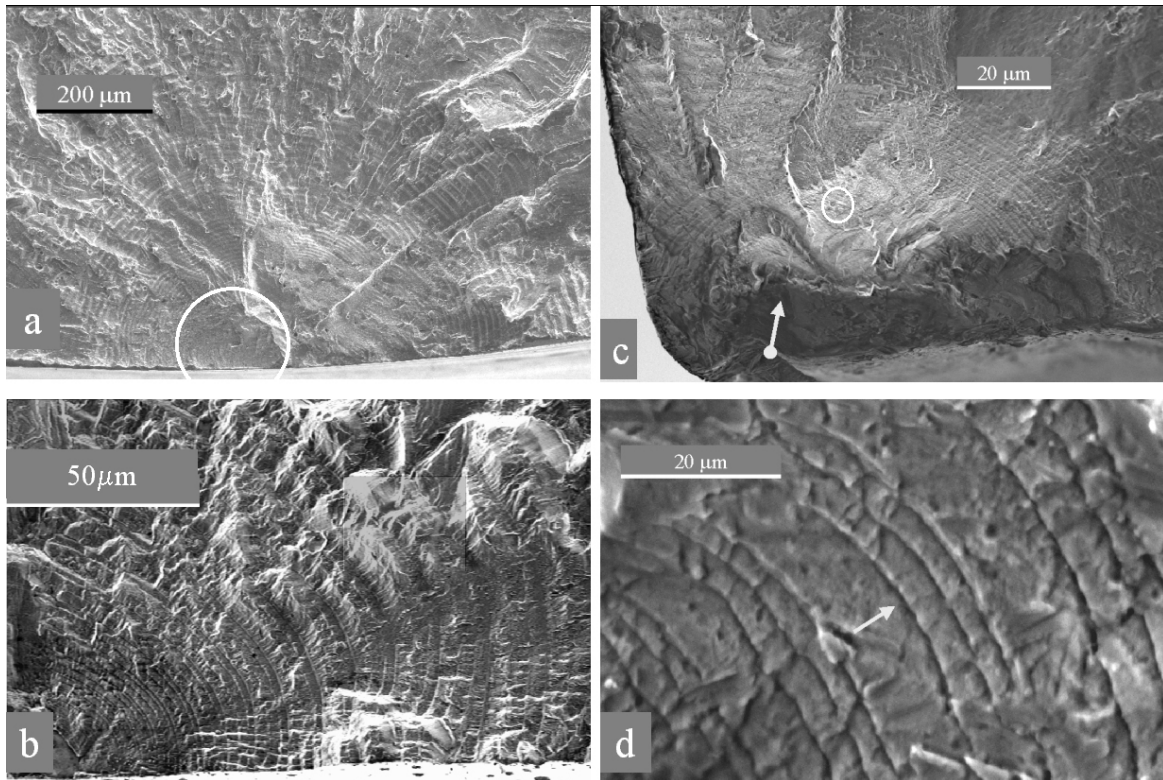
Fig. 5   Typical fractographs from notched coupon tests. a, b and c show macros of the notch root with crack origin and growth patterns. d shows zoomed-in view of the area encircled in c. The growth rate here is of the same order as that in Fig. 4. However, a distinct stress ratio *history* effect is apparent. Notched 2014-T6511.
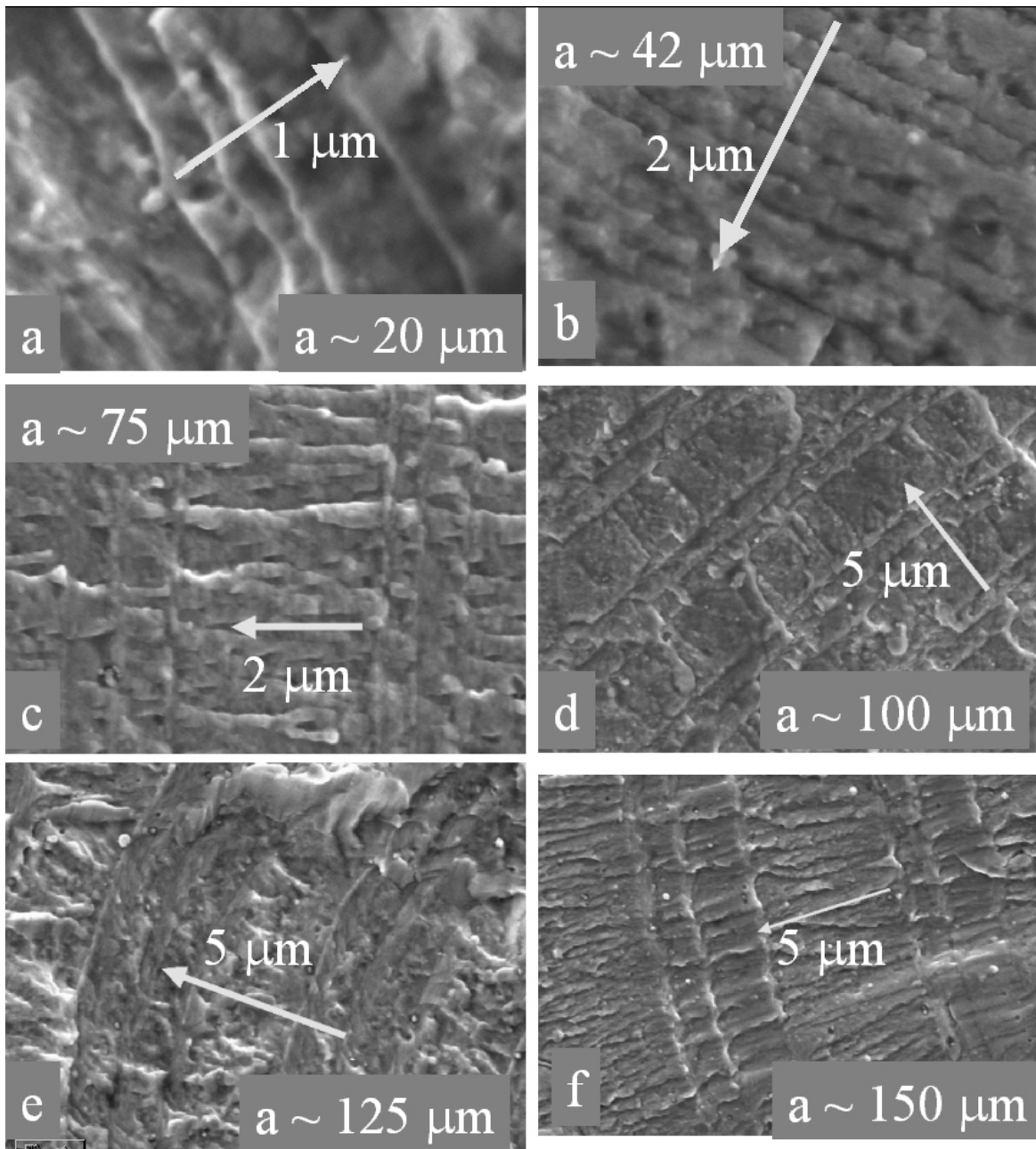
Fig. 6   Marker bands at different crack sizes from the fracture shown in Fig. 5a. Arrows indicate direction of crack growth. Their length serves as scale bar. Growth rate change with crack size is from as low as 10^{-10} to 2.5×10^{-9} m/cycle. Notched 2014-T6511. Fig. 6c underscores the significance of the marking process. In the absence of markers even the direction of crack growth would be masked by unrelated morphology.
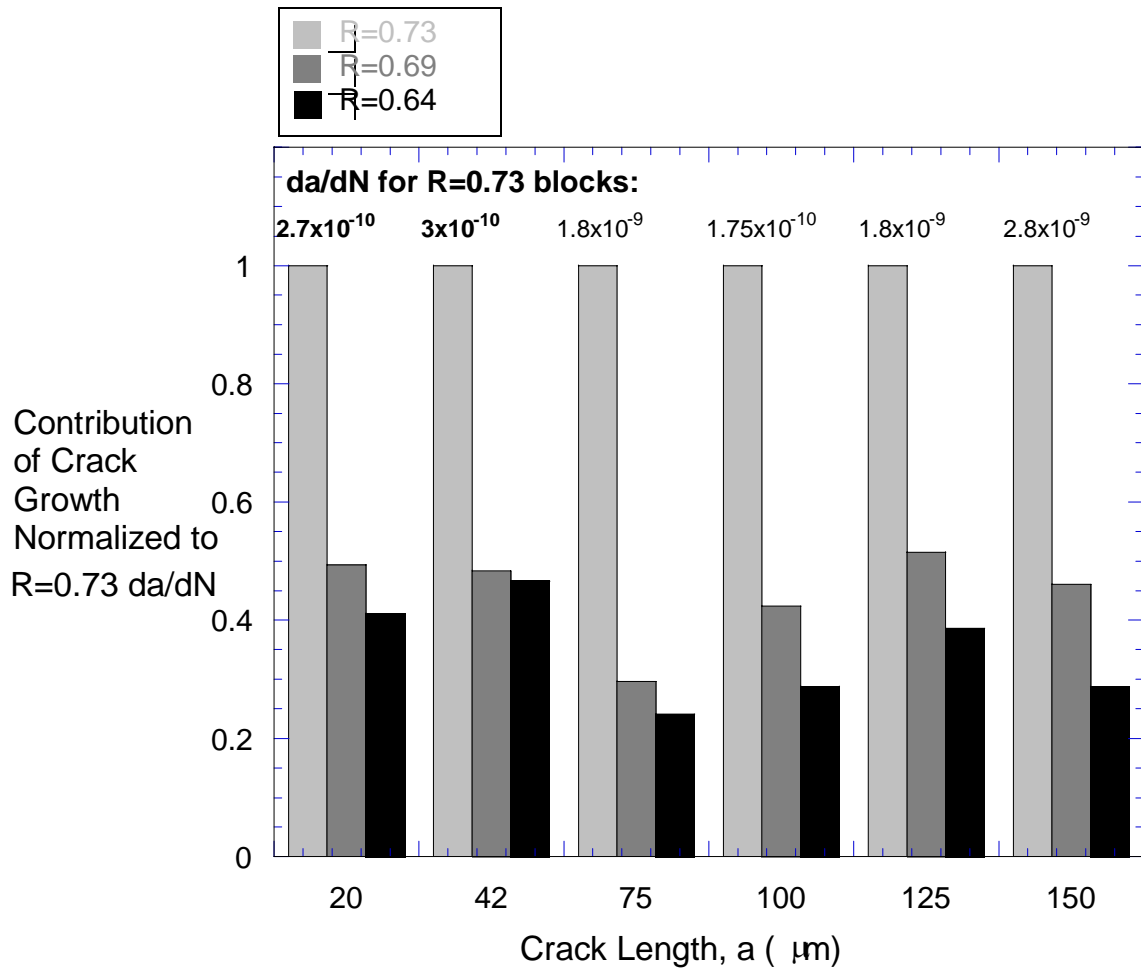
Fig. 7   Effect of stress ratio variation on crack growth rate as summarized from the fractographs in Fig. 6. Notched 2014-T6511.
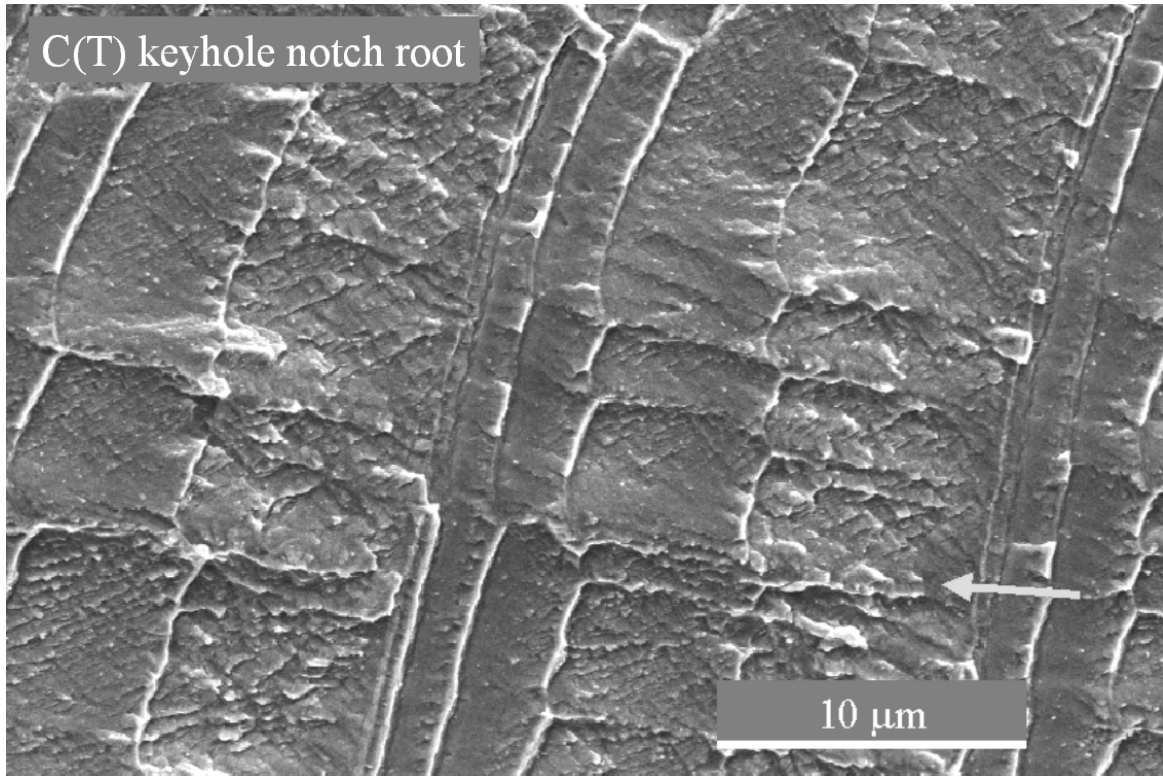
Fig. 8   Fractograph showing striation band variation under 5-step variation of stress ratio [13]. Dramatic reduction in growth at lowest stress ratio is due to partial crack closure. 2014-T6511 C(T).
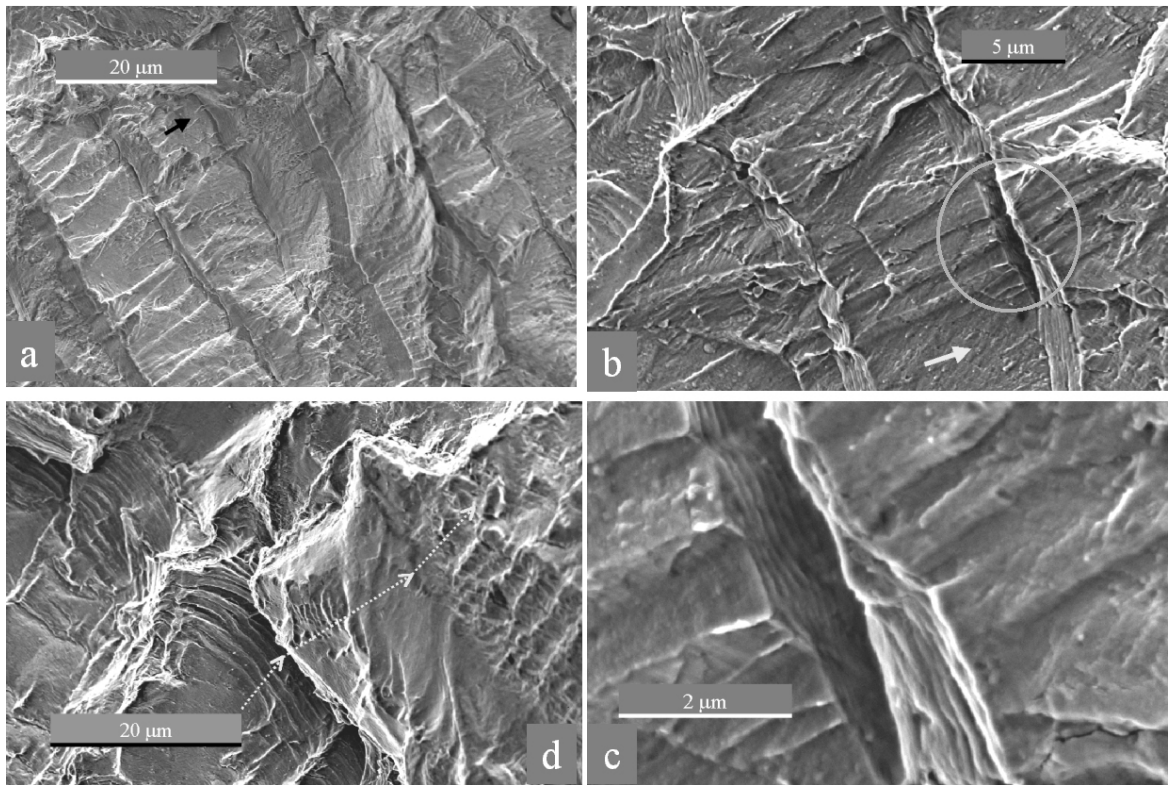
Fig. 8

Fig. 9 Consequences of crack extension mechanism incompatibility between baseline and marker loads. a) Disproportionate increase in marker component indicating retarded crack growth in baseline cycles, b – d) crack branching. c) shows zoomed in view of b). Notched 2014-T6511.
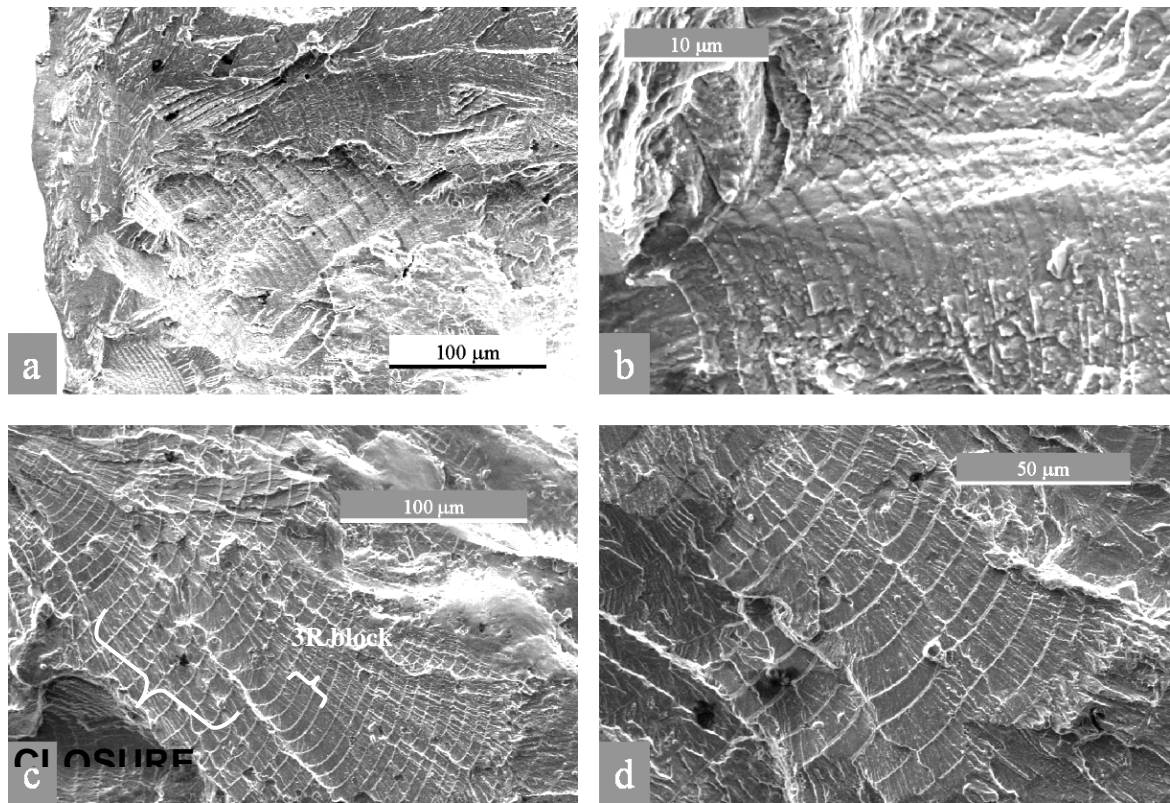
Fig. 10. Small crack fractographs from notch root region of keyhole 2024-T351 C(T) specimen. (a, b, c) show three different crack formation sites at the notch root., (d) provides a zoomed in view of c) to enable quantitative assessment of crack opening load and stress ratio effect. From the three-band sets, we observe two equally spaced and the third corresponding to lowest R with noticeably diminished spacing. This demonstrates the total absence of stress ratio history effect (equal pair) and partial crack closure at lowest R.
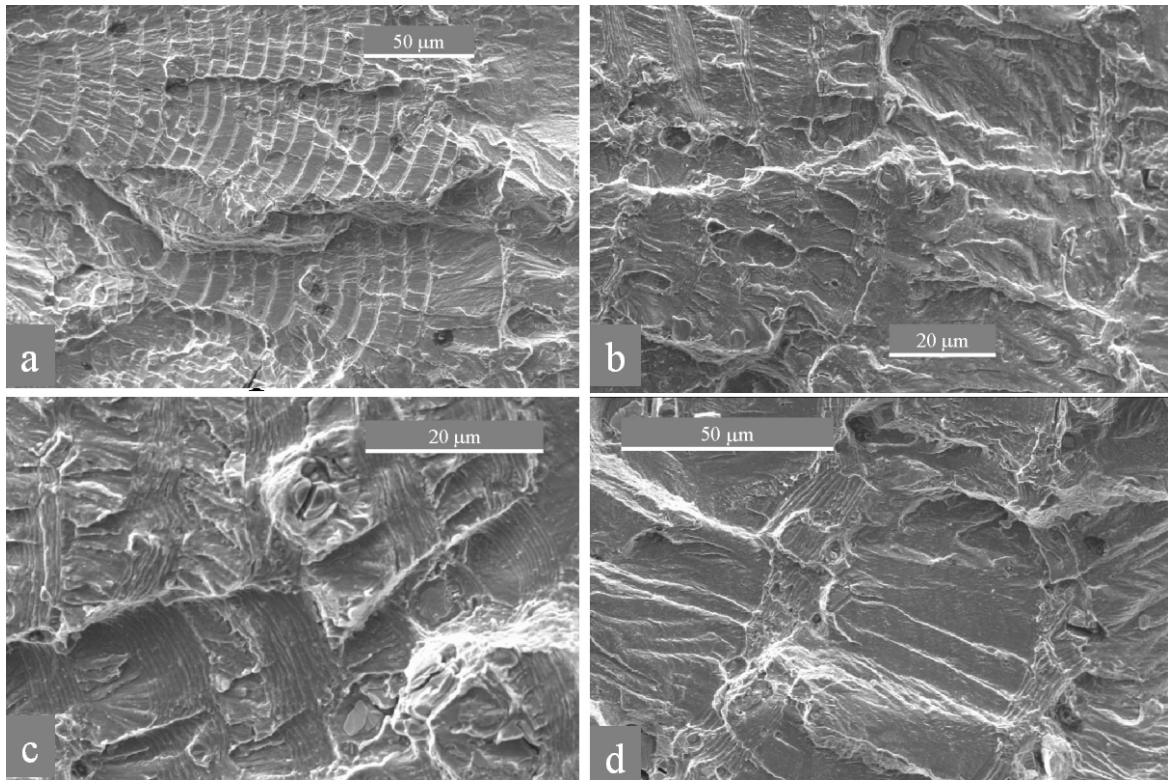
Fig. 11 Progressive increase in fractional contribution of marker cycles to crack growth under programmed loading. a, b, c and d are from progressively increasing crack size. This appears to suggest retardation under lower amplitude cycling, rather than acceleration under the marker loads. Keyhole notched 2024-T351 C(T).
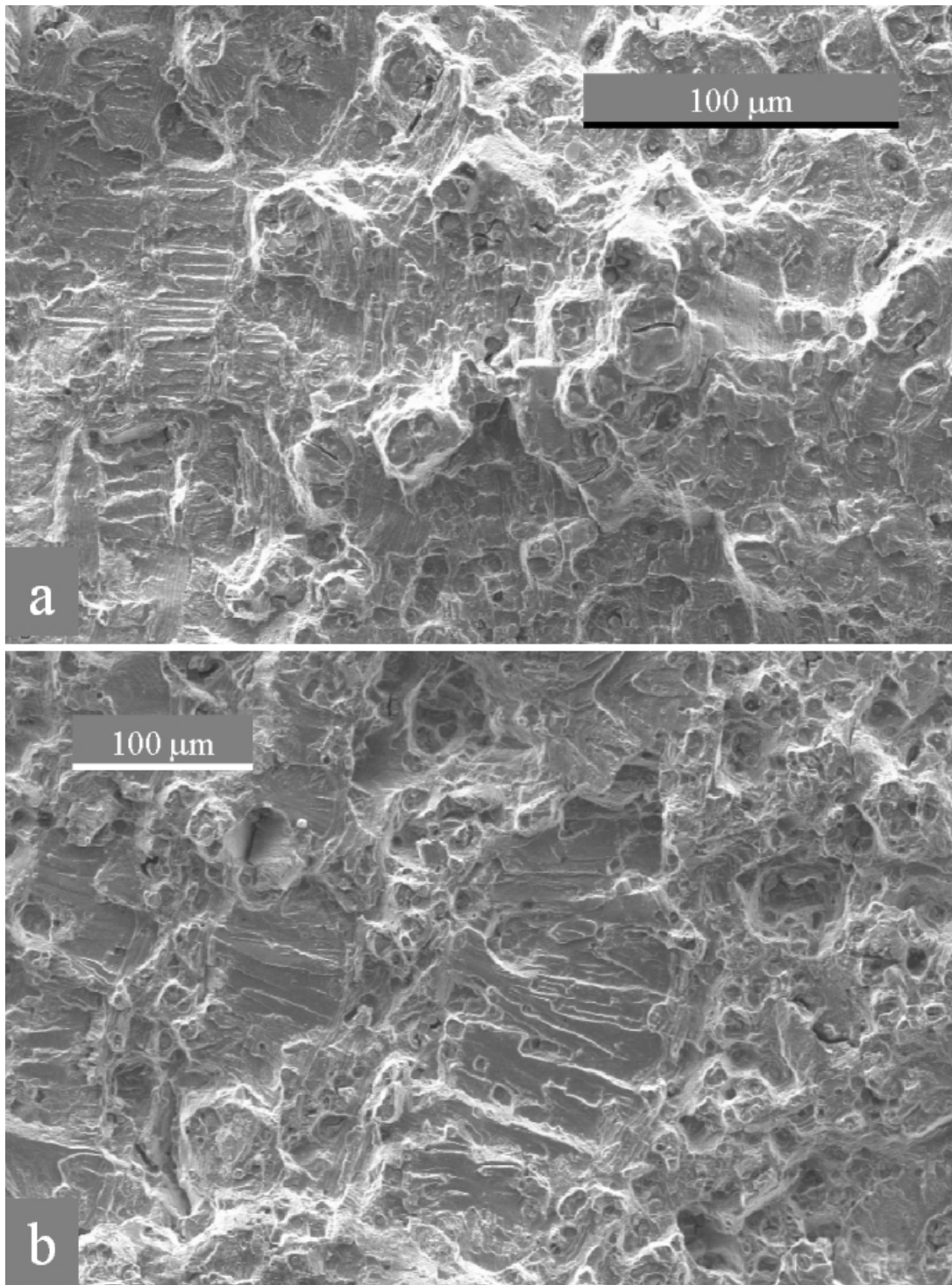
Fig. 12 Markers begin to dominate at high crack growth rates. Flat region corresponding to low amplitude cycling is vastly reduced. Crack growth in low amplitude cycles appears to be effectively arrested at certain locations due to local crack plane orientation and roughness. Keyhole notched 2024-T351 C(T).
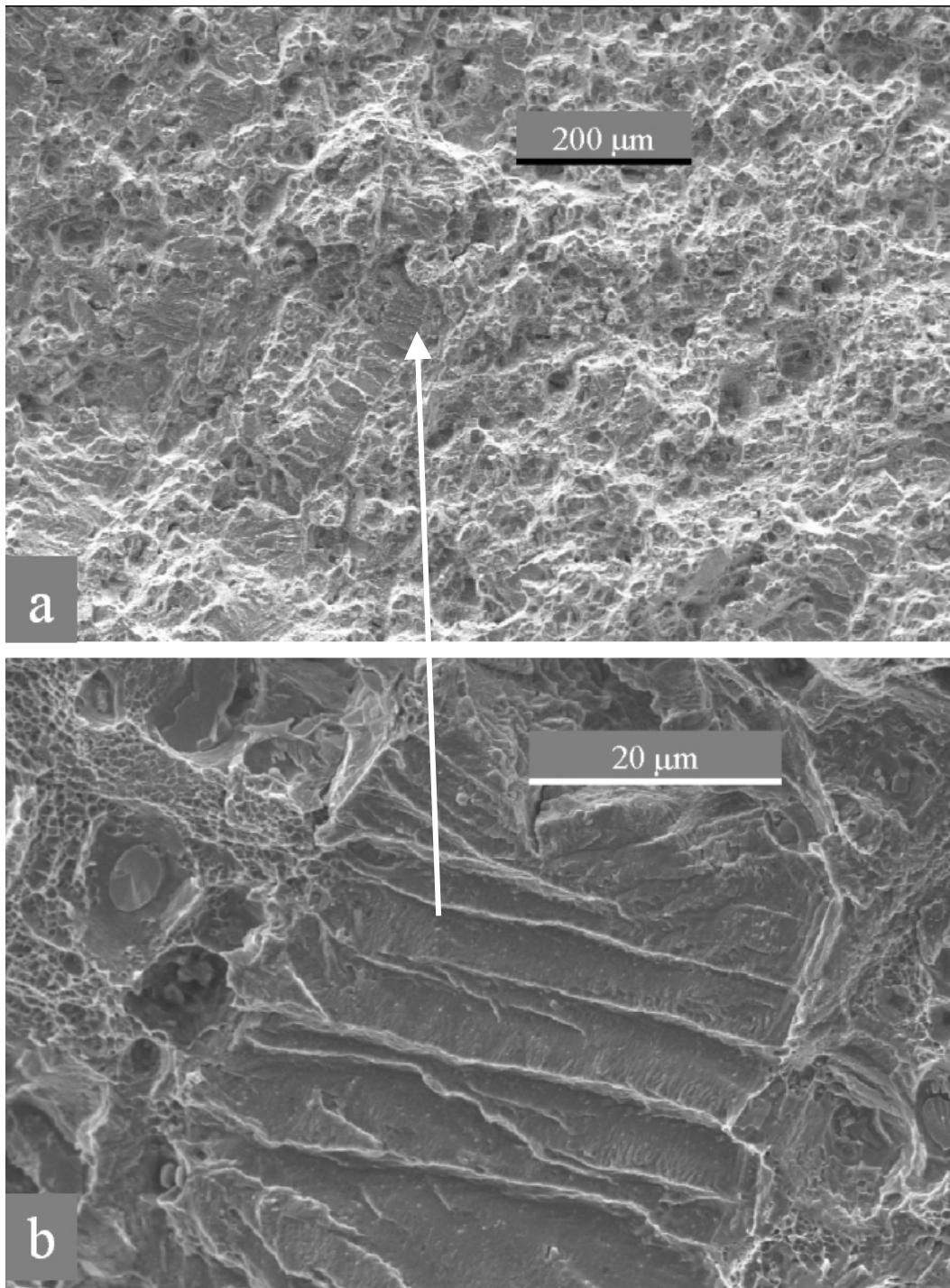
Fig. 13 Crack extension predominantly under high amplitude markers. Low amplitude crack growth down to vanishing proportions as shown by rare pockets of flat region in a) that is zoomed into in b). b) shows a mix of fatigue and quasi-static component in the form of ductile micro-void coalescence normally associated with static fracture. Keyhole notched 2024-T351 C(T).
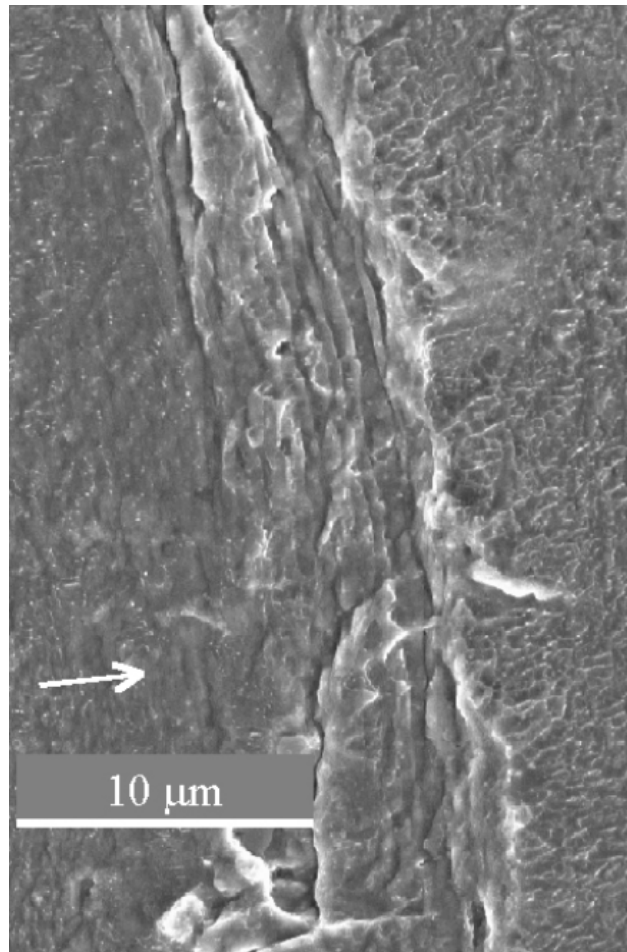
Fig. 14 By contrast to air, vacuum is not conducive to fatigue striation formation - even at growth rate as high as 10^{-6} m/cycle. Note the 'tacky' texture of striation bands. It would appear that crack-tip slip reversibility comes in the way of discernible striation formation. Notched 2014-T6511.

Fig. 15 Notch root crack formation and growth under periodic transition between air and vacuum. a-c show typical fractographs with progressive degree of zoom-in. Macro in a) shows two crack formation sites marked by arrows. Regions on the fracture surface are numbered 1 to 8 with odd numbers indicating Air and even numbers corresponding to Vacuum. Notched 2014-T6511.

Fig. 16 Typical fractographs from vacuum region of fatigue fracture. d) is zoomed in area encircled in c). Note even spacing, indicating total absence of stress ratio history effect. Notched 2014-T6511.

Fig. 17 Typical fractographs confirming the absence of any transition effect associated with environment change. Switching from air to vacuum or vice-versa causes an immediate change in crack growth behavior. This indicates absence of 'environment history' effect. Notched 2014-T6511.

Fig. 18 Summary of crack growth rates in air and vacuum as determined from quantitative fractography. Notched 2014-T6511.

ENVIRONMENT - RELATED LOAD HISTORY EFFECTS IN ELEVATED TEMPERATURE FATIGUE OF A NICKEL-BASE SUPERALLOY
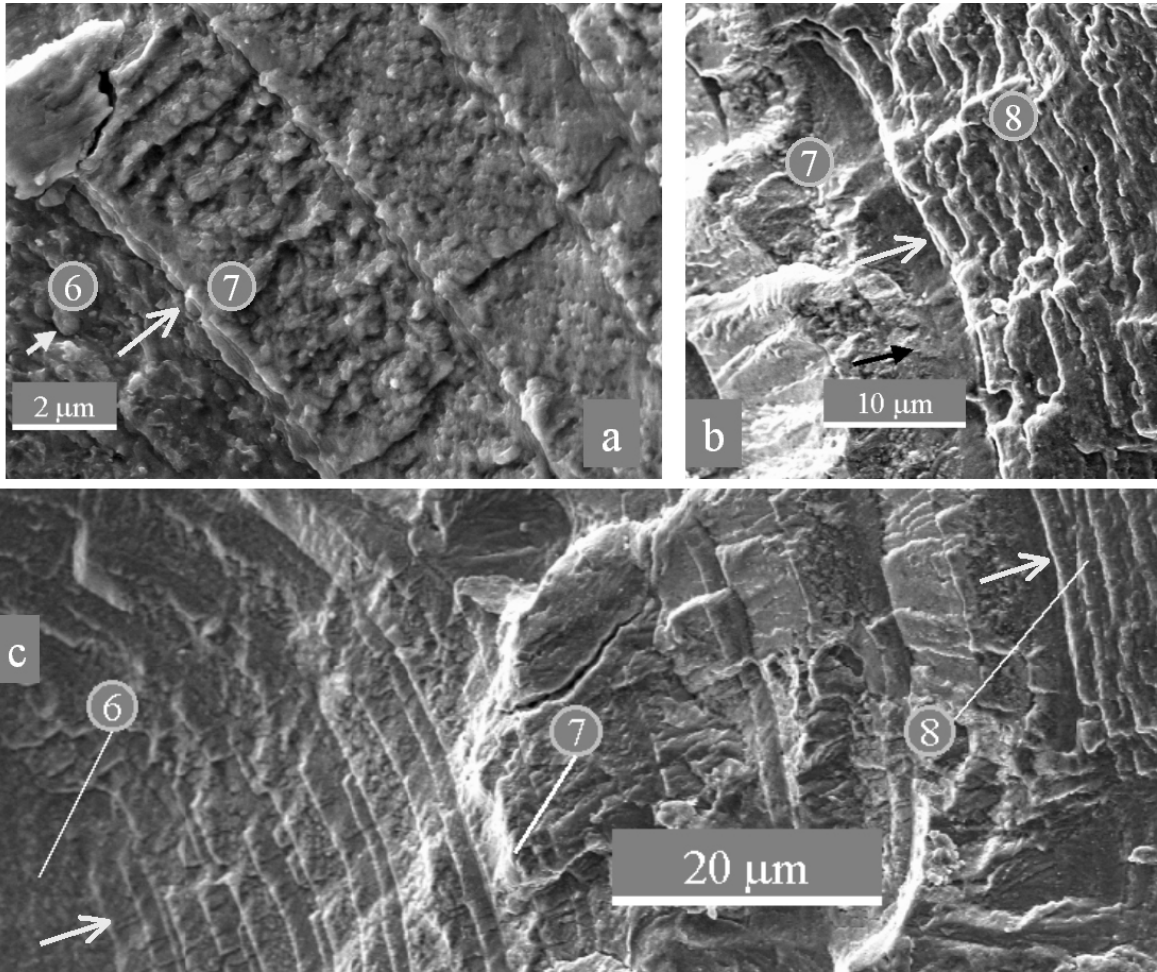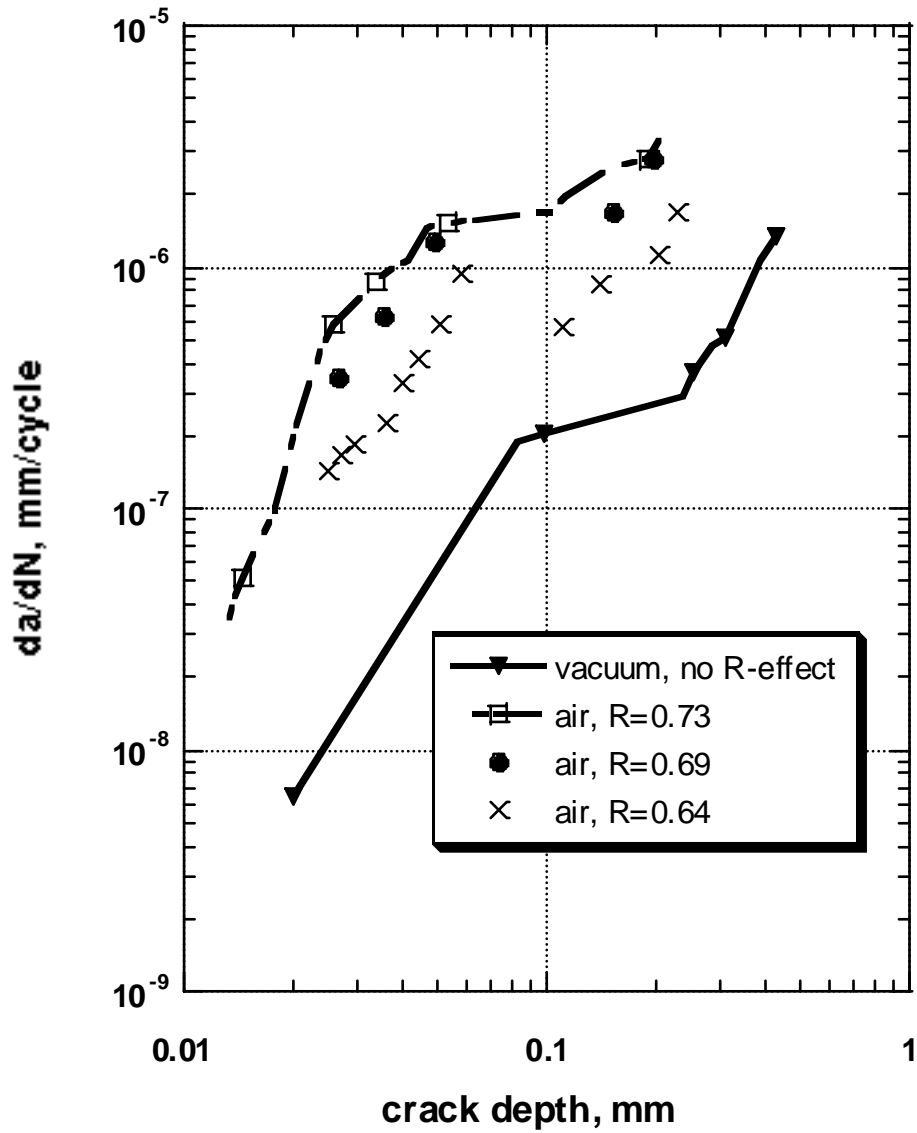
N.E. Ashbaugh[*], W.J. Porter[*], A.H. Rosenberger[**] and R. Sunder[***]

Near-threshold elevated temperature fatigue crack growth rates in nickel-base superalloy IN-100 are sensitive to load history effects that cannot be attributed to crack closure. The effects disappear in vacuum, suggesting operative mechanisms that are environment related. Experiments on compact-tension coupons under low amplitude loading show that programmed step-wise reduction in stress ratio causes noticeably retarded crack growth that cannot be explained from crack closure considerations. The effect rapidly diminishes with increasing stress-intensity range, indicating a near-threshold phenomenon. This effect is altogether absent in vacuum tests at elevated temperature. The experiments also indicate crack growth retardation when fatigue loading is mixed with hold-time. This appears to be caused by incompatible macro and micro crack front orientation associated with differences between the nature of sustained load and fatigue cracking.

INTRODUCTION

Load interaction effects causing acceleration and retardation of the fatigue process continue to sustain the attention of ongoing research. This study was prompted by the recent observation by the authors [1] of noticeable 'closure-free' crack growth retardation in an Al-alloy caused by a minor reduction in applied stress ratio. The effect was attributed to moderation of environmental action that is controlled by history-sensitive residual crack tip stress state in the plastic zone ahead of the crack tip, a conclusion supported by repeat tests in vacuum. If load history effects occur through moderation of environmental action, they ought to be even more pronounced in elevated temperature fatigue. This paper describes research that explores such a possibility.

EXPERIMENTS AND RESULTS

The experiments were performed using compact tension, C(T), specimens cut from nickel-base superalloy IN100 and tested under two-step high-stress ratio (Hi-R) programmed loading along with marker loads for fractographic detection (see Fig.1). Crack growth under the lower-R step occurs through the larger plastic zone left behind by the higher-R step. In addition to the two steps of Hi-R fatigue cycling, a hold-time

was periodically added in an attempt to induce time-dependent crack extension and its interaction with fatigue loading.

To confirm the absence of crack-closure under the Hi-R steps, S_{op} was fractographically determined using the load sequence shown in Fig. 2a. after Sunder and Prakash [2]. The sequence consists of 10 steps of 2000 cycles, each interspersed with ten marker cycles. The marker cycles are dominant and control crack opening stress, S_{op}. Crack extension over the intermediate 2000 cycle steps will be sensitive to this S_{op}, which is assumed to be constant[1]. Given S_{max} = Const and steadily increasing S_{min} over each step, crack extension will be constant while $S_{op} > S_{min}$ and recede rapidly when $S_{op} < S_{min}$. Fig. 2b shows a typical fractograph from this test. In this picture, the periodic narrow bands correspond to the 10 marker cycles. The first six broad bands are equally spaced, followed by four bands of receding width. This is indicative of partial crack closure over the first six steps of the load program, and corresponds to $S_{op} \sim 30\%$ of S_{max}. The Hi-R two-step tests were performed with S_{min} in the Hi-R steps exceeding 45% of highest applied loads. We assume crack closure did not occur in these steps.

Fatigue crack growth rates were determined through high-resolution Scanning Electron Microscopy (SEM) of fractures obtained under the programmed load sequences. The experiments were preceded by pilot studies to optimize test parameters in order to facilitate quantitative optical and SEM fractography. Of the tests reported in this paper, two were conducted in air at 482ºC and 650ºC. The third was conducted in high vacuum (approximately 10^{-9} torr) at 650ºC.

To improve the quality of fractography, we replaced the high amplitude markers in Fig. 1 with a 10,000 cycle low R, low-amplitude (Lo-R-Lo-Amp) markers. $S_{max} > S_{op}$ in these markers ensured sufficient growth did occur. As confirmed by Fig. 3, the fact that some growth did occur during the Lo-R-Lo-Amp markers was further evidence of a fully-open crack at Hi-R.

Conventional crack measurement techniques are not best suited to study Hi-R (closure-free) load interaction effects. Their resolution is not fine enough to quantify crack extension in individual steps, which in turn must not exceed the interval over which such load interaction is effective[2]. Further, near threshold crack growth rate cannot be estimated from striations because such striations if any, also cannot be resolved. These limitations were overcome by the Lo- R-Lo-Amp markers that serve the dual purpose of keeping crack opening stress level low as well as introducing clearly discernible, fine growth marks. Assuming crack growth rate to be constant during a step[3], growth rate was estimated as the ratio of marker-band spacing to cycle count interval. Thus, even though individual striations cannot be resolved, growth rate can be accurately estimated from marker band spacing.

---

[1] Based on the assumption that closure is plasticity driven and given plastic zone size far exceeding crack extension in individual steps of 2000 cycles.

[2] Assuming residual compressive stresses are driven by baseline to overload plastic zone size, one may expect the effect to manifest itself over a portion of the Hi-R plastic zone size.

[3] In order to preclude transient effects, step cycle count in our experiments was suitably selected to ensure that the associated marker band spacing does not exceed a fraction of plastic zone size.

The Lo-R-Lo-Amp markers were identifiable both through optical as well as SEM fractography. Markers were evident in both elevated temperatures studied as well as in air and vacuum environments. Typical fractographs from the near-threshold region pertaining to testing at 650ºC in air appear as Fig. 4. In these pictures, crack extension from the higher-R step is shown by the white arrow, while the black arrows indicate crack growth from the lower-R step. The pictures are arranged in order of increasing crack growth rate (increasing crack size). The difference in growth rate between the two steps is dramatic at near-threshold levels, as seen in Fig. 4a. However, the difference rapidly recedes with increasing growth rate as underlined in the bottom picture that shows equal growth in the two steps.

Note that the difference in ΔK between the fractographs in Fig. 4a and Fig. 4d is just 2-3 MPa√m and it was traversed in 2 mm of crack extension. This behavior is indicative of the extreme nature of this retardation effect. The same effect was observed in air tests at both temperatures. However, a repeat test in vacuum did not reveal such an anomaly: growth rate in both steps was found to be identical. The same observation had been made previously from similar tests in air and vacuum at room temperature on an Al-Cu alloy [1]. The effect appears to be environment related and manifests through history-dependent variation of threshold stress intensity, ΔK_{th}. If threshold stress intensity is sensitive to load history, it really cannot be deemed a material constant. This sensitivity to environment may also explain why this parameter can be extremely sensitive to the exponent defining decreasing stress-intensity in ASTM-E647 standard practice for determination of threshold stress intensity. One may expect such sensitivity to disappear were the test to be performed in vacuum.

Fig. 5 summarizes fractographic estimates of crack growth rate from the three comparative tests. As expected, vacuum crack growth rates are lower than in air. Further, air growth rate at 650ºC exceeds rates at 482ºC given the same stress intensity range. Crack growth rates in the two Hi-R steps tend to converge for increasing stress intensity range. However, as indicated earlier, the environment-induced load interaction effect significantly affects near-threshold behavior in air.

The substantial retardation of near-threshold crack growth rates discussed above was caused by a reduction in stress ratio of approximately 0.05. This in turn represents an overload ratio of approximately 15%. Given the relationship between plastic zone size and maximum stress intensity, a 15% overload will cause an approximately 25% increase in plastic zone size. Thus, crack growth at the lower of the two Hi-R steps occurred through a plastic zone 25% larger than that associated with constant amplitude fatigue. It would follow that residual compressive stresses induced by such an overload bring down near-tip hydrostatic tensile stresses to an extent that causes such a consistent and noticeable increase in near-threshold fatigue resistance associated with reduced environmental action. This new finding comes as a surprise given that most experiments on the effect of overloads use overload ratios in excess of 30%. Retardation under smaller overloads is generally considered negligible. As shown by this study, the effect can be substantial in the near-threshold regime. By the very nature of the da/dN curve in the near-threshold regime, even a small, load history – induced increase in ΔK_{th} can obviously cause dramatic retardation.

Interaction of Fatigue and Sustained Load Crack Growth

Threshold stress intensity for fatigue crack growth is usually a fraction of the threshold for sustained load (stress corrosion) cracking. The duty cycle of aero-engine components includes substantial hold-times associated with sustained, high load action, typical of cruise conditions. In the event the stress intensity associated with such load exceeds the threshold for sustained load cracking, a crack which until this point may have grown in fatigue, will now extend under sustained load. From this point, crack growth will be more complex in nature, given the substantial difference between the two types of cracking. Fatigue cracking is driven by cyclic slip and is transgranular by nature. Sustained load cracking is driven by environmental attack resulting in debond of grain boundaries and is intergranular by nature.

The response of a crack subject to enforced change in extension mode is seen in Figs. 6a-c. This test was performed in air at 650ºC with periodic application of a 1000 s hold-time at maximum load. The macro in Fig. 6a shows the flat fatigue fracture surface and the uniform, straight front of the fatigue crack at the commencement of hold-time. Sustained load cracking is controlled by tensile hydrostatic stress. The lower end of the crack front in Fig. 6a is close to the specimen surface and in view of local plane stress conditions, is more resistant to sustained-load cracking. Initial crack extension under sustained load is retarded as the crack front is transgranular, with grain boundaries largely protected from environmental action. However, once access is gained to them, emerging debonded grain boundaries act as conduits for additional environmental passage. The result is multi-plane crack extension and tunneling, creating a highly disoriented crack front (Fig. 6b). Fig. 6c is indicative of subsequent progress of the crack front in fatigue. A comparison of marker band spacing before and after the sustained load indicates substantial retardation in fatigue crack growth rate after the sustained load. The retardation may be attributed to macro- and micro- incompatibility in crack front orientation with preferred conditions associated with constant amplitude fatigue.

Sustained-load elevated-temperature cracking in IN-100 is environment-induced and, as shown in Fig. 6, progresses along grain boundaries. Similar sustained load applied at elevated temperature in vacuum does not cause noticeable crack growth. In most locations on the fracture, we could barely observe any response to the hold-time. However, at a few locations like the one shown in Fig. 7, one observes local slip, leading to local, self-arresting, Mode II transgranular advance of the crack front. This creates the effect of local crack branching. However, subsequent fatigue loading is not conducive to the advancement of the branched crack. Under such conditions, the branched Mode II crack may, in fact, somewhat relieve cyclic slip at the primary crack front, leading to momentary retardation.

SUMMARY

Schijve [3] lists several mechanisms that are known to cause acceleration and retardation effects in fatigue crack growth. Prediction models used in engineering practice are built either around residual stress (such as the Wheeler [4] and Willenborg [5] models) or around the crack closure mechanism (Elber [6]). Models based on residual stress are empirical by nature and involve calculating a certain retardation coefficient, tuned to describe load history – sensitive reduction in instantaneous crack growth rate, while closure-based models attempt to simulate closure stress variation under complex loading.

The significance of the present study lies in identifying *moderation of environmental action by crack-tip stress state* as an important operative mechanism of overload-induced retardation. As a consequence of this effect, ΔK_{th} appears to increase, leading to a rightward shift in the near-threshold da/daN curve. The effect was isolated by designing test conditions that precluded the influence of fatigue crack closure. The environment - connection was confirmed through repeat experiments in vacuum which failed to produce any retardation due to history – sensitive crack tip stress state.

This study also reveals interaction effects between transgranular and intergranular cracking. Retardation due to instantaneous deviation from the path of least resistance should not come as a surprise.

Further work is proposed to establish a reproducible experimental procedure that would enable correlation of ΔK_{th} with variable amplitude loading conditions. Establishment of such a correlation would contribute to improved crack growth predictions under spectrum loading, including elevated temperature usage conditions.

ACKNOWLEDGEMENTS

REFERENCE LIST

(1) Sunder, R., W.J. Porter, and N.E. Ashbaugh, The Role of Air in Fatigue Load Interaction, submitted to *Int. J. Fat. Fract. Engg. Mat. & Struct*, 2001.

(2) Sunder, R., and R.V. Prakash, Crack Closure Measurement Through Fractographic Markers, Submitted to *Int. J. Fatigue,* 2002.

(3) Schijve, J., Observations on the Prediction of Fatigue Crack Growth Propagation Under Variable Amplitude Loading, Fatigue Crack Growth Under Spectrum Loads, ASTM STP 595, American Society for Testing and Materials, 1976, pp. 3-2

(4) Wheeler, O.E., Journal of Basic Engineering, *Trans. ASME*, March 1972, pp. 181-186.

(5) Willenborg, J.D., Engle, R.M., and Wood, H.A., A Crack Growth Retardation Model Using an Effective Stress Concept, AFFDL-TM-FBR-71-1, Air Force Flight Dynamics Laboratory, 1971.

(6) Elber, W., The Significance of Fatigue Crack Closure, Damage Tolerance in Aircraft Structures, ASTM STP 486, American Society for Testing and Materials, Philadelphia, 1971, pp. 230-242
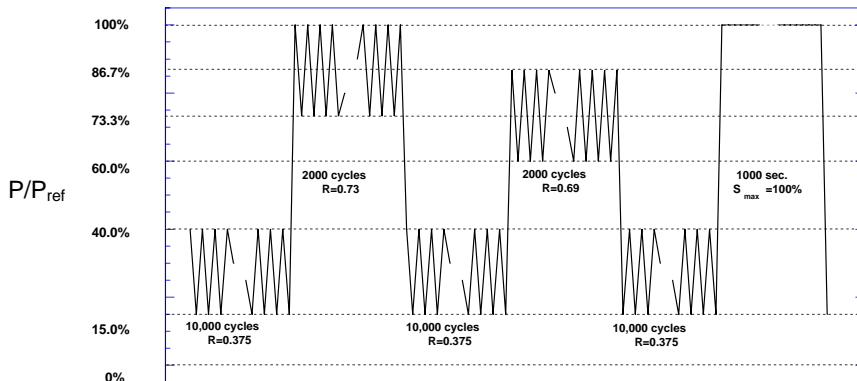
FIGURE 1 High R low amplitude (Hi-R-Lo-Amp) load sequences used to investigate environment-related load interaction effects. Hold-time introduced to investigate interaction between sustained and fatigue load cracking.
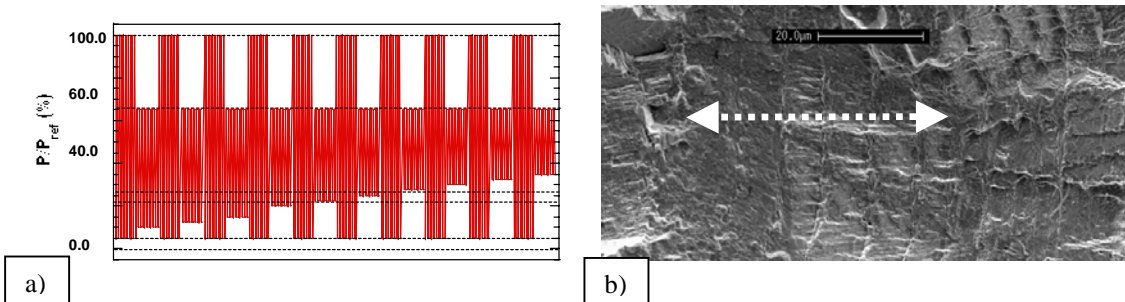
FIGURE 2 a) Load sequence used for fractographic determination of crack opening stress, S_{op}. b) Fractograph obtained under a). Double-ended arrow spans first six bands which appear equally spaced. Remaining four bands show receding spacing. This indicates that ΔK_{eff} in the first six steps of a) was constant. It would follow that $S_{op} >= S_{min}$ in these steps, suggesting $S_{op} = 30\%$ of S_{max}. To preclude crack closure, Hi-R steps in subsequent tests were designed to ensure that S_{min} was well in excess of this value. Test performed on C(T) specimen, IN-100 tested at 482ºC.
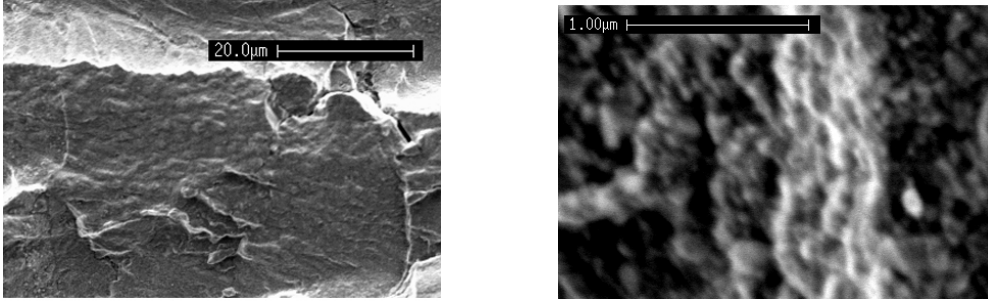
FIGURE 3   Marker band from the 10,000 Lo-R-Lo-Amp cycles is fine and clearly discernible. The bottom picture shows zoomed-in view of the marker at left of top picture. Marker at right of top picture is more pronounced because it includes crack extension from hold time.

FIGURE 4 Relative contribution of the two Hi-R steps with increasing crack size (growth rate). Fractographs a-d) span a total crack growth interval of 2 mm. White arrow spans crack extension from the higher R. IN-100 at 650°C in air.
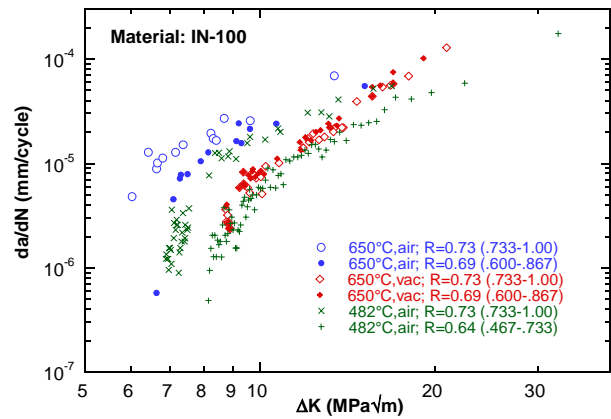
FIGURE 5 Crack growth rates derived from marker bands on fracture surface. 10 mm thick C(T) specimens. Material: IN-100 nickel-base superalloy.
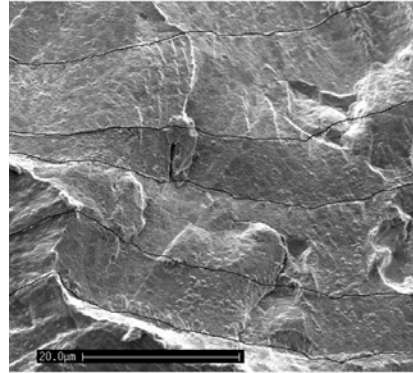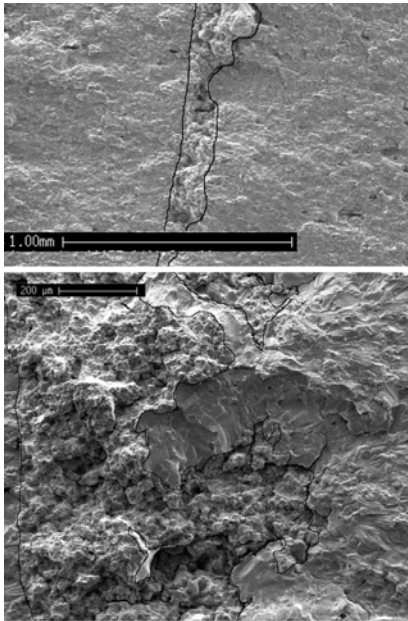
FIGURE 6 Fatigue – hold-time interaction. a) Crack extension during 1000s hold-time. Note how crack extension tapers down towar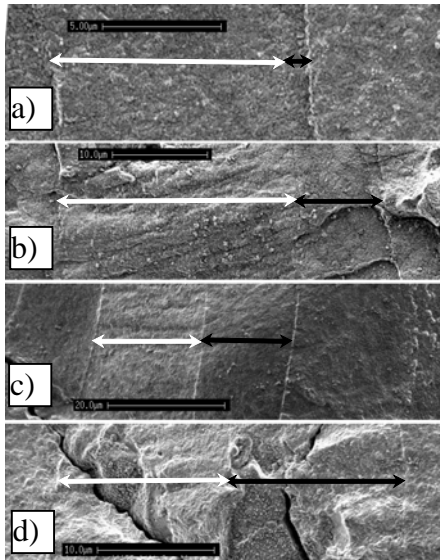ds specimen surface. Also note uniform fatigue crack front that becomes highly non-uniform during hold-time. b) Zoomed-in view of a) showing convoluted sustained load crack front 'straightened out' by fatigue cracking of ligaments. c) Zoomed-in view of b) showing retarded fatigue after hold-time due to disoriented front
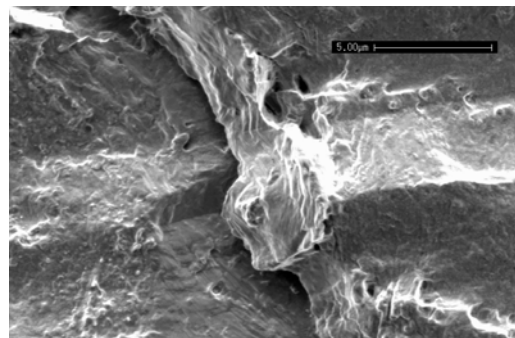
FIGURE 7 Localized crack branching by slip during hold-time in vacuum at elevated temperature. The faces of the branched crack 'slid' in Mode II as indicated by the matching shape of the displaced faces.

Fatigue by Diffusion-Induced Brittle Micro-Fracture[+]

R. Sunder

BiSS Research, 41A, 1A Cross, AECS 2nd Stage, RMV Extn.
Bangalore 560 094, India.   *e-mail: rsunder@vsnl.com*

Where there is potential for gas-metal diffusion, fatigue crack formation and extension can proceed by brittle micro-fracture (BMF). As slip is internal to the material and insensitive to hydrostatic stress, it may not be affected by either environment or mean (residual) stress. During the rising half of a fatigue load cycle, increasing notch root and crack-tip hydrostatic stress further enhanced by local constraint, can cause almost *instantaneous* crack front cyclic diffusion embrittlement (CFCDE). As a consequence, BMF component of fatigue crack extension by tensile de-cohesion or shear failure will be promoted in addition to Mode II by irreversible cyclic slip. The BMF component will be sensitive to crack-tip stress state as well as stress history in variable-amplitude fatigue and therefore, will diminish or vanish altogether in vacuum. The CFCDE-BMF model explains accelerated transgranular fatigue by environmental action. It also appears to explain a variety of other phenomena including the residual stress effect in metal fatigue.

INTRODUCTION

Modeling crack extension as a consequence of crack-tip contour collapse to accommodate slip irreversibility[1] essentially restricts it to a Mode II process. Bowles confirmed this possibility at intermediate growth rates through observations of crack-tip slip and consequent branching from the plane normal to loading in tests on aluminium alloys in vacuum[2]. Schijve et al[3,4] observed however, that aggressive environment promotes a flat fatigue fracture surface, indicative of crack extension by tensile de-cohesion, which, by definition, is a Mode I process. They associated accelerated crack growth with reduced critical tensile stress as a consequence of environmental action that promotes failure by rupture, rather than by slip. Environment-induced embrittlement can lead to reduced plastic deformation ahead of the crack tip. This will however not affect crack closure because the wake material is also similarly affected[4]. Similar embrittling action has also been associated with hydrogen transport into the bulk material by mobile dislocations[5,6] as discussed by Shulte et al[7] in the framework of a time-dependent (rather than fatigue) process. Based on fractographic evidence, Schijve and Arkema[4], and Vogelesang and Schijve[4] argue that environment-accelerated fatigue crack growth rate may be attributed to reduced resistance to Mode I crack extension, rather than to any reduction in fatigue crack closure.

The significance of environment to the fatigue process is underscored by the order-of-magnitude acceleration in fatigue crack growth rates in air by comparison to vacuum[7],

---

not to mention even higher growth rates in more aggressive environments. While remaining essentially transgranular, fatigue crack growth rate is known to be extremely sensitive to the particular environment in effect[8,9]. Crack-tip contour collapse[1] to accommodate slip irreversibility does not readily tie up with such evidence. This study attempts to interpret metal fatigue as the synergy of at least two operative mechanisms, viz. slip and diffusion at the crack tip. The next section describes a possible model involving the combined action of diffusion and slip to explain well-established fatigue crack growth behavior. It is consistent with well-established empirical understanding as well as with emerging evidence on crack growth behavior as documented in a separate paper[10]. These include the effect of environment and load history on near-threshold fatigue crack growth in an Al-alloy and a Ni-base super-alloy at elevated temperature.

Significance of diffusion theory

Time-dependent effects of environment on material behavior have been characterized using diffusion theory. These include the phenomenon of dynamic strain aging[11], dynamic embrittlement[12], hydrogen-embrittlement[13] and nitrogen embrittlement[14]. According to diffusion theory, the mere presence of a gaseous environment around a solid promotes diffusion of the former into the latter. Diffusion is a necessary precursor to chemical reaction. By introducing slip barriers and reducing inter-atomic cohesion, diffusion by itself is an agent of embrittlement and strain hardening, *even in the absence of chemical reaction*.

Diffusivity index is a measure of how prone a particular gas – metal combination is to diffusion[15]. The index increases in inverse proportion to the ratio of their atomic radii. Estimates of the index are complicated by the presence of alloying elements and also by the polycrystalline nature of engineered materials. Intergranular diffusivity is much greater than transgranular diffusivity and is in fact referred to as 'short-circuit' diffusion[15]. Chemical bonding restricts diffusivity. Aluminum-oxide for example is an excellent naturally-forming protective barrier against diffusion in aluminum alloys exposed to atmospheric action. Nascent aluminum reacts 'instantaneously' with atmospheric oxygen to form such a layer. Oxide barriers may be a significant impediment to diffusion. Even so, their formation too is *preceded* by, and therefore subject to, the laws governing the diffusion process.

Analytical extension of diffusion theory to cyclic loading conditions is complicated by a variety of factors including lack of material constants suitable for polycrystalline materials and the absence of closed-form solutions for crack-tip cyclic-inelastic stress distribution and its variation during cyclic loading / unloading including the effect of interaction between hydrostatic and shear stresses. For a given material, rate of gas diffusion is accelerated by increasing temperature and local hydrostatic tensile stress and reduces with depth of penetration. Therefore the process will be affected by crack-tip response to cyclic loading as affected by prevailing monotonic and cyclic plastic zones and crack closure.

Most previous work on the subject considers the diffusion process as being time-dependent, intergranular and encompassing material depth of the order of at least a few grains[11-14]. Transgranular diffusion has also been studied, but under conditions that differ considerably from those associated with fatigue[16,17].

Fatigue crack growth rate when plotted against partial pressure (for a given ΔK and frequency) shows a quantum, near-order-of-magnitude increase around a particular
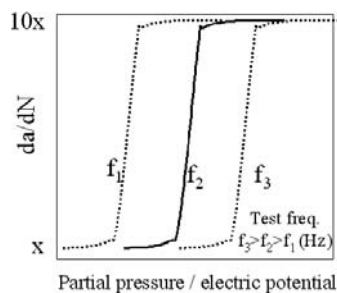
Fig. 1 The effect of partial pressure on fatigue crack growth rate at given ΔK showing trend reported in [18]. Dotted lines have been transposed to reflect the effect of frequency. Similar trend in growth rates has been reported as a function of potential of electric potential of corrosive medium [8]. Growth rate is shown in log scale.

value[18]. A qualitatively similar graph was obtained for the effect of electric potential on corrosion fatigue crack growth rate for an Al-alloy[8]. These are schematically described in Fig. 1, which indicates the existence of a certain transitional point on the horizontal axis representing a rapid transition in growth rate. On either side of this point, growth rate change appears marginal. This may be an indication that for the materials in question, environmental action proceeds extremely rapidly and is self-limiting at the same time.

There are several reasons why crack-tip cyclic diffusion embrittlement may be largely self-limiting by nature. Given constant and uniform hydrostatic stress and temperature, rate of diffusion will diminish as an inverse function of depth. Crack-tip hydrostatic stress diminishes as an inverse square root function of depth. Chemical reaction such as oxidation can form an almost impregnable diffusion barrier. The transient zone between the two plateaus in Fig. 1 may be associated with saturating environment action (diffusion-oxidation) over load rise time. Much higher frequencies may be associated with load rise times shorter than that required for diffusion process saturation. This may explain why fatigue is largely frequency-insensitive – even when accelerated by environmental action. Crack extension in each cycle exposes fresh material to diffusion in the next rising load half-cycle. Thus, the process is *cyclic*, rather than time-dependent.

Slip being internal to the material and a measure of inelastic shear response, is insensitive to environment *and* hydrostatic stress. In contrast, diffusion is sensitive to *both* these factors. Other inputs being the same, activation energy of diffusion increases with both partial pressure of active environment component as well as with tensile hydrostatic stress. By implication, both mean stress and stress-history effects will manifest through environment-related mechanisms such as diffusion. This may explain sensitivity of crack formation and short-crack behavior to stress level and stress history. These cannot be traced to crack closure, which by definition requires a wake.

If the diffusion process can substantially accelerate transgranular crack growth, the question arises as to why it does not do so quite independent of fatigue (except in materials prone to stress-corrosion cracking). This is explained by the schematics in Fig. 2a-c. Given similar local stress levels, grain boundaries offer the preferred path of
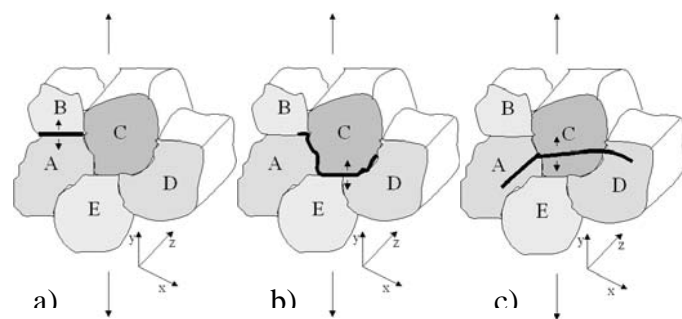
Fig. 2 Possible crack front profiles in intergranular cracking. a) Intergranular crack growing between grains A and B up to tri-grain boundary with grain C. Conditions are not favorable for crack extension beyond this point. b) Inter-granular crack front tracing boundary between grain C and B,A,E,D. Crack front between A and C is not favorably oriented. c) Transgranular crack front.

diffusion. An intergranular crack will thus see minimal resistance, particularly given enhanced diffusivity under tensile stress along a grain boundary exposed to environment (as shown in Fig. 2a for a crack growing between grains A and B in the x-axis from left to right). The grain boundary however represents a slip barrier by way of a crystallographic discontinuity. It is therefore not a preferred path for crack extension by fatigue. If a crack does grow along this path, it will be arrested at

the next tri-grain boundary as shown in Fig. 2a as such a point represents a slip barrier. It also represents a diffusion barrier: the boundary with grain C is aligned with the loading axis. Diffusion beyond this point is inhibited by the absence of tensile stresses normal to the new grain boundary.

Grain dimensions are at least an order of magnitude greater than the dimensions associated with near-threshold crack tips and crack extension. A crack front running along multiple grain boundaries will be shielded by (grain sized) shear walls associated with vertical shifts in crack plane (as shown by Fig. 2b of a crack growing in the z-axis). The boundary between grains A and C represents such a shift in plane. Given local strain-controlled conditions, stresses on any given crack plane will tend to be relieved by un-cracked ligament in adjoining grains. This will lead to a non-uniform crack front evolved by discontinuous crack driving force. There will be even greater stress relief in the event of multi-plane intergranular cracking. Finally, the very extension of the crack front serves as a fatigue retardation factor given the need to dissipate cyclic slip across a much wider area. Under these conditions intergranular fatigue may be self-limiting, rather than self-perpetuating.

On the other hand, cyclic slip occurring along transgranular crystallographic planes contributes to a *single, contiguous and un-convoluted* crack front. Even if there may be minor crack plane deviations between grains (as in Fig. 2c), a transgranular crack front represents the shortest path between its end points along which slip planes remain focused. This does not preclude minor discrete planar shifts at grain boundaries, but these shifts are insignificant by comparison to grain size and may not contribute significantly to local stress relief from vertical shifts in crack plane.

A transgranular crack by comparison to an intergranular crack represents greater potential for slip. At the same time, by virtue of a cohesive and sharp crack front growing under conditions of local constraint, near-tip elements will also develop greater magnitude of tensile hydrostatic stress conducive to increased diffusivity. Such diffusivity may be much smaller than the levels associated with a grain boundary. However, given the possibility that it occurs uniformly across the entire crack front, it becomes significant as long as it is at least of the same order as crack growth rate, which under near-threshold conditions approaches inter-atomic distance. While the significance of the diffusion process is obvious, it is also clear that its *translation to crack extension requires cyclic slip*. For the same reason, K_{th} for sustained load cracking is usually much greater than ΔK_{th} for fatigue crack growth – for a given material and environment combination.

The foregoing discussion underscores the significance of a contiguous, un-convoluted crack front associated with transgranular fatigue cracking. Finally we note the importance of near-tip tensile hydrostatic stresses associated with rising applied stress, superposed over prevailing mean stress (or residual stress). Several models have been proposed to explain the interaction of slip and environment in accelerating fatigue crack initiation[19, 20]. These involve specific chemical reactions.

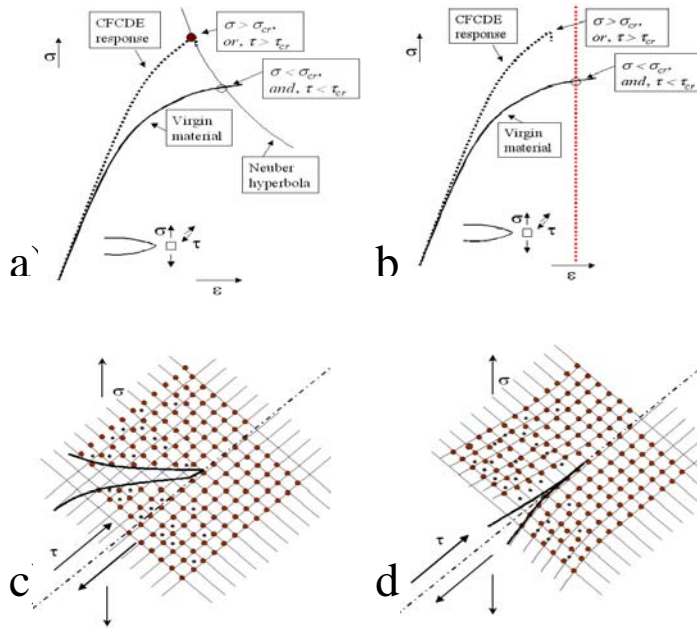## CRACK FRONT CYCLIC DIFFUSION EMBRITTLEMENT (CFCDE)

Fig. 3 Transgranular crack response to cyclic loading under the combined action of slip and diffusion. a) Response of notch to applied load. Local stress/strain will be defined by Neuber hyperbola. Diffusion (CFCDE) embrittled material may exhibit dynamic strain hardening as a result of which, local stress may rise towards rupture stress in tension or shear, while the virgin material is likely to have merely yielded to the required extent. b) Same as (a) with the exception that in the case of a crack-tip as opposed to a notch, local response is totally strain-driven, leading to possible failure in shear through lack of ductility. c) Mode I crack extension by cleavage in case of exceedance of local critical tensile stress. d) Mode II crack extension by exceedance of local critical shear strain (loss of ductility). Crack then opens in Mode I under applied axial load, representing a mixed-mode case. Both c) and d) are cases of "brittle micro-fracture" (BMF).

Fig. 3 schematically describes diffusion-embrittled crack-tip response to applied load. Fig. 3a shows the possibility of a blunt crack (of finite stress concentration) that will essentially exhibit a 'Neuber' type of stress-strain response to applied load. Fig. 3b is applicable to a 'LEFM-type' sharp crack tip that will essentially see local strain control. Real crack behavior may be bounded by these two extremes. In both cases, diffusion embrittled crack-tip material behavior will deviate from ductile matrix behavior. Inability of diffusion-embrittled crack-tip material to accommodate cumulative slip during the rising load half-cycle can manifest itself in different ways:

1. Strain-hardening of crack-tip area. This increases local stress component and can lead to rupture by exceedance of critical rupture stress. The same result can follow from environment-induced decrease in critical rupture stress – even if the material did not harden. Fig. 3c illustrates the consequent crack extension by tensile de-cohesion.

2. *Decreased ductility.* The crack tip suffers premature shear failure as material is unable to accommodate strain accumulating along major slip plane(s) (Fig. 3d). Note that even though the failure occurs along a shear plane (Mode II), prevailing tensile stresses will now proceed to open the crack in Mode I.

The diffusion process in cyclic crack extension is associated with a freshly exposed surface subject to extremely high tensile hydrostatic stress in each rising load half-cycle. This makes the process substantially different from the well-understood phenomenon of time-dependent diffusion. We refer to this process as "*Crack Front Cyclic Diffusion Embrittlement" (CFCDE)*. In this definition, the term "Crack Front" refers to the process being restricted to the material immediately ahead of the crack front and the term "Cyclic" to underline the cycle-by-cycle nature of the process. The extension of the crack in Fig. 3c,d on a cycle-by-cycle basis may be deemed as "*Brittle Micro-Fracture" (BMF)*. Thus, while the classical model of fatigue crack extension essentially assumes that crack-tip material *only deforms and does not fail*, the CFCDE-BMF model assumes

that that the environment-sensitivity of cycle-by-cycle crack extension in fatigue may be attributed to *micro-fracture by cleavage or shear failure.*
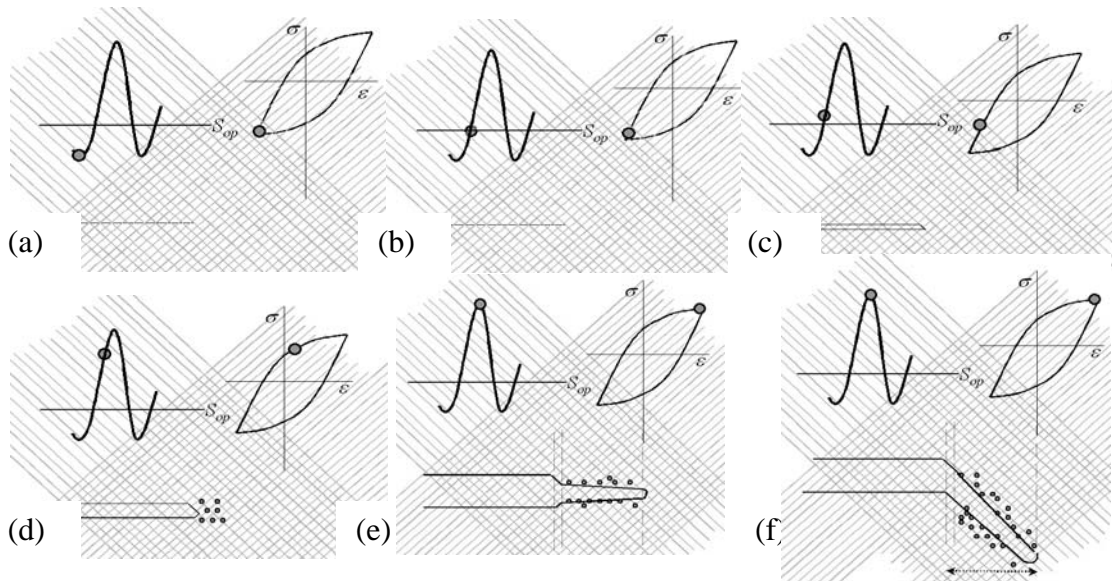

Fig. 4 Crack-tip response to cyclic loading under combined slip and diffusion. Point in applied load cycle is shown by small circle. Local stress-strain response of near-tip element appears alongside. a) & b) Negligible crack tip response as applied stress is below S_{op}. c) Crack is fully open, but near-tip element is in compression. d) Crack tip blunting/extension by slip, together with onset of diffusion associated with increasing near-tip tensile hydrostatic stress. e) Diffusion-embrittled material suffers BMF by cleavage. f) Variation on (e) with BMF by shear. Note that in both cases, there will be some blunting from yield of un-diffused interior. Re-sharpening during unloading will form a striation line in accordance with Laird model. Environment-sensitive BMF component determines striation spacing, while crack-tip blunting/re-sharpening determines striation morphology.

Fig. 4 schematically describes the CFCDE-BMF model applied to a transgranular fatigue crack in environment. Each schematic shows the crack tip itself, the corresponding point in the load cycle both in applied terms as well as in terms of location on a hypothetical stress-strain hysteresis loop at a notional point in front of the crack tip. Consideration of near-tip stress-strain behavior is central to interpreting mean-stress / stress history effects. While matrix stress-strain response is assumed in the schematic, it may be noted that crack-tip response will be affected by CFCDE.

Laser interferometry measurements of the separation of a micro-indent pair less than 50 microns apart and about 50 microns ahead of a fatigue crack tip in an Al-alloy provide compelling evidence of crack closure[21]. This was evident from the relative insensitivity of their separation to load variation below a certain tensile level. Fractographic experiments have also provided consistent and reproducible evidence that cannot be attributed to phenomena other than closure[22]. Accordingly, Figs. 4a,b show negligible change in local stress-strain when the applied stress changes from S_{min} to S_{op}.

Crack-tip diffusion / oxidation can occur over the rising half of the load cycle, effectively commencing from the point of crack opening (Fig. 4b). The process is initially retarded or arrested by near-yield compressive stresses in the cyclic plastic zone, which effectively shuts out diffusion (Fig. 4c). From crack opening load to maximum applied load, crack-tip stresses will increase from near compressive yield to near tensile rupture stress and lead to rapid increase in CFCDE (Fig. 4d). Under given environment and partial pressure, the process will be retarded by local yield and enhanced by local constraint. This makes CFCDE sensitive to instantaneous local material properties, crack front shape and material thickness. For example, the presence of a yield ligament or highly discontinuous crack front is likely to lead to reduced CFCDE by virtue of local stress relaxation.

Figs 4e and 4f describe alternate scenarios of cleavage (BMF) as described by Fig. 3. Cleavage occurs as a consequence of either the inability of diffusion-affected material to accommodate cumulative dislocation movement along crack-tip slip planes, or as a consequence of local hydrostatic stress exceeding local critical rupture stress. In macro terms, the embrittled crack tip cleaves because it is unable to slip to the extent *enforced* by diffusion-free material in the interior. Cleavage can occur either along the plane of maximum tensile stress or along the slip plane. Such freedom of +/-45° change in BMF plane may cause vertical meandering of the crack front even within a grain. Ranganathan et al identified "pseudo-cleavage facets with typical fishbone structure" oriented with slight deviation from crystallographic plane of near-threshold fracture surface on Al-alloy tested in air[23].

To be of sufficient significance to metal fatigue, CFCDE depth only needs to be of the order of current crack growth rate. In absolute terms, this would range from threshold level of about 10^{-7} mm (or less) to about 10^{-3} mm (or more, close to fracture). This corresponds to levels ranging from inter-atomic distance up to about a micron. Over this depth, material properties can differ significantly from bulk properties. Environment-sensitive BMF component must be substantial in order to explain the difference between crack growth rate in air and vacuum, which for many materials is of an order of magnitude in the near threshold region. Thus, near-threshold fatigue crack growth rates in air may be largely BMF.

Under near-threshold conditions, BMF may not occur all across the front over each load cycle. When the crack does not locally extend in a given cycle, it suffers greater exposure to diffusion, thereby increasing the probability of BMF in the next cycle. This renders the crack front highly uniform even under near-threshold conditions.

As a phenomenon, CFCDE carries unique attributes. Its currency is restricted to only about one half of the rising portion of the effective load cycle. Further, the occurrence of BMF *requires* the onset of crack-tip slip. CFCDE limitation by oxidation-induced barriers may explain why metal fatigue is largely frequency-insensitive and at the same time environment-sensitive. Perhaps, fatigue may be more frequency-sensitive in the event of diffusion without chemical reaction.

In the event CFCDE was driven *largely* by hydrostatic tensile stress, fatigue crack growth rate would also be driven largely by K_{max}, which is not the case. One may conclude that hydrostatic tensile stress moderates the extent to which CFCDE will accelerate da/dN for a given ΔK_{eff}. CFCDE may be termed as a moderator of potential BMF for a given extent of crack-tip slip (Mode II).
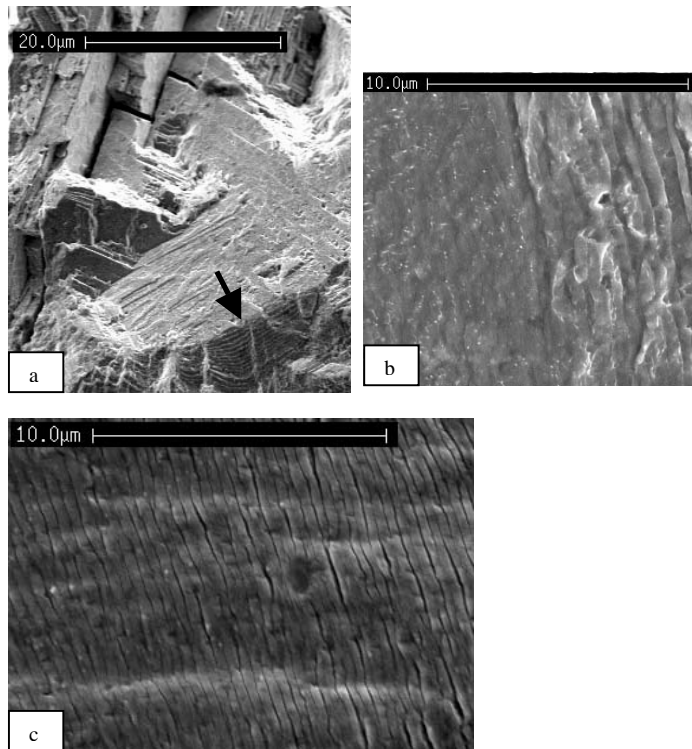
Striation Formation

Fig. 5 a) Fatigue fracture surface of nickel-base superalloy. Crack growth is from top to bottom. Arrow marks switch from room temperature to elevated temperature (482 C). Note the faceted surface showing growth along crystallographic planes in Mode II at room temperature. Fracture surface assumes flat plane at elevated temperature, with formation of clearly visible growth bands. b) Crack growth in vacuum in Al-Cu alloy under programmed loading. At right are barely visible striations from 10 marker cycles, though growth rate exceeds 1 micron per cycle. c) Typical fatigue fracture surface from Al-Cu alloy tested in air. Though growth rate is much less than in b), striations are clearly visible. The dark lines may indicate crack contour collapse into a deep valley appearing as a secondary crack. Crack extension by collapse may be negligible, but the effect on striation morphology is distinct.

CFCDE-enhanced BMF described by Fig. 4 provides a convincing explanation for fatigue striation formation. This is illustrated by the fractographs in Figs. 5-8 and associated schematics. These fractographs were obtained from experiments that are described elsewhere[24-26]. Fig. 5a shows a fractograph from a compact tension specimen cut from a nickel-base super-alloy and pre-cracked at room-temperature before continuing testing at elevated temperature. The picture shows the crack growing from top to bottom with the arrow indicating point of temperature transition. We observe a faceted crack growth at room temperature presumably along crystallographic planes with no sign of striations. It would appear that crack extension was by pure Mode II along planes of preferential slip. Upon increase of test temperature, fatigue is accelerated by CFCDE and is conducive to striation form as seen at the bottom.

Fig. 5b shows striations in an Al-Cu alloy tested at room temperature in vacuum that indicate a relatively high growth rate of about 10^{-3} mm/cycle. Even at this growth rate, the striations from 10 large applied cycles are poorly defined. Their 'tacky' appearance and uneven spacing, suggestive of predominant Mode II, with high ductility and possible re-fusion, leading to distortion of the striations even if they did form. Note also, that the striations appear 'shallow', as their boundaries do not appear to see much change in elevation. This contrasts with the picture in Fig. 5c of the same material fatigued in air. Clear striation marks are seen, with dark lines that may seem to be secondary cracks. These may in fact be the collapsed contour associated with Mode II as envisaged by the Laird model. It is clear however, that they cause negligible crack extension, as most of it may be attributed to CFCDE-induced BMF, resulting in growth rate approximately an order of magnitude greater than in vacuum. Thus, if this was vacuum, the density of the lines would have been x10 times greater and therefore not visible because of the vanishing gap between them.
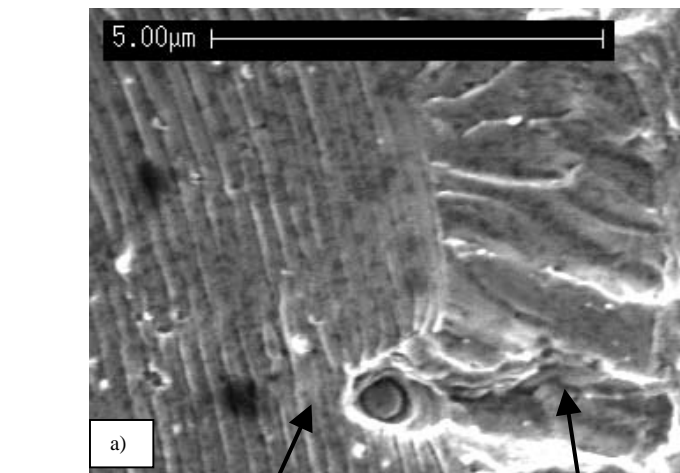
Fig. 6 a) Typical fractograph from Al-Cu alloy shown transition from high amplitude to low amplitude cycling without change in S_{max}. While slip component was adequate at higher growth rate to form the lines that separate striations at left, it was not so at near-threshold growth rates at the right (10^{-6} mm/cycle). As a consequence, the fatigue fracture surface is featureless from the perception of growth signature. (b) and (c) schematically describe the possible crack-tip cycle-by-cycle response.
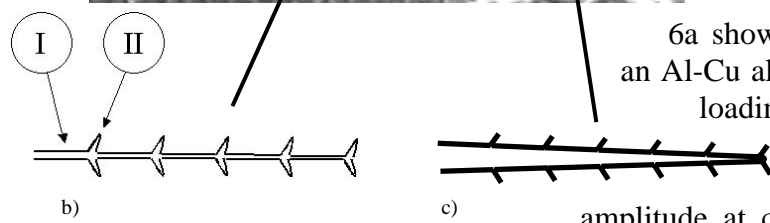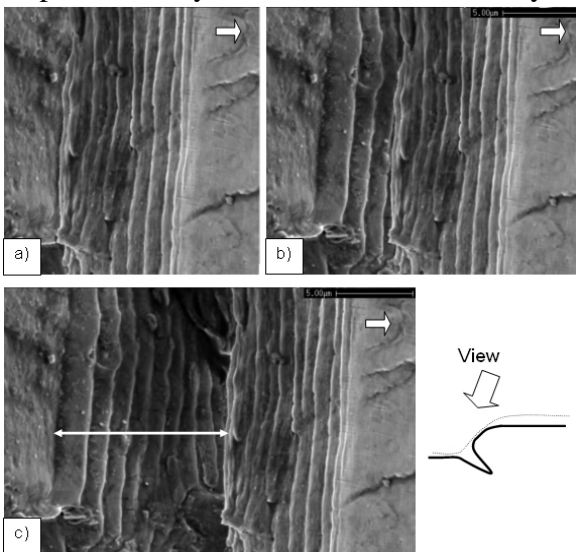
Fig. 6a shows a typical fractograph from an Al-Cu alloy tested under programmed loading. The transition from left to right is associated with a step-wise reduction in load amplitude at constant S_{max}. This causes a reduction in growth rate without change in plastic zone size (load interaction effects are minimized). While clear striations are seen in the Paris regime at the left (just under 10^{-3} mm/cycle), the fatigue fracture surface at reduced growth rate (10^{-6} mm/cycle) becomes striation-less, with local changes in fracture plane becoming the dominant morphological feature. Figs. 6b,c schematically describe the associated striation geometry. In both cases, crack front blunting/re-sharpening (contour collapse) may be involved. However, slip reversal by itself contributes little by way of crack extension. Slip plane orientation along the crack front associated with slip reversal from the blunting/re-sharpening process also keeps the fracture plane flat at least at the microscopic level. This capability is lost with reducing crack growth rate as the extent of crack front slip reversal apparently diminishes to vanishing proportions, allowing local fracture plane to meander into the formation of the undulations seen at right. One may conclude that cyclic slip promotes a uniform crack front, apart from contributing to the formation of
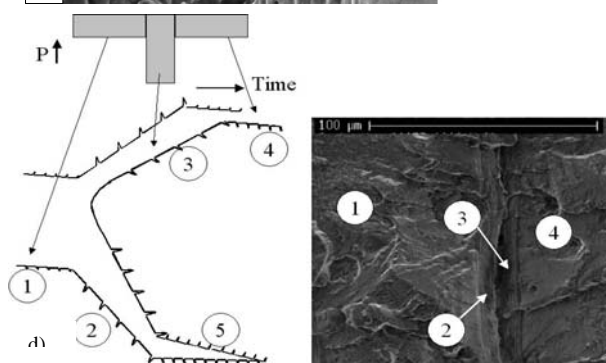
Fig. 7 a-c Photographic reconstruction of crack branching in an AL-Cu alloy caused by switch in load amplitude as shown schematically in (d). Even though only 10 large amplitude cycles were applied, an illusion is created of up to 20 striations. (a) and (b) were reconstructed from (c) by photographically 'closing' the branched crack. As shown by the white bar in (c), the opening left by the branched crack is about 0.01 mm. (d) schematically describes possible mixed-mode striation formation mechanism. The corresponding regions are marked on the zoomed-out view shown at right in (d). As indicated in Fig. 6, low growth rate regions appear featureless possibly in view of negligible reverse slip component.

distinct striation boundaries.

Step-wise change in load amplitude at constant S_{max} will not cause a change in crack plane if no substantial change in dominant mode occurs. A change in Mode I/II proportion can however cause such a switch at higher growth rates as illustrated by the fractographs in Fig. 7. This picture was obtained from programmed load testing on an Al-Cu alloy involving the periodic application of 10 large amplitude cycles, with 2000 low amplitude cycles in between, maintaining constant S_{max} in both steps. While the crack will grow in Mode I at the lower amplitude, the 10 large cycles will see increased Mode II component. As discussed elsewhere in this paper, this is caused by crack-tip cyclic plasticity increasing more rapidly with increasing growth rate than the CFCDE-BMF component. The increasing Mode II component leads to crack branching along duplex slip planes, and gradual rotation of the fracture plane from flat to slant plane[3,4]. In the process, one of the crack branches will arrest as illustrated in Fig. 7. Such branching may create the illusion of 20 striations from 10 cycles as reconstructed photographically by the sequence of Figs. 7c, 7b and 7a. Fig. 7d schematically illustrates the process. Regions 1 and 4 are featureless regions corresponding to lower load amplitude. Regions 2 and 3 are the two branched cracks shown schematically as five striations (for brevity instead of the 10 actually produced by the ten large cycles). The lower fracture surface retains the branched crack shown as the non-propagating region 5. The schematic also indicates the blunting associated with the switch in load amplitude. Note that the residual opening of the non-propagating branched crack is of the order of 0.01 mm as shown by the white bar in Fig. 7c.

It is not essential for crack-tip contour collapse to occur for striation bands to form. For the visual contrast to indicate a distinct band, it is adequate for crack plane to change at least once in each cycle. This can occur by a switch during crack extension from exceedance of critical tensile stress/strain to critical shear stress/strain as illustrated in Fig. 3. Compelling evidence in support of this comes from internal cracks that grow in vacuum under conditions of constraint associated with plane strain conditions. Fig. 8 shows examples of embedded interfacial fatigue cracks that grow and coalesce to separate secondary particulates from the matrix in Al-Cu alloys. The fractograph in Fig. 8a was obtained from 2024-T351, while the rest are from 2014-T6511. All these experiments involved repetitive application of a three step programmed load sequence, with each 2000-cycle step separated by 10 cycles of high amplitude markers[24]. The steps were at high stress ratio and the high-amplitude in the markers was achieved by reducing S_{min}, i.e., there was no overload effect from the markers. The high-amplitude cycles mark crack progress by local switch in crack plane. This is evident from the clearly defined concentric circles marking the progress of the embedded circumferential crack as shown by the arrow in Fig. 8a. Figs. 8b,c show several such cracks that seem to eventually separate the particulate from the matrix. Fig. 8d shows the embedded crack indicated by the arrow in Fig. 8b, rotated and zoomed in for clarity. This crack is growing on the side wall of the particulate and hence represents an angular view with better definition of the change in elevation between bands. The arrow marks the small initial circular embedded crack whose projection appears as an ellipse. Fatigue cracks as small as 100 nm have not been reported in the literature. Seen on the left are marks left behind by the 10 marker cycles applied after every 2000 cycles at lower amplitude. The change in elevation between the bands appears marginal (of the order of 0.01 micron), yet is extremely well defined. The band width is indicative of a growth rate of the order of 5×10^{-9} mm/cycle. Clearly, such dimensions cannot be associated with crack-tip blunting followed by contour collapse, which by definition, would have to occur along a conical plane for a circular embedded crack. This being unlikely, one may conclude that the bands were
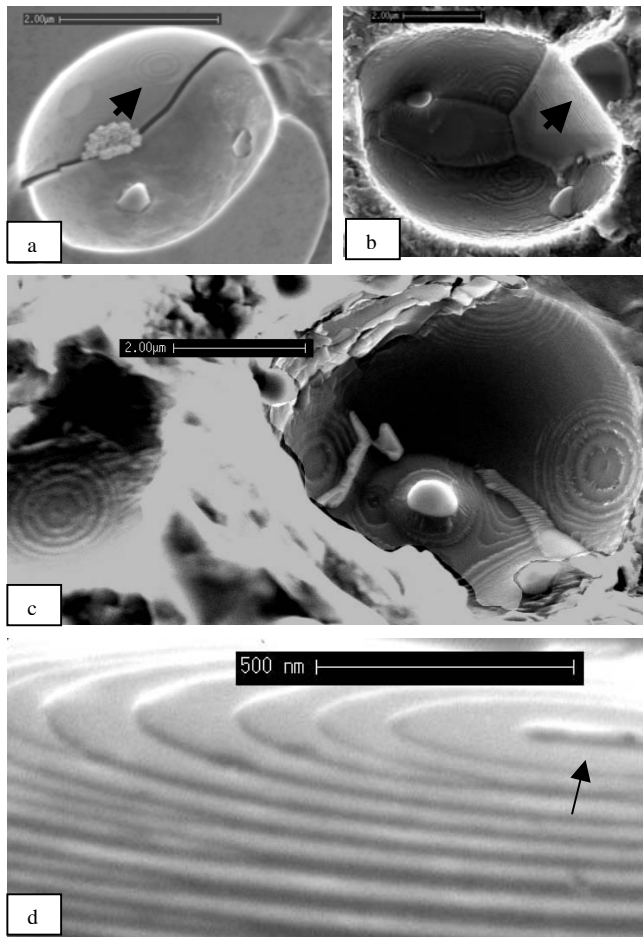
Fig. 8 Growth bands associated with fatigue separation of secondary particulates from the matrix in an Al-Alloy under programmed loading conditions[24]. These bands were noticed within the cavities observed on the fatigue fracture surface. As the process is internal to the material, it may be deemed to occur in vacuum. Each growth band is from 2000 cycles of low-amplitude and 10 high-amplitude marker cycles. a) 2024-T351 alloy. Arrow shows growth pattern on the side-wall of the void associated with penny shaped interference crack. Such cracks form all around the particulate to eventually coalesce and thereby separate it from the matrix. (b-d) are from experiments on 2014-T6511. (b, c) show multiple cracks. The one on the left in (c) appears perfectly circular in view of normal projection. (d) is zoomed in and rotated view of the crack on the side wall pointed by the arrow in (b). 'Initial' crack radius is of the order of 100 nm. Growth rate is of the order of 10^{-9} mm/cycle, estimated from cycle count of 2010 over each band. This suggests crack extension that may not have occurred in each cycle, but progressively evened out, leading to excellent definition of uniform growth bands.

indeed caused by momentary switch in crack extension mode leading to a terrace-type morphology.

Figs. 5-8 suggest possible ways in which fatigue growth bands form. The classic cycle-by-cycle fatigue striation lines form by slip reversal / contour collapse associated with crack-tip blunting/re-sharpening. It may be noted that the role of this mechanism in the presence of environment may largely be that of marking growth, rather than causing it. Growth bands can be observed at very low growth rates even if individual cycles may not cause them and even if average growth rate is less than inter-atomic distance. These growth bands are caused by momentary rotation in fracture plane due to change in critical stress component (tension versus shear). The remarkable uniformity of crack front even at such low growth rates may be attributed to the self-stabilizing nature of crack front geometry. As local crack extension is displacement driven, any local spurt will lead to instantaneous local unloading and associated crack arrest, until the front evens out. Growth marks including striations become discernible when there is sufficient crack extension between them to cause visual 'projection-induced contrast' between neighboring planes.

In air, dominance of CFCDE-induced separation keeps the crack plane normal to loading direction and thereby protects striations from obliteration by Mode II. One may conclude that in a mixed mode sequence, Mode I may be *followed* by Mode II. When sliding follows opening mode, there is less danger of striations obliterated by rubbing. This is supported by the possibility that CFCDE-induced de-cohesion at the crack tip is accompanied by continued slip in the CFCDE-free interior, leading to face opening by blunting.

DISCUSSION

Fatigue involves the interplay of multiple phenomena and associated mechanisms. The well-known Laird model provides a classical 'text book' explanation of how a fatigue

crack can extend by slip. However, such a model may only be valid for vacuum or other such conditions, ideally conducive to cyclic slip. Available evidence appears to indicate that atmospheric fatigue is associated with a substantial component of crack extension, associated with de-cohesion by shear or tension. Discovery of crack closure provided the tools to interpret and model stress ratio and stress history effects in fatigue. However, treating closure as the sole mechanism may have been incorrect and sometimes unconvincing as pointed out by several researchers[26,32].
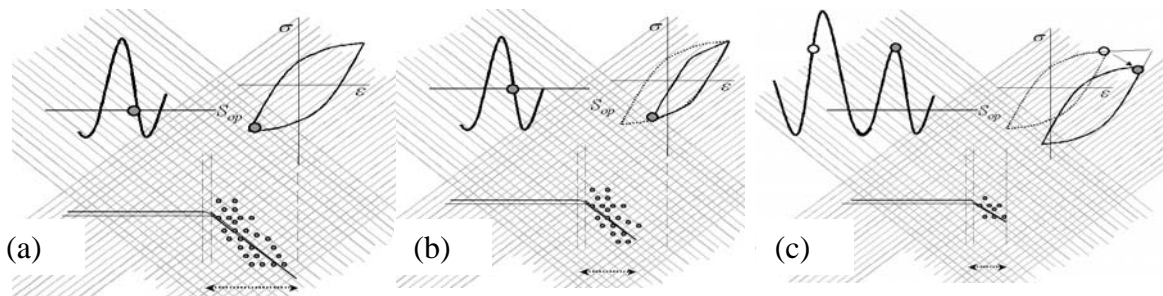
CFCDE-induced load history effect

Fig. 9 Schematic near-tip stress-strain response at lower (a) and increased (b) closure level. Even if closure has increased, the same level of hydrostatic stress is attained in (a) and (b). However, closure truncates hysteresis loop size indicating reduced slip and therefore retarded crack extension (even if CFCDE levels may be comparable). (c) As a consequence of overload induced compressive residual stress, the stress-strain hysteresis loop is pushed further into compression. As a consequence of reduced tensile hydrostatic stress, CFCDE is arrested. The overload plastic zone 'squeezes' CFCDE down and the crack tip responds as if it was in a more inert environment. Both (b) and (c) indicate retarded fatigue, but for different reasons. (b) is from closure, (c) from diminished environmental action.

Most interpretations of stress history effects center around the crack closure phenomenon[27]. Fig. 9 contains schematics that form a framework to re-interpret these phenomena using the CFCDE model. Fig. 9a is a carry over for reference from Fig. 4f. Fig. 9b describes the effect of increased S_{op}. As a consequence of reduced ΔK_{eff}, the extent of crack-tip slip is also reduced as reflected by the reduced hysteresis loop width. This in turn will reduce crack growth rate even if CFCDE levels do not come down significantly. Fig. 9c shows the consequence of reduced near-tip mean stress induced in this case by a prior overload. Note that because S_{op} remains unchanged, so does the width of the stress-strain hysteresis loop. However, the loop is now pushed 'downward' by residual compressive stresses from the overload plastic zone. The reduced mean stress will induce reduction (by superposition) in local hydrostatic tensile stress. Thus, even though the slip (Mode II) component (indicated by hysteresis loop width) remains unchanged, the CFCDE component will see a marked reduction, resulting in reduced crack extension by BMF. This may be a tangible explanation for the well-known effect of residual stress in metal fatigue.

As shown by Fig. 9, two processes operate synergistically when an overload is applied. As widely observed in the literature, crack closure level will steadily increase with growth into the overload plastic zone. It may be initially reduced by blunting, but will rise to a peak after some growth, causing the well-known phenomenon of delayed retardation. On the other hand, compressive residual stresses caused by the overload will immediately come into play after the overload. These will attenuate the CFCDE component, leading to retarded crack growth. Depending on the loading conditions, the magnitude and proportion of the two components may vary. Though their detailed

consideration is beyond the scope of this paper, it would follow that all significant operative mechanisms must be considered while interpreting load interaction effects.

CFCDE and plastic zone kinetics

CFCDE is closely related to plastic zone kinetics, because these control near-tip stress re-distribution under cyclic loading. Plastic zone size increases as a power of two function of stress intensity. Crack growth rate increases as a power function of ΔK, with the exponent always in excess of two (between 3 and 6 for most structural materials). By implication, cyclic crack extension expressed as a fraction of plastic zone size will increase with ΔK driven by an exponent given by m - 2 (where m is the exponent in the growth rate equation).
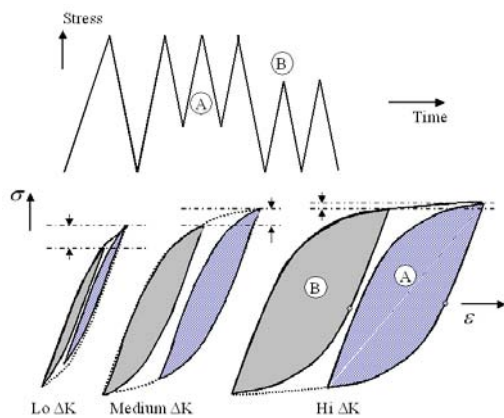

Fig. 10 Schematic of near-tip stress-strain response of embedded cycles based on notch root simulations[28]. A and B are cycles of equal amplitude embedded within a larger cycle. A is tied to maximum and B to the minimum in the load sequence. While one may expect the ratio of damage due to A and B will remain constant, the schematic clearly indicates this will not be the case in view of the nature of the stress-strain hysteresis loop. As shown by the relative shift in stress-strain loops from A and B, fatigue crack growth under cycles B will see maximum retardation at low ΔK. With increasing ΔK, the shift in loops reduces to vanishing proportions, suggesting negligible retardation at high ΔK. As these schematics related to CFCDE effect attenuated by shift in mean stress, one may expect that CFCDE-related load interaction will diminish with increasing ΔK.

The stress-strain hysteresis loops in Figs. 4 and 9 refer to a notional point ahead of the fatigue crack tip. If we now proceed to fix this point by distance from crack-tip given as a fraction of plastic zone, it would follow that the magnitude of cyclic stresses seen by the point in each load cycle will steadily increase with crack growth rate, driven by the reduction in distance from crack tip, due to its increasing rate of advance with increasing ΔK. This can be schematically visualized by a widening stress-strain hysteresis loop and associated increase in local inelasticity as shown in Fig. 10 for three distinct stages of fatigue: near-threshold (including crack formation and short crack), intermediate and high crack growth rates.

Fig. 10 describes element stress-strain response to the same applied load sequence, but at increasing ΔK. The load sequence shown at left consists of an overload cycle followed by identical baseline cycles that are applied at two different stress ratios, arranged such that S_{max} at Hi-R is equal to overload S_{max} and S_{op} at Lo-R (or, S_{min}, assuming a fully open crack) is equal to overload S_{min}. These cause near-tip stress-strain hysteresis loops embedded within the overload loop and represent the *maximum possible* history-sensitive shift in loop position. Loop position determines mean stress, which in turn will affect CFCDE. The dotted horizontal lines in the Figs. 10 show the extent of this shift. It is evident that the shift in mean stress diminishes with increasing ΔK, serving as an indication that the associated CFCDE-related history effect will also diminish.

It has been shown by notch root response simulation[28] that load sequence – sensitive shift in embedded loops for a given cyclic-stress strain curve will be controlled by the extent of cyclic inelasticity in major cycle and the ratio of major to minor cycle magnitude. It would follow that the CFCDE process will be extremely sensitive to load history under near-threshold conditions and may in fact explain why ΔK_{th} is so sensitive

to K-gradient in a decreasing-K test. Further, *load history-sensitive* CFCDE may be expected to diminish with increasing ΔK and also with decreasing overload ratio.

A third parameter to which CFCDE will be sensitive is introduced by the kinetics of fatigue crack growth. Crack advance during the rising load cycle will 'drag' near-tip elements into increased inelasticity (and hydrostatic stress associated with saturation in CFCDE or elimination of any benefit from compressive residual stress). Once again, CFCDE – related load history effects will be accentuated at near-threshold conditions and may be expected to diminish with increasing growth rate.

A few other aspects of fatigue are discussed below from a CFCDE-BMF standpoint.

Significance of plastic zone. The monotonic plastic zone acts as a crack-tip shield in two ways: it limits maximum crack-tip stress and induces a compressive residual stress component if subsequent cycling is under lower S_{max}. The cyclic plastic zone represents the volume of material that will see cyclic inelastic tension-compression. The mean stress component within this zone will be controlled by two parameters: current stress ratio and ratio of current monotonic plastic zone size to largest preceding plastic zone boundary on the crack plane (history effect). Overloads will reduce mean stress levels in the cyclic plastic zone and thereby reduce diffusivity levels causing retarded crack growth. One may note that elastic, ideally plastic modeling used by some analytical models would indicate crack-tip stress ratio R = -1, irrespective of applied stress ratio. By implication, fatigue would be insensitive to mean stress and residual stress effects, which is not the case.

Environment and crack-tip radius. Crack tip blunting occurs by slip. CFCDE essentially promotes BMF over slip. In experiments on Al-alloys and steels, Gach and Pippan[28] observed that at a given ΔK, crack-tip radius is sharp in corrosive environment, less so in air and blunt in vacuum. This is compelling evidence in support of the CFCDE-BMP model.

Significance of unloading half-cycle. The unloading half-cycle in case of Mode II is significant by way of crack extension due to collapse of crack-tip contour[1]. In case of crack extension in the loading cycle by de-cohesion, unloading becomes significant for other reasons. Under stable conditions, the entropy of diffusion renders it irreversible. However, the rapid decrease in hydrostatic stress (during unloading) tending towards compressive yield may in fact 'squeeze out' diffused gaseous atoms back into the atmosphere, provided they have not reacted already to form irreversible chemical bonds. Even if the extent of this process may be negligible, unloading creates conditions for the *onset of slip* in the *next* loading half-cycle by way of a re-sharpened crack tip. This in turn will ensure that fatigue crack extension remains transgranular and along a cohesive and un-convoluted crack front.

Load history and thresholds. Fatigue crack growth rate in air will be sensitive to residual stress, right down to the point of crack formation. Unlike crack closure, diffusion – related retardation does not require a crack wake and can occur even when the crack is fully open. Diffusion is absent in vacuum and so will effects attributed to it. These include closure-unrelated stress ratio, load history and residual stress effects including their effect on ΔK_{th}. Evidence in support of these observations is available[25]. The possibility that vacuum fatigue including vacuum threshold will be *stress ratio and stress-history – insensitive* – unless factors such as crack closure or blunting come into play carries far reaching implications. Threshold measurements for a steel in air and vacuum as well as experiments at elevated temperature on a nickel-base super-alloy in air and in vacuum appear to support this observation[26, 32]. ΔK_{th} can be treated as a

history-sensitive material parameter bound by two extremes: a minimum value corresponding to high stress, high stress intensity and high stress ratio conditions (peak CFCDE) and a maximum value corresponding to vacuum (zero-CTCDE). It may follow that near-threshold residual stress and load history effects may be modeled merely by accounting for their effect on threshold stress intensity.

Stress Ratio Effect. Increasing stress ratio (mean stress) will contribute to increasing density of crack-tip elements, rapidly reaching high tensile stress under increasing load. For a given ΔK_{eff}, CFCDE will increase with increasing ratio K_{op} / K_{max} (or R, if $K_{min} > K_{op}$). The CFCDE model explains stress ratio effects independent of the closure phenomenon, though the two mechanisms may operate synergistically.

Thickness effect. Constraint-enhanced hydrostatic stress in the mid-thickness region will promote CFCDE by comparison to near-surface regions that see relaxed hydrostatic stress due to local plane stress. This will cause enhanced BMF in the mid-thickness area, and lead to crack front curvature. It may be noted that reduced mid-thickness crack closure also produces the same effect. Interestingly, given similar ΔK_{eff}, *plane stress* conditions will be associated with a cyclic plastic zone size that is about three times larger than under plane strain. Dislocation theory would then predict correspondingly *greater* near-surface growth rates, which is the opposite of what one observes.

The short crack effect. At a given ΔK, short cracks experience higher tensile applied stresses superposed with K-driven local stress. This will enhance CFCDE-driven BMF crack extension and may in fact explain why short cracks grow faster than long cracks at a given ΔK. If this is indeed so, the short crack effect should diminish in vacuum. Further, short cracks will also see stress ratio and stress history effects as detailed above (even if closure is absent). Available data indicating inhibition of surface crack formation in vacuum, and noticeable applied stress, and load sequence effects appear to indicate behavior consistent with the CFCDE model[25,26].

Crack formation kinetics are near-threshold by nature and in the absence of a wake, "closure-free". As residual stress operates through environmental action, differences in crack formation kinetics under similar applied cyclic stress magnitude may be attributed to environment – related factors. High tensile mean stress will accelerate crack formation at the notch root due to intensified diffusion. High compressive residual stress will effectively 'shut out' diffusion and thereby practically arrest the process of surface crack formation. This makes internal defects compete as potential crack initiators because their formation and growth is environment insensitive (mean stress independent). If the notch surface is sufficiently protected by compressive residual stresses (e.g. by shot-peening), surface crack formation will be inhibited. By the same token, enhanced fatigue life (by delayed or arrested surface crack formation) can be achieved by way of a suitable protective coating representing diffusion barrier. It would follow, that both compressive residual stresses and diffusion barriers may operate by diffusion-control. It would also follow that life to crack formation in vacuum may serve as the limit for retardation by diffusion-inhibition. For the same reason, the da/dN curve for vacuum may be the limiting (intrinsic) growth rate characteristic of a material.

Fatigue Limit. Assuming that ΔK_{th} is determined by propensity for CFCDE in a given environment, it may follow that a fatigue limit may not exist if CFCDE is possible. While a growing crack limits CFCDE, a stationary crack ensures potential increase in depth of CFCDE during successive load cycles. For a stationary crack, this will progressively increase the probability of BMF in the next cycle.

Transients. CFCDE occurs on a cycle-by-cycle basis. When the environment is changed from air to vacuum or the other way around, the effect on crack growth rate would be immediate, as indicated by available experimental evidence[25]. By implication, CFCDE-related retardation will take effect immediately after an overload as CFCDE is essentially driven by plastic zone ratios. This was the framework of the Wheeler[33] and Willenborg[34] models, though they may have lacked phenomenological rationale at the time. It may be noted that crack closure cannot explain immediate retardation after an overload as pointed out by Lang[29]. It may be noted that CFCDE does preclude the possibility of embrittlement depth in excess of growth rate. A brief cycle-dependent transition is therefore not ruled out.

Limit crack growth rate. Mode II crack extension by collapse of crack contour carries a geometric limit imposed by crack contour and its related parameter, CTOD. BMF crack extension even in essentially ductile materials is limited only by depth of CFCDE.

Limitation of laboratory data. Interpolative prediction requires reproducibility of similarity criteria. Constant amplitude fatigue crack growth rate data obtained in routine laboratory testing represent a certain combination of ΔK_{eff} and CFCDE. Interpretation of crack growth behavior due to change in closure level as indicated in Fig. 9b would constitute interpolation of these data. However, the conditions described by Fig. 9c represent a change in CFCDE component that cannot be simulated by constant amplitude ambient test conditions. To obtain pertinent experimental data, one must reproduce a similar degree of CFCDE – either by applying periodic overloads to induce compressive residual stress ahead of the crack tip, or by testing in controlled environments. Prediction of fatigue crack growth under variable amplitude loading based on closure alone would therefore be questionable – unless the exercise is restricted to vacuum conditions and based on vacuum data.

CONCLUSIONS

1. Environment-enhanced fatigue may occur by incremental brittle fracture (BMF) induced by crack front cyclic diffusion embrittlement (CFCDE). CFCDE occurs rising crack-tip hydrostatic tensile stresses in the rising half of each fatigue cycle. BMF occurs by quasi-static micro-fracture of embrittled crack-tip material unable to accommodate accumulating slip.

2. Clear striations are formed in atmospheric fatigue due to the flat crack growth band by de-cohesion, followed either by a fine line corresponding to crack contour collapse (slip) or local change in fracture plane, or both. Distinct striations do not form in vacuum due to lack of the de-cohesion component and possible re-fusion of collapsed contour.

3. The CFCDE-BMF model explains the residual stress effect in metal fatigue. It also appears to explain a variety of other fatigue phenomena.

REFERENCES

1. Laird, C, Mechanisms and Theories of Fatigue, Fatigue and Microstructure, ASM, Metals Park, 1978, pp. 149-204

2. Bowles, C.Q., The Role of Environment, Frequency and Waveshape during Fatigue Crack Growth in Aluminium Alloys, Delft University of Technology, Report LR-270, Delft, The Netherlands, 1978.

3. Vogelesang, L.B., and Schijve, J., Environmental Effects on Fatigue Failure Mode Transition Observed in Aluminium Alloys, Delft University of Technology, Report LR-289, Delft, Netherlands, 1979.

4. Schijve, J., and Arkema, W.J., Crack Closure and the Environmental Effect on Fatigue Crack Growth, Delft University of Technology, Aerospace Eng. Report VTH-217, Delft, 1976.

5. Tien, J.K., Thompson, A.W., Bernstein, I.M., and Richards, R.J., Metallurgical Transactions, Vol. 7A, 1976, pp. 821-829.

6. Albrecht, J., Bernstein, I.M., and Thompson, A.W., Metallurgical Transactions, Vol. 13A, 1982, pp. 811-820.

7. Shulte, K., Nowack, H., and Lutjering, G., Environmentally Induced Fatigue Crack Propagation under Variations in the Loading Conditions, in ASTM STP 1049 (W.B. Lisagor, T.W. Crooker, B.N. Leis, Eds), American Society for Testing and Materials, Philadelphia, 1990, pp. 347-373.

8. Spiedel, M.O., Blackburn, M.J., Beck, T.R., and Feeney, J.A., Corrosion Fatigue and Stress Corrosion Crack Growth in High Strength Aluminum Alloys, Magnesium Alloys and Titanium Alloys Exposed to Aqueous Solutions, Corrosion Fatigue: Chemistry, Mechanics and Microstructure, NACE, 1972, pp. 324-345.

9. Marcus, H.L., Williams, J.C. and Paton, N.E., The Influence of Gaseous Environments on Corrosion Fatigue, Corrosion Fatigue: Chemistry, Mechanics and Microstructure, NACE, 1972, pp. 346-358.

10. Sunder, R, Application of Crack Front Cyclic Diffusion Embrittlement Model to Variable Amplitude Fatigue, Submitted to FFEMS, 2002.

11. Atkinson, J.D., and Yu, J., The Role of Dynamic Strain-Ageing in the Environment Assisted Cracking Observed in Pressure Vessel Steels, Fatigue Fract. Engng. Mater. Struct., Vol. 20, No. 1, pp. 1-12, 1997.

12. Bika, D., and McMahon, C.J., A Kinetic Model for Dynamic Embrittlement, Phys. Stat. Sol., Vol. 131, pp. 639-649.

13. Goldstein, R.V., Balueva, A.V., A Model for the Behaviour of Materials with Cracks under Hydrogen Embrittlement Conditions, Fatigue Fract. Engng. Mater. Struct., Vol. 20, No. 9, pp. 1269-1277, 1997.

14. Ostberg, G., A Commentary on the Role of Nitrogen in Enhancing Slow Crack Growth in C-Mn Steel, Fatigue Fract. Engng. Mater. Struct., Vol. 21, No. 8, pp. 913-918, 1998.

15. Callister, W.D., An Introduction to Materials Science and Engineering, John Wiley & Sons, Inc, 1991, pp. 97-107.

16. Fritz, J.D., Parks, B.W., and Pickering, H.W., Coherency Stress and Transgranular Stress Corrosion Cracking of Cu-18Au Alloy, ASTM STP 1049, ASTM, Philadelphia, 1990, pp. 76-85.

17. Flanagan W.F., Lee, J.B., Massinon, D., Zhu. M., and Lichter, B.D., Role of Selective Dissolution in Transgranular Stress Corrosion Cracking: Studies of Transient and Steady-State Dealloying in Copper-Gold Alloys, ASTM STP 1049, ASTM, Philadelphia, 1990, pp. 86-99.

18. Bradshaw, F.J., and Wheeler, C., The Effect of Gaseous Environment and Fatigue Frequency on the Growth of Fatigue Cracks in Some Aluminium Alloys, Int. J. Fract. Mech., 1969, Vol. 6, pp. 255-268.

19. Thompson, N., Wadsworth, N.J., and Loat, N., Phil. Mag., 1, 113 (1956).

20. Shen, H., Podlaseck, S.E., and Kramer, I.R., Acta Met., 14, 341, 1966.

21. Ashbaugh, NE, Dattaguru, B., Khobaib, M., Nicholas, T., Prakash, R.V., Ramamurthy, T.S., Seshadri, B.R., and Sunder, R., Experimental and Analytical Estimates of Fatigue Crack Closure in an Aluminum-Copper Alloy. Part I: Laser Interferometry and Electron Fractography, Fatigue Fract. Mater. Struct, Vol 20, No. 7, 1997, pp.951-961

22.   Sunder, R., and Dash, P,K, Measurement of Fatigue Crack Closure Through Electron Fractography, Int. J. Fatigue, Vol 4, 1982, pp. 97-105.

23.   Ranganathan, N., Benguidab, M., Henaff, G., Adiwijayanto, F., Quantitative Fracture Surface Analysis of Fatigue Crack Propagation under Variable Amplitude Loading, ASTM STP 1203 (J.E. Masters and L.N. Gilbertson, Eds), American Society for Testing and Materials, Philadelphia, 1993, pp. 71-94.

24.   Sunder, R., Porter, W.J., Ashbaugh, N.E., Fatigue Voids and Their Significance (To appear in FFEMS, 2002).

25.   Sunder, R., Porter, W.J., Ashbaugh, N.E., The Role of Air in Fatigue Load Interaction (To appear in FFEMS, 2002).

26.   Sunder, R., Porter, W.J., Ashbaugh, N.E., Rosenberger, A.H., and Nicholas, T., Influence of Environment on Load Interaction Effects in Fatigue Crack Growth under Spectrum Loading, Proceedings, Airframe Structural Integrity Programme Conference, Williamsburg, Dec. 11-13, 2001.

27.   Elber, W., Engineering Fracture Mechanics, Vol. 2, 1970, pp. 37-45.

28.   Sunder, R., Rainflow Applications in Accelerated Cumulative Fatigue Analysis, The Rainflow Method in Fatigue, Y. Murakami, Editor, Butterworth Heinemann, 1992, pp. 67-76.

29.   Lang, M., A Model for Fatigue Crack Growth, Part I: Phenomenology, Fatigue Fract. Engng. Mater, Struct., Vol 23, No. 7, pp. 587-601, 2000.

30.   Vasudevan, A.K., Sadananda, K., and Loust, N., A Review of Crack Closure, Fatigue Crack Threshold and Related Phenomena, Materials Science and Engineering, A188 (1994), pp. 1-22.

31.   Gach, E, and Pippan, R., Cyclic Crack Tip Deformation – The Influence of Environment, Proceedings, 10th International Conference on Fracture, Dec. 2001, Paper ICF100420OR.

32.   Cooke, R.J., Irving, P.E., Booth, G.S. and Beevers, C.J., Eng. Fract. Mech. 7, 69 (1975)

33.   Wheeler, O.E., Journal of Basic Engineering, Trans. ASME, March 1972, pp. 181-186.

34.   Willenborg, J.D., Engle, R.M., and Wood, H.A., A Crack Growth Retardation Model Using an Effective Stress Concept, AFFDL-TM-FBR-71-1, Air Force Flight Dynamics Laboratory, 1971.

R. Sunder, N.E. Ashbaugh, W.J. Porter and A.H. Rosenberger[*]

Multi-Mechanism Synergy in Variable-Amplitude Fatigue[1]

ABSTRACT: Fractographic studies on Al-alloys and a nickel-base super-alloy point to the combined action of three major load-interaction mechanisms in controlling crack growth under variable-amplitude loading. These are crack closure, residual stress and crack front incompatibility. Crack front incompatibility attenuates crack tip response to applied load and can also increase crack closure stress. Notch root residual stress affects crack closure, while crack tip residual stress moderates environment-enhanced fatigue crack extension. The latter effect disappears in vacuum. Carefully designed experiments designed to isolate the effect of individual mechanisms provide a framework to model their synergistic action, consistent with microscopic observations of crack growth bands in variable amplitude fatigue.

KEYWORDS: crack growth mechanisms, thresholds, residual stress effect, crack closure, crack front incompatibility

Introduction

Several load interaction mechanisms *together* determine crack growth under variable amplitude loading [1]. Significant among these are fatigue crack closure [2], residual stress in the overload plastic zone [3,4] and crack front incompatibility [5]. Realistic modeling requires analytical, or at least correlative representation of the quantitative effect of each of these mechanisms. However, none of the predictive models described in the literature addresses the question of multi-mechanism synergy in variable-amplitude fatigue.

Early residual stress based models proposed by Wheeler [3] and Willenborg [4] continue to be widely used. The models assume increased resistance to fatigue through compressive residual stress, as reflected by an empirically determined retardation constant that attenuates growth rate. Both models are correlative by nature: crack growth rate is corrected by a retardation factor given by baseline to overload plastic zone ratio, raised to an empirically determined exponent. An exponent, selected to suit available experimental data on overload effects may then be used to make predictions. Both these models fail to explain possible acceleration as well as delayed retardation after overloads.

Unlike the strictly correlative models that preceded it, the crack closure mechanism lends itself to analytical modeling [6-10]. Closure models operate on the premise that retardation / acceleration in crack growth is *uniquely* associated with a change in *effective* stress intensity determined in turn by crack opening stress. Thus, increased crack opening stress after an overload will cut off a greater part of subsequent baseline loading, leading to retarded crack growth.

More recently, a parameter called K_{PR} (for K-propagation) was proposed as a load-history sensitive variable that determines a fraction of the applied load cycle, which will grow the crack [11]. K_{PR} is determined empirically by cycling at threshold stress intensity range at progressively increasing mean level in order to pinpoint a stress intensity above which, fatigue crack extension does occur. The authors point out significant differences between K_{PR} and closure approach. K_{PR} always exceeds closure stress, explained by the rationale, that at the instant the crack opens, near tip stresses will still be compressive and therefore not contribute to crack growth. Further, unlike crack closure, K_{PR} is shown to increase instantaneously after a tensile overload and its authors attribute this to the immediate development of protective compressive residual stresses at the crack-tip.

K_{PR} is associated with both constant amplitude as well as variable amplitude fatigue and it may be determined in a reproducible manner using a well-defined process. Further, it explains both acceleration as well as retardation. Transient K_{PR} behavior after single and multiple overloads is modeled through empirical correlation of measured K_{PR} values in such experiments [12].

K_{PR} conceptually relies on the assumption that threshold stress intensity, K_{th} is an independent material constant. The well-known sensitivity of K_{th} to a number of factors including load history appears to question this premise [13, 14].

The inadequacy of available prediction models lies in their inevitable exaggeration of the effect of a single load interaction mechanism for success in accounting for observed crack growth retardation. The motivation for this study stems from the multi-mechanism nature of load interaction effects and the need for their study in isolation as a step towards synergistic modeling.

The next section explains experiments that enabled fractographic study of three major load interaction mechanisms in relative isolation. This is followed by a description of fractographic observations. The paper concludes with a framework for modeling multi-mechanism synergy that may serve future developments in fatigue life prediction.

Experimental Procedure

Mechanism isolation was the primary objective of our fractographic studies. Specially designed programmed load sequences were applied to highlight the action of individual mechanisms. While none of these sequences may be similar to those seen in real-life situations, they provide a unique opportunity for fractographic assessment of how individual mechanisms may induce load interaction.

A load sequence with constant S_{max} and varying S_{min} is unlikely to see any closure-induced load interaction effect. If on the other hand, a sequence is designed to have cycles of equal range, but varying maximum stress, it will potentially see at least two load interaction effects, crack closure as well as residual stress. If the stress ratio of all these cycles is kept above a certain level, they are all likely to see a fully open crack, thereby eliminating crack closure as a potential load interaction mechanism. The primary

cause of crack front incompatibility is mechanism change due to substantial change in crack driving force. Crack extension mechanism is known to change as growth rate moves from one broad bandwidth to another. Therefore, the effect will be seen if the growth rate distribution among cycles is such that they tend to spill onto the next mechanism bandwidth. These considerations formed the basis for our interpretation of fractographic evidence.

The focus of our study was near-threshold fatigue. This region is significant because it controls durability. It also happens to be the most sensitive to load history effects. Unfortunately, near-threshold fatigue is not conducive to conventional electron fractography based on striation measurement. Striations typically form in the growth range 10^{-4} to 10^{-2} mm/cycle. Even though electron microscopy can resolve much smaller
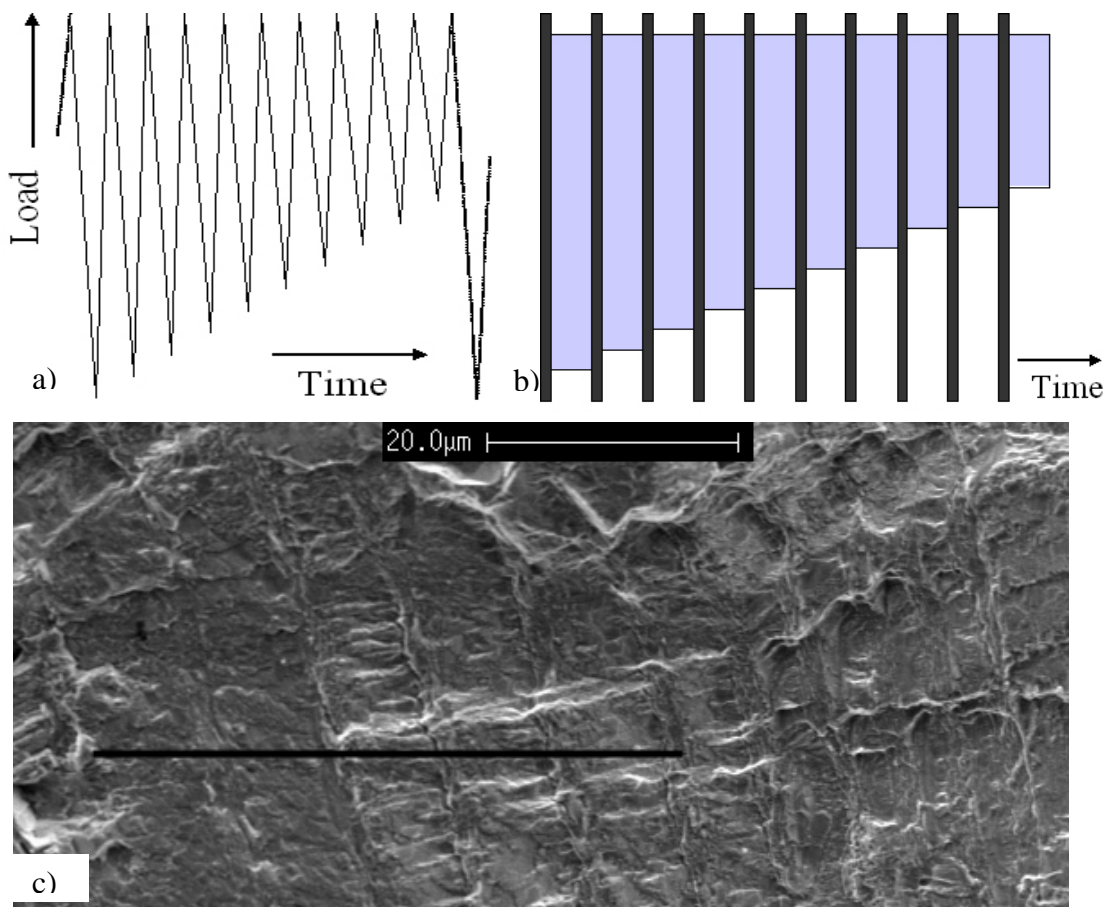

FIG. 1 – (a) Load sequence originally proposed for fractographic measurement of crack closure. When applied repetitively, crack opening stress will be determined by the extreme loads. For cycles with $S_{min} <= S_{op}$, striations will be equally spaced. Their count is a measure of S_{op}. (b) Load sequence in (a) modified for use under conditions where striations from individual cycles may not be visible. (c) Typical fractograph from IN-100 at elevated temperature with load sequence in (b) on C(T) specimen. Five equally - spaced striations shown by bar correspond to $S_{op}/S_{max} = 22.5\%$. Several experiments on Al-alloys yielded similar results.

dimensions, other morphological features overshadow the relatively 'shallow' growth marks. To overcome this problem, microscopic banding was resorted to, whereby, a large number of cycles are embedded between marker cycles. While neither of these may by themselves form discernible striations, transition from one to another leads to clearly visible striation-band patterns. This technique permits fractographic observation of growth rates as low as 10^{-8} mm/cycle[2].

While markers enforce discernible crack front marks on the fracture surface, they can also grow the crack, apart from introducing their own influence on the fatigue process. To reduce these effects, marker load cycles were Hi-range, Lo-R to reduce or avoid altogether any overload effect.

Crack closure measurements were made using the 'Closure' sequence shown in Fig. 1 adapted from the one described in [15]. It is based on the premise that under a repetitive load sequence causing negligible crack extension by comparison to plastic zone size, crack opening stress, S_{op}, will be constant and determined by the extreme loads in the sequence. Then, given S_{op} = Const, and S_{max} = Const, cyclic crack extension will be identical for those cycles with $S_{min} <= S_{op}$. Equally-spaced marker band count in the Closure sequence cannot be attributed to any other known phenomenon[3].

The original method was based on striation spacing from individual cycles as shown in Fig. 1a. This was extended to near-threshold fatigue by incorporating multi-cycle blocks with marker loads as shown in Fig. 1b. A typical fractograph from a IN-100 C(T) specimen tested at elevated temperature under this load sequence appears in Fig. 1c. The five equally spaced striation bands covered by the thick line on the figure point to an S_{op}/S_{max} value of 22.5% as indicated by the dotted line covering the first five load steps in Fig. 1b.

Closure-free load interaction was studied using the '3-R' sequence described in Fig. 2a. It includes three steps of equal amplitude and cycle count with marginally varying stress ratio (0.73, 0.69 and 0.65). Known load interaction mechanisms such as closure cannot explain load interaction effects at Hi-R with such marginal variation of R. The markers effectively preclude closure in the Hi-R steps as confirmed by independent measurements through fractography and laser interferometry [20]. The dotted line indicates expected S_{op} from the marker cycles.

Large cycle steps interspersed with markers enabled the use of fractography to investigate near- and sub-threshold fatigue crack growth, including crack formation. Marker cycle count is controlled to cause sufficient growth to 'mark', but at the same contribute less than 10% of total growth. Marker spacing may thus serve as a measure of crack growth during Hi-R cycles. In order to reduce transients, Hi-R step cycle count is selected to ensure that marker spacing is only a fraction of plastic zone size.

---

[2] The development of appropriate markers involved iterative experiments. Different marker types had to be developed for Al-alloys, Ti-alloy and nickel-base super-alloy. Details of these sequences appear elsewhere [16-19].

[3] In particular, given the power relationship between ΔK and crack growth rate.

Fig. 2b shows a typical fractograph from a 2014-T6511 notched coupon tested to failure under repeated application of the load sequence shown in Fig. 2a. It shows well
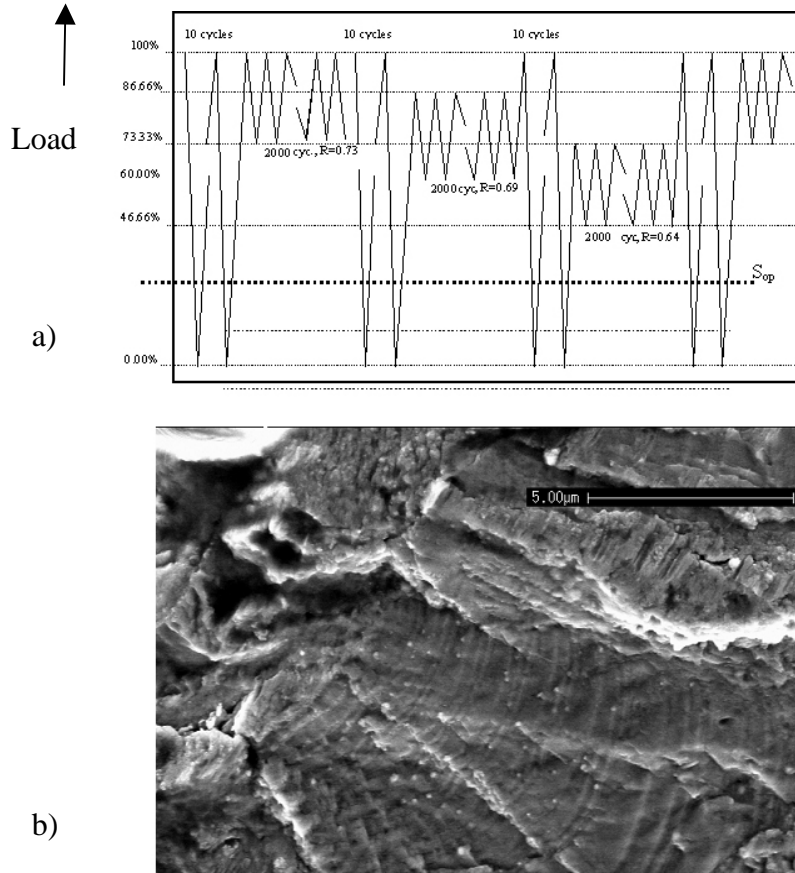

FIG. 2 – (a) Typical 3R load sequence used in near-threshold experiments to isolate closure-unrelated load interaction effects. S_{min} at the lowest R is pegged at 0.466 of highest stress (or at about twice the expected S_{op}) to ensure a fully open crack at all three R's. Further, the Lo-R markers in between are also expected to 'beat down' closure level. (b) Typical marker bands from the 3R sequence about 15 microns away from the crack formation site at top left. Crack growth rate at highest R is about $0.5x10^{-6}$ mm/cycle, while at the lowest R, it is about 10^{-7} mm/cycle. The approximately 1:5 retardation is remarkable considering a fully open crack and marginal R-ratio change from 0.73 down to 0.64. A 1:10 retardation was observed over the same R-change on IN-100 nickel-base super-alloy tested at elevated temperature.

defined sets of three bands, with the widest one in each set obviously corresponding to the R = 0.73 step. Crack growth in this step is about three times greater than the extension due to the third step at R = 0.64. Note also that highest growth rates seen at bottom right are of the order of $5x10^{-7}$ mm/cycle. Striations from individual cycles cannot be resolved at this growth rate.

Crack Front Incompatibility. At certain growth rates under 3-R loading, the difference in magnitude between marker and baseline cycles causes visible mechanism change.

Fractographs of such regions provide evidence of microscopic crack front incompatibility.

In addition a variation of the 3-R sequence was used in experiments on Ni-base super-alloy at elevated temperature. A dwell period was included at max load to induce sustained load cracking in air and blunting in vacuum. The goal of these experiments was to examine the effect of transition from trans-granular to inter-granular mode, which constitutes a microstructure-induced CFI mechanism.

In a few experiments, the Closure and 3-R sequences were combined in order to confirm assumptions regarding the fatigue crack being fully open in the 3-R programs. In all experiments, the sequences were repeated to failure under test frequency ranging from 2 to 20 Hz depending on cycle magnitude. Fatigue kinetics was measured on the fatigue fracture surface using a high-resolution scanning electron microscope with digital imaging.

The tests were performed on two Al-alloys (2014-T6511 and 2024-T351), Ti-6Al-4V C(T) and IN-100 nickel-base super-alloy [16-19]. The Al-alloy tests included notched coupons to examine natural crack formation and early crack growth. Some tests on Al-alloy and Ni-base super-alloy were repeated in vacuum. Baseline step size and marker cycles required modification in a few experiments. Thus, vacuum test step size was increased from 2000 to 5000 cycles to accommodate reduced growth rates and IN-100 experiments used Lo-R high-cycle markers to adapt to material-sensitive fracture morphology. Also, the elevated temperature IN-100 experiments used only two R-steps to simplify fractography.

Fractographic Observations

Long crack closure. Under near-zero applied stress ratio, long crack closure level, S_{op}/S_{max}, is between 0.2 and 0.3, where, S_{max} is the highest stress in the load programme. The same observations were made on 2024 and 2014 Al-alloys as well as in IN-100 nickel-base super-alloy at 482 deg. C. This includes near-threshold conditions with growth rates down to and below 10^{-6} mm/cycle. In the materials studied, our measurements discount the possibility of near-threshold behavior being related to increasing closure levels. Other authors also question exaggerated closure levels at threshold [14].

Analytical modeling assumes S_{op}/S_{max} to be closely related to the so-called constraint factor associated with plane strain conditions [10]. S_{op}/S_{max} is assumed to increase substantially with transition from plane strain to plane stress conditions.

A flat fracture surface is associated with plane strain and the formation of shear lips is associated with transition to plane stress. Fractographic evidence does indicate increase in S_{op}/S_{max} close to the surface as opposed to the mid-thickness region [15]. However, the increase is only marginal being of the order of about 10% of S_{max}. Further, we were unable to obtain fractographic evidence suggesting any increase in closure levels with switch from normal to inclined mode of fatigue crack growth. This applies to 'stable' conditions as opposed to local mode change that can occur in the event of a single overload.

S_{op}/S_{max} can increase considerably in the event of intense local crack front incompatibility which essentially imposes local mixed-mode cracking. An example of

such a possibility appears in Fig. 3 where striation bands in neighboring grains indicate substantial grain-to-grain variation in S_{op}/S_{max} across the crack front. This fracture was obtained under the 3-R load sequence, where closure is not expected, as supported by the evidence at top left, showing equally spaced bands as was the case all over the fracture surface. The bottom right region shows two equally spaced bands while the third one is
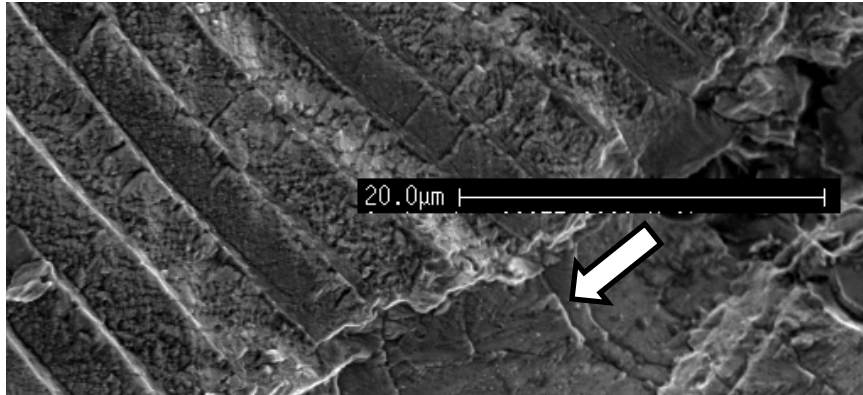

FIG. 3 – Dramatic grain-to-grain variation in S_{op}. All three marker bands are equally spaced under the 3-R sequence at top left, while in the neighboring grain, crack extension at the lowest R is about three times less than in the other two. This appears to indicate grain orientation-sensitivity of closure. Long crack in 5 mm thick 2014-T6511 C(T) specimen. Each band is from 2000 load cycles. Arrow indicates crack growth direction.

substantially narrow. Judging from the load levels indicated in Fig. 2 for the 3-R sequence, S_{op}/S_{max} in this region would be just over 60%. Grain-to-grain change in S_{op}/S_{max} may be associated with variation in grain or crack plane orientation It is likely that at lowest R, there may have been local orientation-induced obstacles to crack opening in Mode II that were overcome at higher stress ratio. This would be an analog of asperity or roughness induced closure [21, 22].

   Short crack closure. When cracks form at notches, applied stress level and stress concentration factor determine short, part-through crack closure levels. If the notch is blunt and applied stress levels are high, S_{op}/S_{max} can drop to as low as 0.05, with considerable hysteresis in closure behavior [23, 24]. Notch root yield in tension leading to local compressive residual stresses upon unloading causes a reduction in local stress ratio. Such behavior is consistent with notch fatigue concepts based on Local Stress-Strain approach [25]. As a consequence, apparent S_{op}/S_{max} can increase to as high as 0.55 [23, 26]. This is illustrated by fractographs in Fig. 4 obtained from a test on a notched Al-alloy coupon. The test was performed under a programmed load sequence consisting of a Closure sequence followed by five repetitions of the 3-R sequence. The corresponding striation band patterns appear correspondingly as 'C' and '3R' in the figure. Fig. 4a shows the notch surface at the left, with the first 'C' pattern commencing less than 0.05 mm from the notch root. Both the first and second 'C' blocks indicate 9 out of 10 striation bands to be equally spaced, suggesting $S_{op}/S_{max} = 0.55$. Evidence supporting this assessment appears in the form of band spacing during the five 3-R blocks. As indicated in the zoomed in picture Fig.4b, the third band is less than half the

first one, while the first and second are of similar spacing. Refer now to the 3-R load sequence description in Fig. 2a to note that such band spacing would follow from S_{op}/S_{max} between 0.47 and 0.6.

Fig. 4c is from a region farther away from the notch root. Here, we find that the 3-R bands are equally spaced (crack fully open). This is backed by the 'C' bands, of which, five or six are equally spaced, suggesting an S_{op}/S_{max} value close to 0.3, typical of long crack behavior. The appearance of striation bands in Fig. 3 (bottom right) and Fig. 4b is strikingly similar. Both indicate high S_{op}/S_{max}, but were caused by vastly different conditions. The former may have been induced by local mixed-mode conditions, while the second was clearly a consequence of reduced notch root stress ratio due to compressive residual stresses.
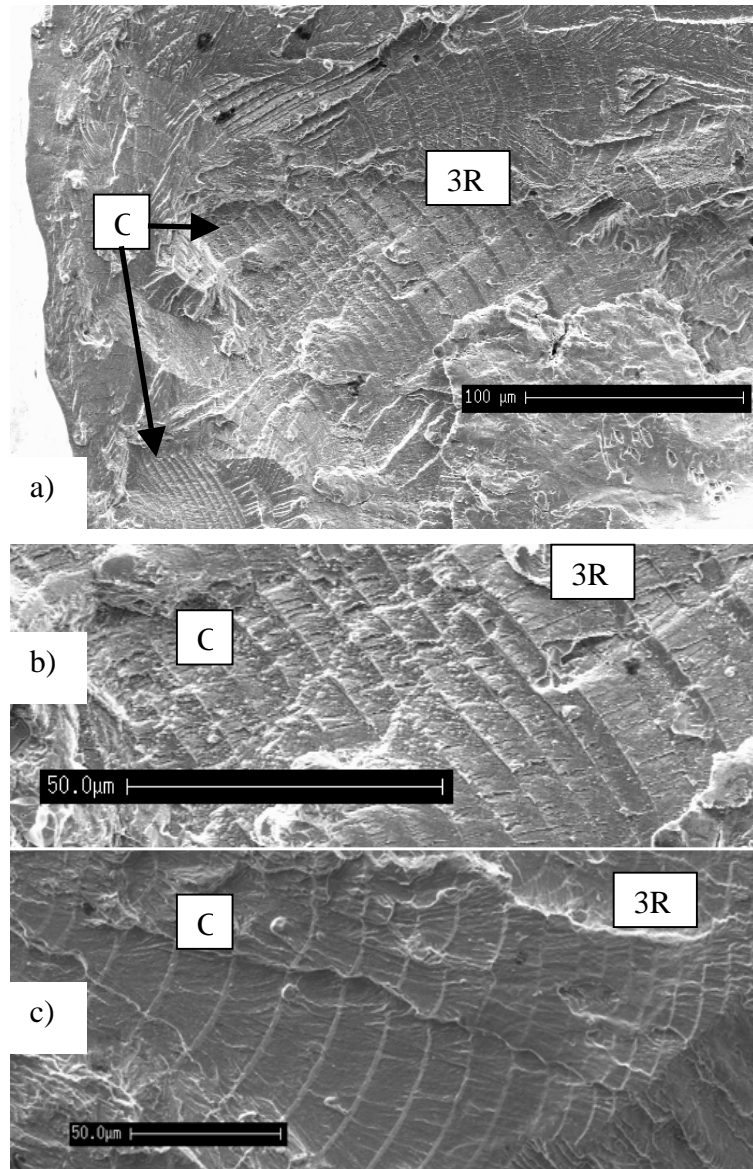
FIG. 4 – Notch root marker bands under combined action of closure block (C) (described in Fig. 1b) and five repeats of the 3-R sequence (3R) described in Fig. 2a. Material: 2024-T35. C(T) specimen with 2 mm dia key hole notch. (a) Notch root area with notch surface at left. (b) is zoomed in region from (a). (c) region about 0.35 mm from notch surface. Note that closure stress drops off to long crack level as crack grows out of notch root area of high compressive residual stresses.

Note that in both cases, middle striation band spacing is identical to the highest-R band. It underscores the "cut-off" role played by closure in multi-mechanism synergy. This is different from an "attenuation" effect, whereby a load cycle is made "less severe", rather than a part of it being "cut off" from action.

In summary, fractographic observations confirm the presence and nature of fatigue crack closure as a load interaction mechanism that cannot be ignored if realistic estimates are to be made of fatigue crack growth in variable amplitude fatigue. S_{op}/S_{max} can rise to

as high as 0.55 – 0.6 in small cracks growing within a notch root compressive residual stress field [26]. This is in contrast to short cracks at blunt notches or un-notched surfaces that are known to exhibit closure levels, as low as 0.05 [23]. Crack closure can also increase substantially – up to 60% or more, in the event of barriers to opening caused by local mixed mode conditions (CFI). However, in the absence of CFI, long cracks do not appear to indicate closure beyond 25 to 30% of maximum load. Further, this value does not seem to increase under near threshold conditions.

Residual Stress Effect. The residual stress effect in metal fatigue has been known for more than 150 years. However, its operative mechanisms are not entirely clear. The fractographs in Fig. 4 demonstrate one operative mechanism of residual stress – reduction in local stress ratio leading to an increase in S_{op}/S_{max}. The fractograph in Fig. 2 shows gradual "attenuation" of striation band spacing as opposed to the abrupt "cut off" associated with crack closure, seen in Figs. 3, 4. The significance of attenuation versus cut-off deserves clarification in the light of the nature of the 3-R load sequence. The relative load levels in the three Hi-R steps are designed in such a manner that if the crack is partially closed only in the lowest step, two equal bands should appear. However, if the crack is partially closed even in the middle step, the lowest R band would be barely visible (because the crack would be barely open) given the power relationship between growth rate and K_{eff}. There are potentially three explanations for gradually attenuated band spacing under the 3-R sequence. One possibility is that S_{op}/S_{max} was not constant. This is discounted by equally spaced bands observed elsewhere and particularly at higher growth rates, characterized by greater potential for closure transients due to more rapid increase with crack size in growth rate as opposed to plastic zone size. The second possibility is the natural dependence on stress ratio of growth rate at the three different stress ratios. This may also be discounted by the equally spaced bands at other locations. Besides, the extent of attenuation observed cannot be explained by the relatively minor variation in stress ratio of 0.05 per step. Recent research suggests a third possibility for growth rate attenuation under the 3-R programme [17]. Residual compressive stress from higher-R cycles increases resistance of lower-R cycles to environmental fatigue. Moderation of environmental action appears to be a major operative mechanism of the residual stress effect. This was confirmed by experiments in air and vacuum on a notched 2014-T6511 coupon [17] and also in air and vacuum at elevated temperature on IN-100 C(T) specimen [19] (See Fig. 5). Both materials showed attenuated growth in the lower R cycles in air as did a Ti-alloy C(T) coupon. However, the effect vanishes in vacuum under the same applied loading conditions. In experiments on the Al-alloy coupon, switching the environment between air and vacuum caused an immediate change (both ways) in the ratio of striation band spacing. If this effect was due to any mechanistic phenomenon such as closure or roughness, one would have observed a transient region following the environment switch. This was not the case. Instead, environment switch caused immediate change in growth rate pattern from equally spaced in vacuum to attenuation in air and vice versa. The suggestion that environmental fatigue crack extension may contain two components: environment-sensitive brittle failure and crack-tip blunting / re-sharpening, is not new [27, 28]. What is new, is the suggestion that the first component may be moderated by history-sensitive residual stress [17, 18]. As indicated in a separate paper [29], crack tip hydrostatic stress superposed on history sensitive crack-tip residual stress may be expected to exert a strong influence on crack tip
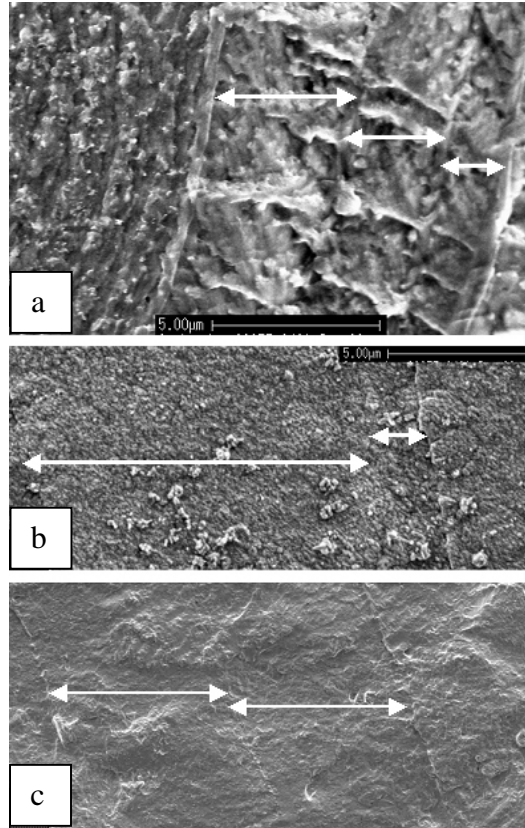
FIG. 5 – (a) Marker bands under 3-R load sequence in vacuum (left) and after switch over to air (right). Crack growth from left to right. 2014-T6511 notched Al-alloy coupon. Long crack marker bands in IN-100 nickel base super-alloy 5 mm thick C(T) coupon at 650 deg. C under 2-R load sequence in air (b) and in vacuum (c). Note the equally spaced bands in vacuum indicating absence of load history or stress ratio effects. Crack closure was absent as indicated by independent measurements. This is also confirmed by bands in (a) that indicate immediate response to change in environment from vacuum to air. If closure was present, there would have been a transient zone required to build up closure.

lattice and surface diffusion of environment components. This in turn will change crack-tip stress-strain response and induce a load-history sensitive brittle failure mode at the microscopic crack tip surface level. Fractographic evidence indicates this effect is a near-threshold phenomenon that diminishes with increasing growth rate. For modeling purposes, this may be treated as an effect on K_{th}.

Crack Front Incompatibility (CFI) may be broadly defined as any geometric deviation from crack front geometry under constant amplitude loading under the same load. Early work by Schijve et al highlighted the significance of CFI as a load interaction mechanism [5]. In experiments with engineered CFI through shaping of crack initiators, it was shown that CFI affects stress intensity for a given crack size. Let us consider fractographs showing typical instances of both microscopic as well as macroscopic crack front incompatibility and their likely effect on the fatigue crack growth process.
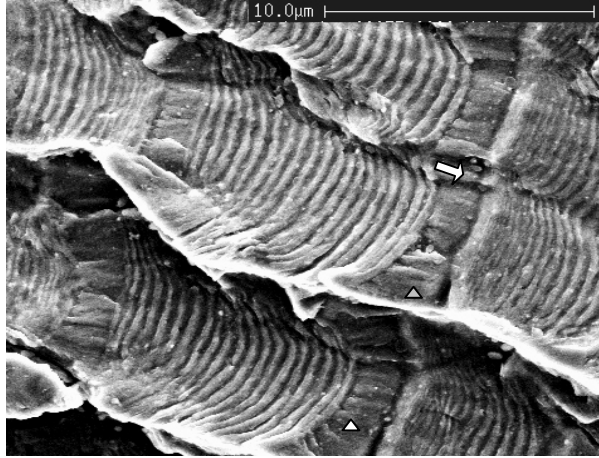
FIG. 6 – Example of microscopic crack front incompatibility (triangles) under mix of small and large cycles with similar K_{max} [16]. As large cycles are in the intermediate range (over 10^{-4} mm/cycle), their striations tend to curve forward within individual grains. Small cycles correspond to near-threshold growth rate, associated with a straight crack front.

Fig. 6 shows microscopic CFI at the grain level in an Al-alloy subject to programmed loading. Seen in the middle are 20 striations from high amplitude marker cycles. On either side is a step of 500 low amplitude cycles. Growth rates in the two regions are approximately 4×10^{-4} and 4×10^{-6} mm/cycle respectively. Both growth rates fall into the region where the fatigue fracture is flat. Crack extension in individual grains appears to proceed at different planes associated with preferential orientation. Crack front curvature at higher growth rate indicates retarded growth along grain boundaries that may be due to various reasons including discrete change in plane, along with potential stress free conditions at grain boundary, particularly if they separated to relieve cyclic tri-axial stress in the cyclic plastic zone. If as suggested earlier, the lower growth rate were largely due to environment-enhanced embrittlement, it would follow that the associated process is insensitive to grain boundary conditions. The twenty striations appear to be equally spaced even though crack front curvature progressively increases. Further, the 500-cycle steps preceding and following the markers also appear unaffected by curvature. The one on the left saw a straight front at commencement, while the one at the right needs to straighten it. One may conclude that such microscopic CFI has a negligible effect on fatigue and may be ignored. From a practical standpoint, a more significant conclusion would be that as long applied load sequence does not force a change in crack extension *plane*, there will be no CFI component. Considering growth rate to be a potential criterion that indicates mode, one may conclude that for the material and thickness in question, there will be no CFI component provided no individual cycle causes a crack extension in excess of 10^{-4} mm/cycle.
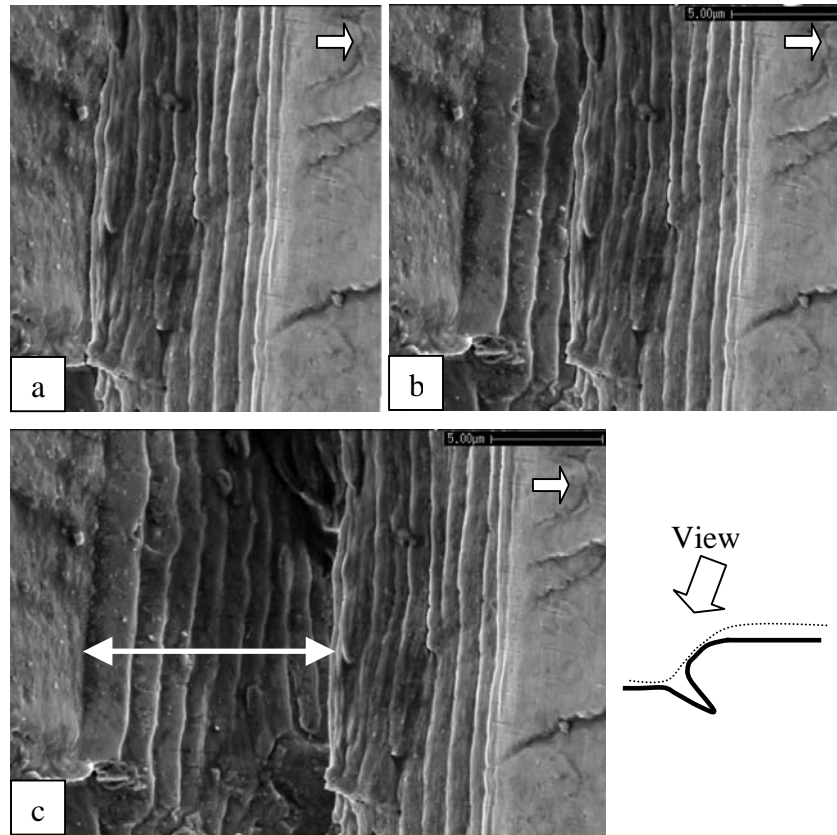
FIG. 7 – Crack branching during 10 large amplitude cycles after a low amplitude near-threshold crack extension segment. As seen in (c), an illusion is created of 20 striations from 10 cycles, while in fact, these are two sets of striations, one from each branched crack. This is confirmed by the photographic reconstruction of the separation as seen in (b) and (a) by moving the image of striations from the top branch to the left, to effectively close the opening caused by the lower branch.

Higher crack growth rate is associated with a substantial slip component promoting shear mode crack extension. On fatigue failures, this is associated with the formation of shear lips that gradually expand to cover the entire crack front on an inclined plane. If the crack was grown at low growth rate to ensure a flat fracture surface, a sudden increase in crack growth rate can cause branching along slip planes. This can be obvious if more cycles are involved as shown in Fig. 7. Fig. 7a, b were photographically reconstructed from the original picture that appears as Fig. 7c. On the left and right, we see the flat mode associated with baseline loading and growth rate under 10^{-5} mm/cycle. Application of 10 marker cycles of higher amplitude creates the illusion of 20 striations. What we actually see are 10 striations each from each of the branched cracks, thanks to the substantial residual opening (0.02 mm) of the non-propagating branched crack. Figs 7a,b show how the fracture would appear if this breach did not exist. Several CFI aspects show up in this case that are likely to affect subsequent fatigue crack growth. If prior cracking were to occur under the same higher load amplitude, branching may perhaps not have taken place as the crack front may have already inclined. The fact that striation

spacing does not show any variation over the 10 cycles (about 0.05 mm of crack growth) indicates the absence of any transient effect associated with the plane transition. However, crack branching and or deflection will cause reduced stress intensity [21, 22] and associated retardation. Note that in these experiments, increase in cyclic load was achieved by reduced minimum load and not by overloads.
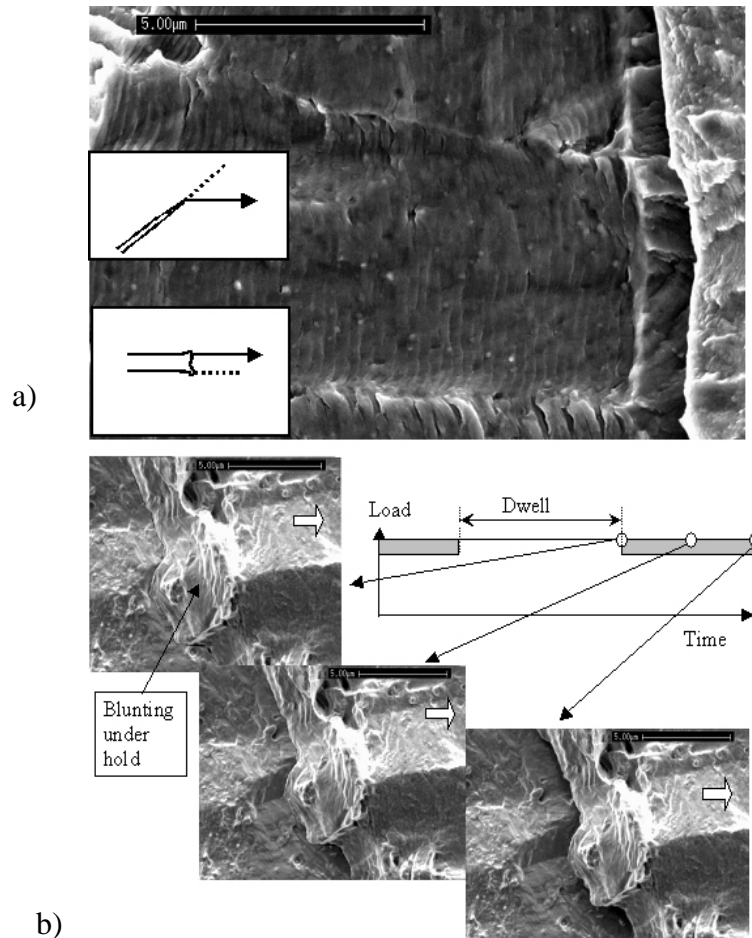

FIG. 8 – Examples of branched crack growth from a blunted tip in air (a) and in vacuum (b). (a) Crack branching after switch from high to low amplitude in an Al-alloy C(T) specimen. Schematics at left show possible orientation of the two branched cracks seen at right. (b) Evidence of crack branching after blunting due to hold-time in vacuum at 650 deg. C. 5 mm thick C(T) specimen cut from nickel-base super-alloy. Top two pictures reconstructed photographically from the one at bottom right, by 'closing' the breach caused by non-propagating branched crack.

Crack branching will also retard subsequent crack growth under lower amplitude cycling associated with flat fracture. This may occur due to at least two reasons: reduced stress intensity range due to branching/kinking and relaxed iso-static crack tip stresses also due to branching, that will reduce the environment-enhanced component of crack

extension. Finally, crack closure may increase substantially due to crack branching and thereby virtually shut out the action of smaller amplitude Lo-R cycles until the crack plane straightens out once again.

Fig. 8a shows the unusual case of crack branching associated with a transition from large to small amplitude loading. Two schematics describe the branched flat mode (reduced growth rate) crack at the right. The top schematic assumes the higher growth rate crack was already in slant mode. On switch to lower amplitude cycling, one branch continues along the same plane, while the dominant crack grows returns to flat mode. The schematic at the bottom appears to be more likely. The crack tip under large cycle amplitude was blunt, as confirmed by the step indicated by the arrow at right. Then, crack branching is due to re-initiation of two parallel cracks at the blunt crack tip from previous loading.

Another example of crack branching appears in Fig. 8b from an IN-100 C(T) specimen tested at elevated temperature in vacuum with hold time. Hold time blunts the crack in vacuum and subsequent cycling causes two cracks to re-initiated as shown by the photographic closure of the breach due to the non-propagating crack. In both cases, the blunt crack tip appears to have a radius of 3 to 5 microns.
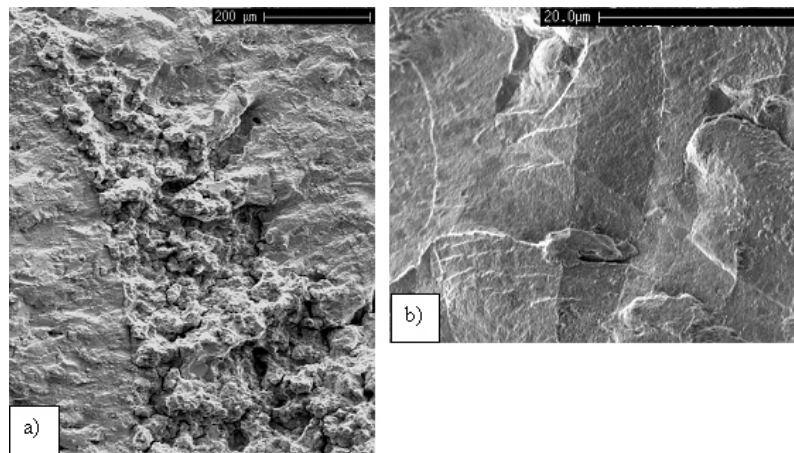

FIG. 9 – (a) Inter-granular cracking during hold time in air at 650 deg. C. Fatigue cracking immediately after return to cyclic loading was retarded (b). Note reduced marker band spacing at lower R.

Fig. 9 illustrates an example of CFI due transition between trans-granular and inter-granular cracking. This fracture was obtained using the same load sequence as the one that caused the fracture shown in Fig. 8b from an IN-100 C(T) coupon, but tested in air at elevated temperature. Hold time between fatigue cycling causes inter-granular cracking as indicated by the crack front tracing grain boundaries in Fig. 9a. Sustained load cracking is extremely sensitive to local tensile iso-static stress, which is greatest in the mid-thickness area. This induces tunneling and associated crack front curvature. CFI is induced at both transition points and in both cases, tends to retard crack growth. At the onset of sustained loading, crack extension is retarded until the trans-granular crack front can find the closest grain boundary. If trans-granular diffusion is inhibited, environmental diffusion will occur along grain boundaries already open in the wake and proceed along
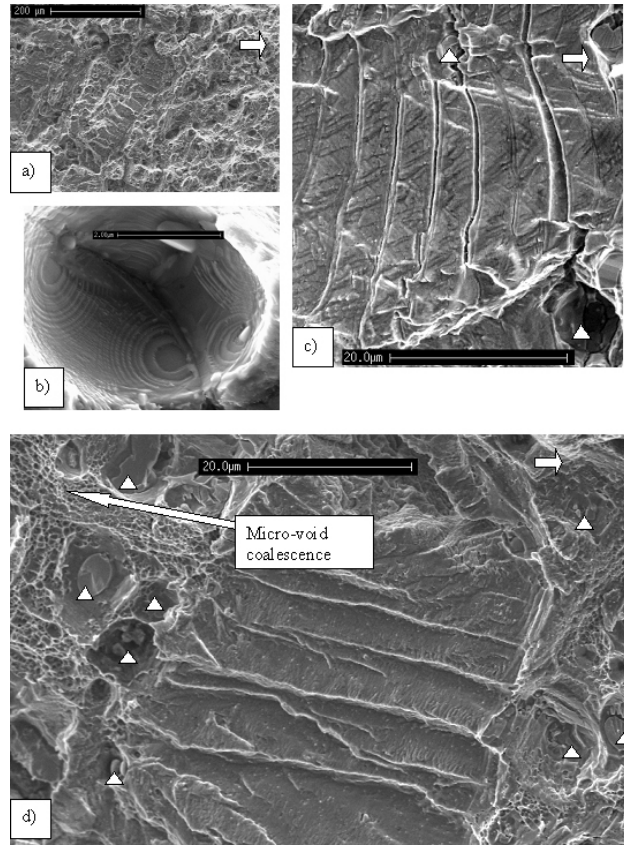
FIG. 10 – (a) Tortuous crack burst during marker loads occurring at higher growth rate. Small flat region in the middle is from a Hi-R step of 10 cycles (b) Zoomed-in view of a typical void formed around a particulate [30]. Concentric circles mark the growth of penny-shaped interface cracks that coalesced to separation. This occurs before the major crack sheared the particulate as shown by triangles in (c) Local crack branching at single marker striations close to particulate voids. (d) Zoomed-in view of (a) showing individual fatigue voids indicated by triangles, region of void-free retarded growth during a Hi-R low amplitude step and a cluster of coalesced micro-voids associated with local quasi-static ductile fracture. Note the difference in size between micro-voids and fatigue-voids. Long crack in Al-alloy.

them to highly stressed areas immediately ahead of the crack tip. Separation of grains ahead of the crack tip will lead to rupture of un-cracked crack tip ligaments, opening up an entire inter-granular crack front.

On resumption of fatigue cycling, the highly convoluted inter-granular crack front retards fatigue crack extension by attenuating crack driving force due to CFI. Supporting evidence comes by way of retarded growth by comparison to the point just before hold time. Further, as shown in Fig. 9b, growth rate at lower R is much lower than at higher R. The two bands were identical before hold time. It would appear that after hold time, growth rate dropped to near-threshold levels, where, residual stresses further retard growth rate at lower-R as a consequence of increased K_{th}. After sustained load cracking, a transient zone is observed where crack front recovers its original shape. At this point, growth rate in the two steps become even once again. This fractograph appears to

confirm that residual compressive stress will enhance K_{th} in environment. If the test were to be continued in vacuum after hold time in air, one may have also observed CFI retarded growth, but with *equal* bands under the two stress ratios.

Some Al-alloys contain a concentration of secondary particulates that represent slip barriers. When crack growth rate is of the same order as their size, which is usually a few microns, the particulates will tend to accumulate sufficient shear strain to cause quasi-static cleavage. The macro in Fig. 10a shows a typical highly pock-marked region of accelerated crack growth along a shear plane connecting multiple particulates. Fig. 10b is a zoomed-in view of a typical fatigue void formed by the coalescence of multiple interface cracks forming around a secondary particulate [30].

Fig. 10c highlights the mix of particulate voids (triangles) along with clusters of coalesced micro-voids associated with local ductile rupture. As shown in the figure, crack extension during large cycles is likely to be accelerated by the quasi-static component, while growth during the subsequent low amplitude cycles will be retarded, if not arrested due to substantial 3-D crack front disorientation. Rupture along a jagged plane connecting particulates creates the impression of increased void density. As observed elsewhere, this phenomenon will cause momentary crack acceleration during overloads, followed by substantial retardation under smaller cycles [17, 31, 32].
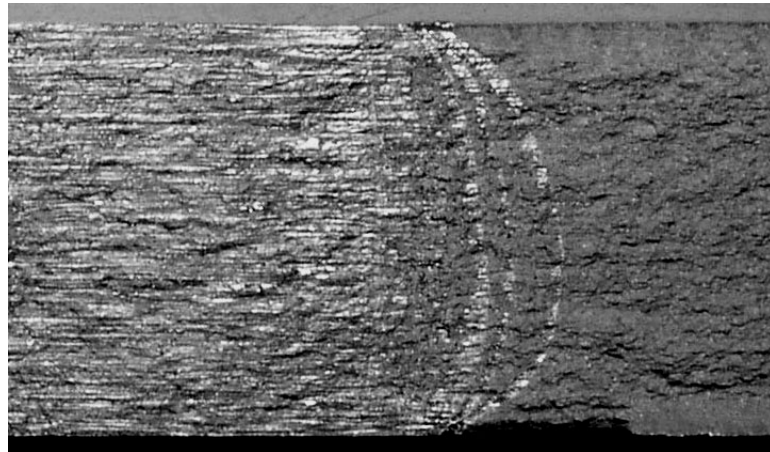

FIG. 11 – Appearance of fatigue fracture surface of 10 mm thick C(T) specimen cut from 7075-T1351. Specimen was subject to 50% periodic overloads every 2000 cycles of low amplitude baseline loading. Bright area including bands at right are fatigue under baseline loading. Note the sudden quasi-static pop-ins as overload K_{max} approaches K_{1c} under load control. Region at right is static fracture at last overload.

Finally, Fig. 11 shows a macroscopic manifestation of CFI under the influence of periodic overloads in a 10 mm thick high strength 7075 Al-alloy C(T) specimen. The crack front is marked by light shaded fatigue bands formed during baseline cycling. Up to a crack size marked by the arrows, the crack front remains straight. Beyond this point however, K_{max} due to the overload approaches K_{1c}. Crack extension in the overload cycle thus becomes sensitive to local fracture resistance. While the mid-thickness area is under plane strain, the surface region sees plane stress conditions, where K_c would be the operative fracture toughness. This promotes crack front tunneling (pop-in), with the mid-

thickness area tending to static fracture, while crack extension is marginal at the surface. Increased crack front curvature after each overload leads to stress intensity re-distribution across the crack front. The mid-thickness region gets unloaded, while the surface area is overloaded. Finally, at the point marked by the right most crack front signature, surface stress intensity has risen to a point that static fracture cannot be forestalled anymore. At the point of fracture, crack front tunneling is to an extent of 4 mm, which is almost half the specimen thickness. This sizeable deviation may be modeled as a function of the difference between K_{1c} and K_c.

The conditions depicted in Fig. 11 are in a sense, similar to those in Fig. 10. In both cases, the proximity of a critical parameter (shear deformation in Fig. 10, K_{1c} in Fig. 11) determined occurrence of CFI. However the latter case may also serve as a unique example of crack acceleration, even premature fracture. It is indeed possible that if the crack had grown all along under large cycles, the crack front may have tilted earlier on, thereby enforcing plane stress conditions and increased resistance to fracture.

The above list of CFI mechanisms is by no means complete, but it may provide a sampling of the different geometric combinations that need to be addressed to model variable amplitude fatigue in a manner that is microscopically consistent. Other materials systems, particularly engineered materials, may exhibit even more complex forms of crack front incompatibility.

Discussion

Fractographic evidence appears to suggest a certain synergistic model of multi-mechanism load interaction under variable amplitude loading. CFI attenuates crack tip stress field from what may apply to constant amplitude conditions. It can do so through blunting under overload or dwell-time, tunneling, out of plane rotation, branching and roughness. The exception to this rule (as shown in Fig. 11) is when CFI may actually accelerate fracture because of a "reverse CFI", i.e., slant mode under constant amplitude versus enforced flat mode in variable amplitude fatigue.

CFI also increases S_{op} by stalling crack opening, either through direct obstruction or at least friction between crack faces [22]. Plasticity induced closure levels do not appear to change significantly and remain a fraction of the applied maximum load, typically, 20 to 30%. Application of overload will therefore directly affect S_{op}, but only to this extent. However, CFI can raise S_{op}/S_{max} to as high as 60% or more, even in the absence of any tensile overload. The presence of debris on fatigue fractures, particularly associated with CFI appears to support this possibility.

Notch root residual stress directly affects crack closure, which is determined by local mean stress. Crack tip residual stress moderates environmental action to control the brittle fraction of crack extension in the rising load half-cycle. This component of the residual stress effect will be strong when K_{eff} is near-threshold and will reduce with increasing growth rate. The effect appears to be altogether absent in vacuum.

Fig. 12 describes a possible sequence of calculations that may be employed to predict variable amplitude fatigue crack growth. CFI must be assessed first because both crack tip stress response as well as closure appear to depend on it. This is followed by assessment of residual stress effect on crack closure and on K_{th}. Crack driving force K_{eff} is then computed, to lead to an estimation of fatigue crack extension:
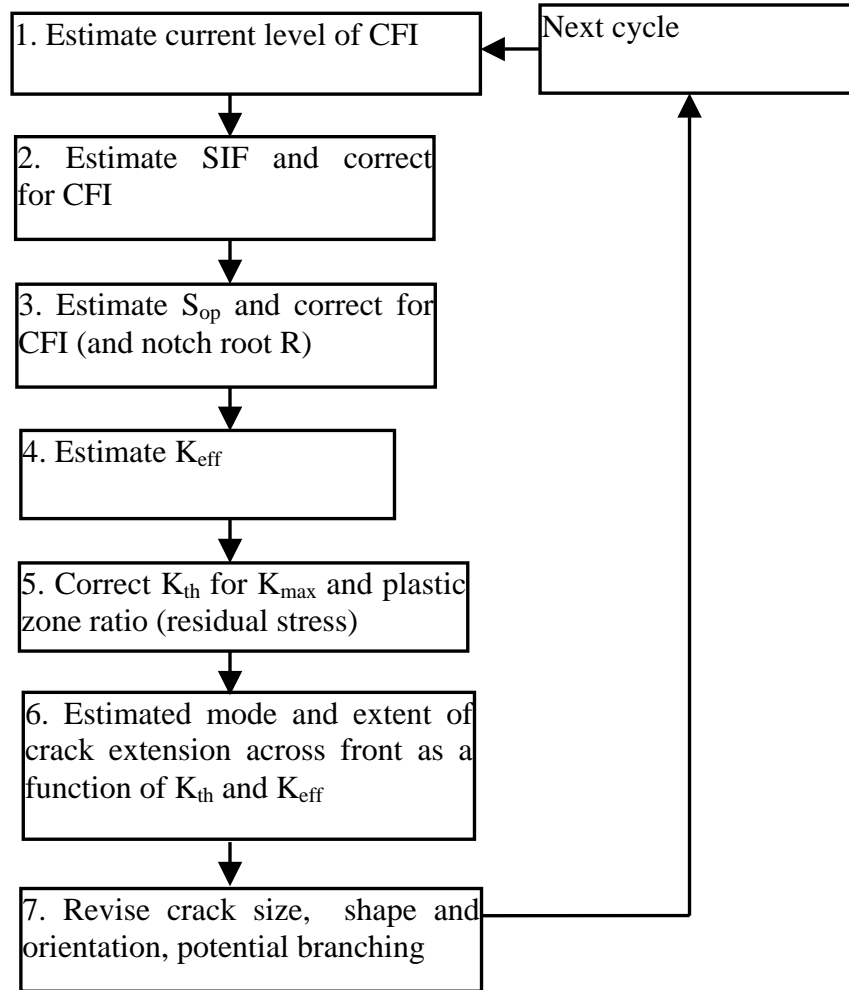
```
┌─────────────────────────────────┐        ┌──────────────────┐
│ 1. Estimate current level of CFI │◄───────│  Next cycle      │
└─────────────────────────────────┘        └──────────────────┘
             │                                        ▲
             ▼                                        │
┌─────────────────────────────────┐                  │
│ 2.  Estimate  SIF  and  correct  │                  │
│ for CFI                          │                  │
└─────────────────────────────────┘                  │
             │                                        │
             ▼                                        │
┌─────────────────────────────────┐                  │
│ 3. Estimate $S_{op}$ and correct for │              │
│ CFI (and notch root R)           │                  │
└─────────────────────────────────┘                  │
             │                                        │
             ▼                                        │
┌─────────────────────────────────┐                  │
│ 4. Estimate $K_{eff}$            │                  │
└─────────────────────────────────┘                  │
             │                                        │
             ▼                                        │
┌─────────────────────────────────┐                  │
│ 5. Correct $K_{th}$ for $K_{max}$ and plastic │     │
│ zone ratio (residual stress)     │                  │
└─────────────────────────────────┘                  │
             │                                        │
             ▼                                        │
┌─────────────────────────────────┐                  │
│ 6. Estimated mode and extent of  │                  │
│ crack extension across front as a│                  │
│ function of $K_{th}$ and $K_{eff}$ │                │
└─────────────────────────────────┘                  │
             │                                        │
             ▼                                        │
┌─────────────────────────────────┐                  │
│ 7. Revise crack size,  shape and ├──────────────────┘
│ orientation, potential branching │
└─────────────────────────────────┘
```

FIG. 12 – Flow-chart describing sequence of modeling synergy in variable amplitude fatigue. Of the three mechanisms CFI is accounted for first because it can also affect S_{op}. This is followed by S_{op}. Crack driving force is then estimated and corrected for current level of CFI and S_{op}. Finally, history dependent K_{th} is estimated as a function of load history, leading to crack extension over the current counted load cycle.

1. Assessment of CFI needs to provide two indexes, one related to attenuation of crack tip response to applied load, the other related to enhancement of closure. These determine how crack geometry differs from the one associated with constant amplitude conditions of the same magnitude as the current load cycle. Both indexes will be determined by the same parameters, but not necessarily in the same fashion. For example, blunting will attenuate crack tip response to applied stress. However, it will also tend to keep the crack open.
2. Correct SIF for CFI. This step estimates K-distribution across the crack front similar to the requirement for part-through and 3D crack geometries. Such an approach will assist in modeling tunneling, branching and out-of-plane rotation, which in turn will affect SIF as well as S_{op}.

3.   Estimate S_{op} distribution across the crack front. S_{op} will be sensitive to local residual stress distribution as well as CFI as discussed under item 1. It is known that mid-thickness Sop is lower than at surface and this in turn can affect crack front shape. Also, CFI due to near-surface plane rotation or branching will induce increased S_{op}. Conversely, blunting and underloads will both reduce S_{op}.

4.   Estimate crack driving force K_{eff} across the crack front as the difference between local K_{max} and K_{op}.

5.   Estimate K_{th} distribution across the crack front as a function of residual stress distribution and local triaxiality. These will determine environmental action and may be ignored for vacuum conditions, where K_{th} may be treated as a material constant.

6.   Compute crack extension across the crack front. Suitable da/dN equation may be used, that accounts for K_{eff}, K_{th}, K_{max} and appropriate value of K_c, which in turn, will depend on plane strain / plane stress conditions.

7.   Update crack front geometry, CFI and residual stress indexes for the next iteration. This is the step where the incidence of crack branching will be established, and so also, the point where one may ignore branching and perhaps associated probabilistic aspects. For example, the probability of branching would be remote if all the load cycles thus far, caused crack growth in the near-threshold range, This is also the step, where transients are tracked. For example, in the event of a crack emanating from a notch, closure levels will be high if tensile overloads caused notch root compressive residual stresses in the unloaded condition. However, as shown earlier, at some distance from the notch surface, the crack tip will no longer see these effects and is likely to behave as a long crack.

Potential flaws in our interpretation of multi-mechanism synergy include the following:

1.   All observations are based on fractographic inputs. However, only a small fraction of a fatigue fracture surface carries discernible marker bands that permit quantitative measurements. Inherent in our approach is the assumption that what is depicted by visible marker bands is a fair representation of overall fatigue crack kinetics. Such an assumption would be questionable in the event quasi-static crack extension and other modes not associated with a marking process control fatigue kinetics.

2.   Our observations do indicate noticeable CFI-related variation in S_{op}. However, we have been unable to obtain quantitative data on how growth rate itself is affected by CFI. This may be a potentially rewarding goal for future work including micro-mechanical modeling as demonstrated in recent work [33]. In the meantime, available expressions for CFI - attenuated crack driving force and increased closure may be assumed to apply [21, 22].

Conclusions

1.Fractographic evidence indicates crack closure, residual stress and crack front incompatibility (CFI) *together* cause load interaction in variable amplitude fatigue.

2.Near threshold crack closure does not appear to exceed 30% of maximum applied stress at low stress ratio. However, it can rise to as high as 60% under two conditions. One is reduced local stress ratio in notch root fatigue due to compressive residual stress and the other is considerable conflict in local crack plane orientation causing obstruction to opening.

3.Residual stress appears to have two operative mechanisms. One is change of local stress ratio and through it, closure, as pointed out above. The other is moderation of environmental action and associated change in threshold stress intensity. Comparative tests in air and vacuum on two different materials support this conclusion.

4.CFI appears to be a major load interaction mechanism that mainly causes retardation. It is manifest in many ways including crack tip blunting, crack front shape change, enforced mixed mode conditions, crack deflection, crack branching and increased closure due to one or more of these. It occurs due to mismatch in crack extension plane between successive cycles.

5.A sequential scheme is proposed for modeling multi-mechanism synergy under variable amplitude loading.

References

1.	Schijve, J., Observations on the Prediction of Fatigue Crack Growth Propagation under Variable Amplitude Loading, *ASTM STP 595,* American Society for Testing and Materials, Philadelphia, 1976, pp. 3-23.

2.	Elber, W., The Significance of Fatigue Crack Closure, *Damage Tolerance in Aircraft Structures, ASTM STP 486,* American Society for Testing and Materials, Philadelphia, 1971, pp. 230-242.

3.	Wheeler, O.E., Journal of Basic Engineering, Trans. ASME, March 1972, pp. 181-186.

4.	Willenborg, J.D., Engle, R.M., and Wood, H.A., A Crack Growth Retardation Model Using an Effective Stress Concept, *AFFDL-TM-FBR-71-1*, Air Force Flight Dynamics Laboratory, 1971.

5.	Schijve, J., Fatigue damage accumulation and incompatible crack front orientation, *Eng. Fract. Mech.,* Vol. 6 (1974) pp. 245-252.

6.	Baudin, G., and Robert, M., Crack growth life prediction under aeronautical type of loading, *Proc. 5th European Conf. On Fracture*, Lisbon (1984) pp. 779-792.

7.	de Koning, A.U., A simple crack closure model for prediction of fratigue crack growth rates under variable amplitude loading. *Fracture Mechanics (Roberts, R., Ed), ASTM STP 743*, (1981) pp. 63-85.

8. Aliaga, D., Davy, A., and Schaff, H., A simple crack closure model for predicting fatigue crack growth under flight simulation loading, *Durability and Damage Tolerance in Aircraft Design,* (A. Salvetti and G. Cavallini, Eds.), EMAS, Warley (1985) pp. 605-630.

9. Newman, J.C., A crack-closure model for predicting fatigue crack growth under aircraft spectrum loading, Methods and Models for Predicting Fatigue Crack Growth under Random Loading, (Chang, J.B., and Hudson, C.M., Eds.), ASTM STP 748 (1981) pp. 53-84.

10. Newman, Jr, J.C., Phillips, E.P., Everett, R.A., fatigue life and crack growth prediction methodology*, An Assessment of Fatigue Damage and Crack Growth Prediction Techniques, AGARD Report 797*, AGARD, Neuillu sur Seine, 1994, Paper 2.

11. Lang, M., A Model for Fatigue Crack Growth, Part I: Phenomenology, *Fatigue Fract. Engg. Mater, Struct.*, Vol. 23, No. 7, pp. 587-601, 2000.

12. Lang, M, and Marci, G., The Influence of Single and Multiple Overloads on Fatigue Crack Propagation*, Fatigue Fract. Engg. Mater, Struct.,* Vol. 22, No. 4, pp. 257-271, 1999.

13. Vasudevan, A.K., Sadananda, K., and Loust, N., A Review of Crack Closure, Fatigue Crack Threshold and Related Phenomena, *Materials Science and Engineering,* A188 (1994), pp. 1-22.

14. Hopkins, S.W., Rau, C.A., Leverant, G.R., and Yuen, A., Effect of various programmed overloads on the threshold for high-frequency fatigue crack growth, *Fatigue Crack Growth Under Spectrum Loads, ASTM STP 595*, American Society for Testing and Materials, 1976, pp. 125-141.

15. Sunder, R., and Dash, P,K, *Measurement of Fatigue Crack Closure Through Electron Fractography,* Int. J. Fatigue, Vol 4, 1982, pp. 97-105.

16. Ashbaugh, N.E., Porter, W.J., Prakash. R.V., and Sunder, R., A Fractographic Study of Load Sequence Induced Mixed-Mode Fatigue Crack Growth in an Al-Cu Alloy, *Mixed-Mode Crack Behavior, ASTM STP 1359*, K.J. Miller and D.L. McDowell, Eds., American Society for Testing and Materials, West Conshohocken, PA, 1999, pp. 258-278.

17. Sunder, R., Porter, W.J., and Ashbaugh, N.E., The role of air in fatigue load interaction, Fatigue *Fract. Engng Mater Struct* Vol 26, 2003, pp. 1-16,.

18. Sunder, R., An explanation for the residual stress effect in metal fatigue, *Fatigue 2002 – Proc. 8th International Fatigue Congress*, Stockholm, 2002, EMAS, pp. 3339-3350.

19. Ashbaugh, N.E., Porter, W.J., Rosenberger, A.H., and Sunder, R., Environment - Related Load History Effects in Elevated Temperature Fatigue of a Nickel-Base Super-alloy*, Proc., Fatigue 2002*, Stockholm, June 2-7, 2002.

20. Ashbaugh, N.E., Dattaguru, B., Khobaib, M., Nicholas, T., Prakash, R.V., Ramamurthy, T.S., Seshadri, B.R., and Sunder, R., Experimental and Analytical Estimates of Fatigue Crack Closure in an Aluminum-Copper Alloy. Part I: Laser Interferometry and Electron Fractography, *Fatigue Fract. Engg. Mater. Struct,* Vol. 20, No. 7, 1997, pp.951-961.

21. Ritchie, R.O., Mechanisms of fatigue crack propagation in metals, ceramics and composites: Role of shielding, *Materials Science and Engineering*, Vol. A103, 1988, pp. 15-28.

22   Suresh, S., Models for fatigue crack deflection, *Fatigue '84,* C.J. Beevers, Ed., Vol 1, EMAS, 1984, pp. 555-563.

23.   Sunder, R., Prakash, R.V., and Mitchenko, E.I., Fractographic Study of Notch Fatigue Crack Closure and Growth Rates, *ASTM STP 1203*, J.E. Masters and L.E. Gilbertson, Eds., American Society for Testing and Materials, West Conshohocken, PA, 1993, pp. 113-131.

24.   Sunder, R., Notch root crack closure under cyclic inelasticity, *Fatigue Fract. Engng. Mater. Struct.,* Vol. 16, pp. 677-692.

25.   Morrow, J.D., Wetzel, R.M., and Topper, T.H., Laboratory Simulation of Structural Fatigue Behavior, *Effects of Environment and Complex Load History on Fatigue Life, ASTM STP 462*, American Society for Testing and Materials, Philadelphia, 1970, pp. 74-91.

26.   Anandan, K. and Sunder, R., Closure of part-through cracks at the notch root*, Int. J. Fatigue,* Vol. 9, pp. 217-222.

27.   Vogelesang, L.B., and Schijve, J., Environmental Effects on Fatigue Failure Mode Transition Observed in Aluminium Alloys, Delft University of Technology, *Report LR-289*, Delft, Netherlands, 1979.

28.   Schijve, J., and Arkema, W.J., Crack Closure and the Environmental Effect on Fatigue Crack Growth, Delft University of Technology Fac. Aerospace Eng. *Report VTH-217*, Delft, 1976.

29.   Sunder, R., Fatigue crack growth as a consequence of environment-enhanced brittle-micro fracture, *Fatigue Fract. Engng. Mater. Struct*., Accepted for publication, 2003

30.   Sunder, R., Porter, W.J., and Ashbaugh, N.E., Fatigue voids and their significance, *Fatigue Fract. Engng Mater Struct Vol* 25, 2002, pp. 1015-1024.

31.   Sanders T.H., Jr., and Staley, J.T., Review of Fatigue and Fracture Research on High-Strength Al-Alloys, *Fatigue and Microstructure*, American Society for Metals, Metals Park, OH, 1978, pp. 467-516

32.   Staley, J.T., How Microstructure Affects Fatigue and Fracture of Aluminum Alloys, Presented at the International Symposium on Fracture Mechanics, George Washington University School of Engineering and Applied Science, Washington, D.C., Sep. 11-13, 1978.

33.   Bennett, V., and McDowell, D.L., Polycrystal Orientation Effects on Microslip and Mixed-Mode Behavior of Microstructurally Small Cracks, *ASTM STP 1359,* K.J. Miller and D.L. McDowell, Eds., American Society for Testing and Materials, West Conshohocken, PA, 1999, 203-228.

This page intentionally left blank

A MISSION-ELEMENT APPROACH FOR CRACK GROWTH UNDER TURBINE ENGINE SPECTRA

James M. Larsen[*], Andrew H. Rosenberger[*], and George A. Hartman[†]

The U.S. Air Force is embarking on a technology development initiative to extend the useful lifetime of major, fracture-critical components in currently fielded gas turbine engines. A key element of this program is the development of improved methods for prediction of fatigue crack growth. Current approaches for life management of engine components tend to ignore potential benefits in crack propagation lifetime that may occur as the result of load interaction phenomena that under variable amplitude spectrum loading. The objective of the current project was to assess the role of load-interaction effects in an advanced Ni-base superalloy when subjected to loading events representative of turbine engine usage.

INTRODUCTION

Current deployment plans by the U.S. Air Force dictate that most aircraft be used well beyond their original design lifetimes [1-3]. This situation motivates the continual improvement of life-management and life-extension methods and technologies for both aging airframes and their propulsion systems. To address the issue of aging engines, the U.S. Air Force is embarking on a technology development and implementation initiative, known as the Engine Rotor Life Extension (ERLE) program [4], which is organized to reduce the cost of sustainment of its current fleet of advanced turbine engines. The ERLE program, which is part the larger Versatile Affordable Advanced Turbine Engine (VAATE) program [5] and its National Turbine Engine Durability initiative, has the goal of extending the useful lifetime of major, fracture-critical components in currently fielded gas turbine engines, while maintaining or improving overall engine safety and reliability. Full achievement of the ERLE objectives will require improvements in a broad range of technologies, including nondestructive evaluation, engine usage and health monitoring, life prediction and fracture mechanics, data fusion, and component repair. The current paper highlights effects of engine operating spectra on fatigue crack growth.

[*] Air Force Research Laboratory, Materials and Manufacturing Directorate, AFRL/MLLMN
2230 Tenth Street, Ste 1, Wright-Patterson Air Force Base, Ohio 45433-7817, U.S.A.

[†] University of Dayton Research Institute, Structural Integrity Division
300 College Park, Dayton, Ohio 45469-0128, U.S.A.

TURBINE ENGINE MISSION LOADING

It is well known that loading spectra of major rotating components in engines typically exhibit less variability than spectra experienced by aircraft structures [6-9]. The major cycles in engine mission spectra for rotating components result from variations in engine speed produced by throttle excursions for take-off, in-flight maneuvers, and landing. For components exposed to elevated temperatures, there is additional stress imposed by thermal gradients and thermal transients produced by variations is operating conditions and heat transfer within the engine. The maximum loading tends to occur at takeoff, although additional, but infrequent, full-power excursions may also reach this maximum level. Hold periods of constant stress occur at relatively moderate stresses, which occur during cruise or transit portions of the mission. Major rotating components, such as advanced disks and spacers, are typically designed such that their maximum stresses at full power are only marginally below the component burst stress at the operating temperature.

Engine-component design practices, combined with the relatively controlled nature of the mission spectra, tend to avoid the large effects of load sequence, or load interaction, on crack growth that are often common in fatigue spectra of airframe structures. Depending on the nature of the load sequence, such load interaction effects can produce either crack acceleration [10] or crack retardation, although the latter is far more common. Crack retardation tends to occur in fatigue cycles that follow an overload, and this effect can be extremely significant, particularly as the overload ratio (OLR) increases. Here we define the OLR to be σ_{max} of the overload divided by σ_{max} of the subsequent cycles. Airframe spectra may contain cycles with OLRs well in excess of 2 or 3, while experience with engine spectra has suggested that a limiting OLR of 1.25 is relatively common. Such conclusions were drawn by a NATO AGARD task group established in the early 1980s to develop a loading standard for fighter aircraft engine disk usage [11]. This task group developed TURBISTAN, a test spectrum applicable for titanium alloys operating at or near ambient temperature.

Loading Spectra for High-Temperature Major Rotating Components

Data on engine usage profiles are continually collected and used to update the life analyses. Recent analyses of such data for a high temperature nickel-base-superalloy disk revealed that, when compared with cooler Ti-alloy engine components, the fatigue cycles in the Ni-alloy components exhibit a larger relative amplitude in stress, and a significant compression cycle occurs when the engine is powered down and cools slowly to ambient temperature [9]. These components may also experience an appreciable out-of-phase stress-temperature relationship for many fatigue cycles. The majority of the maximum loads in cycles with high values of maximum load were centered on a value of approximately 0.7 times the maximum mission load. In terms of overload ratio, this corresponds to values of OLR approximately centered about a

value of 1.4, with a substantial number of cycles above this level, suggesting a possibly significant beneficial effect of load sequencing. In general, the spectrums reviewed did not exhibit significant periods of sustained loading, and the limited sustained loading that was observed occurred at relatively moderate loads.

LOAD SEQUENCE EFFECTS IN IN100 AT ELEVATED TEMPERATURE

The powder metallurgy, nickel-base alloy IN100 was chosen as a representative material for assessment of the role of turbine-engine load-sequence effects on crack growth. This material was selected for several reasons: (1) it is in widespread use in advanced engines, (2) a substantial database for this alloy was available, and (3) it is representative of other high performance, powder-metallurgy, nickel-base alloys used throughout the turbine engine industry. The specific IN100 chosen for the current experiments was superplastically forged and heat treated by Pratt & Whitney to produce a fine uniform microstructure of primary gamma-prime grains in gamma-gamma prime matrix [6,9].

An earlier U.S. Air Force contract report by Pratt & Whitney served as a key reference for background information on the material [**Error! Bookmark not defined.**]. This report demonstrated that the main parameters controlling high-temperature fatigue crack growth in this alloy were temperature, frequency, and stress ratio. For most experiments, however, the range in ΔK over which the tests were performed was limited by the relatively low fatigue frequencies used and the resulting long test times. Key conclusions from the report include assessments of the roles of the various testing parameters. For example, at a frequency of 0.167 Hz, crack growth rates at a given ΔK increased by a factor of 3 to 4 as temperature increased from 538 to 732 °C. Similarly, in tests at a temperature of 649 °C and frequencies ranging from 0.00833 to 20 Hz, growth rates decreased by a factor of approximately 5 to 7 as frequency increased. Tests performed at 649 °C, a frequency of 0.167 Hz, and stress ratios ranging from 0.1 to 0.8 resulted in an increase in crack growth rate by a factor of approximately 3 with increasing R.

When considering effects of variable-amplitude loading, it is convenient to define loading parameters in terms of the stress ratio of the baseline fatigue cycle, the overload ratio (OLR), and the number of baseline cycles between overloads (CBO). These parameters are depicted schematically in Fig. 1, which shows blocks of constant-load-amplitude fatigue interrupted by periodic overloads. By testing under repeated blocks of such cycles, one can quantify the effects of load interactions that simulate the key elements comprising a typical engine mission. Figure 2 shows the effects of applying one cycle at an OLR of 1.25 and 1.5, followed by 40 cycles of baseline fatigue loading at an R of 0.5. As shown, increasing from no overload (OLR = 1.0) to a relatively modest overload (OLR = 1.5) results in a reduction in the crack growth rate of approximately a factor of 4 due to the action of the overload. This effect is further revealed in Fig. 3, which shows the effect of increasing the number of CBO from 5 to

40 with an OLR of 1.5. As shown, this increase in the number of CBO produced a reduction in crack growth rate by a factor of 5 or more, indicating that the influence of this parameter on crack growth rate is of the order of those due to variations in temperature, frequency, and stress ratio.

Improved Experimental Methods for K-controlled Crack Growth

To extend the understanding of load-sequence effects in IN100, a focused study of crack growth rates was conducted under repeated mission-element cycle blocks of the type shown in Fig. 1. In this study, spectra were applied under constant-K-controlled conditions, rather than the constant-load-controlled conditions. This specialized testing method incorporated a greatly improved direct-current potential-difference technique for measurement of crack length, having an effective crack length resolution of approximately 5 µm. The stability of this technique resulted in substantial improvements in both the accuracy and precision of calculations of da/dN, and the time required to perform key experiments was greatly reduced as a result of the improvements in crack-length sensitivity. Tests were performed on C(T) specimens using repetitive fatigue blocks composed of a single overload followed by a block of constant-ΔK cycles. In each case the crack was extended until it became clear that a macroscopic steady state crack growth rate had been achieved, which was indicated by a linear crack-length vs. cycles (a vs. N) response. In this manner any transient behavior due to changes in the type of spectrum being applied was clearly identified and excluded from the valid data.

These tests were performed under a variety of loading conditions, which are exemplified by the data presented in Fig. 4. This graph plots crack growth rate as a function of the number of CBO for OLRs of 1.125, 1.25, 1.375, and 1.5. The tests were performed in air at 649 °C, a frequency of 0.167 Hz, R = 0.5, and K_{max} of the baseline cycles = 20 MPa√m. The horizontal line represents the crack growth rate observed under the baseline constant-K-amplitude condition. When CBO is zero, the crack growth rate corresponds to constant amplitude cycling under the overload condition. As CBO is increased, the resulting average crack growth rate soon drops below the baseline rate. At a CBO of 40, the growth rates for the higher OLR experiments fell almost an order of magnitude below the baseline behavior. As may be seen, the crack growth rate behavior curves for the various OLRs cross as CBO increases. As would be expected, the higher OLRs produce initially higher growth rates, but the benefits of the larger overloads are greater as CBO increases. As a result, the four OLRs ranging from 1.125 to 1.5 have a similar influence when CBO is approximately 12; at this point the reduction in crack growth rate is approximately a factor of 3 below the baseline. This finding is significant, because it shows that substantial reductions in da/dN can be produced by very mild overloads. Similar results for baseline fatigue with K_{max} = 30 MPa√m are presented in Fig. 5. For this K_{max} level, the benefits of the overload are somewhat less than for the K_{max} = 20 case.

For the data of both Figs. 4 and 5, the growth rate for OLR = 1.375 is below that of OLR = 1.5 until CBO reaches 40. Other experiments, not shown here, revealed that these data cross at this point, and the OLR = 1.5 condition produced the lowest growth rate for CBO > 40. In addition, it was found that the greatest reduction in crack growth rate occurred in the approximate range of 1.0 < OLR < 1.3 [9].

To further reveal the behavior of the observed load-interaction effect, the procedure depicted in Fig. 6 was performed, wherein the results for a given OLR were used to deduce the instantaneous crack growth rate following an overload. Under this procedure, the local crack growth rate following an overload is deduced by subtracting effects of successive cycle blocks. For example, subtracting the crack growth during a 20-CBO block from the growth observed during a 40-CBO block gives the apparent average growth rate contribution from cycles 21 through 40, which eliminated the apparent effect of the initial portion of the block, including the overload.   By performing this procedure on successively smaller blocks, the data shown in Figs. 7 and 8 were obtained. In general, these data indicate that the local crack growth rate following an overload is reduced almost immediately, and that continued crack growth retardation is nearly constant until the subsequent overload interrupts and restarts the process. In many cases the reduction in growth rate exceeded an order in magnitude. For the K_{max} = 20, Fig. 7, the larger OLRs resulted in growth rates near, or equal to, zero (crack arrest) under the baseline cycling.

SUMMARY AND CONCLUSIONS

To address the growing financial and logistical costs of sustainment of turbine engines, the U. S. Air Force is investing in a range of science and technology initiatives to improve and extend capabilities for component life management. One avenue for improvement in life management methods lies in the improvement in methods for prediction of load sequence events under representative mission spectra.

The potential magnitudes of the effects of key turbine-engine mission usage variables were assessed using data from the superalloy IN100 from the literature, plus experiments using a constant-K-controlled capability. This method, which employed a greatly improved direct current potential difference technique for measurement of crack length, provided a unique capability to perform highly specialized load-sequence experiments quickly. It was shown that the role of mission load sequence events can produce variations in crack growth rate that are as significant as those produced by the primary variables of temperature, frequency, and stress ratio. In tests of simplified mission elements containing relatively modest overloads, reductions of crack growth rate of a factor of four were observed, and the greatest sensitivity in crack-retardation occurred over the interval of overload ratios from 1.05 to 1.3.   These findings indicate that a potentially significant beneficial effect of load sequences may be expected under typical mission loading.
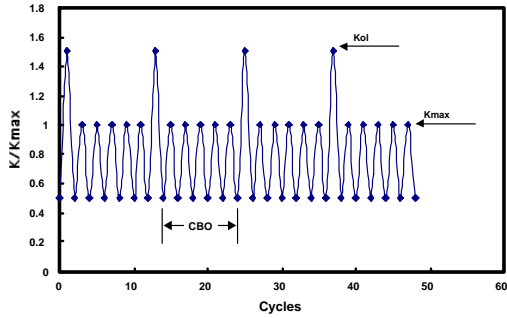
Figure 1. Simplified mission containing repeated overloads and a fixed number of cycles between overloads (CBO).
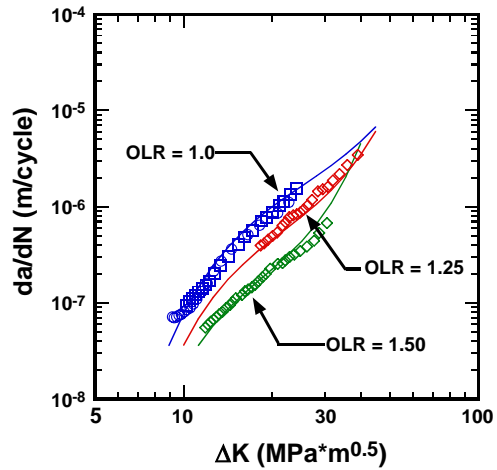
Figure 2. Effect of overload ratio (OLR) on crack growth; T = 649°C; R = 0.5, Freq. = 0.167 Hz, CBO = 40.
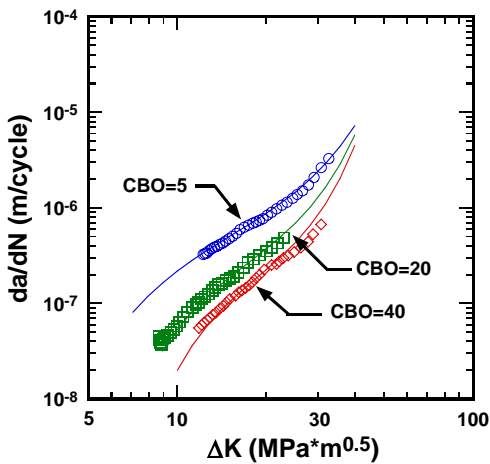
Figure 3. Effect of number of cycles between overloads (CBO) on crack growth; T = 649°C; R = 0.5, Freq. = 0.167 Hz, OLR = 1.5.
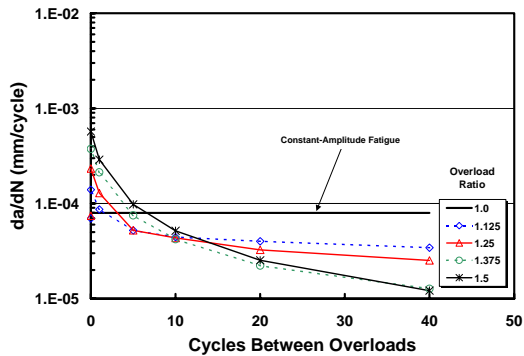
Figure 4. Crack growth behavior plotted as a function of the number of cycles between overloads (CBO) for K-controlled block loading illustrated in Fig. 1. T=649°C, Frequency = 0.167 Hz, R = 0.5, K_{max} = 20 MPa*m$^{0.5}$.
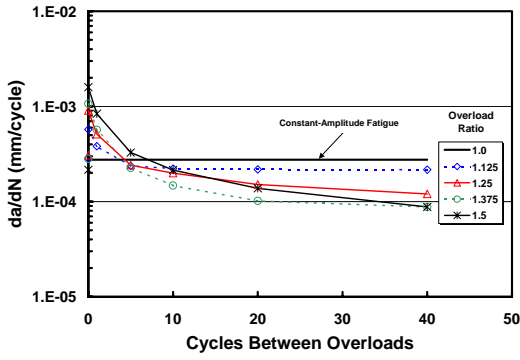
Figure 5. Crack growth behavior plotted as a function of the number of cycles between overloads (CBO) for K-controlled block loading illustrated in Fig. 1. T=649°C, Frequency = 0.167 Hz, R = 0.5, K_{max} = 30 MPa*m$^{0.5}$.
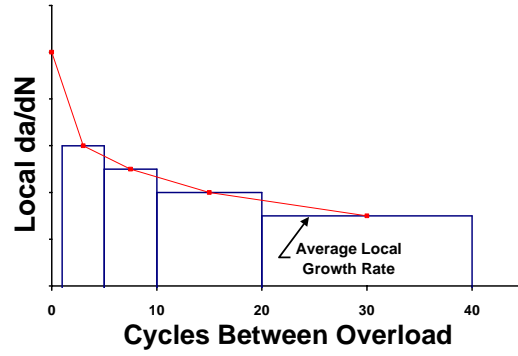
Figure 6. Schematic of the average local crack growth rate in the baseline cycling following an overload block.
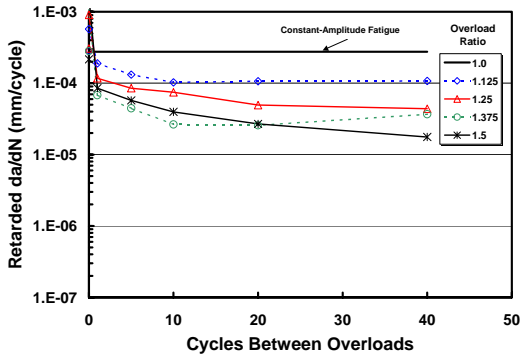
Figure 7. Local crack growth during the cycles following an overload block; plotted as a function of the average number of cycles between overload following the scheme in Fig. 6. T=649°C, Frequency = 0.167 Hz, R = 0.5, K_{max} = 20 MPa*m$^{0.5}$.
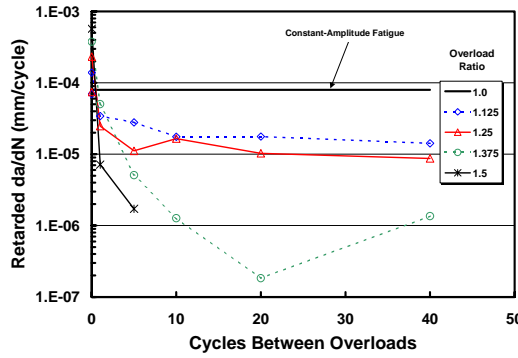
Figure 8. Local crack growth during the cycles following an overload block; plotted as a function of the average number of cycles between overload following the scheme in Fig. 6. T=649°C, Frequency = 0.167 Hz, R = 0.5, K_{max} = 30 MPa*m$^{0.5}$.

REFERENCES

1. SAB (Scientific Advisory Board), Report of the Ad Hoc Committee on Life Extension and Mission Enhancement for Air Force Aircraft, U.S Air Force Scientific Advisory Board, Washington, D. C., Department of the Air Force, Report TR-94-01, 1994.
2. NMAB (National Materials Advisory Board), Aging of U.S. Air Force Aircraft, National Research Council, National Academy Press, Washington, D.C., Publication NMAB-488-2, 1997.
3. Hadcock, R. N., "Aging Airframe Structural Life Enhancement: An Overview," presented at The First Joint DOD/FAA/NASA Conference on Aging Aircraft, Ogden, Utah, July, 1997.
4. Larsen, J. M., Rasmussen, B., Russ, S. M., Sanbongi, B., Morgan, J., Jira, J. R., Blodgett, M. P., Moran, T. J., Johnson, D. A., LeClair, S., Shaw, D., Stange W. A., Meininger, M., and Fecke, T. G., "The Engine Rotor Life Extension (ERLE) Initiative and Its Contributions to Increased Life and Reduced Maintenance Cost", Proceedings of the 6th National Turbine Engine High Cycle Fatigue (HCF) Conference, Jacksonville, FL, 5-8 March 2001.
5. Stricker, J., "Advanced Turbine Engines – A Strategic Vision", presented at the World Aviation Conference, San Diego CA, Nov., 1999.
6. J. M. Larsen, B. J. Schwartz, and C. G. Annis, Jr., "Cumulative Damage Fracture Mechanics Under Engine Spectra," Air Force Materials Laboratory Report AFML-TR-79-4159, Wright-Patterson AFB, OH, 1979.
7. Larsen, J. M. and Nicholas, T., "Cumulative Damage Modeling of Fatigue Crack Growth," AGARD Conference Proceedings No. 368, Engine Cyclic Durability by Analysis and Testing, Advisory Group for Aerospace Research and Development, Neuilly sur Seine, France, 1984, pp. 9-1 – 9-15.
8. Larsen, J. M. and Nicholas, T., Engineering Fracture Mechanics, Vol. 22, No. 4, 1985, pp. 713-730.
9. Larsen, J. M., Rosenberger, A. H., Hartman, G. A., Russ, S. M., and John, R., "The Role of Spectrum Loading in Damage-Tolerance Life Management of Fracture Critical Turbine Engine Components," in press, proceedings of the Symposium on Aging Mechanisms and Control - Monitoring and Management of Gas Turbine Fleets for Extended Life and Reduced Costs, NATO Research and Technology Organization, Manchester, U.K., 8-11 Oct. 2001.
10. Russ, S. M., Rosenberger, A. H., Larsen, J. M., and Johnson, W. S., "Fatigue Crack Growth Predictions for Simplified Spectrum Loading: Influence of Major Cycles on Minor-Cycle Damage Rates," same as Ref 9.
11 Mom, A. J. A, Evans, W. J., and ten Have, A. A., "TURBISTAN, a Standard Load Sequence for Aircraft Engine Discs," AGARD Conference Proceedings No. 393, Damage Tolerant Concepts for Critical Engine Components, Advisory Group for Aerospace Research and Development, Neuilly sur Seine, France, 1985, pp. 20-1-20-11.

Sushant K. Jha[2], James M. Larsen[1], Andrew H. Rosenberger[1] and George A. Hartman[3]

Mechanism-Based Variability in Fatigue Life of Ti-6Al-2Sn-4Zr-6Mo

---

Abstract: The variability in fatigue life of a Ti-6Al-2Sn-4Zr-6Mo alloy was studied. The cumulative life distribution plot was found to be composed of two distinct failure mechanisms, designated as Type-I and Type-II. The likelihood of Type-I vs. Type-II failure shifted with respect to the stress level, such that at lower stress levels there was increased probability of Type-II failure. It was also found that the variability in life was introduced primarily at the crack nucleation stage, specifically, formation of a stage-I crack across an equiaxed primary-α particle.

Keywords: microstructure, fatigue life variability, crack nucleation, crack growth, probability of failure, deformation, slip transfer

Introduction

One approach in life assessment of fracture-critical turbine engine components is based on life for "initiation" of a crack in one out of 1000 components. Thus many components with considerable residual life may be prematurely discarded. Conventionally, this type of approach is not physically based and involves empirical extrapolation of data. Since the stochastic nature of fatigue is often accounted for by varying parameters in the empirical models, the role of microstructure in life variability has not been widely addressed, and the source of variability remains unclear. However, the trend in the aircraft industry towards extending lives of in-service components beyond their initial design life [1,2] demands a more accurate assessment of life and its variability.

The present research is directed at understanding the role of microstructure in the variability in the fatigue life of Ti-6Al-2Sn-4Zr-6Mo (Ti-6-2-4-6), a high-strength $\alpha+\beta$ titanium alloy. It is demonstrated that a significant potential for life extension exists through a mechanism-based evaluation of the cumulative life distribution. It is also shown that the variability in life of Ti-6-2-4-6 is controlled primarily by the crack nucleation stage, specifically, formation of a stage-I crack across an equiaxed primary-α particle.

---

[1]Air Force Research Laboratory, Materials and Manufacturing Directorate, AFRL/MLLMN, Wright-Patterson AFB, Dayton, OH 45433.
[2]Systran Federal Corporation, 4027 Col. Glenn HWY, Suite 210, Dayton, OH 45431.
[3]The University of Dayton Research Institute, 300 College Park, Dayton, OH 45469.
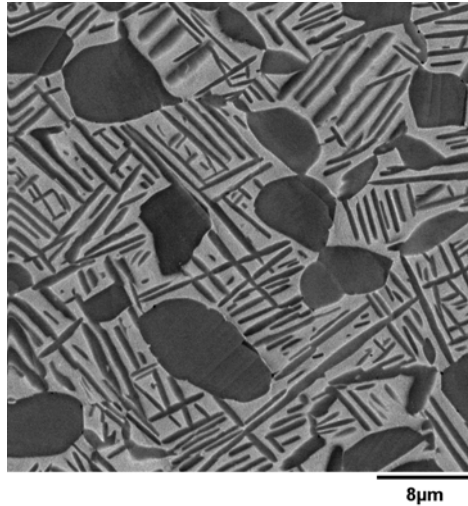
Figure 1 – *Microstructure of the Ti-6-2-4-6 alloy*

Material and Experimental Procedure

The microstructure of the Ti-6-2-4-6 alloy used in this study is presented in Fig. 1. As shown in the figure, the microstructure had a duplex nature and consisted of equiaxed primary-α particles and α platelets in a transformed β matrix. Testing was performed on round-bar stress-life (S-N) fatigue specimens with a uniform gage section of length 12 mm and diameter of 4 mm. All fatigue specimens were machined from the same parent disk, which exhibited a highly uniform microstructure. The specimens were low stress ground and then electropolished to minimize any surface residual stress as well as to produce uniform surface condition. The S-N type fatigue tests were conducted using an MTS 810 servohydraulic test system equipped with a 458 controller. The tests were performed in tension-tension fatigue at room temperature and a lab-air environment. A frequency of 20 Hz and a stress ratio of 0.05 were used. At selected stress levels, an Infrared Damage Detection System (IDDS) was used to detect nucleation of cracking. Fractography and EDS analysis were performed using a Cambridge S360FE scanning electron microscope.

Results and Discussion

Variability in Total Life

The fatigue life behavior of the Ti-6-2-4-6 alloy is shown in Fig. 2(a). Only the mean lives are plotted in this figure. Multiple tests were conducted at selected stress levels as indicated by numbers in parentheses (Fig. 2(a)). The variability in life is shown in Fig. 2(b). As shown in the figure, decreasing stress level, σ_{max}, produced an increase in average fatigue life, but this was accompanied by a substantial increase in the variability in fatigue life. While most failures occurred by surface crack nucleation, one sample at the σ_{max} of 860 MPa and few samples at the σ_{max} of 820 MPa failed by subsurface nucleation. However, as shown in Fig. 2(b), the lives of surface and subsurface failures

overlapped each other, indicating that the variability in life is not correlated with surface vs. subsurface crack nucleation in this case.

The cumulative probability of failure with respect to cycles at the σ_{max} levels of 1040, 925, 900, 860 and 820 MPa are shown in Fig. 3. The log-normal distribution function was used. The data are plotted in log-normal probability space, which is based on linearization of the cumulative distribution function (CDF). Slopes of the fitted lines indicate that the scale of variability increased as stress level decreased. This type of behavior with decreasing stress level has been reported in other materials [3,4]. However there are also studies where the scale of variability did not change significantly with stress level [5,6,7]. It seems that, whenever total life is largely comprised of crack growth, for example, in the case of aluminum alloys containing constituent particles [5], the scale of variability stays similar with respect to stress level. It is interesting to note in Fig. 3 that an arbitrary extrapolation of data to a probability of failure of 0.1% (1 in 1000) leads to a lower predicted life at lower stress level.
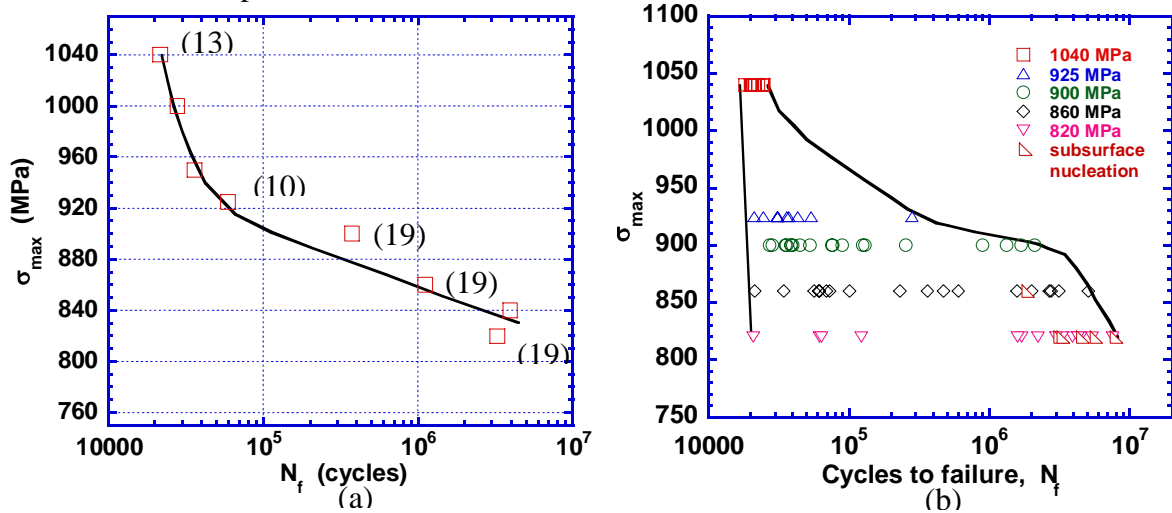
Figure 2 – *Fatigue life behavior of Ti-6-2-4-6: (a) Mean lives, and (b) Life variability*
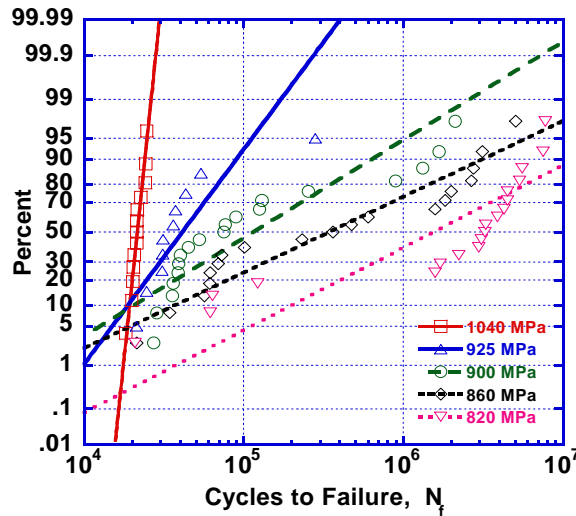
Figure 3 – *Probability of failure plots at selected stress levels*

Dual Failure Mechanisms?

A comparison between the probability of failure plots, or the cumulative distribution functions (CDF), at a high and a low stress level (σ_{max} = 1040 and 820 MPa respectively) is presented in Fig. 4(a). At the higher stress level (1040 MPa), experimental data points grouped into a single failure population, while at the lower stress level (820 MPa) data seemed to group into two distinct populations. The difference in life between the two populations was about two orders in magnitude. A close examination of the CDFs at lower stress levels (σ_{max} = 900, 860 and 820 MPa), presented in Figs. 4(b to d), indicated a step-like behavior of the experimental points at each of these levels. This kind of behavior points towards the possibility of two distinct failure mechanisms. These mechanisms are designated as Type-I and Type-II. In a recent study [8] on fracture of brittle materials, although different from the present study, similar step-like nature of experimental points on a CDF plot was observed and existence of multiple mechanisms was noted.
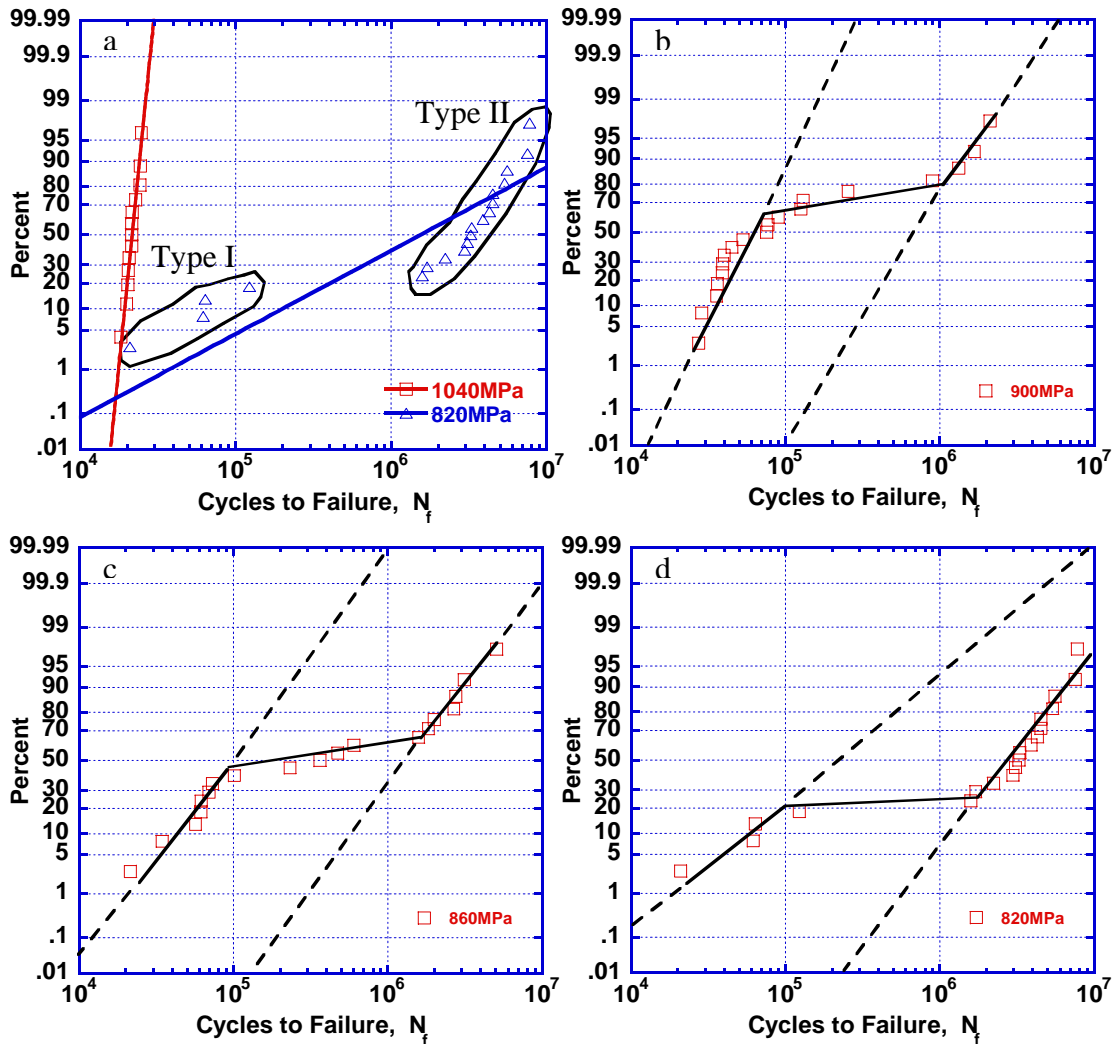
Figure 4 – *Dual failure mechanisms*

The failure-points representing the Type-I and the Type-II failures can be plotted as two separate distributions. These are shown in Figs. 5 (a to c) for the σ_{max} levels of 900, 860 and 820 MPa. At each stress level, the experimental points for the two types of failure fell linearly. The separation between the lines at the probability of failure of 50% was two orders in magnitude at all stress levels (Figs. 5(a to c)). It is also interesting to note that the experimental points shifted between Type-I and Type-II failures such that the likelihood of Type-II failures increased with decreasing stress level. The characteristics of Type I vs. Type II failures are presented in Fig. 6(a and b). Fig. 6(a) shows that the probability of type I failure increased rapidly with increasing stress level and then leveled off towards higher stress levels. Figure 6(b) shows the comparison between mean lives of Type-I vs. Type-II failures with respect to stress level. The mean life showed an increasing trend with decreasing stress level in each mechanism.
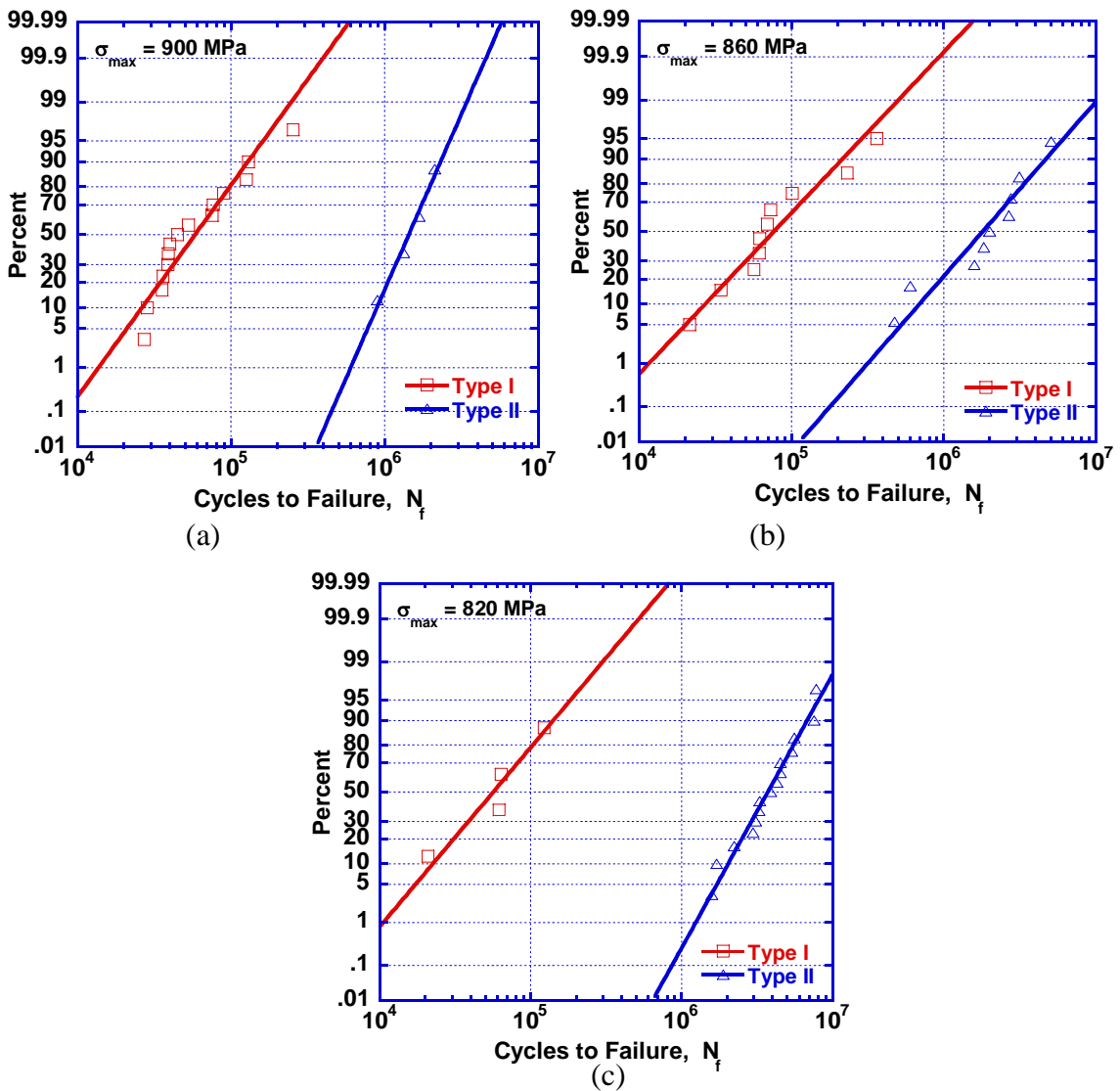
Figure 5 – *Probability of failure plots for the Type I and the Type II mechanism at stress levels of (a) 900 MPa, (b) 860 MPa, and (c) 820 MPa*
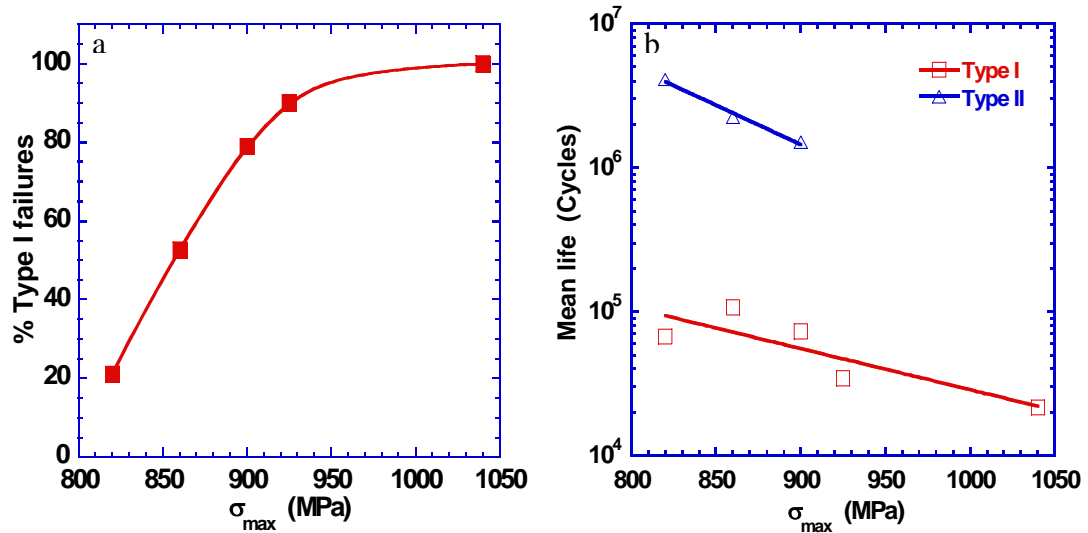
Figure 6 – *Characteristics of the two type of failures: (a) Likelihood of Type I vs. Type II failure with respect to stress level, and (b) Comparison between mean lives in Type I vs. Type II failure*

Life Extension

Figure 7 illustrates the potential for life extension when a mechanism-based approach is adopted. The life for 0.1% probability of failure is shown when the data are arbitrarily extrapolated. This is compared to the case when the data are divided into the two types of mechanisms and the life for 0.1% probability of failure is determined on the basis of the worst-case mechanism, that is, the Type-I. About 5 fold extension in life is seen at the σ_{max} of 900 MPa by considering the Type-I failures (Fig. 7).
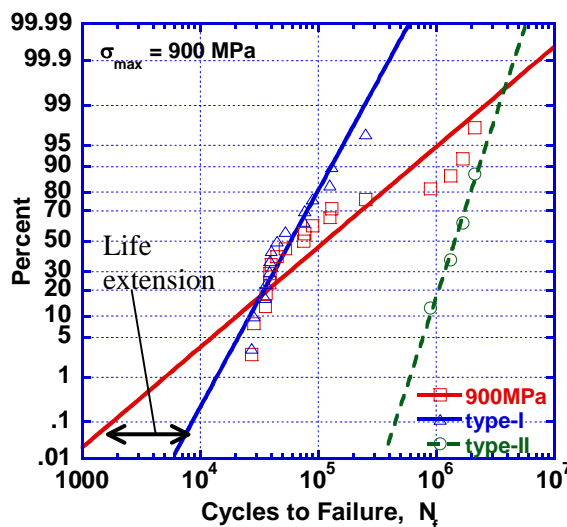
Figure 7 – *Illustration of life extension based on the worst case mechanism, i.e., Type I*

It is of interest to study the source of variability in fatigue life and to determine the physical basis for distinction between the Type-I and the Type-II failure. Mating fatigue fracture surfaces at the σ_{max} level of 860 MPa for the case of a Type-I failure (N_f = 61501 cycles) are shown in Fig. 8. The mating fracture surfaces from a separate specimen at the same stress level but for a Type-II failure (N_f = 2755245 cycles) are shown in Fig. 9. The fracture surfaces indicated presence of a flat area at the origin of the crack. Such an area was seen at all stress levels, irrespective of the life. The size and morphology of these areas corresponded to that of the equiaxed primary-α particles. The results from the EDS analysis on the flat areas on each fracture surface are also presented alongside these figures (Figs 8 and 9). It is interesting to note that the size of the flat area at the crack origin remains similar, irrespective of the large difference in fatigue lives. This indicates that the variability in life was caused at the stage of formation of the flat area at the crack origin.

8µm

8µm
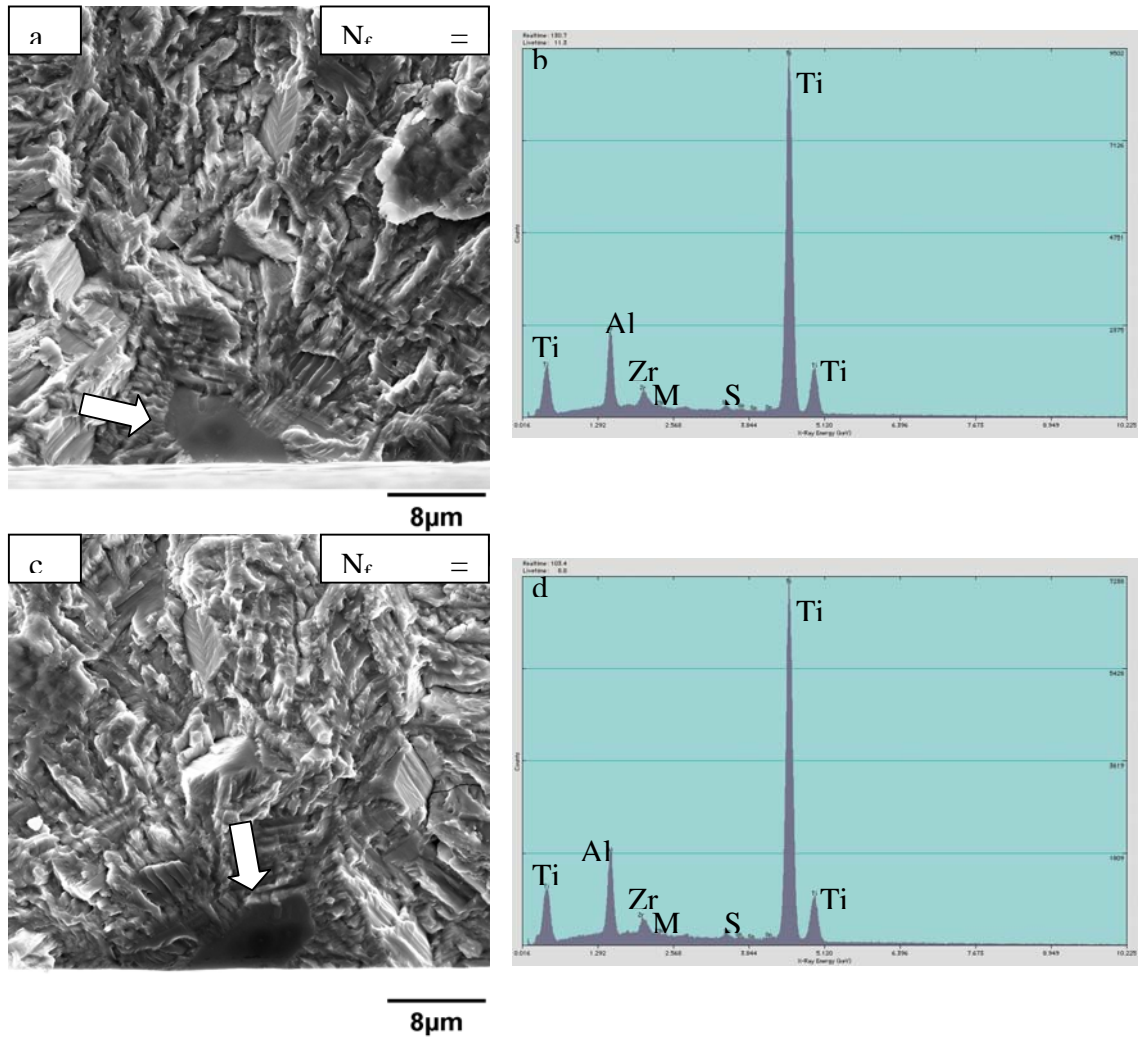
Figure 8 – *Fatigue fracture surface of a Type I failure at σ_{max} = 860 MPa: (a) one side of fracture surface, (b) EDS pattern for (a), (c) the other side of fracture surface, and (d) EDS pattern of (c)*
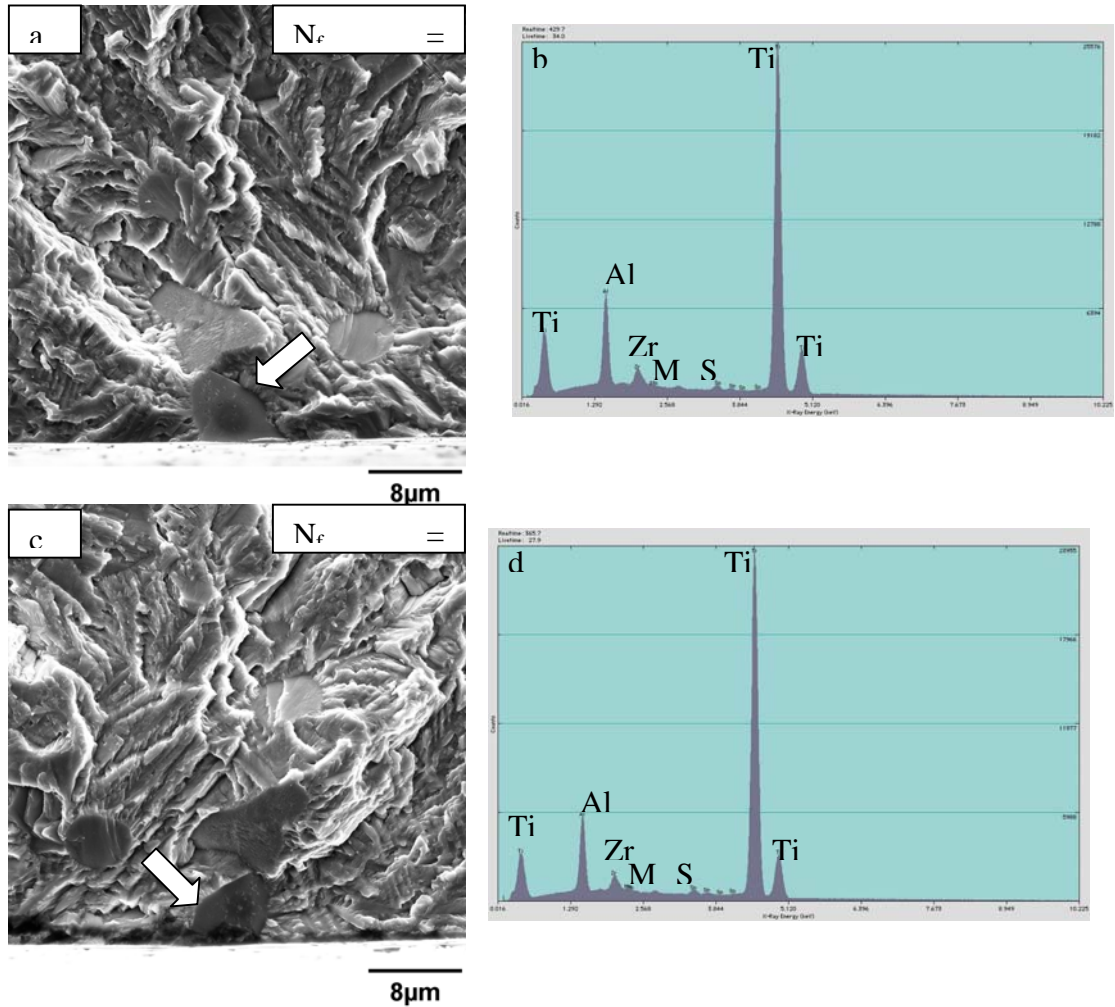
Figure 9 – *Fatigue fracture surface of a Type II failure at σ_{max} = 860 MPa: (a) one side of fracture surface, (b) EDS pattern for (a), (c) the other side of fracture surface, and (d) EDS pattern of (c)*

The EDS spectra from the opposite fracture surfaces were similar for both Type-I and Type-II failures. The spectrum from each part of the fracture surface showed high aluminum (an α phase stabilizer) content and almost no molybdenum (a β phase stabilizer). This indicates that crack nucleated along a plane through the equiaxed α particle in both the Type-I and the Type-II failure.

The profile of surface-nucleated cracks in samples with failure lives of 25507 and 592024 cycles are presented in Fig. 10 (a) and (b), respectively. It is clear that a stage-I crack, indicated by arrows, nucleated across an equiaxed α particle in both cases. The size of the initial stage-I crack was similar (Fig. 10), irrespective of the significant difference between lives in the two cases. This further shows that the variability in life was introduced at the crack nucleation stage, i.e., formation of a crack across an equiaxed α particle. This raises questions regarding the factors that controls the large variability in life.
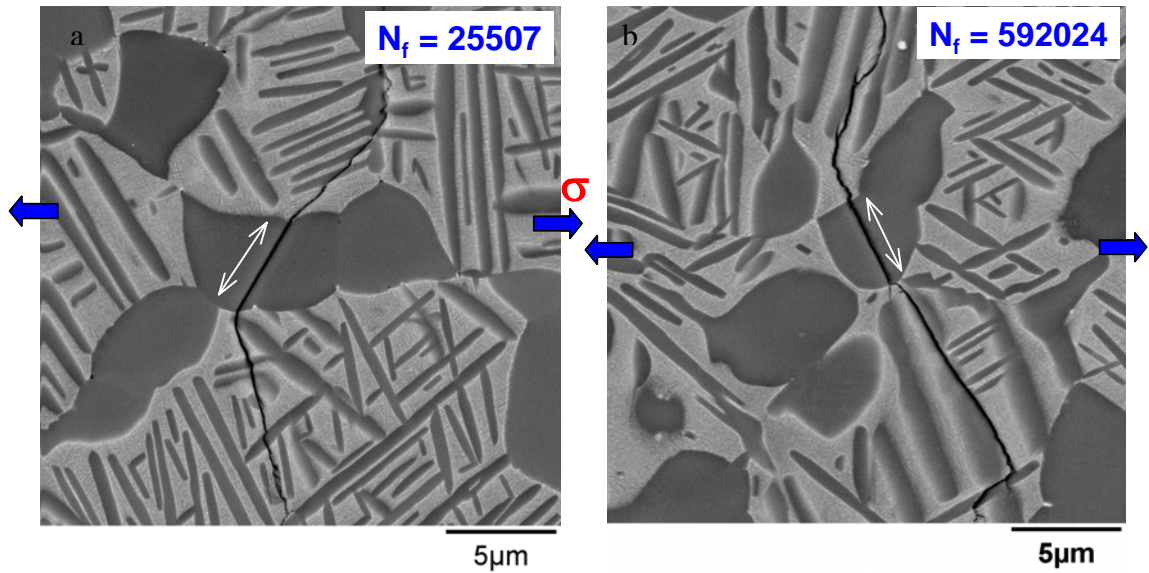
Figure 10 – *Profile of surface cracks: (a) low life, and (b) high life*

Although speculative at this point, it seems that the degree of slip transfer as influenced by the orientation distribution of α particles may control the variability in crack nucleation life, and thus the total life. In the α+β titanium alloys it is known [9,10] that at the start of cycling, deformation is heterogeneous and confined to only a few suitably oriented α particles. The deformation is subsequently homogenized with further cycling through slip transfer to unfavorably oriented particles [9,10]. This type of mechanism is schematically illustrated in Fig. 11. α platelets have been ignored in this
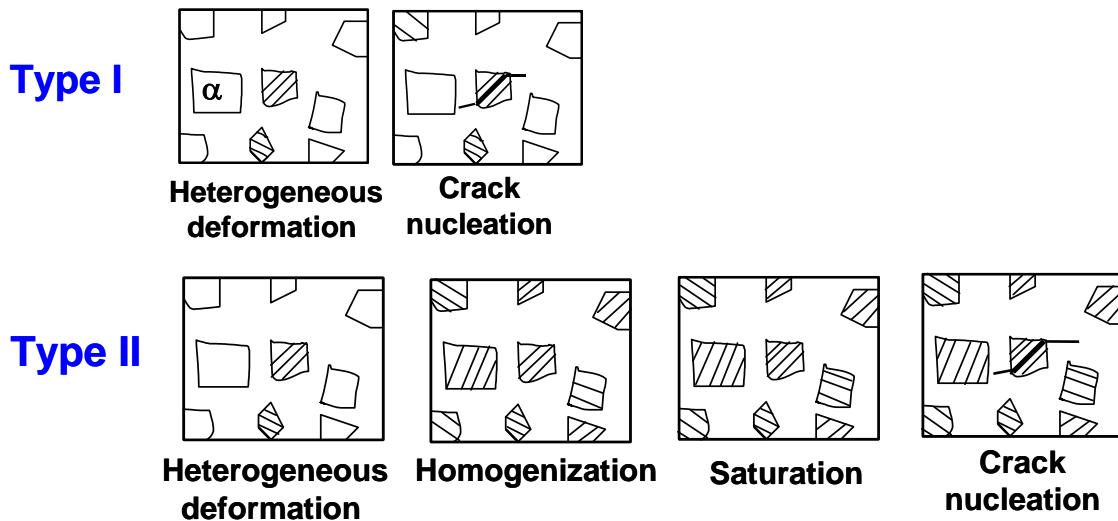
Figure 11 – Schematic illustration of the probable crack nucleation mechanisms in case of (a) Type I and (b) Type II failure

figure for illustrative purposes. It can be suggested that depending on the orientation distribution of a given group of α particles, a crack can nucleate when the deformation is

in the heterogeneous regime (Fig. 11(a)) leading to the Type-I failure. However, if the degree of slip transfer is such that the deformation is homogenized relatively easily, the crack nucleation occurs only after most of the α particles have deformed and the deformation has saturated (Fig. 11(b)), leading to the Type II failure. Clearly, the problem is more complex than illustrated in Fig. 11, due to the duplex nature of the microstructure in this case. Nevertheless, the key to tackling the variability in fatigue lives of Ti-6-2-4-6 seems to lie in the understanding of the formation of crack at the size scale of an equiaxed α particle, i.e., about 2 to 10 μm.

Conclusions

Based on the current research on the fatigue life variability of Ti-6-2-4-6, the following preliminary conclusions can be drawn:

(i) The variability in fatigue lives of Ti-6-2-4-6 increased with decreasing stress amplitude at R = 0.05

(ii) Two types of failure mechanisms were identified based on the step-like morphology of experimental data on the CDF plot. The mean lives of the two types of failures, designated as Type-I and Type-II, differed by two orders of magnitude. Further, the likelihood of one type of failure vs. the other shifted with stress level.

(iii) Prediction of life based on the worst case of the two mechanisms resulted in a significant extension in life, as opposed to the prediction based on an arbitrary extrapolation of all data.

(iv) The variability in life seems to have been introduced at the crack nucleation stage, i.e., formation of the stage-I crack across an equiaxed α particle.

Acknowledgement

References

[1] Magnusen, P. E., Bucci, R. J., Hinkle, A. J., Brokenbrough, J. R., and Konish, H. J., "Analysis and Prediction of Microstructural Effects on Long-Term Fatigue Performance of an Aluminum Aerospace Alloy," *Int. J. Fatigue*, Vol. 19, 1998, S275-S283

[2] Larsen, J. M., John, R., Russ, S. M., Maxwell, D. C., Worth, B. D., Rosenberger, A. H., Li, K., and Porter, W. J., "The Role of Near-Threshold Small-Crack Behavior in Life Prediction of Titanium Alloys for Use in Advanced Turbine Engines," *Small Fatigue Cracks: Mechanics and Mechanisms*, edited by Ravichandran, K. S., Ritchie, R. O., and Murakami, Y., Elsevier Science, Oxford, UK, 1999, 131-142

[3]   Sasaki, S. K., Ochi, Y., and Ishii, A., "Statistical Investigation of Surface Fatigue Cracks in Large-Sized Turbine Rotor Shaft Steel," *Engineering Fracture Mechanics*, Vol. 28, 1987, 761-772

[4]   Goto, M., "Statistical Investigation of the Behavior of Small Cracks and Fatigue Life in Carbon Steels with Different Ferrite Grain Sizes," *Fatigue Fract. Engng. Mater. Struct.*, Vol. 17, 1994, 635-649

[5]   Laz, P. J., Craig, B. A., and Hillberry, B. M., "A Probabilistic Total Fatigue Life Model Incorporating Material Inhomogeneities, Stress Level and Fracture Mechanics," *International Journal of Fatigue*, Vol. 23, 2001, S119-S127

[6]   Tanaka, S., Ichikawa, M., and Akita, S., "A Probabilistic Investigation of Fatigue Life and Cumulative Cycle Ratio," *Engineering Fracture Mechanics*, Vol. 20, 1984, 501-513

[7]   Morris, W. L., and James, M. R., "Statistical Aspects of Fatigue Failure Due to Alloy Microstructure," *Fatigue Mechanisms: Advances in Quantitative Measurement of Physical Damage, ASTM STP 811*, edited by Lankford, J., Davidson, D. L., Morris, W. L., and Wei, R. P., American Society for Testing of Materials, 1983, 179-206

[8]   Knott, J. F., "Probabilistic Aspects of Brittle Fracture," *Mechanisms and Mechanics of Fracture: Symposium in Honor of Prof. J. F. Knott*, edited by Soboyejo, W. O., Lewandowski, J. J., and Ritchie, R. O., TMS, Warrendale, PA, 2002, 79-86

[9]   Beranger, A. S., Feaugas, X., and Clavel, M., "Low Cycle Fatigue Behavior of an $\alpha+\beta$ Titanium Alloy: Ti6246," *Materials Science and Engineering*, Vol. A172, 1993, 31-41

[10]   Feaugas, X., and Clavel, M., "Cyclic Deformation Behavior of an α/β Titanium Alloy-I. Micromechanisms of Plasticity Under Various Loading Paths," *Acta Materialia*, Vol. 45, 1997, 2685-2701

This page intentionally left blank.

Dual Fatigue Failure Modes in Ti-6Al-2Sn-4Zr-6Mo and Consequences on Probabilistic Life Prediction

S. K. Jha[2], J. M. Larsen[1], A. H. Rosenberger[1] and G. A. Hartman[3]

[1]Air Force Research Laboratory
Materials and Manufacturing Directorate, AFRL/MLLMN
Wright-Patterson AFB, Dayton, OH 45433

[2]Systran Federal Corporation
4027 Col. Glenn HWY, Suite 210
Dayton, OH 45431

[3]The University of Dayton Research Institute
300 College Park, Dayton, OH 45469

ABSTRACT

The variability in fatigue life of the Ti-6Al-2Sn-4Zr-6Mo (Ti-6-2-4-6) alloy was investigated. Cumulative life distribution plots were found to be composed of two failure mechanisms. The data could be closely represented by a cumulative distribution function (CDF) resulting from the superposition of the CDFs of the individual mechanisms. An approach for life prediction based on the data due to the worst-case mechanism is suggested.

1. Introduction

The current trend in the aircraft industry towards extending lives of in-service components beyond their initial design life [1,2] has generated considerable interest in a more accurate assessment of life and its variability. One approach in life assessment of fracture-critical turbine engine components is based on life for "initiation" of a crack in one out of thousand components. Thus many components with considerable residual life may be prematurely discarded. Conventionally, this type of approach involves empirical extrapolation of data. The

source of variability remains unclear in such approach. However, considerable potential for life extension appears to exist through a more physically based assessment of variability.

Fatigue life variability is most commonly described by the lognormal probability density function (PDF) [1, 3-7]. There have been attempts to track the variability in life through the size distribution of the relevant microstructural feature [1, 3]. In these cases [1, 3], the variability in life was thought to be controlled by the crack growth life. The life calculations were, therefore, based on crack growth from a size equivalent to the relevant microstructural feature until fracture [1, 3]. In all these studies [1, 3-7], however, the variability in life was controlled by a single failure mechanism, and the probability-of-failure (POF) plot could be represented by a single cumulative distribution function (CDF).

This paper discusses results from our research on the variability in the fatigue life of Ti-6-2-4-6, a high strength $\alpha+\beta$ titanium alloy. The POF (or the CDF) plots were found to have a step-like shape at certain stress levels, and the data could not be described by a single CDF. The shape of the CDF was shown to result from a superposition of two types of failure mechanisms. Such behavior of a CDF has been previously reported [8, 9], although these studies were not related to fatigue. Nevertheless, the existence of two mechanisms as causing the step-like behavior of the CDF was suggested [8, 9]. The objective of this paper is not to discuss the microstructural source of life variability. It is, however, intended as a step towards a mechanism-based assessment of variability. It is demonstrated that a mechanism-based evaluation of the CDF has a significant potential for life extension.

2.   MATERIAL AND EXPERIMENTAL PROCEDURE

The microstructure of the Ti-6-2-4-6 alloy used in this study is presented in Fig. 1. As shown in the figure, the microstructure had a duplex nature and consisted of equiaxed primary-α particles and α platelets in a transformed β matrix. Testing was performed on round-bar stress-

life (S-N) fatigue specimens with a uniform gage section of length 12 mm and diameter of 4 mm. All fatigue specimens were machined from the same parent disk forging, which exhibited a highly uniform microstructure. The specimens were low-stress ground and then electropolished to minimize any surface residual stress as well as to produce uniform surface condition. The S-N type fatigue tests were conducted using an MTS 810 servohydraulic test system equipped with a 458 controller. The tests were performed in tension-tension fatigue at room temperature and a lab-air environment. A frequency of 20 Hz and a stress ratio of 0.05 were used. At selected stress levels, an Infrared Damage Detection System (IDDS) was used to detect nucleation of cracking. Fractography and Energy Dispersive Spectrometer (EDS) analysis were performed using a Cambridge S360FE scanning electron microscope.

3.   VARIABILITY IN TOTAL LIFE

The fatigue life behavior of the Ti-6-2-4-6 alloy is shown in Fig. 2(a). Only the mean lives are plotted in this figure. Multiple tests were conducted at selected stress levels as indicated by numbers in parentheses (Fig. 2(a)). The variability in life is shown in Fig. 2(b). As shown in the figure, decreasing the stress level, σ_{max}, produced an increase in the average fatigue life, but this was accompanied by a substantial increase in the variability in life. While most failures occurred by surface crack nucleation, one sample at the σ_{max} of 860 MPa and few samples at the σ_{max} of 820 MPa failed by subsurface nucleation. However, as shown in Fig. 2(b), the lives of surface and subsurface failures overlapped each other, indicating that the variability in life was not correlated with surface vs. subsurface crack nucleation in this case. This is interesting since, although subsurface crack nucleation has been commonly observed in structural materials [10-13] including titanium alloys [10, 11], it is often accompanied by a "step" in the S-N curve. Also, in a recent study [14], surface vs. subsurface crack nucleation was reported as causing a duality in the

S-N curve. Clearly, the variability in lives in the present case cannot be explained on the basis of surface vs. subsurface crack nucleation.

The cumulative probability of failure with respect to cycles at the σ_{max} levels of 1040, 925, 900, 860 and 820 MPa are shown in Fig. 3. The Lognormal distribution function was used. The data are plotted in the lognormal probability space, which is based on the linearization of the CDF. If all data are considered as belonging to a single distribution then slopes of the fitted lines indicate that the scale of variability increased as the stress level decreased. This type of behavior with decreasing stress level has been reported in other materials [4,5]. There are also studies where the scale of variability did not change significantly with stress level [3,6,7]. However, unlike these studies [3-7], the present study showed a dramatic increase in the range of variability to up to two orders in magnitude at lower stress levels. It is also interesting to note in Fig. 3 that an arbitrary extrapolation of data to a probability of failure of 0.1% (1 in 1000) leads to a lower predicted life at lower stress level.

4.   DUAL FAILURE MECHANISMS

For clarity, the POF plots at the lower stress levels (σ_{max} = 900, 860 and 820 MPa respectively) are plotted separately and presented in Figs. 4(a to c). In each case, a step-like shape of the CDF was observed. At the higher stress level (σ_{max} = 1040 MPa), however, the data were well represented by a single line (Fig. 3). The step-like behavior of CDF at lower stress levels indicated a grouping of data into two failure populations and pointed towards the possibility of two distinct failure mechanisms. These mechanisms are designated as Type-I (the lower-life failures) and Type-II (the higher-life failures), as indicated in the figure. The difference in life between the two types of failure was about two orders in magnitude.

Such step-like shape of the CDF has been reported in previous studies [8, 9] although these were not related to fatigue failures. The presence of two fracture mechanisms was suggested

to cause the step-like CDF in a study on brittle fracture [8]. In the second study, electromigration failure data of AlCu interconnects resulted in a step-like shape of the CDF [9] and was shown to be due to the existence of two distinct failure mechanisms. It can be shown [9] that the shape of the CDF presented in Fig. 4 (a to c) can result from superposition of two sequential mechanisms separated in time (or cycles). The CDF of a lognormal distribution function can be written as:

$$CDF(x) = \tfrac{1}{2}[1 + erf\left(\tfrac{\ln x - M}{S\sqrt{2}}\right)] \tag{1}$$

where, *erf* is the error function, M is the mean of the natural logarithms of the cycles to failure and S is the standard deviation of the natural logarithms of the cycles to failure. The CDF resulting from the superposition of the Type I and the Type II mechanism can be written in the following form [9]:

$$CDF(N) = p_{TypeI}CDF_{TypeI}(N) + p_{TypeII}CDF_{TypeII}(N) \tag{2}$$

where, p_{TypeI} and p_{TypeII} are the probability of occurrence of the Type I and the Type II failures respectively and N is the cycles. Assuming Type I and Type II are distinct mechanisms:

$$p_{TypeI} + p_{TypeII} = 1 \tag{3}$$

The CDF for each mechanism (CDF_{TypeI} and CDF_{TypeII}) can be derived by substituting for the respective values of M (M_{TypeI} and M_{typeII}) and S (S_{TypeI} and S_{TypeII}) in Eqn. (1). These values were determined from the experimental data and are presented in Table I. The combined CDF is plotted in Fig. 5 for the σ_{max} of 900, 860 and 820 MPa. The experimental points are also shown in the figure. It is clear that the combination of the two CDFs (Eqn. 2) represented the experimental data very closely.

Depending on the degree of overlap between the two superposing mechanisms, there can be a few intermediate points in the horizontal region of the "step" [9] (Fig.4). Since the separation between the mean lives of Type I and Type II failures at σ_{max} = 820 MPa was the largest (thus less overlap between the two mechanisms), there was almost no intermediate point and the slope

of the intermediate region was almost flat (Fig. 4(c)). Few intermediate points were present at σ_{max} = 860 and 900 MPa, due to the increasing overlap between the two mechanisms at these stress levels.

The data points representing the Type-I and the Type-II failure can be plotted as two separate distributions. These are shown in Fig. 6 (a to c) for the σ_{max} levels of 900, 860 and 820 MPa, respectively. The intermediate points (presumably due to the overlap between the mechanisms) were also included in this figure. As expected the experimental points for the two types of failure could be fit linearly in the Log-normal space at each stress level. The separation between the lines at the failure-probability of 50% was two orders in magnitude at all stress levels (Figs. 6(a to c)). This is shown in Fig. 7(a). The mean life showed an increasing trend with decreasing stress level in each mechanism (Fig. 7(a)). Also, as mentioned above, the separation between the mean lives increased slightly with decreasing stress level. It is interesting to note that the experimental points shifted between Type-I and Type-II failures (Fig. 6) such that the likelihood of Type-II failures increased with decreasing stress level. This is shown in Fig. 7(b). The probability of the Type I failure initially increased with increasing stress level and then leveled off towards higher stress levels.

It is suggested that a mechanism-based approach be adopted in life prediction. This not only can lead to a more accurate prediction but also a methodology to reliably extend life. For example, the potential for extension in life is illustrated in Fig. 8. In this figure, the life for 0.1% POF at the σ_{max} = 900 MPa is shown when the data were arbitrarily extrapolated. This is compared to the case when the data were divided into the two types of mechanisms. The life was then determined on the basis of the worst-case mechanism, that is, the Type-I. As shown (Fig. 8), this resulted in about 5-fold increase in the expected life at the σ_{max} of 900 MPa.

CONCLUSIONS

Based on the current research on the fatigue life variability of Ti-6-2-4-6, the following conclusions can be drawn:

(i) The variability in fatigue lives of Ti-6-2-4-6 increased with decreasing stress amplitude.

(ii) Two types of failure mechanisms were identified based on the step-like morphology of experimental data on the CDF plot. The mean lives of the two types of failures differed by two orders of magnitude. Further, the likelihood of one type of failure vs. the other shifted with stress level.

(iii) A methodology to predict life based on the worst-case mechanism, which can result in a more accurate prediction, is suggested.

References

[1]   Magnusen, PE, Bucci, RJ, Hinkle, AJ, Brokenbrough, JR, Konish, HJ. Int. J. Fatigue 1998; 19: S275

[2]   Larsen, JM, John, R, Russ, SM, Maxwell, DC, Worth, BD, Rosenberger, AH, Li, K, Porter, WJ. Small Fatigue Cracks: Mechanics and Mechanisms, Edited by K.S. Ravichandran, R. O. Ritchie, and Y. Murakami, Elsevier Science, Oxford, UK, 1999, pp. 131-142

[3]   Laz, PJ, Craig, BA, Hillberry, BM. Int. J. Fatigue 2001; 23: S119

[4]   Sasaki, SK, Ochi, Y, Ishii, A. Engineering Fracture Mechanics 1987; 28: 761

[5]   Goto, M. Fatigue Fract. Engng. Mater. Struct. 1994; 17: 635

[6]   Tanaka, S, Ichikawa, M, Akita, S. Engineering Fracture Mechanics 1984; 20: 501

[7]   Morris, WL, James, MR. Fatigue Mechanisms: Advances in Quantitative Measurement of Physical Damage, ASTM STP 811, Edited by J. Lankford, D. L. Davidson, W. L. Morris, and R. P. Wei, American Society for Testing of Materials, 1983, pp. 179-206

[8]   Knott, JF. Mechanisms and Mechanics of Fracture: Symposium in Honor of Prof. J. F. Knott, Edited by W. O. Soboyejo, J. J. Lewandowski, and R. O. Ritchie, TMS, Warrendale, PA, 2002, pp. 79-86

[9]   Fischer, AH, Abel, A, Lepper, M, Zitzelsberger, AE, von Glasow, A. Microelectronics Reliability 2001; 47: 445

[10] Atrens, A, Hoffelner, W, Duerig, TW, Allison, JE. Scripta Metallurgica 1983; 17: 601

[11] Neal, DF and Blenkinsop, PA. Acta Metall. 1976; 24: 59

[12] Wang, QY, Berard, JY, Dubarre, A, Baudry, G, Rathery, S, Bathias, C. Fatigue Fract. Engng. Mater. Struct. 1999; 22: 667

[13] Murakami, Y, Takada, M, Toriyama, T. Int. J. Fatigue 1998; 16: 661

[14] Jha, SK, Ravi Chandran, KS. Scripta Materialia 2003; 48: 1207

Table I: Parameters for the Type I and the Type II failures derived from the experimental data

σ_{max} (MPa)	All Data			Type I			Type II		
	M	S	p	M	S	p	M	S	p
1040	9.976	0.0878	1	9.976	0.0878	1	-	-	0
925	10.624	0.7251	1	10.41	0.2803	0.90	-	-	0.1
900	11.646	1.4639	1	10.972	0.6449	0.79	14.173	0.3664	0.21
860	12.737	1.797	1	11.242	0.8296	0.53	14.399	0.7685	0.47
820	14.244	1.8282	1	10.937	0.7325	0.21	15.126	0.4747	0.79
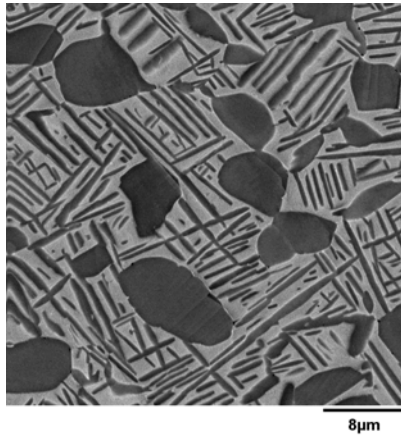
Fig. 1　Microstructure of the Ti-6-2-4-6 alloy
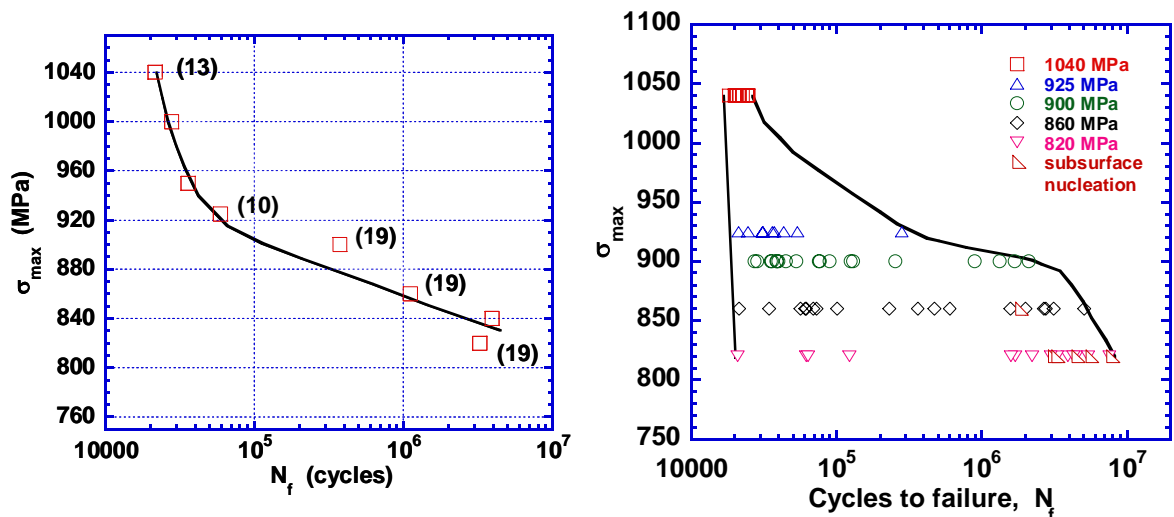
Fig. 2　Fatigue life behavior of Ti-6-2-4-6: (a) Mean lives, and (b) Life variability
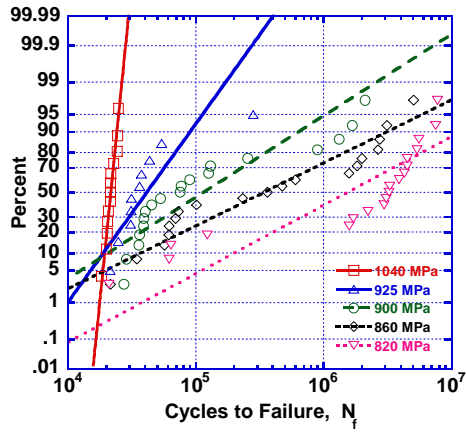
Fig. 3   Probability of failure plots at selected stress levels
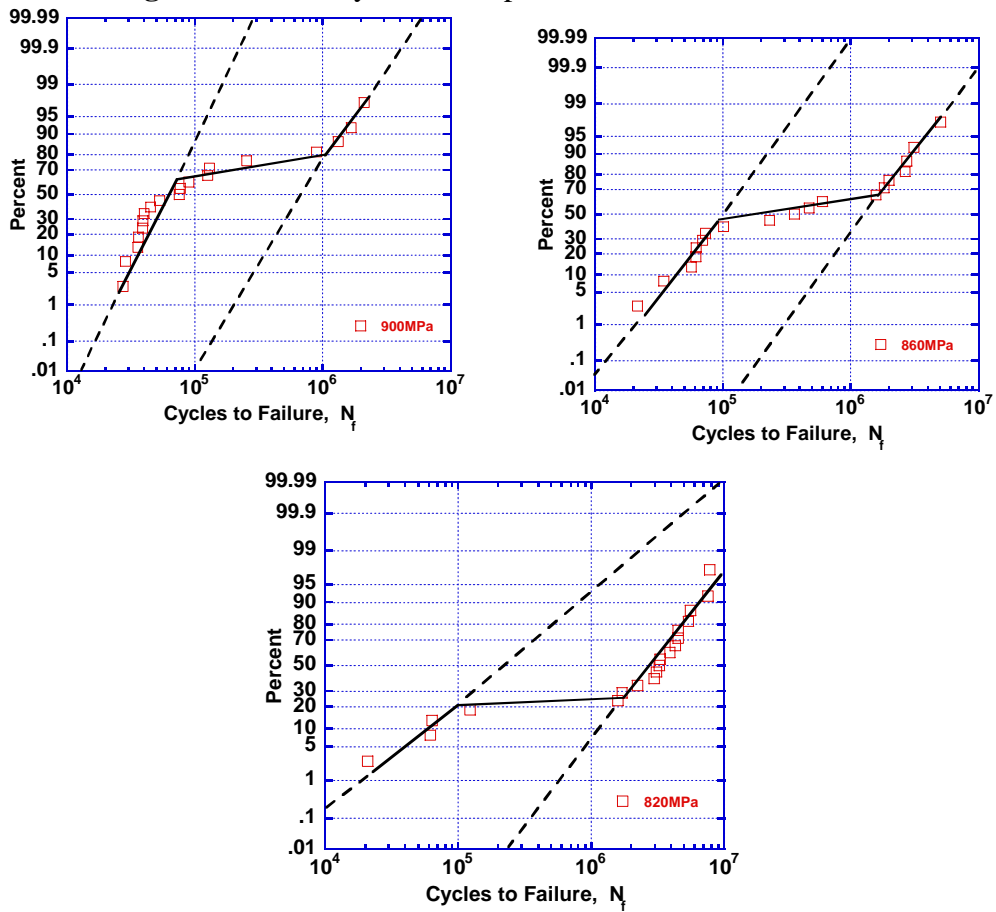
Fig. 4   The step-like nature of the CDFs at (a) σ_{max} = 900 MPa, (b) σ_{max} = 860 MPa, and (c) σ_{max} = 820 MPa indicating dual failure mechanisms
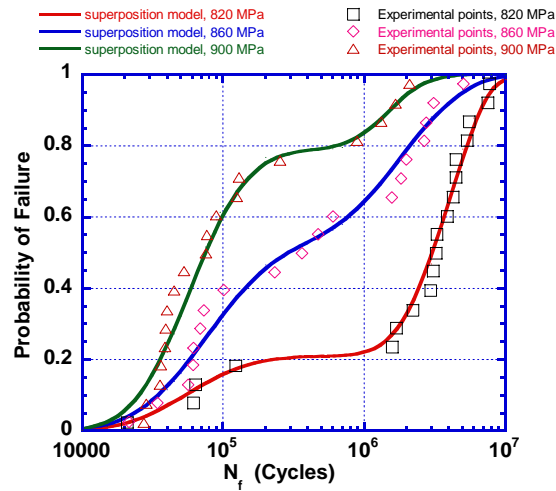
Fig. 5 The representation of the experimental data by CDFs resulting from superposition of the Type I and the Type II failures
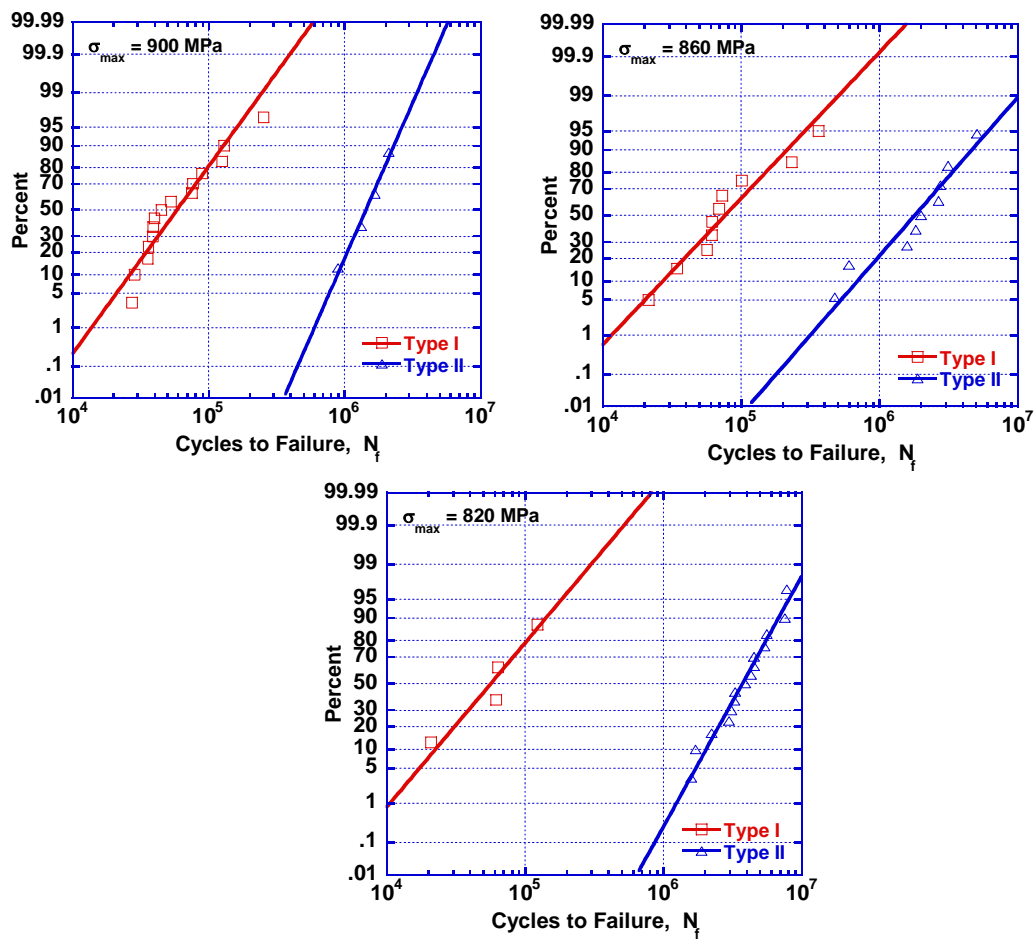
Fig. 6 The POF plots showing the Type I and the Type II mechanism as separate distributions at stress levels of (a) 900 MPa, (b) 860 MPa, and (c) 820 MPa
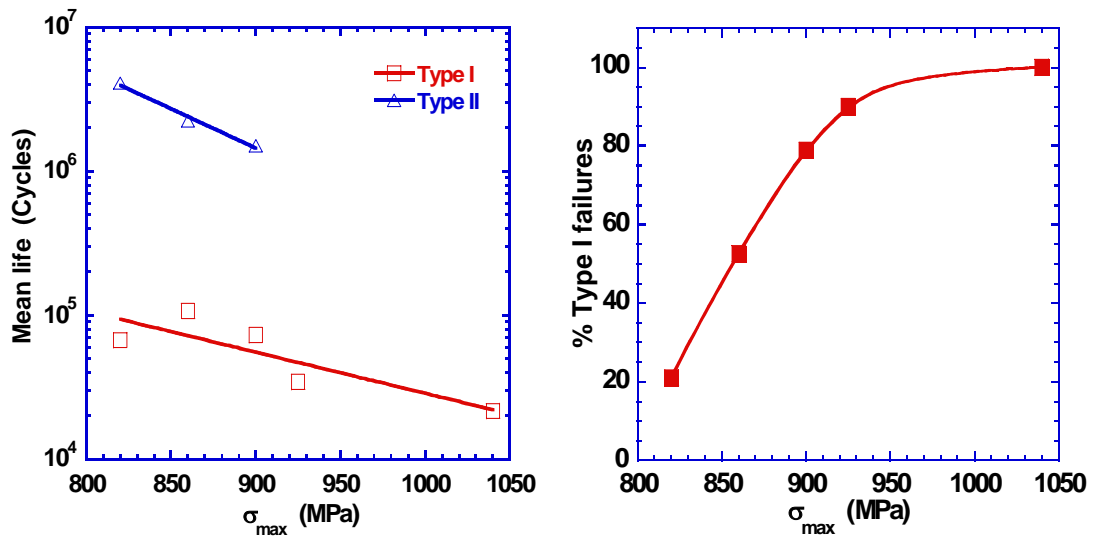
Fig. 7 Characteristics of the two type of failures: (a) Comparison between mean lives of the Type I vs. the Type II failure, and (b) Likelihood of the Type I vs. the Type II failure with respect to stress level
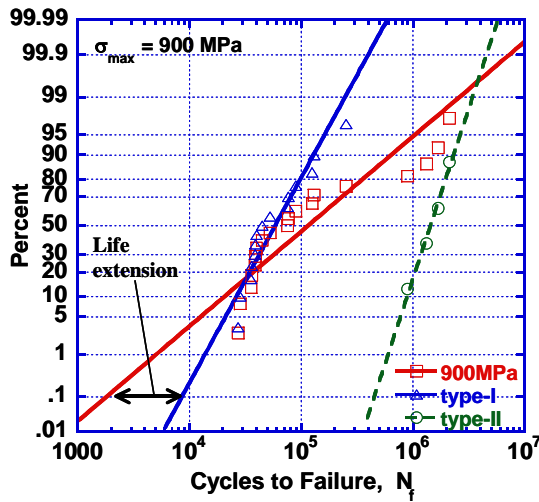
Fig. 8 Illustration of life extension based on the worst case mechanism, i.e., Type I

This page intentionally left blank.

Variability in Fatigue Life of Ti-6Al-2Sn-4Zr-6Mo

S. K. Jha[2], J. M. Larsen[1], A. H. Rosenberger[1] and G. A. Hartman[3]

[1]Air Force Research Laboratory

Materials and Manufacturing Directorate, AFRL/MLLMN

Wright-Patterson AFB, Dayton, OH 45433

[2]Systran Federal Corporation

4027 Col. Glenn HWY, Suite 210

Dayton, OH 45431

[3]The University of Dayton Research Institute

300 College Park, Dayton, OH 45469

Abstract

Variability in fatigue life of the Ti-6Al-2Sn-4Zr-6Mo (Ti-6-2-4-6) alloy was investigated. It was found that the variability in life was introduced at the crack nucleation stage, i.e., formation of the stage-I crack across an equiaxed primary-α particle. Cumulative life distribution plots were found to be composed of two failure mechanisms. The mean lives of the two types of failure differed by two orders of magnitude. Also, the likelihood of failure by the "higher-life" mechanism increased with decreasing stress amplitude. It was also found that the variability in life of Ti-6-2-4-6 could not be tracked through the variability in the size of the relevant microstructural unit. Rather, it is suggested that the life variability can be accounted for through the variability in deformation accumulation in a given α_P as influenced by the orientation of the surrounding α particles.

Keywords: microstructure, fatigue life variability, probability of failure, size scale, deformation, slip transfer

1. Introduction

The current trend in the aircraft engine industry towards extending lives of in-service components beyond their initial design life [1,2] has generated considerable interest in a more accurate assessment of life and its variability. One approach in life assessment of fracture critical turbine engine components is based on life for "initiation" of a crack in one out of a thousand components. Thus many components with considerable residual life may be prematurely discarded. Conventionally, this type of approach involves an empirical representation of the stochastic nature of fatigue. The role of microstructure in life variability has not been widely addressed, and the source of variability remains largely unclear. However, considerable potential for life extension appears to exist through a more physically based assessment of variability.

Another factor that can contribute to life extension is a better understanding of the microstructural size scale at which the fatigue life and the variability are controlled. Often, in damage tolerant design, life calculations are based on the long-crack (that which can be characterized by the Linear Elastic Fracture Mechanics (LEFM)) growth [3]. Consequently, in most studies, the assessment of life variability has been based on the long-crack growth [4-6] as well. It is, however, known that the fatigue process consists of at least four stages including crack nucleation and small-crack growth [7,8]. Since different materials distribute life differently between these fatigue regimes, application of damage tolerant approach based solely on the LEFM can lead to inaccurate design. Indeed, the significance of the small-crack regime in life prediction has been recognized in literature [9,10]. Recently, there has also been increased attention [11,12] towards the crack nucleation regime in life calculations. Certainly, there are some materials, for

example, those containing constituent particles, inclusions or pores [13-15], where a considerable part of the total fatigue life may be expended in large-crack growth. In such cases, the initial crack size for life calculations can be estimated from the size distribution of the relevant microstructural feature, such as inclusions and casting defects [1,16,17]. Also, the initial crack size is sometimes selected arbitrarily [18] on the basis of the expected maximum defect size in the material. Nevertheless, in such materials, the variability in life can be tracked through the size distribution of relevant defects [14]. However, in many materials, including high strength titanium alloys [19-23] crack nucleation occurs at a much smaller size scale, through dislocation-microstructure interactions. In such cases, a large percentage of total fatigue life may be expended in crack nucleation and small-crack growth, especially in high cycle fatigue [19,24]. These stages of fatigue, therefore, cannot be ignored in life prediction and assessment of life variability, especially from a life-extension perspective.

The present research is directed at understanding the role of microstructure in the variability in the fatigue life of Ti-6-2-4-6, a high strength $\alpha+\beta$ titanium alloy. It is demonstrated that a significant potential for life extension exists through a mechanism-based evaluation of the cumulative life distribution. It is shown that the variability in life of Ti-6-2-4-6 is controlled primarily by the crack nucleation stage, specifically, formation of a stage-I crack (size of about 5 μm) across an equiaxed primary-α particle. Conventionally, the understanding has been that, the lower the life is the larger is the size of the microstructural feature or defect that initiates the crack [25-28]. In this study, however, it was found that the variability in life could not be tracked through the

variability in the size of the relevant microstructural unit or the "crack-initiating" particle. Probable mechanisms that explain the fatigue life variability in Ti-6-2-4-6 are proposed.

2. Material and Experimental Procedure

The microstructure of the Ti-6-2-4-6 alloy used in this study is presented in Fig. 1. As shown in the figure, the microstructure had a duplex nature and consisted of equiaxed primary-α particles and α platelets in a transformed β matrix. Testing was performed on round-bar stress-life (S-N) fatigue specimens with a uniform gage section of length 12 mm and diameter of 4 mm. All fatigue specimens were machined from the same parent disk forging, which exhibited a highly uniform microstructure. The specimens were low stress ground and then electropolished to minimize any surface residual stress as well as to produce uniform surface condition. The S-N type fatigue tests were conducted using an MTS 810 servohydraulic test system equipped with a 458 controller. The tests were performed in tension-tension fatigue at room temperature in lab-air at a frequency of 20 Hz and a stress ratio of 0.05. At selected stress levels, an Infrared Damage Detection System (IDDS) was used to detect nucleation of cracking. Fractography and Energy Dispersive Spectrometer (EDS) analysis were performed using a Cambridge S360FE scanning electron microscope.

3. Results and Discussion

3.1 Variability in Total Life

The fatigue life behavior of the Ti-6-2-4-6 alloy is shown in Fig. 2(a). Only the mean lives are plotted in this figure. Multiple tests were conducted at selected stress levels as indicated by numbers in parentheses (Fig. 2(a)). The variability in life is shown

in Fig. 2(b). As shown in the figure, decreasing the stress level, σ_{max}, produced an increase in the average fatigue life, but this was accompanied by a substantial increase in the variability in life. While most failures occurred by surface crack nucleation, one sample at the σ_{max} of 860 MPa and a few samples at the σ_{max} of 820 MPa failed by subsurface nucleation. However, as shown in Fig. 2(b), the lives of surface and subsurface failures overlapped each other, indicating that the variability in life was not correlated with surface vs. subsurface crack nucleation in this case. This is interesting since, subsurface crack nucleation has been commonly observed in structural materials [29-32] including titanium alloys [29,30]. However, in these cases the subsurface nucleation was accompanied by a "step" in the S-N curve that corresponded to the switch between the surface and the subsurface nucleation. Also, in a recent study [33], surface vs. subsurface crack nucleation was reported as causing a duality in the S-N curve, with the subsurface data points showing significantly higher lives when compared to the surface points. Clearly, the variability in lives in the present case cannot be explained on the basis of surface vs. subsurface crack nucleation alone.

The cumulative probability of failure with respect to cycles at the σ_{max} levels of 1040, 925, 900, 860 and 820 MPa are shown in Fig. 3. The log-normal distribution function was used. The data are plotted in log-normal probability space, which is based on linearization of the cumulative distribution function (CDF). Slopes of the fitted lines indicate that the scale of variability increased as the stress level decreased. This type of behavior with decreasing stress level has been reported in other materials [22,23]. However there are also studies where the scale of variability did not change significantly with stress level [14,36,37]. It seems that, whenever total life was largely comprised of

crack growth, for example, in the case of aluminum alloys containing constituent particles [14], the scale of variability remained similar with respect to stress level. It is interesting to note in Fig. 3 that an arbitrary extrapolation of data to a probability of failure of 0.1% (1 in 1000) leads to a lower predicted life at lower stress level.

3.2   Dual Failure Mechanisms

A comparison between the probability-of-failure plots, or the cumulative distribution functions (CDF), at a high and a low stress level (σ_{max} = 1040 and 820 MPa respectively) is presented in Fig. 4(a). At the higher stress level (1040 MPa), experimental data points grouped into a single failure population, while at the lower stress level (820 MPa) the data seemed to separate into two distinct populations. The difference in life between the two populations was about two orders in magnitude. A close examination of the CDFs at lower stress levels (σ_{max} = 900, 860 and 820 MPa), presented in Figs. 4(b to d), indicated a step-like behavior of the experimental points at each of these levels. This kind of behavior points towards the possibility of two distinct failure mechanisms. These mechanisms are designated as Type-I (the lower-life failures) and Type-II (the higher-life failures). In a recent study [38] on *fracture* of brittle materials, a similar step-like nature of experimental points on a CDF plot was observed. This was suggested to be caused by the presence of two fracture mechanisms [38]. In another study [39] on electromigration failure of AlCu interconnects, the presence of two distinct failure mechanisms was shown to cause the step-like nature of the CDFs. It was shown [39] that the "step-like" shape of the CDF (Fig. 4 (b to d)) could be described by a function resulting from superposition of two sequential mechanisms, which were separated with respect to time (or cycles). Depending on the degree of overlap between

190

the two superposing mechanisms, there can be a few intermediate points in the horizontal region of the "step" (Fig.4). Since the separation between the mean lives of Type I and Type II failures at σ_{max} = 820 MPa was the greatest (thus less overlap between the two mechanisms), there were almost no intermediate points and the slope of the intermediate region was almost flat (Fig. 4(d)). Consistent with the superposition model [39], few intermediate points were present at σ_{max} = 860 and 900 MPa, understandably due to the increasing overlap between the two mechanisms at these stress levels.

The points representing the Type-I and the Type-II failure can be plotted as two separate distributions. These are shown in Figs. 5 (a to c) for the σ_{max} levels of 900, 860 and 820 MPa respectively. The intermediate points (presumably due to the overlap between the mechanisms) are also included in this figure. At each stress level, the experimental points for the two types of failure fell linearly, as expected. The separation between the lines at the probability of failure of 50% was two orders of magnitude at all stress levels (Figs. 5(a to c)). This is shown in Fig. 6(a). The mean life showed an increasing trend with decreasing stress level for each mechanism (Fig. 6(a)). Also, as mentioned above, the separation between the mean lives increased slightly with decreasing stress level. It is also interesting to note that the experimental points shifted between Type-I and Type-II failures (Fig. 5), such that the likelihood of Type-II failures increased with decreasing stress level. This is shown in Fig. 6(b). The probability of the Type I failure initially increased with increasing stress level and then leveled off at the higher stress levels.

3.2.1 Life Extension

A mechanism-based approach to life-prediction can, not only lead to a more accurate prediction but a methodology to reliably extend life. Such methodology is illustrated in Fig. 7. In this figure, the life for 0.1% probability-of-failure is shown when the data were arbitrarily extrapolated. This is compared to the case when the data were divided into the two types of mechanisms. The life was then determined on the basis of the worst-case mechanism, that is, the Type-I. As shown (Fig. 7), this resulted in about a 5-fold increase in the expected life at the σ_{max} of 900 MPa.

3.3 What Causes Variability in Life?

3.3.1 Crack Origin

It is of interest to understand the source of the variability in fatigue life and to determine the physical basis for distinction between the Type-I and the Type-II failure. The fatigue fracture surfaces were analyzed to determine the crack nucleation characteristics of the two types of failure. Examples of a surface and a subsurface crack nucleation are presented in Fig. 8. The crack origin could be unambiguously determined in all cases at the convergence of a radial pattern such as the one seen in Fig. 8. The fracture surfaces for the cases of surface nucleation at the σ_{max} levels of 1040, 860 and 820 MPa are presented in Figs. 9, 10 and 11 respectively. Two specimens are shown at each stress level. A flat area, indicated by arrows in the figures, was observed at the crack origin at each stress level (Figs. 9 to 11). The size and morphology of these areas (referred as "crack-nucleation-area" from this point forward) corresponded to that of the equiaxed α_p particle. This was irrespective of the life of the specimens, indicating that in

all cases, crack nucleated from an α_p particle. This also shows that no inclusions or extraneous particles were present at crack origins. In few cases, more than one α_p particle comprised the "crack nucleation area" (Fig. 9(a)).

A number of significant aspects of fatigue of Ti-6-2-4-6 are evident on the fracture surfaces shown in Figs. 9 to 11. Firstly, from comparison between these figures, it is clear that the size of the "crack- nucleation-area" was independent of the stress level. In some other studies [40-42], such flat regions were also observed at the crack origin. However, their area was found to increase with decreasing stress level. These flat areas were thought to be correlated with the life of the specimen [40-42]. Clearly, this is not the case in the present study. Secondly, the variation in life did not depend on the size or the morphology of the "crack-nucleation-area". For example, in spite of significant differences between the sizes of the "crack-nucleation-areas" at $\sigma_{max} = 1040$ MPa (Figs. 9 (a) and (b)), these specimens showed similar lives. Also, at $\sigma_{max} = 860$ MPa (Figs. 10 (a) and (b)) and 820 MPa (Figs. 11 (a) and (b)), although there was two orders of magnitude difference between lives, the size of the "crack-nucleation-areas" were about the same. This indicates that the variability in life may be caused prior to the formation of such flat area at the crack origin.

3.3.2 Chemistry of "Crack Nucleation Area"

In order to determine if the flat area at the crack origin represented a plane through an α_p particle or the interface between α_p and the transformed β phase, EDS analysis was performed on these areas on the mating fracture surfaces. Mating fatigue fracture surfaces at the σ_{max} level of 860 MPa for the case of a Type-I failure ($N_f =$

61,501 cycles) are shown in Fig. 12. The mating fracture surfaces from a separate specimen at the same stress level but for a Type-II failure (N_f = 2,755,245 cycles) are shown in Fig. 13. The results from the EDS analysis on the flat areas on each fracture surface are also presented alongside these figures (Figs. 12 and 13). The EDS spectra from the opposite fracture surfaces were similar for both Type-I and Type-II failures. The spectrum from each part of the fracture surface showed high aluminum (an α phase stabilizer) content and almost no molybdenum (a β phase stabilizer). This indicates that crack nucleated along a plane through the equiaxed α_p particle in both the Type-I and the Type-II failure.

The profile of surface nucleated cracks in samples with failure lives of 25,507 and 592,024 cycles are presented in Fig. 14 (a) and (b), respectively. It is clear that a stage-I crack, indicated by arrows, nucleated across an equiaxed α_p particle in both cases. The size of the initial stage-I crack was similar (Fig. 14), irrespective of the significant difference between lives in the two cases. This raises questions regarding the factor that controls the large variability in life. This, nevertheless, suggests that the variability in life was introduced at the crack nucleation stage, i.e., the process of formation of a crack across an equiaxed α_p particle. Therefore, the variability in the life of this alloy appears to be caused at the size scale of about 2-10 μm.

3.4 Life Partitioning between Crack Nucleation and Propagation

The partitioning of life between crack nucleation and growth is shown in Fig. 15. An initial crack of size 5 μm (which is approximately the size of the equiaxed α_p particle) and penny-shaped was used in the calculations. As shown in Fig. 15 (a), the initial ΔK

(ΔK_i) turned out to be higher than the threshold ΔK (ΔK_{th}) at R = 0.05. Figure 15 (b) shows that at lower stress levels almost all the life was spent in nucleation of a 5 µm crack. At higher stress levels, i.e, σ_{max} = 1040 and 925 MPa, about 60 % of life was still spent in crack nucleation.

Figure 16 shows a comparison between the crack propagation lives, in terms of the mean lives of the Type-I versus Type-II failures and the lower bound on the life at each stress level. It is clear that the lower bound on life was controlled by the crack propagation life, although the variability in life was controlled by the crack nucleation stage. It is not surprising to find that the lower bound on lives correlated well with the crack growth lives that were based on an initial crack on the order of α_p particle size (about 5 µm) (Fig. 16). The total fatigue life of this alloy can therefore be divided into the life for formation of the crack across an α_p particle and the life for propagation of this crack to failure. It is clear that there was a significant contribution of crack propagation in the life of Type I failures (Fig. 16), indicating that cracks nucleated early in the lives of these specimens. On the other hand, lives of Type II failures were dominated by crack nucleation (Fig. 16).

3.5 Crack Nucleation Mechanism

There are at least three factors in the fatigue of Ti-6-2-4-6 that seem to indicate that the variability in life of this alloy was controlled by the degree of deformation accumulation leading to formation of the crack. Firstly, the crack nucleated across equiaxed α_p particle, both in the case of the Type I and the Type II failure. This eliminates the possibility of the difference in life being caused by different types of crack

origins. Secondly, the size of the initial crack or the crack-nucleating α_p particle was independent of the type of failure, i.e., independent of life. This is an interesting result, since in several materials it is believed that the difference in life is caused by the size of the crack-nucleating feature [25-26]. This possibility is, however, essentially ruled out in the present case. Thirdly, the stage-I crack was similarly oriented with respect to the loading axis for both types of failure (Fig. 14), indicating that difference in life was not caused by the difference in the orientation of the stage-I crack. The combination of these factors suggests that the variability in life may have been caused by a mechanism of delayed deformation accumulation in the case of the higher-life failure and vice versa. This is discussed in more detail in the following.

The deformation accumulation within equiaxed α_p particles can be influenced by the degree of slip transfer to surrounding α particles. Therefore, it seems that the degree of slip transfer, as influenced by the orientation distribution of a group of α particles, may control the variability in crack nucleation life and thus the total life. In $\alpha+\beta$ titanium alloys with a mixed lamellar α/β and equiaxed-α structure it is known [43,44] that at the start of cycling, deformation is heterogeneous and confined to only a few suitably oriented α particles. The deformation is subsequently homogenized with further cycling through slip transfer to unfavorably oriented particles [43,44]. This type of mechanism is schematically illustrated in Fig. 17. The α platelets have been ignored in this figure for illustrative purposes. It can be suggested that depending on the orientation distribution of a given group of α particles, a crack can nucleate when the deformation is in the heterogeneous regime (Fig. 17(a)), leading to the Type-I failure. However, if the degree of slip transfer is such that the deformation is homogenized relatively easily, the crack

nucleation occurs only after most of the α particles have deformed and the deformation has saturated (Fig. 17(b)), leading to the Type II failure. Clearly, the problem is more complex than illustrated in Fig. 17, due to the duplex nature of the microstructure in this case. Nevertheless, the key to tackling the variability in fatigue lives of Ti-6-2-4-6 seems to lie in the understanding of the formation of cracks at the size scale of an equiaxed α_p particle, i.e., about 2 to 10 μm.

Conclusions

Based on the current research on the fatigue life variability of Ti-6-2-4-6, the following conclusions can be drawn:

(i)   The variability in fatigue lives of Ti-6-2-4-6 increased with decreasing stress amplitude.

(ii)   Two types of failure mechanisms were identified based on the step-like morphology of experimental data on the CDF plot. The mean lives of the two types of failures, designated as Type-I and Type-II, differed by approximately two orders of magnitude. Further, the likelihood of one type of failure vs. the other shifted with stress level.

(iii)   The variability in life was introduced primarily at the crack nucleation stage, i.e., during formation of the stage-I crack (about 2-10 μm size) across an equiaxed α_p particle.

(iv)   The variability in life seems to be controlled by the degree of deformation accumulation in a suitably oriented α_p particle as influenced by the orientations of the surrounding α particles.

References

[1] P. E. Magnusen, R. J. Bucci, A. J. Hinkle, J.R. Brokenbrough, H. J. Konish, Int. J. Fatigue 19 (1998) S275

[2] J. M. Larsen, R. John, S. M. Russ, D. C. Maxwell, B. D. Worth, A. H. Rosenberger, K. Li, W. J. Porter, in: K. S. Ravichandran, R. O. Ritchie, Y. Murakami (Eds.), Small Fatigue Cracks: Mechanics, Mechanisms and Applications, Elsevier Science, Oxford, UK, 1999, p. 131

[3] M. P. Kaplan, T. A. Wolff, Fatigue and Fracture, ASM Handbook, Vol. 19, 1996, p. 557

[4] B. A. Cowles, Materials Sci. Eng. A103 (1998) 63

[5] J. N. Yang, G. C. Salivar, C. G. Annis, Jr., Engng. Fract. Mech. 18 (1983) 63

[6] S. Akita, M. Ichikawa, Int. J. Fract. 32 (1986) R3

[7] D. W. Hoeppner, AGARD, Conf. Proceedings No. 393, p. 4.2

[8] C. Kaynak, A. Ankara, T. J. Baker, Int. J. Fatigue 18 (1996) 17

[9] J. Lankford, Fatigue Fract. Engng. Mater. Struct. 8 (1985) 161

[10] L. Wagner, G. Lutjering, Z. Metallkde. Bd. 78 (1987) 369

[11] K. Sobczyk, B. F. Spencer, J. Tribicki, Arch. Mech. 52 (2000) 761

[12] K. S. Chan, in: A. F. Blom (Ed.), Fatigue 2002, Proceedings of the Eighth International Fatigue Congress, Vol. 1, p 347, 2002

[13] J. F. Lei, Q. J. Wang, Y. Y. Liu, S. X. Guan, Z. G. Wang, D. Li, Z. Q. Hu, J. Mater. Res. 12 (1997) 2571

[14] P. J. Laz, B. A. Craig, B. M. Hillberry, Int. J. Fatigue 23 (2001) S119

[15] M. T. Todinov, Mater. Sci. Eng. A255 (1998) 117

[16]   M. A. Przystupa, R. J. Bucci, P. E. Magnusen, A. J. Hinkle, Int. J. Fatigue 19 (1997) S285

[17]   B. Skallerud, T. Iveland, G. Harkegard, Engng Fract Mechanics 44 (1993) 857

[18]   D. P. Kendall, Transactions of the ASME 108 (1986) 490

[19]   J. Ruppen, D. Eylon, A. J. McEvily, Metall. Trans. A 11A (1980) 1072

[20]   R. Chait, T. S. DeSisto, Metall Trans. A 8A (1977) 1017

[21]   O. Umezawa, K. Nagai, ISIJ International, Vol. 37 () 1170

[22]   A. Atrens, W. Hoffelner, T. W. Duerig, J. E. Allison, Scripta Metallurgica 17 (1983) 601

[23]   D. F. Neal, P. A. Blenkinsop, Acta Metall. 24 (1976) 59

[24]   J. Lankford, S. J. Hudak, Jr., Int. J. Fatigue 9 (1987) 87

[25]   O. Umezawa, K. Nagai, ISIJ International 37 (1997) 1170

[26]   Y. Murakami, M. Takada, T. Toriyama, Int. J. Fatigue 16 (1998) 661

[27]   W. L. Morris, M. R. James, in: J. Lankford, D. L. Davidson, W. L. Morris, R. P. Wei (Eds.), Fatigue Mechanisms: Advances in Quantitative Measurement of Physical Damage, ASTM, p. 179, 1983

[28]   K. Sobczyk, B. F. Spencer, Jr., Int. J. Fatigue 17 (1995) 521-530, 1995

[29]   A. Atrens, W. Hoffelner, T. W. Duerig, J. E. Allison, Scripta Metallurgica 17 (1983) 601-606

[30]   D. F. Neal, P. A. Blenkinsop, Acta Metall. 24 (1976) 59

[31]   Q. Y. Wang, J. Y. Berard, A. Dubarre, G. Baudry, S. Rathery, C. Bathias, Fatigue Fract. Engng. Mater. Struct. 22 (1999) 667

[32]   Y. Murakami, M. Takada, T. Toriyama, Int. J. Fatigue 16 (1998) 661

[33] S. K. Jha, K. S. Ravichandran, Scripta Materialia 48 (2003) 1207

[34] S. K. Sasaki, Y. Ochi, A. Ishii, Engineering Fracture Mechanics 28 (1987) 761

[35] M. Goto, Fatigue Fract. Engng. Mater. Struct. 17 (1994) 635

[36] S. Tanaka, M. Ichikawa, S. Akita, Engineering Fracture Mechanics 20 (1984) 501

[37] W. L. Morris, M. R. James, in: J. Lankford, D. L. Davidson, W. L. Morris, R. P. Wei (Eds.), Fatigue Mechanisms: Advances in Quantitative Measurement of Physical Damage, ASTM STP 811, 1983, p. 179

[38] J. F. Knott, in: W. O. Soboyejo, J. J. Lewandowski, R. O. Ritchie (Eds.), Mechanisms and Mechanics of Fracture: Symposium in Honor of Prof. J. F. Knott, TMS, Warrendale, PA, 2002, p. 79

[39] A. H. Fischer, A. Abel, M. Lepper, A. E. Zitzelsberger, A. von Glasow, Microelectronics Reliability 47 (2001) 445

[40] H. Yokoyama, O. Umezawa, K. Nagai, T. Suzuki, ISIJ International 37 (1997) 1237

[41] O. Umezawa, K. Nagai, K. Ishikawa, Mater. Sci. Eng. A129 (1990) 223

[42] D. Eylon, J. Mater. Sci. 14 (1979) 1914

[43] A. S. Beranger, X. Feaugas, M. Clavel, Mater. Sci. Eng. A172 (1993) 31

[44] X. Feaugas, M. Clavel, Acta Materialia 45 (1997) 2685

List of Figure Captions

Fig. 1   Microstructure of the Ti-6-2-4-6 alloy

Fig. 2   Fatigue life behavior of Ti-6-2-4-6: (a) Mean lives, and (b) Life variability

Fig. 3   Probability of failure plots at selected stress levels

Fig. 4   Dual failure mechanisms

Fig. 5   Probability of failure plots for the Type I and the Type II mechanism at stress levels of (a) 900 MPa, (b) 860 MPa, and (c) 820 MPa

Fig. 6   Characteristics of the two type of failures: (a) Likelihood of Type I vs. Type II failure with respect to stress level, and (b) Comparison between mean lives in Type I vs. Type II failure

Fig. 7   Illustration of life extension based on the worst case mechanism, i.e., Type I

Fig. 8   Examples of (a) surface and (b) subsurface crack nucleation in Ti-6-2-4-6

Fig. 9   Crack nucleation region of the fracture surface at σ_{max} = 1040 MPa

Fig. 10   Crack nucleation region of the fracture surface at σ_{max} = 860 MPa

Fig. 11   Crack nucleation region of the fracture surface at σ_{max} = 820 MPa

Fig. 12   Fatigue fracture surface of a Type I failure at σ_{max} = 860 MPa: (a) one side of fracture surface, (b) EDS pattern for (a), (c) the other side of fracture surface, and (d) EDS pattern of (c)

Fig. 13   Fatigue fracture surface of a Type II failure at σ_{max} = 860 MPa: (a) one side of fracture surface, (b) EDS pattern for (a), (c) the other side of fracture surface, and (d) EDS pattern of (c)

Fig. 14   Profile of surface cracks: (a) low life, and (b) high life

Fig. 15 Life partitioning between crack nucleation and growth; (a) initial ΔK (ΔK_i) used in the propagation-life calculations, and (b) comparison between the crack nucleation life and the total life with respect to stress level

Fig. 16 Comparison between the crack propagation life, the lower bound on life and lives of Type I and Type II failures

Fig. 17 Schematic illustration of the probable crack nucleation mechanisms in case of (a) Type I and (b) Type II failure

Fig. 1

8µm

Fig. 2

(a)

(b)

Fig. 3

Fig. 4

(a)

(b)

(c)

(d)

206
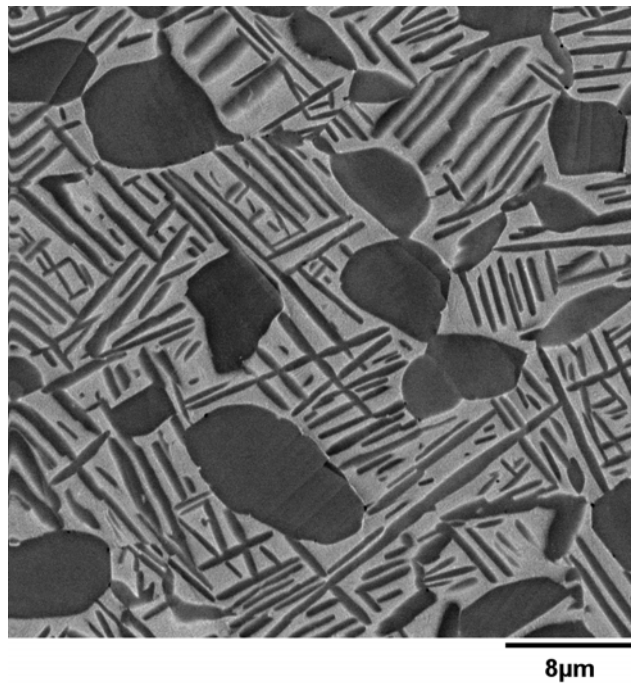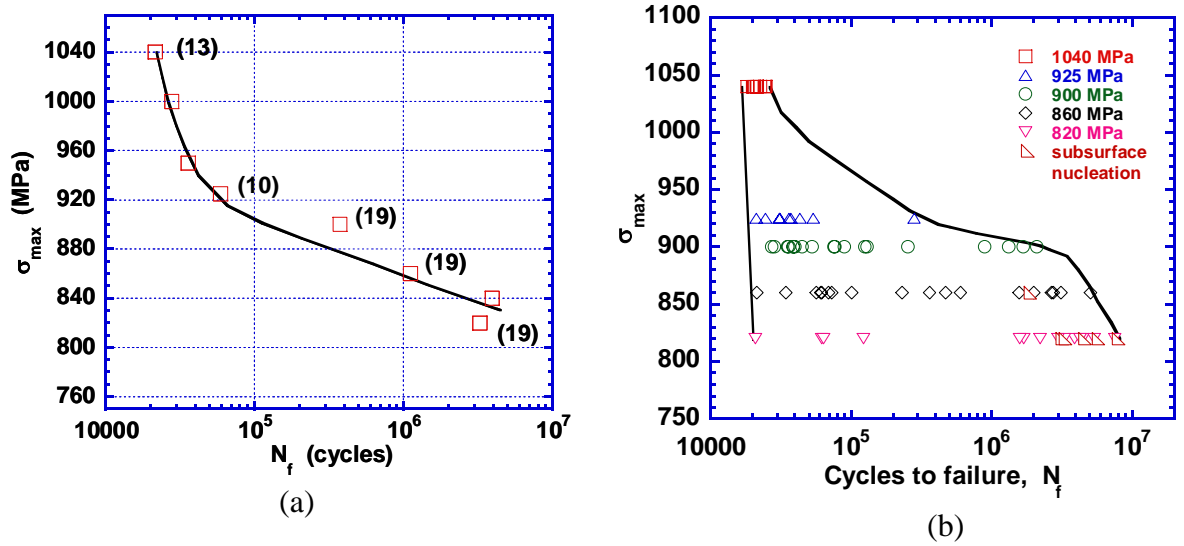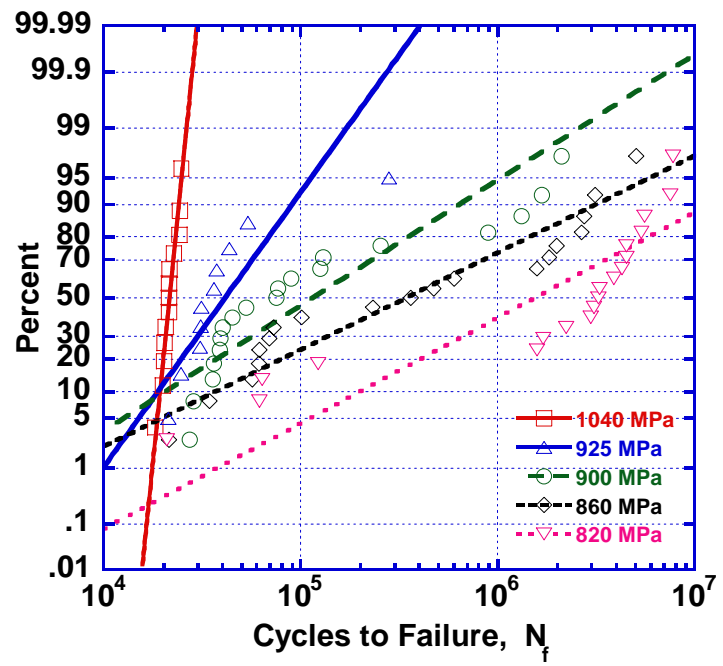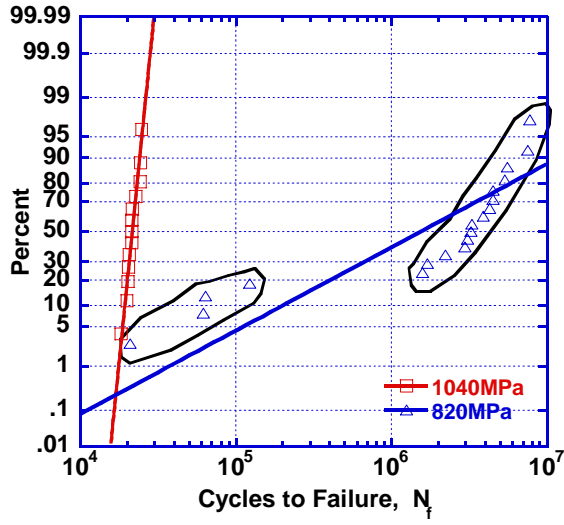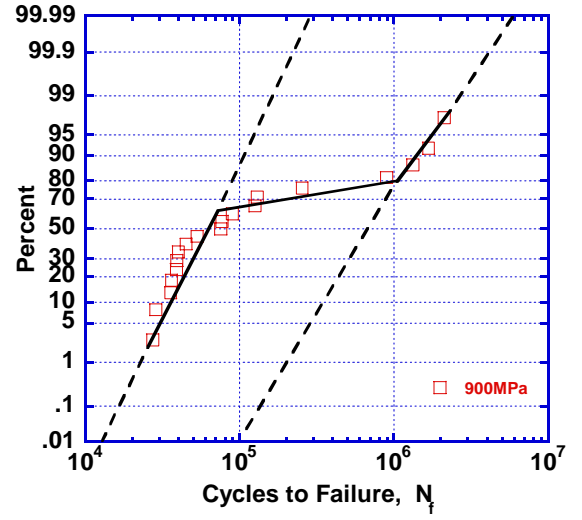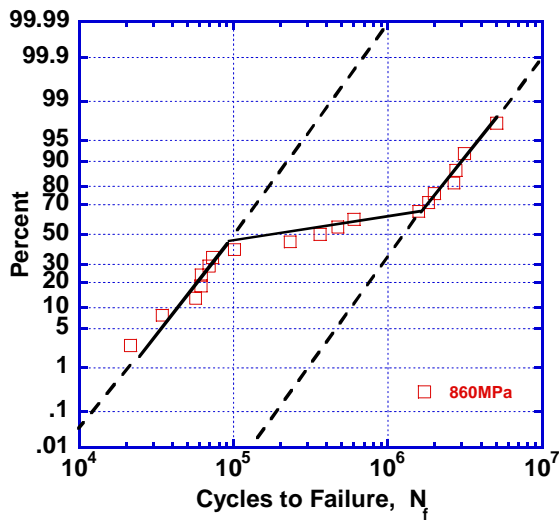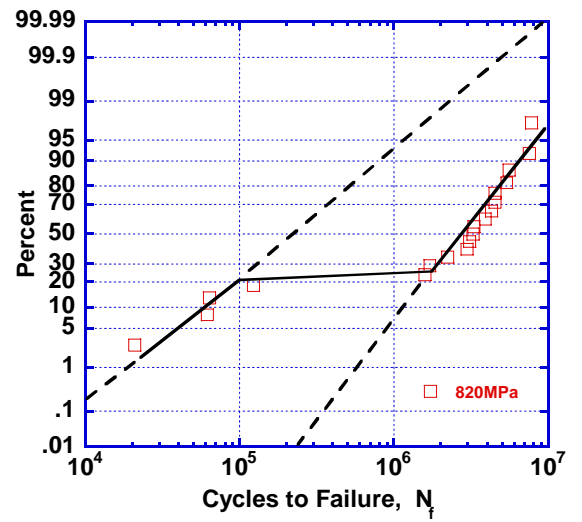
Fig. 5

(a)

(b)

(c)

Fig. 6

(a)   (b)

Fig. 7

209

Fig. 8

(a)   (b)

Fig. 9

(a)   (b)

Fig. 10

(a)   (b)

Fig. 11

(a)   (b)
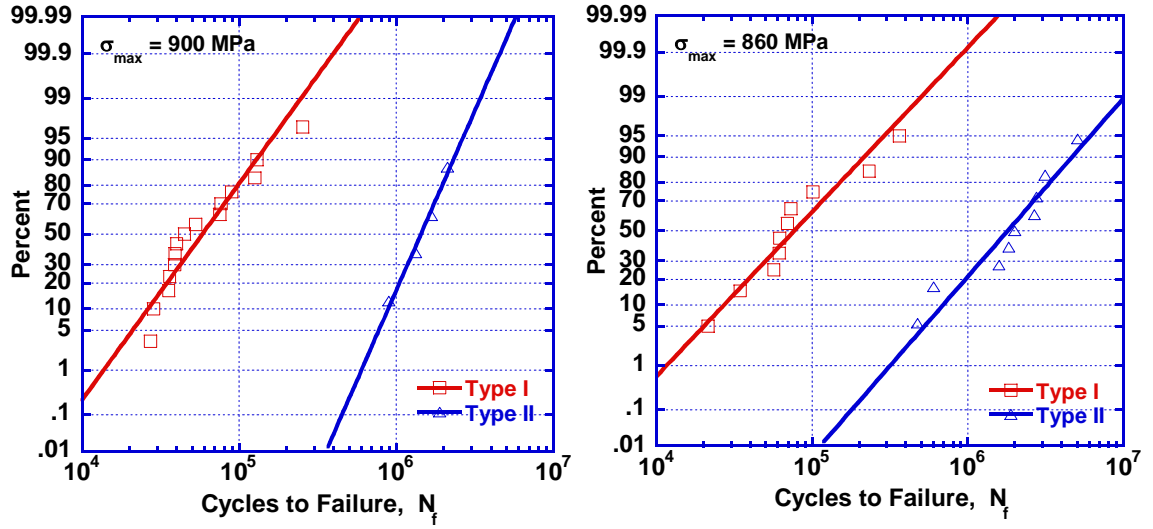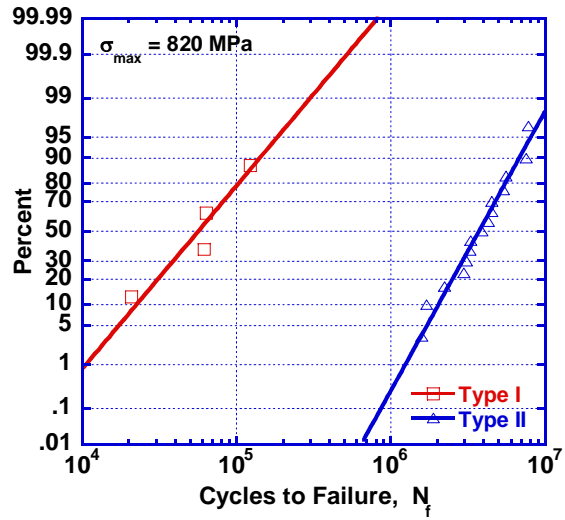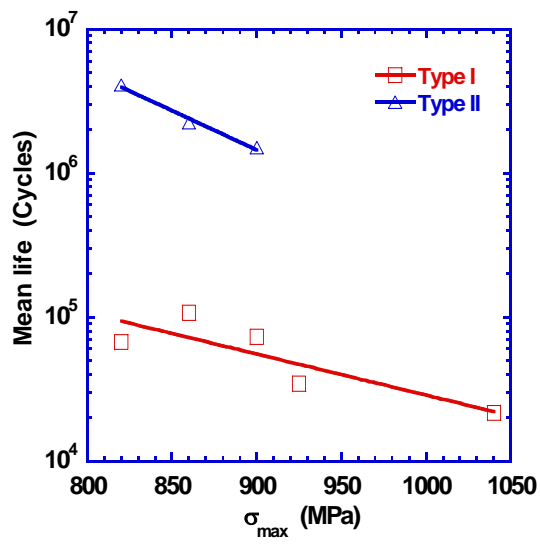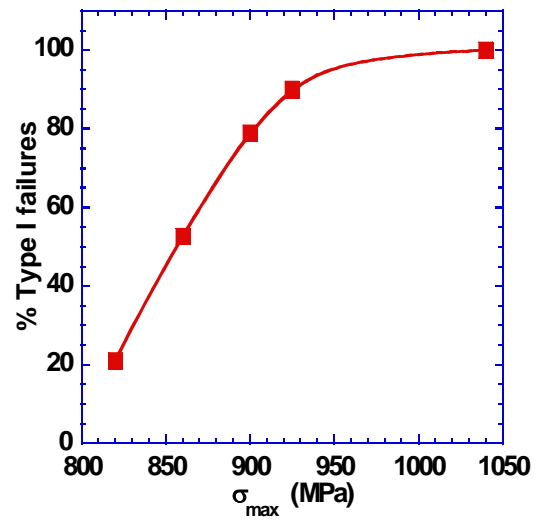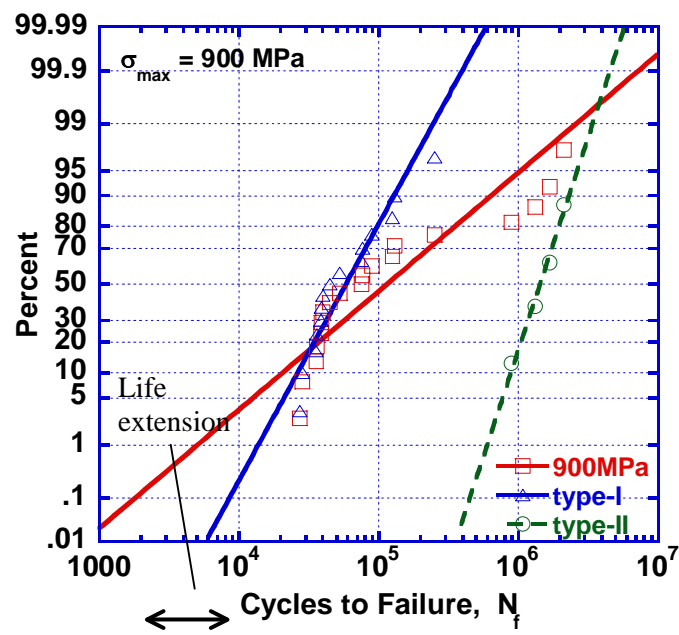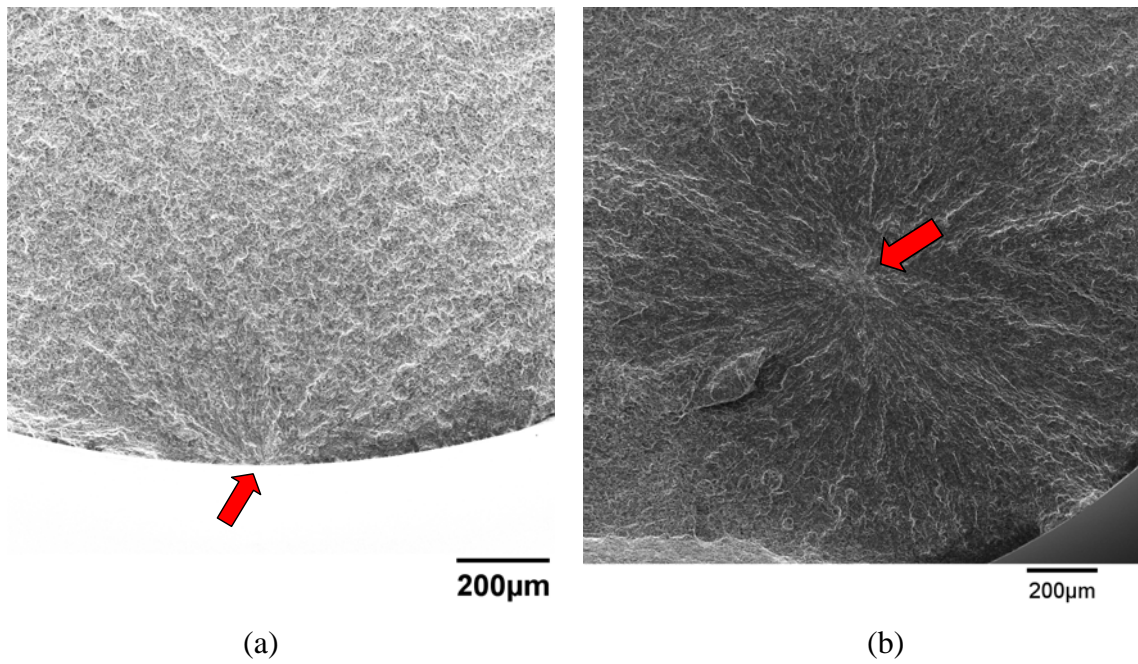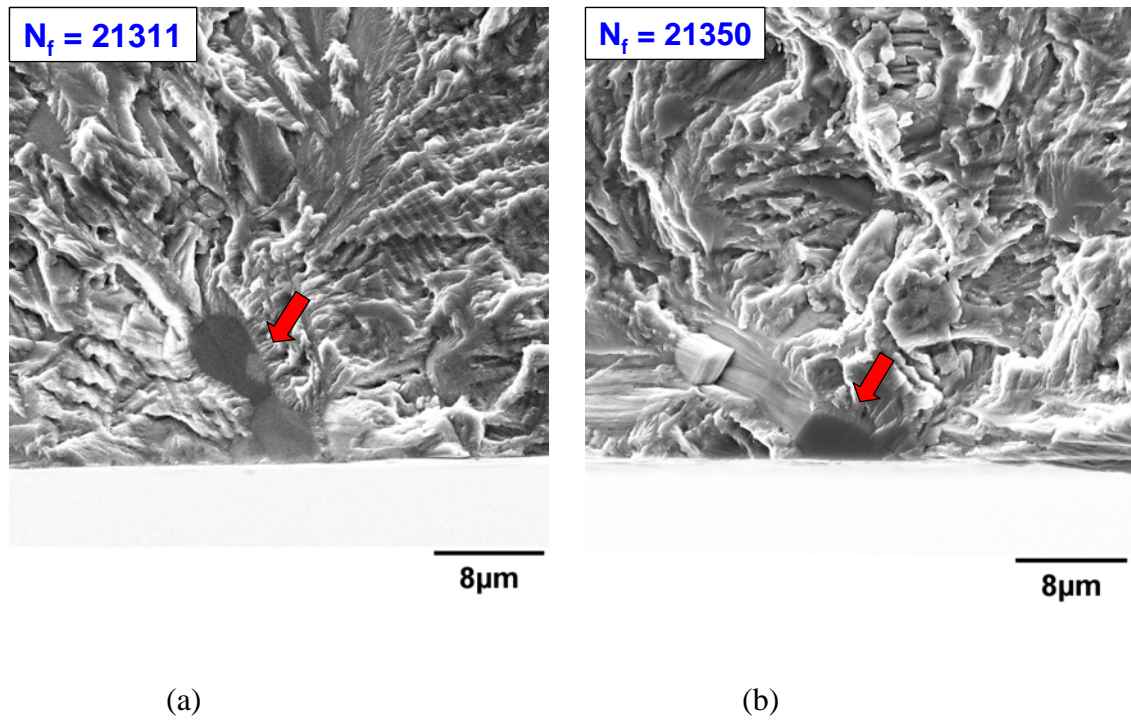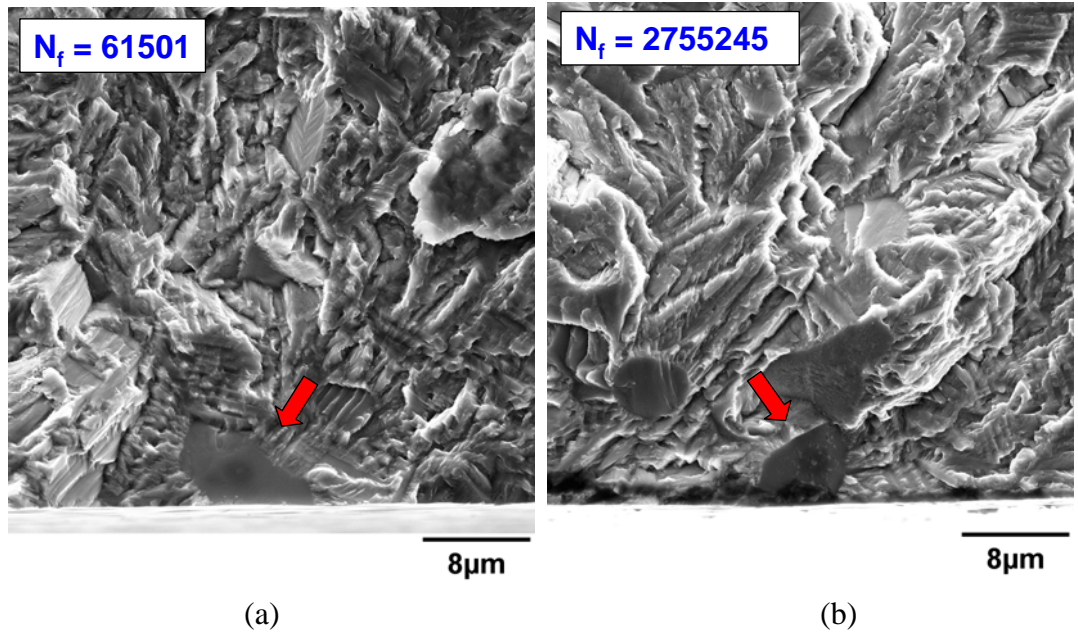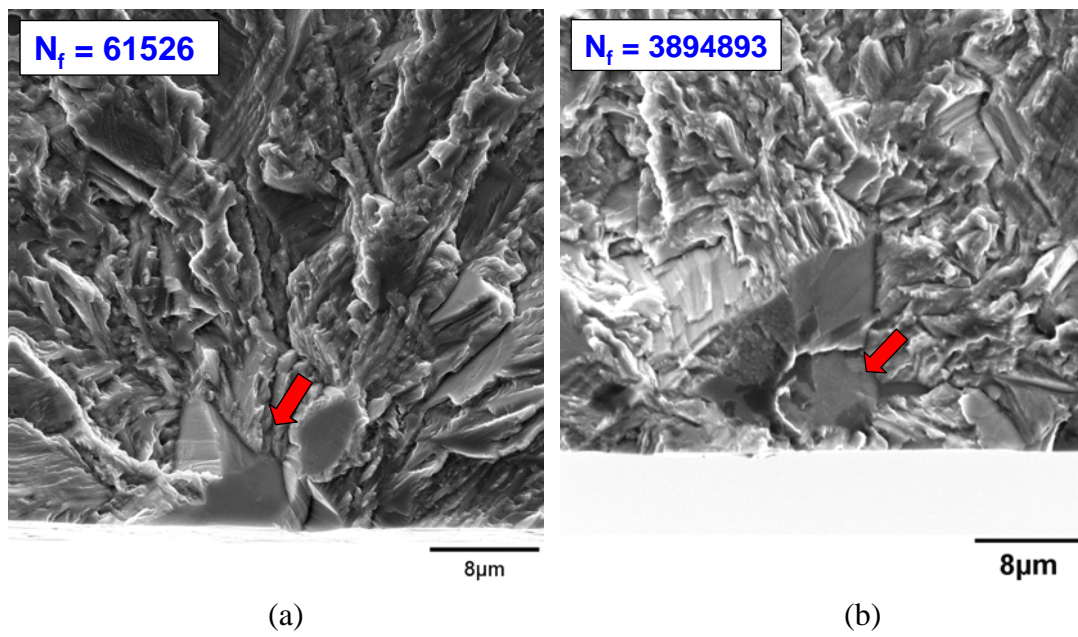
Fig. 12
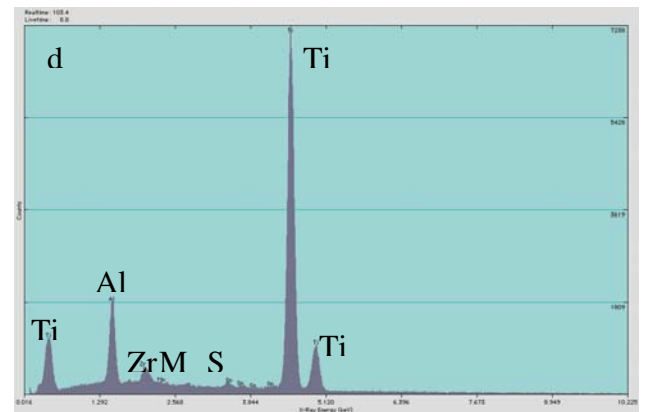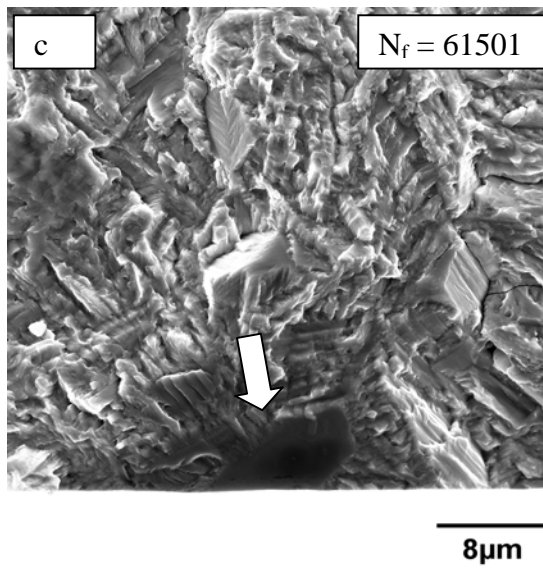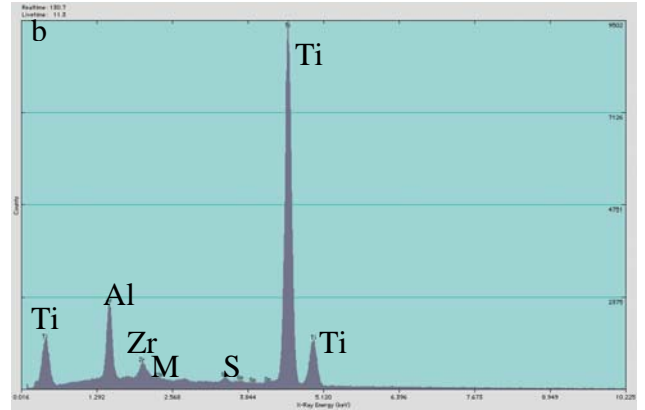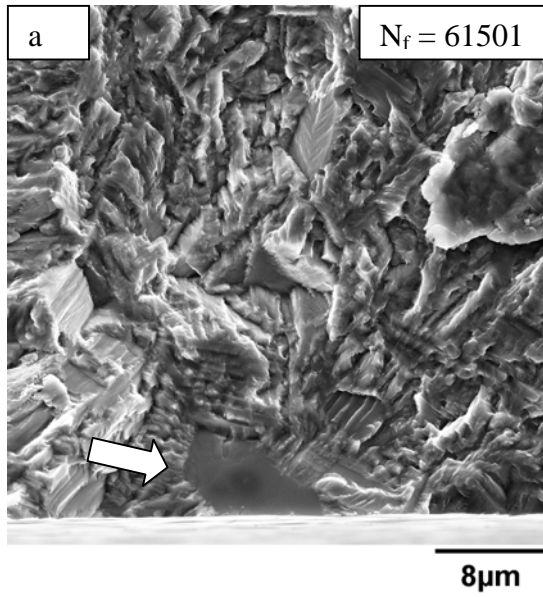
Fig. 13

Fig. 14

(a)   (b)

Fig. 15

(a)

(b)

Fig. 16

Legend:
- Propagation life
- Mean life of all failure points
- Minimum life
- Mean life of Type I failures
- Mean life of Type II failures

Mean life of
Type I failures

Mean life of all
failure points

Propagation life

Cycles

σ_{max}

216

Fig. 17

(a) **Type I**

Heterogeneous deformation

Crack nucleation

(b) **Type II**

Heterogeneous deformation

Homogenization

Saturation

Crack nucleation
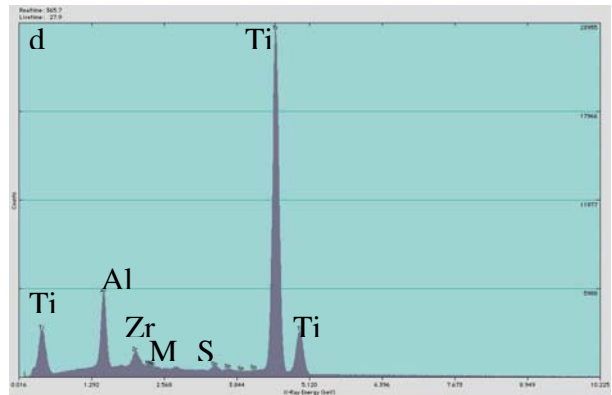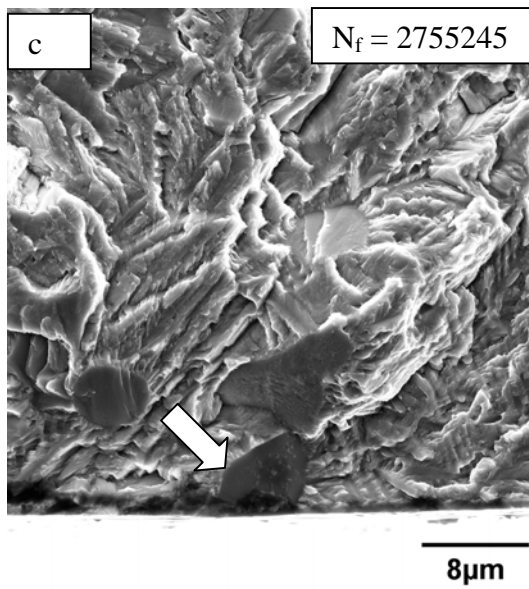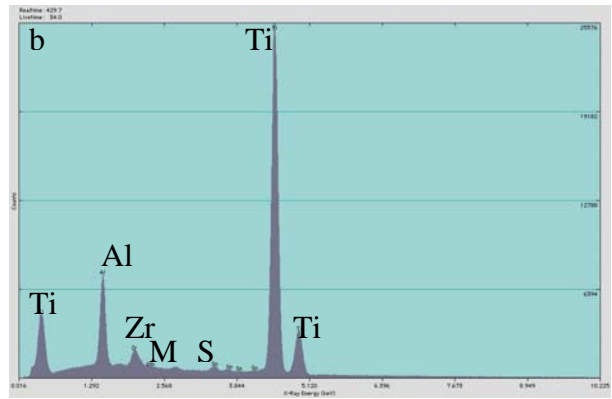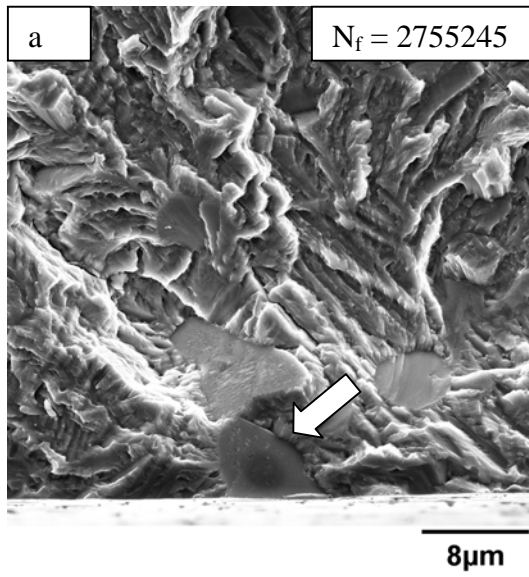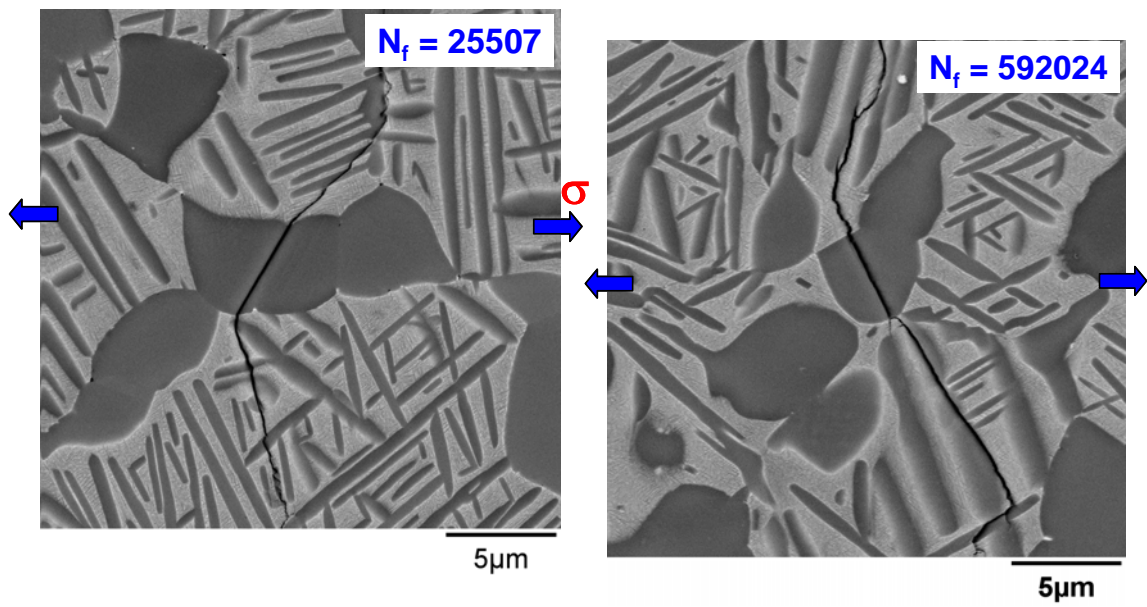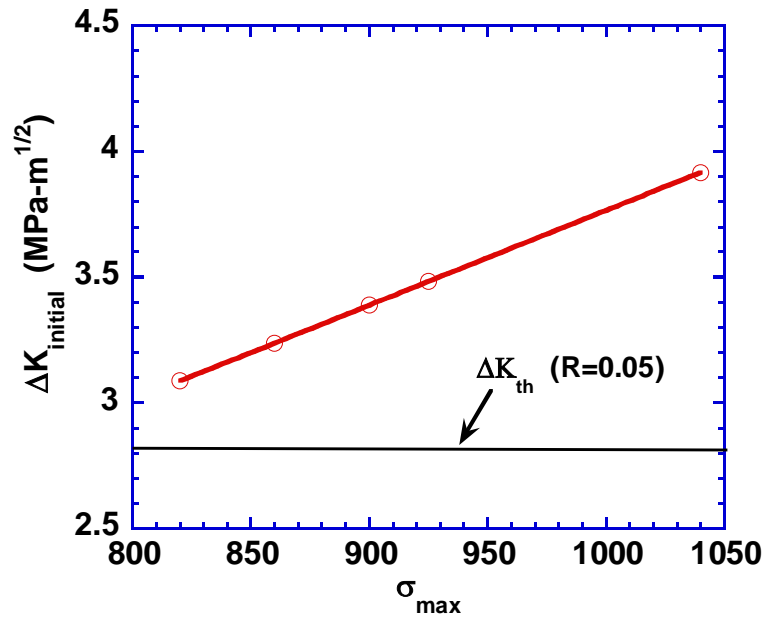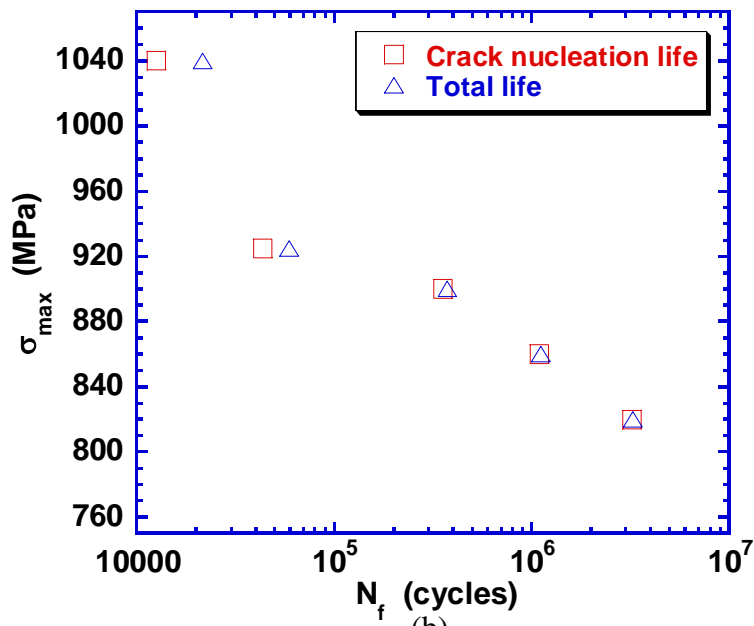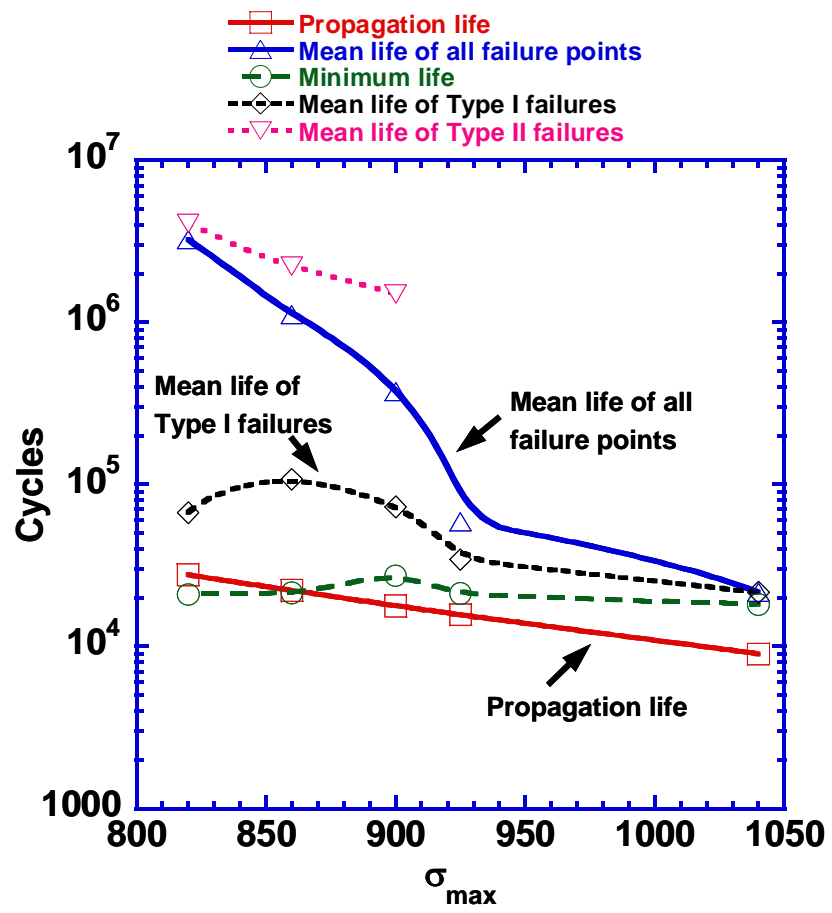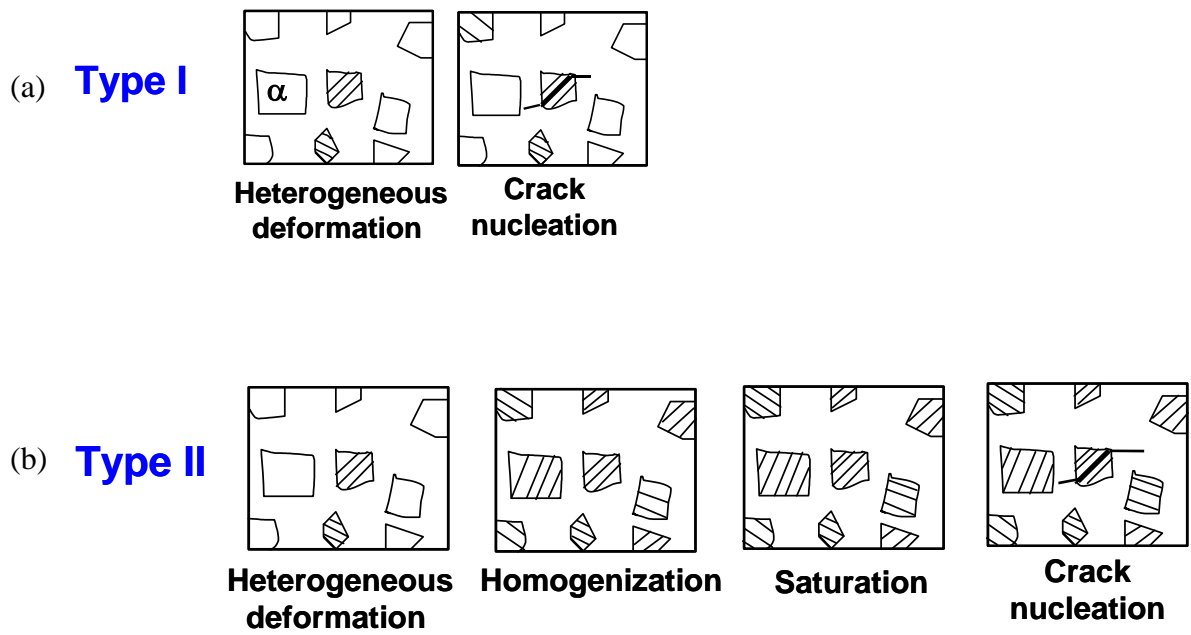
This page intentionally left blank.

INFRARED DAMAGE DETECTION SYSTEM (IDDS)

George A. Hartman* and James M. Larsen;   *Air Force Research Laboratory, Materials and Manufacturing Directorate, AFRL/MLLMN, Wright-Patterson Air Force Base, Ohio 45433-7817, U.S.A.*
* University of Dayton Research Institute, Dayton, OH 45469

ABSTRACT

A sensitive microscope system is used to monitor infrared radiation emitted by a specimen subjected to service loading. Small changes in radiation due to bulk volume dilatation, local work (plasticity, slip, etc.), cavity radiation, modified surface morphology, and other phenomena can be detected and precisely located on the specimen surface. Intensive material science studies can then be directed at the specific local region of the radiation anomaly. Cracks with surface lengths of 15 to 20 μm have been routinely detected in titanium and nickel-base alloys. Additional detection events show no observable surface-connected crack and may be evidence of pre-crack damage evolution. A new camera with improved resolution has recently been installed to detect pre-crack damage evolution events on a regular basis. Studies of the localized damage phenomena at these sites will eventually produce a more thorough understanding of the damage mechanisms under realistic service loading.

Keywords: Infrared, damage detection, crack initiation, damage mechanisms

INTRODUCTION

Damage evolution in metals has traditionally been divided into mechanisms that contribute to initiation of a small crack and those that subsequently cause crack propagation. While there are a number of experimental methodologies available to study both classes of damage evolution, studying crack initiation poses special problems for the researcher. First, the location of a damage event that may lead to crack initiation in an unnotched specimen is unknown – unlike a specimen with a pre-existing crack at a known location. Since the scale of these local damage areas during crack initiation is generally less than 10 μm, their unknown location poses a large logistical problem. If we wish to study a specimen surface 10 mm wide x 10 mm high we need to look at 10^6 areas, each 10 μm square, where damage may be accumulating on a cycle-by-cycle or even intra-cycle basis. Performing this search optically is a daunting task. Even for techniques such as acoustic emission and ultrasonics, precise location of the local damage area is not trivial, especially if there are multiple, simultaneous events.

A preliminary study was begun in 1995 to evaluate the abilities of various research and commercial instruments to identify and precisely locate local damage regions in materials undergoing a variety of service loadings. The technologies reviewed included various types of interferometry, secondary electron emission, acetate (and related) replication methods, acoustic emission, AC potential difference, surface acoustic waves (SAW), optical microscopy, automated optical microscopy, eddy current, thermo-elastic stress analysis, and dye penetrant. Other techniques such as time-reversed ultrasonics and high-resolution acoustic emission have been reviewed since that study. After careful evaluation, surface thermal analysis was chosen as the most likely candidate for development.

Thermal radiation signatures of potential interest in crack initiation include, but are not limited to, thermo-elastic effects, cavity radiation, local plasticity (or any localized inelastic work), changes in surface emissivity, and changes in surface morphology. It should be noted that the equivalent temperature difference associated with a radiation intensity change or the actual temperature change for these phenomena are in the range of a few mK. The specific thermal imaging and analysis techniques used to detect evolving damage are almost certain to vary with the material under study, research objectives, and the physical phenomena expected to give rise to a detectable thermal signature.

We leased and evaluated a commercial thermo-elastic stress analysis system to determine its capabilities and flexibility with respect to crack initiation damage detection and location. Although the commercial system was quite impressive in its sensitivity, it was not possible for our researchers to gain low-level access to the thermal images, modify the number of images used to analyze specific service-loading events, or perform analyses of thermal signatures from sources other than thermo-elastic stress. Accordingly, in 1999 we initiated a development effort to use the best off-the-shelf infrared imaging technology, combined with customized software to develop an Infrared Damage Detection System (IDDS). The purpose of this system is to provide maximum flexibility to researchers who wish to detect and precisely locate localized damage during crack initiation in nominally smooth specimens.

EXPERIMENTAL APPROACH

The AFRL/MLLMN laboratories currently have two IDDS units integrated with material test systems. One is fitted with an older 256x256 resolution camera, and one is fitted with a state-of-the-art 640x512 resolution camera. Both cameras use InSb detectors and are sensitive to radiation in the 3 to 5 μm Mid Wavelength Infrared Radiation (MWIR) band.

Both IDDS units have microscope lenses that allow full-field high-resolution specimen imaging. The newer camera, with its higher pixel count, is capable of observing five times the specimen area while maintaining the same image resolution at the specimen surface. A typical field of view at the specimen surface for this camera might range from 5 x 4 mm to 10 x 8 mm. Since the specimen translates as the applied loads change, the software has integral image motion correction for directly comparing images taken at different applied loads. Image acquisition points within a service-loading event (e.g. loading cycle) are independently adjustable, and images are displayed using a repeating fringe method where the fringe range and color palettes are operator adjustable.

Simple Infrared Damage Detection Methodologies

Rather than attempt to implement more difficult imaging and image analysis techniques immediately, our approach has been to construct a flexible software and hardware base and to incrementally build more sophisticated

capabilities. Our initial IDDS development was therefore focused on thermo-elastic imaging, plus averaging and differencing image analysis, since these are the simplest methods to implement and evaluate.

Thermo-elastic temperature changes are induced by elastic bulk deformation of the material. Measurements of thermo-elastic temperature changes are obtained by subtracting a thermal image taken at one elastic stress state, or applied load, from a thermal image taken at a different elastic stress state. When the specimen is subjected to repeating cyclic loading this is a straightforward process that is widely used in commercial thermal stress analysis systems.

The first, and simplest, damage detection trials in our laboratory were conducted manually by observing an image of the thermo-elastic temperature change of the specimen on a computer display as service loading was applied. With practice, a trained operator can detect cracks between 100 and 400 μm in surface length using this simple method on a titanium alloy. Note that all surface crack lengths discussed here were confirmed with the specimen under full load in a Scanning Electron Microscope (SEM) using backscatter detection.

The first improvement to the simple damage detection method described above is to save one thermo-elastic temperature change image early in the test – presumably before any localized damage has occurred. This reference image is then subtracted from subsequent thermo-elastic temperature change images, yielding a differential image containing only the changes that have accrued during the intervening applied service loading. Figure 1 illustrates a typical differential image with the automatically detected crack and associated SEM image. With this somewhat improved method, a trained operator can detect cracks between 50 and 100 μm surface length on a titanium alloy.

Automation of the damage detection task is clearly the next enhancement step, and several algorithms have been developed to maximize detection sensitivity for crack-like defects as well as less distinct damage areas. Using the best of these algorithms, automatic damage detection applied to differential thermo-elastic images can reliably detect cracks with surface lengths less than 25 μm in a titanium alloy.

Results for various tests using the three simple imaging and image analysis methods discussed in this section are shown in Figure 2. Note the dramatic decrease in crack size detection as the image acquisition and analysis techniques are improved. The advanced IDDS methodologies discussed in the next section should allow further improvement in our damage detection capabilities.

Advanced IDDS Methodologies

The image acquisition and analysis software is in the final stages of a major upgrade to handle the next series of imaging and image analysis methods we wish to evaluate. One imaging method being pursued is direct tracking of changes in the thermal image at the same point in every loading event. This method does away with tracking of changes in the thermo-elastic response and instead focuses directly on changes in the specimen thermal image as service loadings are applied. We intend to evaluate this method for tracking local inelastic events, as well as cavity radiation. Several other imaging methods are also being considered to focus on different physical phenomena, including localized energy dissipation due to microstructure-scale events. Finally, we are poised to launch investigations into image analysis techniques that are more sophisticated than the simple averaging and difference methods. One and two-dimensional Fourier transforms, histogram analysis, and various region-of-interest methods are being considered.

EXPERIMENTAL RESULTS

All of the data in the previous and following discussions were acquired with the 256x256 resolution camera, as the newer, high-resolution camera has just recently come on-line.

IDDS Studies have been conducted on Ti-6Al-4V, Ti-6Al-2Sn-4Zr-6Mo, Ti-17Al, γ TiAl (an intermetallic), and IN100 (a nickel-base superalloy). Figure 3 is a photo of the 256x256 camera, specimen, and load frame used for these research studies. Note that the infrared radiation-blocking curtain has been removed so that the camera, specimen, and grips can be seen. The blocking curtain must be used during testing because the camera sensitivity is such that small changes in reflected radiation from objects in the room would swamp the signals from the specimen.

A typical test consists of careful specimen preparation and setup followed by cyclic specimen loading to simulate a selected service condition. During the early cycles, a baseline infrared image is acquired and subtracted from subsequent images to produce differential images. The operator typically monitors these differential images, although any of the constituent images can be viewed as well. Once the system has stabilized, the detection threshold limits are set and enabled, and the test is allowed to run unattended. Tests of this type typically take two or three hours to set up and run until a local damage event is detected. The test time, of course, depends on the loading conditions and material under study.

It should be noted that, with the IDDS, we have been able to produce two or three specimens per day with very small local damage regions that are precisely located. The ability to provide material scientists with a large number of samples containing known local damage regions allows them to focus their microstructural studies on specific locations associated with the first damage event. This reduces to a manageable level the time required to study the mechanisms leading to the damage.

We appear to be on the threshold of detecting damage events prior to self-similar crack initiation. In one study of different image acquisition and processing methods, a set of nine specimens was tested. Six were confirmed via SEM imaging to have cracks with surface lengths between 10 and 25 μm at the IDDS-specified locations. In the remaining three specimens no surface-connected cracks could be observed, even after extensive SEM observations of the IDDS-specified locations. It is not clear at this time if these detections are false-positives, sub-surface cracks, or pre-crack-formation damage sites.

In another test program using a limited number of specimens of IN100, a nickel-base superalloy, results showed that the IDDS is capable of reliably detecting 15 μm surface length cracks.

SUMMARY

Based on the success of the initial studies using simple imaging and image analysis methods, we are eager to determine if the improved camera resolution and more sophisticated acquisition and analysis algorithms will provide a convenient means of detecting and precisely locating local damage prior to crack initiation. If this is possible, then detailed microstructural studies can be performed in an efficient manner to shed new light on the mechanisms that lead to crack initiation under real-world service conditions.
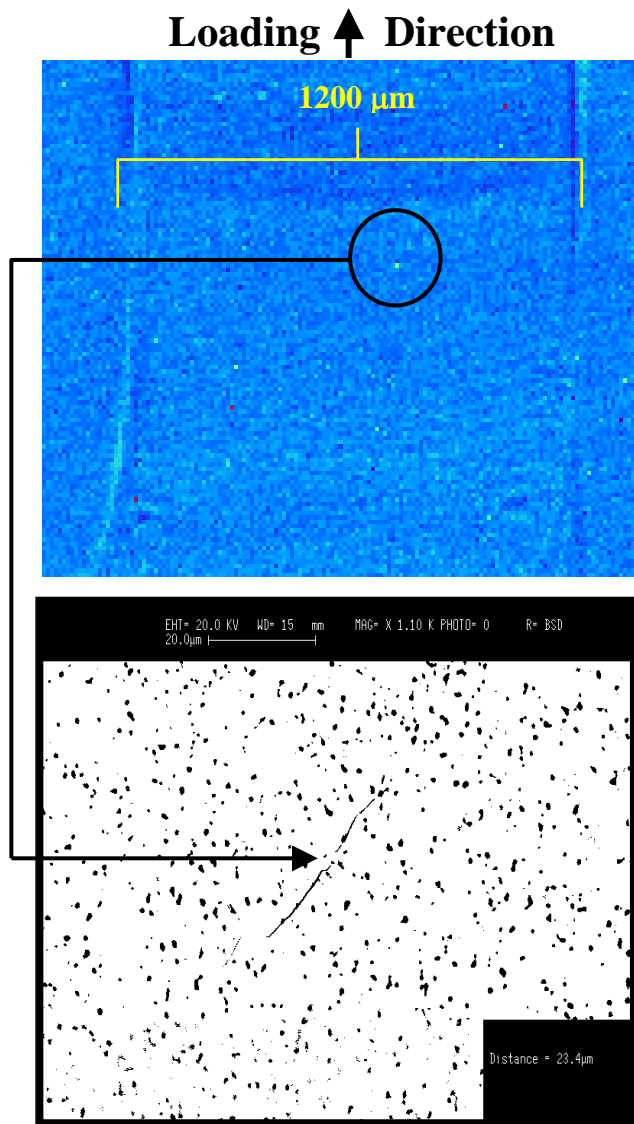
Figure 1. IDDS Automatically Detected Damage Site and SEM Confirmation.
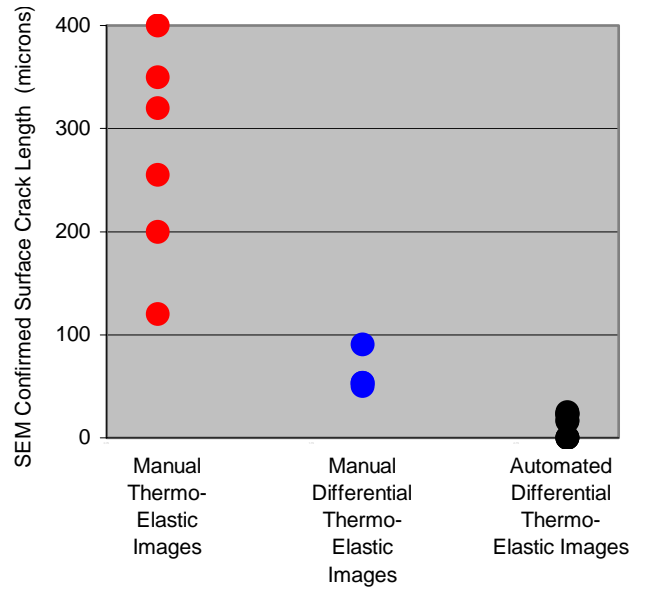
Figure 2. Representative IDDS Data From Multiple Materials Using Simple Imaging and Image Analysis Methods.
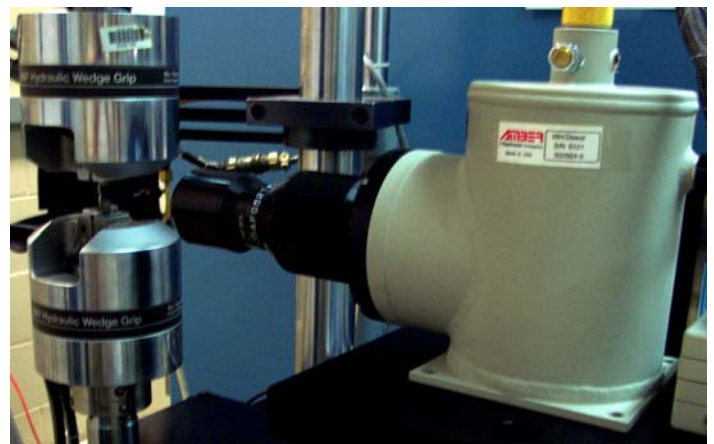
Figure 3. IDDS Camera and Specimen Setup.

This page intentionally left blank.

A fracture mechanics methodology assessment for fretting fatigue

T. Nicholas[3],*, A. Hutson[2], R. John[1] and S. Olson[2]

[1]*Air Force Research Laboratory, ML, Wright-Patterson AFB, OH 45433, USA*
[2]*University of Dayton Research Institute, Dayton, OH 45469, USA*
[3]*Air Force Institute of Technology, AFIT/ENY, Wright-Patterson AFB, OH 45433, USA*

1. Introduction

Fretting fatigue is a type of damage occurring in regions of contact where small relative motions, on the order of tens of microns, occur. It is usually associated with loading conditions where one of the components is subjected to bulk loading, which will cause cracks formed locally near edges of contacts to propagate. Such conditions can lead to premature crack initiation and failure. Fretting fatigue damage in blade/disk interfaces has been indicated as the cause of many unanticipated disk and blade failures in gas turbine engines.

Under laboratory conditions, the synergistic effects of the many parameters involved make determination and modeling of the mechanical behavior of fretting fatigue extremely difficult. In particular, the stress state in the contact region involves very high peak stresses, extremely steep stress gradients, multi-axial stress states and differing mean stresses. Further, there is controversy over whether the problem is primarily one of crack initiation or one involving a crack propagation threshold, and whether or not stress states rather than surface conditions play a major role in the observed behavior. Attempts to examine the stress states leading to the initiation and subsequent propagation of fretting fatigue cracks have been less than successful. In particular, similar stress states have not been found in geometric conditions, which have the same fretting fatigue life [1]. Further, these stress states have been found to depend highly on the assumed coefficient of friction, μ. Finally, the stress states have been multiaxial and involved gradients, making it difficult to predict the values that might lead to crack initiation based on smooth bar fatigue data. An alternate approach has been to look at the problem from a fracture mechanics viewpoint, with an attempt to see if crack driving forces exceed the threshold for crack propagation [2,3]. Many unanswered questions remain about what constitutes an initiated crack length and along what direction should the crack be expected to propagate. To help answer some of these questions, a detailed analysis of the fracture mechanics parameters in the contact region was undertaken. The objectives of this investigation were to analyze several different fretting fatigue conditions analogous to the fatigue limit stress under uniaxial fatigue loading corresponding to a chosen high cycle fatigue (HCF) life. From these, both multi-axial stress fields and mixed-mode stress intensity factors for specific cases were obtained in order to find some commonality which may lead to development of parameters having broad application to fretting fatigue. Variations in coefficient of friction, μ, were also evaluated.

2. Experiments

Tests were conducted using a high frequency test system to simulate the fretting fatigue loading conditions that occur in turbine engine blade attachments. The results of these tests have been reported in [1] and [2]. The apparatus uses flat fretting pads, with a radius at the edge of

contact, against a flat specimen. Normal and shear loads are applied to the specimen as shown in Fig. 1. Prior analysis has shown that the bending moment present in the apparatus is negligible relative to other parameters, and may be disregarded when designing the tests [1].
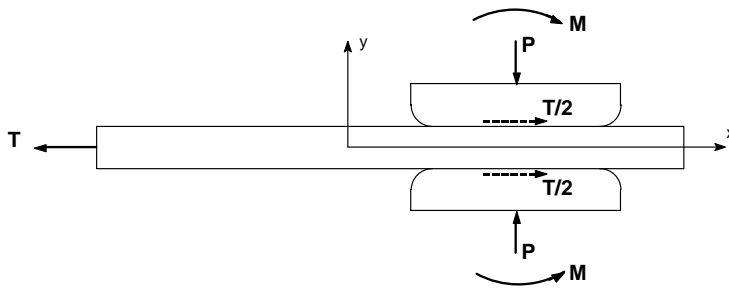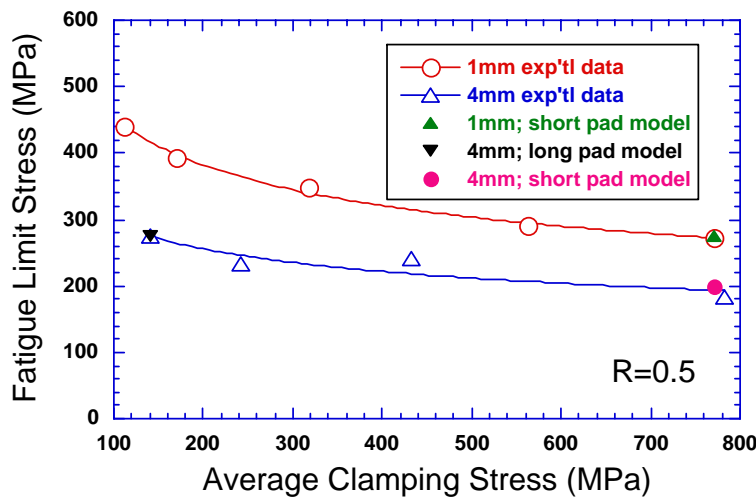

Fig. 1. Test geometry and loading schematic.

Fig. 2. Fatigue limit stress as function of average clamping stress. Conditions modeled are shown.
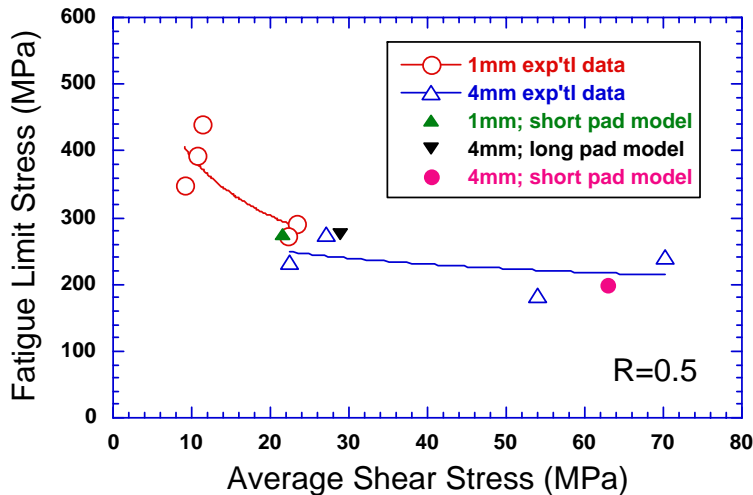

Fig. 3. Fatigue limit stress as function of average shear stress. Conditions modeled are shown.

In this unique test geometry, the axial stress is transferred entirely to the fixture through shear and is determined directly from the load applied to the specimen. As with a conventional fretting fatigue apparatus, the clamping force is constant and only the axial and shear loads are oscillatory. All tests were conducted at 300 Hz under ambient lab conditions. Specimens and pads were taken from forged Ti-6Al-4V plates used in a series of investigations under a U.S. Air Force sponsored high cycle fatigue program [1,4]. For several different pad geometries and clamping loads, the axial stress corresponding to a fatigue life of 10^7 cycles was obtained and used in the analysis described below. The experimental conditions evaluated are summarized in Table 1. The axial stress has been found to be relatively insensitive to the clamping load for the identical geometry in some cases. Figures 2 and 3 show fatigue limit stress data from prior investigations summarized in [2] for the two thickness specimens used here. For the 4mm thick specimen, fatigue strength is relatively insensitive to the average clamping stress as well as the average shear stress. The figures also show the specific conditions modeled in this investigation. In all of the experiments and analysis, the stress ratio, R, is 0.5. The clamping stress and shear stress are based on the undeformed contact length and are average values over that length

and the particular width of the specimen of a given thickness.

Case Number	Specimen Thickness (mm)	Contact Length (mm)	Clamping Load (kN)	Clamping Stress (MPa)	Specimen Axial Stress (MPa)	Contact Shear Stress (MPa)	COF
1	4	6.35	49	610	200	63.0	0.3
2	4	19.05	34	140	275	28.9	0.3
3	4	19.05	34	140	275	28.9	1.0
4	1	6.35	49	770	275	21.7	0.3
5	1	6.35	35	550	275	21.7	0.3
6	1	6.35	35	550	275	21.7	1.0

Table 1. Summary of test cases analyzed.

3. Analysis

3.1 Stress analysis

Stresses in the region of contact were computed using the 2-dimensional finite element method (FEM) assuming linear-elastic material behavior and plane stress conditions. The choice of plane stress was based on experimental observations that cracks tended to initiate closer to the free edge of the specimens rather than in the middle [5]. ABAQUS was selected as the finite element modeling package. The linear elastic assumption may not be accurate for high clamping stresses since prior work [1,2] has shown that contact stress fields less than 100 μm from the location of peak stress near the edge of contact may involve stresses beyond the elastic limit. The analysis performed here is identical to that reported in [1,2] and used eight node quadrilateral elements, with mesh refinement down to sizes of approximately 6.5 μm near the edges of contact.

The FEM analysis of stresses in the contact region is made for an uncracked body. The development of a crack would influence the local contact stresses, which, in this case, are treated as "far-field" for the purpose of the stress analysis and in the K analysis described in the next section. The stress analysis for the contact region assuming the development of a crack and accounting for its compliance is a formidable problem beyond the scope of this investigation. It is noteworthy that such a procedure was accomplished recently and showed, somewhat surprisingly, that the K analysis of the crack emanating from a contact region does not change appreciably if the crack is accounted for in the FEM analysis [6].

3.2 K Analysis

The approach taken to establish the threshold for propagation of a crack in the fretting region is similar to that of Chan et al. [3] where they employed a worst-case notch (WCN) concept. Noting that the stress state is biaxial in an assumed plane stress state, the Mode I and Mode II stress intensity factors are calculated along a crack having an arbitrary orientation with respect to the plane of the contact between the specimen and the pad. While Chan et al. used closed form analytical solutions for the most part, we employ finite element analysis here
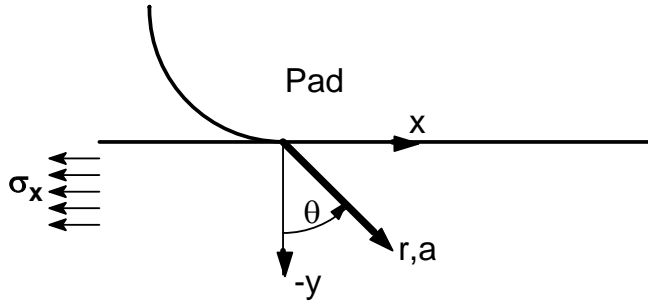
Fig. 4. Nomenclature for orientation in K analysis.

because of the very thin nature of the specimen, which cannot be modeled as a half space. The axis orientation and angle nomenclature are shown in Fig. 4. From the stress analysis, stresses along the crack inclined at an angle θ are computed in the x and y directions and then converted into stresses parallel and perpendicular to the crack. In our approach, we employ the weight function method to calculate the Mode I and Mode II stress intensities along the crack as described later. Note that this is an alternate way to determine K compared to the continuum dislocation formulation used by Chan et al. [3]. Whereas they were concerned with performing calculations for a large number of cases in order to do a parametric study of a wide variety of fretting conditions, necessitating analytical formulations where possible, our study is limited to a few cases. Each of the cases studies here represents a combination of geometries and loadings corresponding to an experiment [1] that produced a fretting fatigue life of 10^7 cycles as determined from a step-loading technique [7].

Two approaches are taken to predict the propagation or non-propagation of a crack in a contact region where the stress field generally produces both Mode I and Mode II stress intensities along the crack. Both of these assume that the crack will initiate due to the high local stresses near the edge of contact. In the first case, it is assumed that the crack will grow along a direction normal to the contact surface and is governed exclusively by pure Mode I. The second approach assumes the crack grows along a straight line having the largest value of an effective stress intensity which is compared with the experimental mixed-mode threshold on that line, including correcting the Mode I threshold for small crack effects as discussed below.

To be able to represent conditions at different values of R ($R = K_{I,min}/K_{I,max}$) with a single parameter, an equivalent stress intensity is used. For the titanium alloy used in this investigation, Mode I crack growth rate and threshold can be represented in the form of a Walker equation,

$$\Delta K_{I,eq} = \Delta K_I (1 - R)^{m-1}$$

(1)

The value of m is assumed to be identical for the threshold and low growth rates, and is calculated from threshold data reported in [8] to be represented by

$$\Delta K_{I,eq,th} = 4.366 - 2.424\, R$$

(2)

For 0≤R≤0.7, the constant in Eq. (1) is found, through a least squares fit, to be m = 0.56. For R < 0, the equivalent ΔK is taken as the maximum value of K. When $K_{I,max}$ is negative, ΔK is taken to be zero.

For mixed-mode behavior, the effective stress intensity factor is defined as

$$\Delta K_{eff} = \sqrt{\Delta K_{I,eq}^2 + \Delta K_{II,eq}^2}$$

(3)

where $\Delta K_{I,eq}$ is determined from the stress field and corrected for different values of R using Eq. (1) while $K_{II,eq}$ is taken simply as ΔK_{II} with no correction for R.

The effective threshold can be modified to account for short crack (SC) effects by introducing the El Haddad parameter, a_0, which produces an ever decreasing threshold as the crack length, a, gets shorter [9] as seen on a Kitagawa type diagram [10]. The Kitagawa type diagram is not limited to simple edge-crack geometries and can, in fact, be utilized for geometries such as those containing notches [11] or those with severe stress gradients as in the contact region being investigated here. The short crack correction produces a threshold in the form

$$K_{eff} = K_{LC} \sqrt{\frac{a}{a + a_0}}$$

(4)

where K_{LC} is the long crack threshold and a_0 is defined as

$$a_0 = \frac{1}{\pi} \left(\frac{K_{th}}{\sigma_e} \right)^2$$

(5)

In Eq. (5), K_{th} is the effective long crack threshold, corrected for R through Eq. (2) for K_{max} rather than ΔK,

$$K_{I,eq,th} = \frac{4.366 - 2.424\,R}{(1 - R)}$$

(6)

while σ_e is the endurance limit stress, also corrected for R. In these and all subsequent equations, K and σ represent maximum values while ΔK and $\Delta\sigma$ represent the ranges of those quantities. The endurance limit stress, represented on a Haigh diagram for constant life of some large number of cycles (10^7 in this case) is conveniently represented for all values of R by the formulation due to Jasper [12] and applied to this material in [7].

$$\sigma_a = \frac{\sigma_{-1}}{\sqrt{2}} \sqrt{\frac{(1 - R)^2}{1 - R\,|R|}}$$

(7)

where σ_a is the alternating stress and σ_{-1} is the maximum of the fatigue limit stress at 10^7 cycles for R=-1. It is easily shown that the maximum of the limit stress at R=0, σ_0, is related to σ_{-1} through

$$\sigma_{-1} = \frac{\sigma_0}{\sqrt{2}}$$

(8)

so that the endurance limit stress in Eq. (5) is taken as

$$\sigma_e = \frac{\sigma_0}{(1-R)}\sqrt{\frac{(1-R)^2}{1-R^2}} \qquad R > 0 \tag{9}$$

It is easily shown that a similar formula can be derived for negative values of R;

$$\sigma_e = \frac{\sigma_0}{(1-R)}\sqrt{\frac{(1-R)^2}{1+R^2}} \qquad R < 0 \tag{10}$$

For the Ti-6Al-4V used here, σ_0 is 569 MPa [1]. No attempt is made here to modify the equations further for negative values of R, as derived in [13], since they are only used to compute the quantity a_0 in this study.

The effective mixed-mode threshold is taken from experimental data as

$$\Delta K_{eff,th} = \Delta K_{I,eq,th}\left[1.5 - 0.5 \exp\left(-0.0418\,\beta\right)\right], \tag{11}$$

$$\beta = \tan^{-1}\left|\frac{\Delta K_{II}}{\Delta K_I}\right| \tag{12}$$

where

The formula, Eq. (11), is used by Chan et al.[3] and the form and constants of the equation are based on the experimental data obtained in [8] on the same titanium alloy being used here. In these equations, β is in degrees and $\Delta K_{I,eq,th}$ is obtained from Eq. (2). A comparison of the form for the driving force, Eq. (3), and the experimental threshold, Eq. (11) can be seen in Fig. 5 where the two equations are plotted against the mode mixity for the same value of ΔK for pure Mode I. The forms of the equations are somewhat different over a range in angle β from 0° to 45°. For some arbitrary value of mode mixity, it is seen that the Mode I driving force would have to be slightly higher than in pure Mode I in order to be at threshold. This difference is discussed further later.

Fig. 5. Comparison of mixed mode driving force and mixed mode threshold for same value of ΔK_I at R=0.

The values of K along a straight line inclined at an arbitrary angle,θ, to the line normal to the contact surface (see Fig. 4), are obtained through the equations:

$$K_I(a,\theta) = \int_0^a h_{11}(r,\theta,a)\sigma_{\theta\theta}(r,\theta)dr + \int_0^a h_{12}(r,\theta,a)\tau_{r\theta}(r,\theta)dr \tag{13}$$

$$K_{II}(a,\theta) = \int_0^a h_{21}(r,\theta,a)\sigma_{qq}(r,\theta)dr + \int_0^a h_{22}(r,\theta,a)\tau_{r\theta}(r,\theta)dr \tag{14}$$

where $\sigma_{\theta\theta}(r,\theta)$ and $\tau_{r\theta}(r,\theta)$ represent the normal and shear stress on the crack surface, respectively, and h_{11}, h_{12}, h_{21}, and h_{22} are the mixed-mode weight functions developed by Beghini et al. [14]. These equations are for an edge crack in an infinite medium. These K_I and K_{II} values were corrected using a surface crack correction factor. For the cracks produced in the fretting fatigue region in [5], an equation for the aspect ratio was obtained in the form

$$a = \gamma (1 - \exp^{-\eta c}) \tag{15}$$

where $\gamma = 213$ and $\eta = 0.005$ are fitting parameters, and "a" and "c" are in units of μm. Knowing "a", "c" was calculated using this equation. Thus we estimate a/c for any crack depth, a. Knowing a/c, the surface crack correction factor, CF, is

$$CF = \frac{1}{\sqrt{\left(1 + 1.464 \left(a/c\right)^{1.65}\right)}} \qquad a/c \leq 1 \tag{16a}$$

$$CF = \frac{1}{\sqrt{\left(1 + 1.464 \left(c/a\right)^{1.65}\right)}} \qquad a/c > 1 \tag{16b}$$

4. Results and discussion

The first case analyzed is the short pad, thick specimen with bulk stress of 200 MPa and clamping load of 50 kN, indicated in Table 1 as Case 1. The first few cycles were simulated in the FE analysis to obtain the stresses at the maximum and minimum applied load. These values were found to stabilize within the first complete cycle. For this case, the stresses are computed along lines of angles of 0°, 10°, 30° and 50°. The normal and shear stresses along the cracks at the different angles are shown in Figs. 6 through 9. For all angles evaluated, the computations show that the shear stress amplitude is small. Further, the stress ratio for the stresses normal to the crack surface, $\sigma_{\theta\theta}$, is nominally about 0.5 for the crack oriented at $\theta=0°$. Normal stresses are seen to decay rapidly with crack length, a, and become compressive for larger angles, $\theta=30°$ and $\theta=50°$.

From these stresses, values of K_I and K_{II} are determined using the equations in the previous section. Further, the short crack corrected threshold for this material, designated SC in
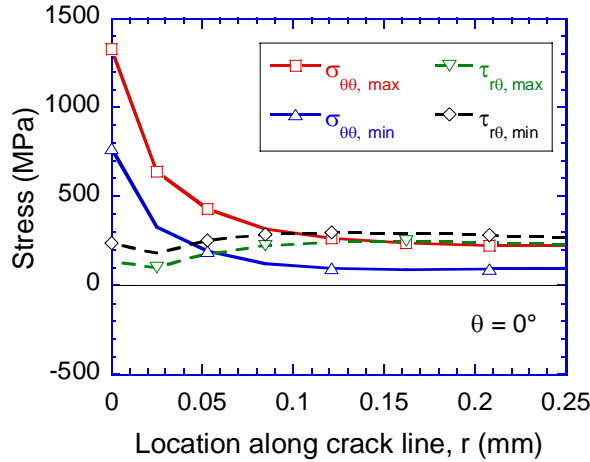
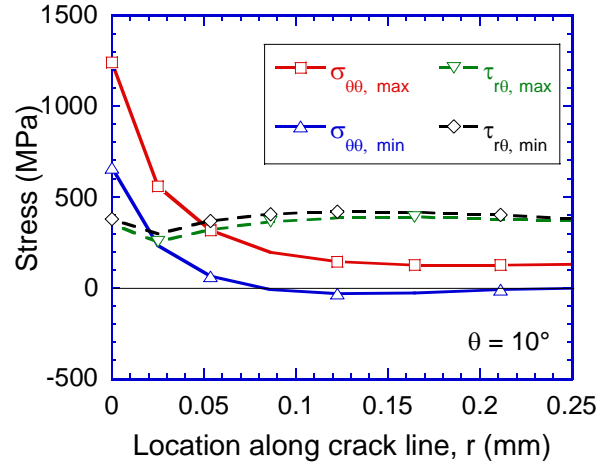Fig. 6. Normal and shear stress along a crack
inclined at an angle θ=0°.

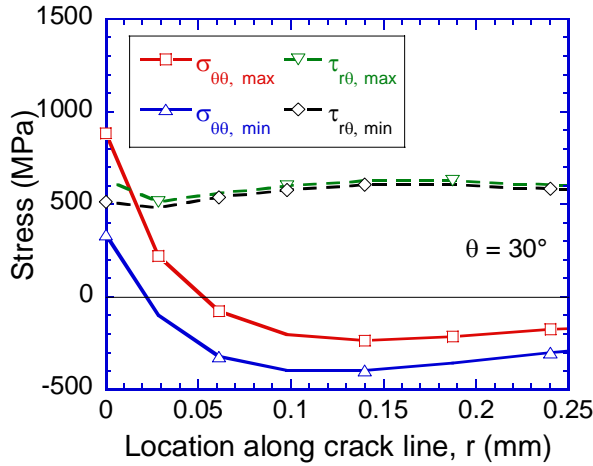Fig. 7. Normal and shear stress along a crack
inclined at an angle θ=10°.

Fig. 8. Normal and shear stress along a crack
inclined at an angle θ=30°.
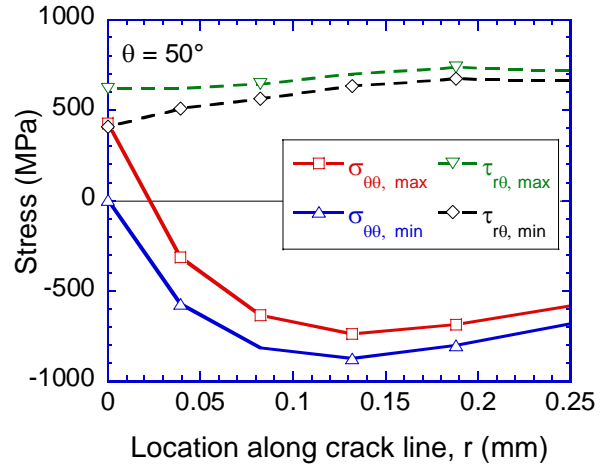

Fig. 9. Normal and shear stress along a crack
inclined at an angle θ=50°.

the figures, is computed for comparison in each case. These values are slightly different for each case since the threshold is corrected for the calculated value of R at each point. The mixed-mode driving force and threshold for each of the four angles are plotted in Figs. 10 and 11 for crack lengths up to 200μm. The figures show that the threshold is exceeded at crack lengths that are fairly large compared to the value of a_0, which tends to be about 30μm for these computations.

From the computations, the crack growth would occur only at crack lengths above 185μm and 166μm for the crack at 0° and 10°, respectively, as shown in Fig. 10. For larger angles of 30° and 50°, Fig. 11 shows that the mixed-mode driving force starts to decrease because K_I starts to decrease with increase in crack length, eventually becoming negative. At that point, the driving force is composed solely of the Mode II contribution. Experimental observations of crack orientations were made and indicate that crack nucleation angles are typically around 45° as shown in Fig. 12. These cracks turn towards a direction normal to the contact surface within crack lengths of the order of tens microns where they become primarily Mode I cracks. Based
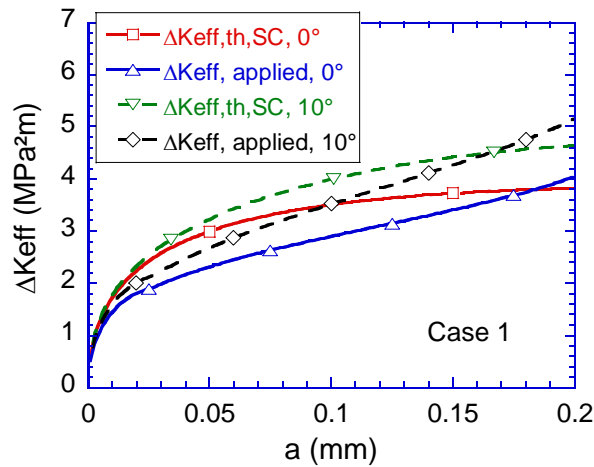
Fig. 10. *Applied and threshold values of ΔK_{eff} for 0° and 10° crack orientations.*
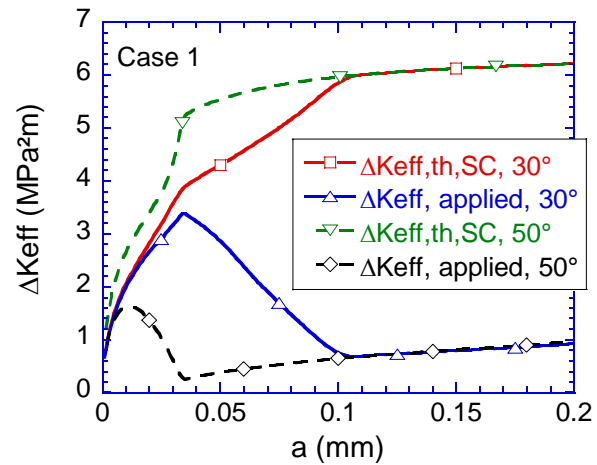
Fig. 11. *Applied and threshold values of ΔK_{eff} for 30° and 50° crack orientations.*

on these observations, the remainder of the analyses will look only what happens along a line θ=0° which is perpendicular to the contact surface.

For Case 1 at 0° the maximum and minimum values of the Mode I and Mode II driving force are presented in Fig. 13. For K_I, the computations show that the stress ratio, R, used in the equations for $K(R= K_{I,min}/K_{I,max})$, is very close to the applied stress ratio for the load, T, in Fig. 1, which was 0.5 for all cases studied. Figure 13 also shows that at 0°, the Mode II component is smaller than that for Mode I but, more importantly, that ΔK_{II} is quite small. The mode II driving
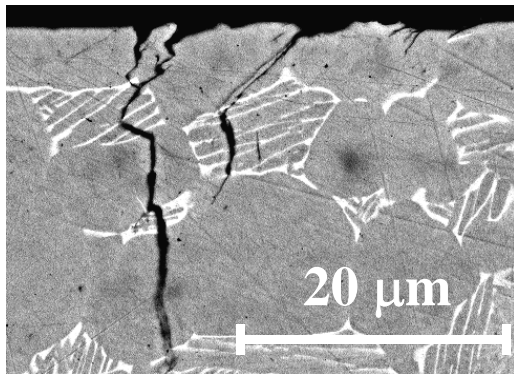
Fig. 12. *Cross-section of a fretting fatigue cracked specimen prior to fracture.*

force is seen to be numerically larger at minimum load than at maximum load. This is due to the physics of the problem as well as the signs used for shear stress, which are consistent with the nomenclature shown in Fig. 4. While the driving force for mixed-mode K is found to be almost the same for Mode I as for mixed mode based on the use of Eq. (3), the difference in the threshold is much larger as can be deduced from Fig. 5. In the computations, a typical ratio of Mode II to Mode I is about 0.25 to 0.3 which shows, in the figure, a difference in the threshold of about 20-25 percent from that of the driving force for the same value of the Mode I quantity.

The crack driving force and threshold for pure Mode I, Case 1 is presented in Fig. 14 and should be compared with those quantities shown in Fig. 10 for the mixed-mode case at θ=0°. For the Mode I case, and for subsequent comparisons, the values are obtained from the quantities calculated at maximum load. Since the calculations did not continue by unloading to the minimum at R=0.5, the value of ΔK_{II} was taken =0 for the remainder of the computations for the driving force. Also, the value of R was chosen as R=0.5 for the K calculations. For this and subsequent computations, only θ=0° is considered. Under these conditions, the driving force is seen to be somewhat similar for Mode I (Fig. 14) compared to mixed mode (Fig. 10), whereas the threshold for Mode I is much smaller than that for the
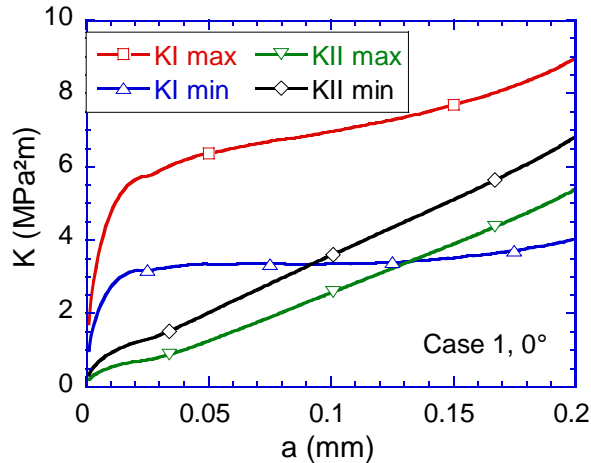
231

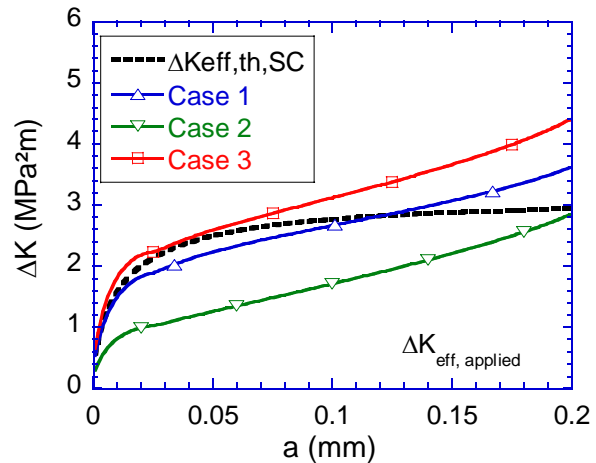*Fig. 13. Maximum and minimum values of K for Mode I and Mode II at θ=0°.*

Fig. 14. Crack driving forces for Mode I assumption, Cases 1-3, R=0.5.

mixed-mode computation. At a crack length of 200μm, the threshold for Mode 1 is 2.95 MPa√m while for the mixed mode it is 3.82 MPa√m for the same crack length. The difference, attributed to the difference in the driving force, Eq. (3), compared to the experimental data described by Eq. (11), raises questions about whether Eq. (3) is an appropriate form for an effective mixed-mode parameter, or if the experimental data, which exhibit some amount of scatter and depend on the methods by which they were obtained, are a good representation of the threshold behavior of this particular material.

Comparisons among the 6 cases in Table 1 are now made using pure Mode 1 quantities, values of K at maximum load only and assuming R=0.5 and $\Delta K_{II}=0$. The comparisons are made to evaluate the effects of specimen thickness, clamping load, and coefficient of friction (COF) on the tendency of a crack to grow or not grow under the experimentally observed loading conditions corresponding to a fatigue life of 10^7 cycles. The results of these computations are summarized in Fig. 14 for Cases 1-3 and Fig. 15 for Cases 4- 6.
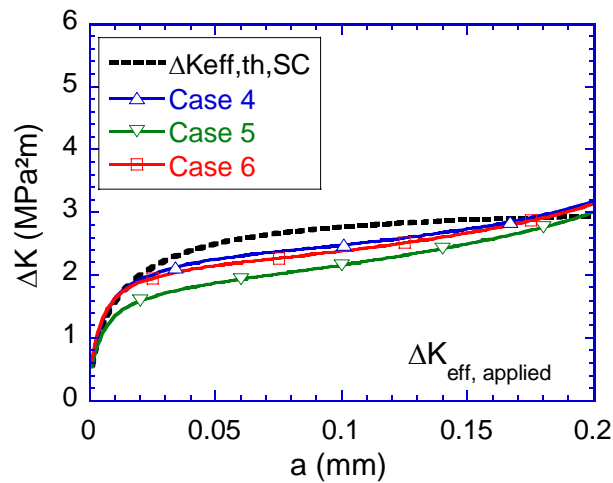
Fig. 15. Crack driving forces for Mode I assumption, Cases 4-6, R=0.5.

Comparing Case 1 to Case 2, the differences are a much higher average clamping stress and somewhat higher average shear stress in Case 1 compared to Case 2 (see Table 1). The curves show that in Case 1 (Fig. 14), the crack growth is close to occurring for all crack lengths even though the growth condition does not occur until the crack is over 100μm long. In Case 2, on the other hand, the driving force is well below the threshold until the crack reaches a length of almost 200μm. There appears to be more of a tendency for crack growth to occur at either a higher clamping stress or a higher shear stress. Case 3 represents the same conditions as Case 2 except that the COF has been increased from 0.3 to 1.0. This change produces a tendency

232

for the crack to grow at any crack length and appears to model what happened experimentally better than when using the lower value of the COF.

Another comparison on the effect of average shear stress can be made by comparing results for Case 4 (Fig. 15) to those of Case 1 (Fig. 14). The main difference here is the specimen thickness where, for the thinner specimen in Case 4, the average shear stress is lower than in Case 1. Here, as in Case 1, there seems to be a condition where the crack is on the verge of growing at all crack lengths although, numerically, the crack is predicted to not grow between crack lengths of 16 and 175μm. These results tend to show that the failure of a specimen at 10^7 cycles is relatively insensitive to average shear stress, an observation that was made and reported in previous work [1].

Sensitivity to average clamping stress can be predicted by comparing Case 5 to Case 4 (Fig. 15). Here, all conditions are identical except that the clamping force is 35kN in Case 5 compared to 50kN in Case 4 for the short pad and thin specimen. Reducing the average clamping stress produces a condition where there is slightly less of a tendency to grow than for the somewhat higher clamping stress of Case 4. This is the same trend observed in comparing Cases 1 and 2, above, where the lower clamping stress reduced the tendency for cracks to propagate. Another observation supporting the conclusion that higher average clamping stresses tend to produce conditions favorable for crack growth or failure to occur can be made by comparing the results of Cases 1, 4, and 5 for the short pad with Case 2 for the long pad. In all of these cases, the COF was the same and the axial and clamping loads were similar. However, the short pad has a contact length about one third that of the long pad and, consequently about three times the average clamping stress as shown in Table 1. The long pad, Case 2, shows a distinct difference between the driving force and the threshold whereas in the short pad cases, the difference between driving force and threshold was small.

The last comparison is made by changing the COF from 0.3 to 1.0 for the short pad with the 1mm thick specimen. This results in Case 6 which can be compared with Case 5 for COF=0.3 in Fig. 15. Here it is seen that the increase in COF produces a slightly higher driving force, but the growth of a crack is still not predicted until the crack length is nearly 200μm. This increase is not as dramatic as in the cases of a 4mm thick specimen with a long pad, discussed above. In both cases, however, a higher value of COF makes the prediction of crack growth more likely and thus closer to the experimental observation of failure under these conditions.

5. Conclusions

1. A fracture mechanics methodology appears to hold more promise for predicting failure or fatigue limit stresses than analysis of the stress field. The reason for this is that a threshold stress intensity is available for long cracks under Mode I only or mixed-mode conditions and can be easily corrected for short crack effects. On the other hand, knowledge of the stress field involving steep gradients requires a gradient stress failure model, which is not readily attainable from smooth bar failure data.

2. The form of the equation for the mixed-mode driving force is rather insensitive to small values of ΔK_{II} whereas the mixed-mode threshold is more sensitive to ΔK_{II} based on a fit to experimental data.

3. Stress intensity K can easily be calculated from FEM results and compared with long crack threshold data.

4. For the specific experimental geometry used here, the worst-case scenario for a crack to propagate occurs along θ=0° (normal to contact surface) or θ=10° for any crack length beyond the very smallest values.

5. An increase in the clamping stress increases the driving force in Mode I while a change in average shear stress seems to make very little difference in the applied K.

6. Both stress and corresponding K solutions are very sensitive to the assumed value of COF, μ. In the cases studied, where failure occurred at 10^7 cycles, no failure was predicted for μ = 0.3. The other case evaluated, μ=1.0 appears to be much most realistic for predicting the experimentally observed failures. Further work is needed to explore higher values of μ and μ ≠ constant which has shown some promise in preliminary computations [15].

References

[1]   Hutson, A.L., Nicholas, T., Olson, S.E. and Ashbaugh, N.E. "Effect of Sample Thickness on Local Contact Behavior in A Flat-on-Flat Fretting Fatigue Apparatus," *Int. J. Fatigue*, 23, Supp. 1, 2001, pp. 445-453.

[2]   Nicholas, T., Hutson, A.L., Olson, S. and Ashbaugh, N., "In Search of a Parameter for Fretting Fatigue," *Advances in Fracture Research, Proceedings of ICF-10*, K. Ravi-Chandar, B.L. Karihaloo, T. Kishi, R.O. Ritchie, A.T. Yokobori Jr. and T. Yokobori, Eds., Paper # 0809, CD ROM, Elsevier, 2001.

[3]   Chan, K.S., Davidson, D.L., Lee, Y-D. and Hudak, S.J., Jr., "A Fracture Mechanics Approach to High Cycle Fretting Fatigue Based on The Worst Case Fret Concept: Part I - Model Development," *Int. J. Fracture*, Vol. 112, 2001, pp. 299-330.

[4]   Hutson, A.L. and Nicholas, T., "Fretting Fatigue Behavior of Ti-6Al-4V against Ti-6Al-4V Under Flat on Flat Contact with Blending Radii," *Fretting Fatigue: Current Technology and Practices, ASTM STP 1367*, D.W. Hoeppner, V. Chandrasekaran and C.B. Elliott, Eds., American Society for Testing and Materials, West Conshohocken, PA, 2000, pp. 308-321.

[6]   McVeigh, P.A., "Analysis of Fretting Fatigue in Aircraft Structures: Stresses, Stress Intensity Factors, and Life Predictions," Ph.D. Thesis, School of Aeronautics and Astronautics, Purdue University, West Lafayette, IN, 1999.

[7]   Maxwell, D.C. and Nicholas, T., "A Rapid Method for Generation of a Haigh Diagram for High Cycle Fatigue," *Fatigue and Fracture Mechanics: 29th Volume, ASTM STP 1321*, T. L. Panontin and S. D. Sheppard, Eds., American Society for Testing and Materials, West Conshohocken, PA, 1999, pp. 626-641.

[8]   Campbell, J.P. and Ritchie, R.O. "Mixed-Mode, High-Cycle Fatigue-Crack Growth Thresholds in Ti-6Al-4V. Part I. A Comparison of Large- and Short-Crack Behavior, *Engng. Fract. Mech.*, 67, 2000, pp. 209-227.

[9]   El Haddad, M.H., Smith, K.N. and Topper, T.H., "Fatigue Crack Propagation of Short Cracks," *Journal of Engineering Materials and Technology*, Vol. 101, 1979, pp. 42-46.

[10] Kitagawa, H. and Takahashi, S., "Applicability of Fracture Mechanics to Very Small Cracks or the Cracks in the Early Stage," *Proc. of Second International Conference on Mechanical Behaviour of Materials*, Boston, MA, 1976, pp. 627-631.

[11] Moshier, M.A., Nicholas, T. and Hillberry, B.M., "High Cycle Fatigue Threshold in the Presence of Naturally Initiated Small Surface Cracks," *Fatigue and Fracture Mechanics: 33rd Volume, ASTM STP 1417*, W.G. Reuter and R.S. Piascik, Eds., American Society for Testing and Materials, West Conshohocken, PA, 2002, pp. 129-146.

[12] Jasper, T.M., "The Value of the Energy Relation in the Testing of Ferrous Metals at Varying Ranges of Stress and at Intermediate and High Temperatures," *Philosophical Magazine*, Series. 6, Vol. 46, Oct. 1923, pp. 609-627.

[13] Nicholas, T. and Maxwell, D.C., "Mean Stress Effects on the High Cycle Fatigue Limit Stress in Ti-6Al-4V," *Fatigue and Fracture Mechanics: 33rd Volume, ASTM STP 1417*, W.G. Reuter and R.S. Piascik, Eds., American Society for Testing and Materials, West Conshohocken, PA, 2002, pp. 476-492.

[14] Beghini, M., Bertini, L. and Fontanari, V., "Weight Function for an Inclined Edge Crack in a Semi-plane", *Int. J. Fracture*, 99, 1999, pp. 281-292.

[5] Hutson, A.L., Neslen, C. and Nicholas, T., "Characterization of Fretting Fatigue Crack Initiation Processes in Ti-6Al-4V," *Tribology International*, 36, 2003, pp 133-143.

[15] Naboulsi, S. and Nicholas, T., "Reassessment of the Constant Coefficient of Friction Assumption in Fretting Fatigue Analysis," *Int. J. Solids Structures*, (in press)

This page intentionally left blank.

Determination of Young's Modulus of Grains in a Gamma Titanium Aluminide Alloy

W.J. Porter, III[*], R. John, and S. Olson[*]

Air Force Research Laboratory, Materials and Manufacturing Directorate (AFRL/MLLMN), Wright-Patterson Air Force Base, Ohio 45433, U.S.A.
[*] University of Dayton Research Institute (UDRI), Dayton, Ohio 45469, U.S.A.

Abstract

An experimental and analytical process for determining the elastic response of grains in a gamma titanium aluminide alloy was developed. Three-dimensional finite element models were employed to deduce the transversely isotropic properties. The results are compared with those reported for polysynthetically-twinned materials.

Keywords: Titanium aluminide; Young's modulus; Elastic; Finite element; Polysynthetically-twinned materials

Introduction

As efforts continue to mature gamma titanium aluminide alloys from the laboratory into industrial application, significant work remains to accurately model the behavior of these intermetallic materials under service load conditions. The development of accurate models is dependent upon the input of reliable material properties that, in the case of gamma alloys, reflect the anisotropy intrinsic to their make-up. Of particular interest is development of models to predict elastic and plastic behavior as a precursor to fatigue initiation and crack growth. In a review of information pertaining to Young's modulus measurements for γ-TiAl alloys, primarily those for polysynthetically-twinned (PST) materials, the reported data showed significant differences based on alloy chemistry and lamellar spacing, as well as lamellar orientation [1,2]. The lack of information regarding the elastic behavior of these alloys is in contrast to the well-understood effects of lamellar orientation on plastic deformation and fracture [3-7]. From this review it was concluded that development of a consistent set of Young's modulus measurements was requisite to develop an accurate, finite element-based model. This paper describes an integrated experimental and analytical technique to determine the Young's modulus as a function of lamellar grain orientation.

Material and Experimental Procedure

The alloy investigated in the present study had a nominal chemistry of Ti-46.5Al-3Nb-2Cr-0.2W (at%). The initial ingot was cast by induction skull melting and was received as a portion of a pancake forging (10 x 20 x 2 cm). The forged material was heat treated in air at 1400°C for 24 hours and then homogenized at 900°C for an additional 24 hours before air cooling. The alpha-transus temperature for this alloy is 1340°C.

The surfaces of the forging were ground to remove the heavy oxide that formed during heat treatment. Thin plates, approximately 2.6 mm thick, were electro-discharge machined (EDM) from the center region of the forging. The plates were taken from the center of the forging in an effort to obtain material that was minimally affected by oxygen pick-up during the air heat treatment. The plates were ground to remove the EDM recast layer and polished to a 600 μm finish and then etched to reveal the large grain microstructure. Dogbone tensile samples were EDM'd from the plates such that a single grain, with a minimum diameter of 5 mm, encompassed the gage sections. The gage section grains were chosen to provide various surface grain orientations, nominally 0, 45, 67 and 90°, with respect to the tensile loading direction. An example of a dogbone tensile specimen is shown in Figure 1.

After the tensile specimens were EDM'd, the recast layer on the edges of the sample was removed by grinding and the sample was polished on all sides to a 1 μm finish. Finally, the specimens were immersion etched in Krolls reagent to reveal the microstructure of the entire sample (Figure 1).

The surface and edge (where possible) orientations of all grains in the sample were determined through metallography. The surface and edge orientations of the gage section grain are shown in Table 1. The gage thickness and width of the specimens in this study are also reported in this table. A schematic showing how these angles are defined is found in Figure 2.
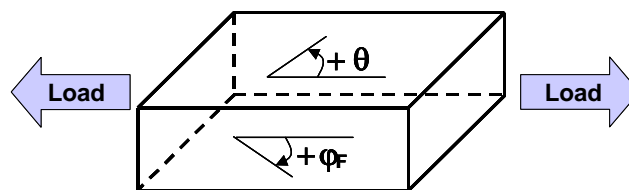
Figure 1: Tensile specimen containing a single grain in the gage section.

Figure 2: Schematic of lamellar orientation in the primary grain in the gage section.

Strain gages with a grid size of 0.381 x 0.508 mm were used to measure deformation within the central grain. Gages were placed on the top and bottom surfaces and were located as near the center of the gage section as possible. Elastic deformation was measured in the longitudinal direction with respect to the loading direction.

All testing was done at room temperature using a servohydraulic machine in load control mode. To ensure that deformation was restricted to the elastic region, the samples were loaded to maximum stress levels of either 25 or 50 MPa, depending on the surface orientation.

Results and Discussion

The microstructure following the supertransus heat treatment was near-fully lamellar with the presence of scattered, fine gamma grains at the grain boundaries. An example of the microstructure is shown in Figure 3. The average grain size was approximately 7 mm in diameter with lamellar spacing ranging from 1 to 3 μm.

Figures 4a-d shows the elastic stress-strain response for four of the orientations investigated. Only 10-20% of the data collected are shown in these plots. The slight separation seen between the top and bottom strain gages, apparent in some of the specimens, was investigated by rotating the specimen

about its longitudinal and transverse axes and retesting. This behavior was determined to be intrinsic to the test specimen after similar results were found for each test before and after specimen rotation.

Table 1: Dimensional and Microstructural Orientation Information of Test Specimens.

Specimen Number	Gage Thickness, B (mm)	Gage Width, W (mm)	Lamellar Orientation of Grain in Gage Section (°)	
			Surface (θ)	Edge Front (φ_F)
00-690	2.19	3.50	-3.0	1.0
00-692	2.31	3.38	42.0	-10.0
01-254	2.40	3.65	84.5	20.0
01-909	2.10	3.67	-88.5	14.0
01-910	2.38	3.68	-67.0	-31.0
01-911	2.44	3.32	-45.5	29.0
02-000	2.65	3.68	3.0	1.0

Figure 3: Microstructure of Ti-46.5Al-3Nb-2Cr-0.2W (a%) after 1400°C/24hr heat treatment (polarized light image).
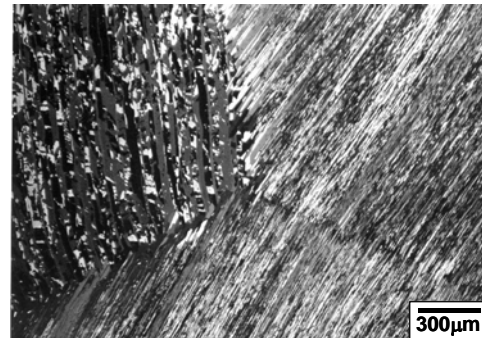
The range of longitudinal modulus values measured in this study (157-173 GPa), irrespective of orientation, is consistent with modulus values reported in the literature for polycrystalline and polysynthetically-twinned (TiAl + Ti_3Al) lamellar materials [1-2,7]. Several investigations [1-2] have shown that the elastic properties of the grain are transversely isotropic.

Hence, an iterative procedure based on detailed 3-dimensional finite element (FE) analysis was used to deduce the transversely isotropic properties of the grains. An initial set of homogenous grain properties was obtained from limited constituent properties available in the literature. Using this initial property set, the stress-strain behavior of the seven large-grain specimens were predicted. The initial property set used in the FE analyses was modified to minimize the error between the predicted elastic moduli and the measured response for the various specimens.

Detailed FE models, containing on the order of 60,000 to 70,000 degrees-of-freedom, were constructed for each specimen. The models comprised the entire gage section and shoulder region of each sample plus 2.5 mm into each grip section. Individual grains in each specimen are represented in the FE models based on grain mapping and orientations from SEM observations and metallography. The FE model for specimen 02-000 is shown in Figure 5. One end of the specimen was held in a fixed position
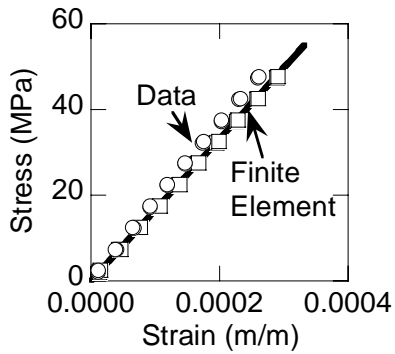
while the other was allowed axial, but planar (i.e. twist-free) movement, simulating clamped end conditions during loading. The elastic FE analyses were conducted using ABAQUS with transversely isotropic material properties used for the individual grains.
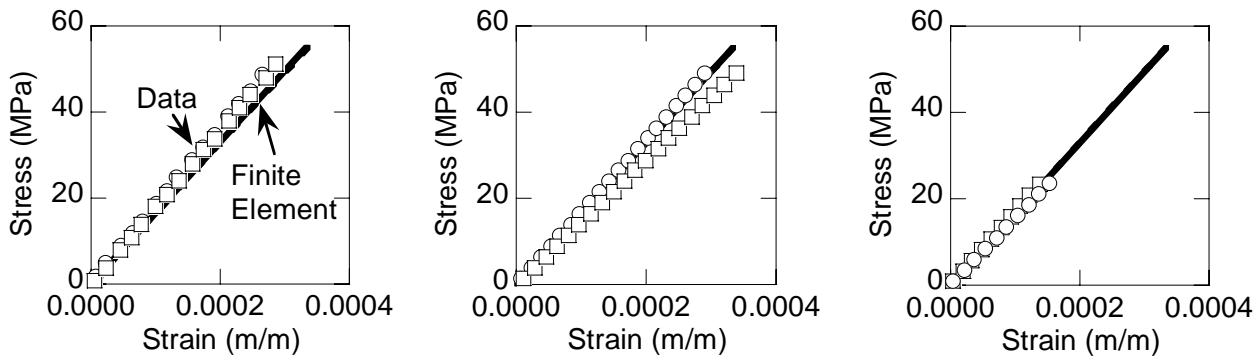
(a) Spec. 00-690

(b) Spec. 00-692

(c) Spec. 01-254

(d) Spec. 01-910

Spec.	Difference between experimental and predicted (%)	
	Top	Bottom
00-690	2.2	4.4
00-692	-5.9	1.4
01-254	1.9	-3.2
01-909	-2.3	-0.6
01-910	-0.7	4.9
01-911	-2.4	-2.1
02-000	-2.6	2.4

(e)
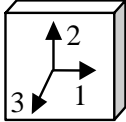
Figure 4: (a-d) Comparison of measured and predicted stress vs. longitudinal strain response from selected samples. Data are from top (hollow squares) and bottom (hollow circles) surfaces of each specimen. FE predictions (solid and dashed lines) are based on the modified properties listed in Table 2. (e) Difference between experimental and predicted results.

The detailed FE analysis requires transversely isotropic properties for each grain in the specimen. These grain properties are not readily available in the open literature for lamellar γ-TiAl alloys. Therefore, we used available single-crystal constituent properties (TiAl and Ti_3Al) [8-12] to derive the grain properties. The chemistry, and subsequently the mechanical properties, of the constituents may differ from that of the two-phase lamellar structure in the present alloy. As a first approximation, these constituent properties were used to derive the initial set of lamellar grain properties using laminate models [13,14]. The initial results are shown in Table 2. As discussed earlier, these properties were modified through an iterative process based on correlation with the experimental results as shown in Figure 4. The modified set of properties (Table 2) fall within the range of values reported in the literature for Young's and shear modulus [8-12].

Most of the reported data regarding Young's modulus for lamellar gamma titanium aluminides were determined using PST material. PST material allows for specimens to be machined with all lamellar orientations controlled by the experimenter. The technique presented in this study allows the experimenter to control, in a practical sense, only the surface angle (θ) when machining specimens. Therefore, to determine the validity of the deduced set of grain properties, the 'Modified Properties' in Table 2 were used to calculate effective moduli for an equivalent Ti-46.5Al-3Nb-2Cr-0.2W PST material in a given orientation. Figure 4e shows the percentage difference between the experimental

240

and analytical results for all specimens tested. Table 3 compares the predicted PST properties to the reported Young's modulus for a variety of PST materials as a function of lamellar orientation. Young's modulus predicted using the modified properties are ~ 4 to 15% lower than that predicted using the initial properties. The current predictions for the longitudinal moduli are close to the data reported by Parthasarathy et al. [2] for Ti-48Al and ~ 13% higher than that reported by Boehlert et al. [1] for Ti-46Al. However, the data for Ti-51Al [1] are significantly lower (~18-33%) than that predicted for the current material.

Table 2: Input Properties for 3D Finite Element Analysis

Property	Initial Properties	Modified Properties	
$E_1 = E_2$ (GPa)	186.2	164.0	Assumes 90% γ + 10%
E_3 (GPa)	218.6	186.0	α$_2$ and lamellar structure
G_{12} (GPa)*	72.33	63.08	
$G_{13} = G_{23}$ (GPa)	66.85	72.0	
ν_{12}	0.2872	0.30	
$\nu_{13} = \nu_{23}$	0.1458	0.15	

*G_{12} (GPa) = $E_1/2(1+\nu_{12})$

Figure 5: Finite element model of specimen number 02-000. Mesh for 02-000 - (23,859 nodes and 20,510 elements). Each grain was assigned specific properties based upon its metallographically-determined orientation. Shades of gray represent the grains in the sample.
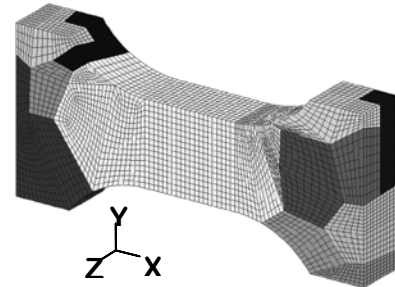
Table 3: Comparison of predicted effective longitudinal modulus of PST with available data.

PST Orientation (°)	Effective Longitudinal Modulus for a PST (GPa)				
	FE – initial [This Study]	FE – modified [This Study]	Parthasarathy et al. [2] (Ti-48Al)	Boehlert et al. [1] (Ti-46Al)	Boehlert et al. [1] (Ti-51Al)
0	186	164	169, 182	142	110, 135
20	178	165		145	
30	172	166	146, 168		
90	219	186	183, 205		

Additional orientations are presently being investigated for Young's modulus determination and transverse stiffness measurements are being conducted to ascertain Poisson's ratio values. The deduced transversely isotropic properties of the grains are being used to evaluate the elastic stress variation in polycrystalline materials using 3–dimensional finite element models [14]. Finally, the efforts at modeling elastic behavior are a precursor to developing physically based elastic-plastic models aimed at predicting the tensile, and eventually, fatigue initiation and crack growth behavior of gamma titanium aluminide alloys.

Summary and Conclusions

1. An integrated experimental and analytical technique was developed to deduce the elastic response of grains in a gamma titanium aluminide alloy. A microstructurally-based 3-dimensional finite elelment analysis was used to successfully determine a consistent set of orthotropic elastic properties for individual grains.
2. Although direct comparison with the PST data is difficult due to limited experimental data for gamma titanium aluminide alloys with varying formulations, the orthotropic elastic properties in this study are consistent with the available PST results. The elastic properties for the lamellar material are different than those expected based solely on the constitiuent properties.
3. Additional experiments and analyses are in progress to determine the elastic-plastic behavior of the grains.

Acknowledgments

References

1. Boehlert CJ, Zupan M, Dimiduk DM, Hemker KJ. Gamma Titanium Aluminides 1999, Warrendale, PA: TMS; 1999. p. 669.
2. Parthasarathy TA, Dimiduk DM. Private Communication, Air Force Research Laboratory, AFRL/MLLM, Wright-Patterson AFB, OH 45433, U.S.A, 1998.
3. Yamaguchi M, Inui H, Yokoshima S, Kishida K, Johnson DR. Mater. Sci. Eng., 1996; A213:25.
4. Yokoshima S, Yamaguchi M. Acta Mater., 1996; 44:873.
5. Inui H, Oh MH, Nakamura A, Yamaguchi M. Acta Metall. Mater., 1992; 40:3095.
6. Parthasarathy TA, Mendiratta MG, Dimiduk DM. Acta Mater., 1998; 46:4005.
7. Kim Y-W. JOM, 1994; 46: 30.
8. Yoo MH, Zou J, Fu CL. Mater. Sci. Eng., 1995; A192-193:14.
9. Tanaka K, Ichitsubo T, Inui H, Yamaguchi M, Koiwa M. Phil. Mag. Lett., 1996; 73:71.
10. Tanaka K, Okamoto K, Inui H, Minonishi Y, Yamaguchi M, Koiwa M. Phil. Mag. A 1996; 73:1475.
11. He Y, Schwarz RB, Migliori A, Whang SH. J. Mater. Res., 1995; 10:1187.
12. Yoo MH, Fu CL. Met. Trans A, 1998; 29A:49.
13. Pagano NJ, Mechanics of Composite Materials, Vol. 2, New York, NY: Academic Press; 1974; p. 23.
14. Frank GJ, Olson SE, Brockman RA Intermetallics, 2003; 11:331.

Measurement and Modeling of Orthotropic Elastic Behavior of Grains in a Gamma Titanium Aluminide Alloy

R. John, W.J. Porter, III[*], and S. Olson[*]

Air Force Research Laboratory

Materials and Manufacturing Directorate (AFRL/MLLMN)

Wright-Patterson Air Force Base

OH 45433, U.S.A.

[*]University of Dayton Research Institute (UDRI), Dayton, OH 45469, U.S.A.

Abstract

Gamma titanium aluminide (γ-TiAl) alloys have been under development for use in rotating components for gas turbine engines. Detailed 3-dimensional (3D) grain-level finite element models are being developed to predict damage initiation and accumulation in γ-TiAl during service loading. These models require knowledge of the orthotropic nature of the elastic and plastic deformation of individual grains. While the elastic properties of gamma and alpha-2 single-phase materials have been extensively studied, the elastic response of fully lamellar two-phase materials has not received the same degree of attention. This paper describes an integrated experimental and analytical approach to deduce the elastic grain properties in a γ-TiAl. Specimens with gage sections composed of specifically-oriented individual lamellar grains were tested in tension. 3D finite element analyses were used to deduce the elastic grain properties. These grain properties were used to accurately predict the elastic properties of polysynthetically-twinned (PST) and polycrystalline γ-TiAl.

1. Introduction

Gamma titanium aluminide (γ-TiAl) alloys are being targeted for application in a wide range of aerospace components such as turbine blades, impellers, thermal protection systems and automotive components such as engine valves and turbocharger rotors [1-6]. Based on the intermetallic gamma (face-centered tetragonal) and alpha-2 ($D0_{19}$-modified hexagonal close-packed) phases, TiAl and Ti_3Al, respectively, these alloys are noted for their high temperature (~ 800°C) strength retention, lightweight, good oxidation resistance, and stiffness [1,5,6]. γ-TiAl alloys exhibit relatively low ductility and low damage tolerance at lower temperatures, and hence significant effort has been directed at understanding the corresponding design issues related to crack initiation and small crack growth [1,7-19].

Biery et al. [8], Knaul et al. [9], and Pollock et al. [10] investigated localized strains and crack initiation at notches. Using a displacement-mapping technique, Biery et al. [8] showed that the strains at the notch root are localized to one or a small group of γ grains. The peak strain was higher and more localized than that predicted by continuum finite element modeling. Larsen and Worth [11] and Li et al. [12] conducted a detailed investigation of the influence of grain orientation on crack initiation from sharp notches. Larsen and Worth [11] showed that, during tension-tension fatigue loading of specimens with a single, artificial, semi-circular flaw, most of the γ-TiAl specimens did not fail at the location of the flaw. Damage initiation occurred at locations away from the machined notch, indicating that closely aligned and unfavorably oriented colonies were responsible for crack initiation. Based on detailed examination of crack initiation mechanisms, Li et al. [12] showed that the apparent threshold is critically dependent on the

orientation of the particular colony that cracks. Following initiation, the crack growth exhibits significant small crack behavior [13,15]. Using grain-level experiments and finite element modeling, Arata et al. [14] showed that such crack growth in a γ-TiAl depends on relative lamellae misorientation and offsets between neighboring colonies. The results from these studies [8-19] highlight the need for microstructure-based analysis for prediction of crack initiation and small crack growth.

Some of the recent deformation and fracture modeling efforts in γ-TiAl based on microstructural representation include Refs. [14,20-24]. The advantages and limitations of these approaches are discussed in Ref. [25]. The microstructure-based analytical approaches, which include detailed 2-dimensional (2D) and 3-dimensional (3D) grain-level finite element modeling, require knowledge of the orthotropic nature of the elastic and plastic deformation, and fracture behavior of individual grains. While the elastic properties of gamma [26-31] and alpha-2 [27,32,33] single-phase materials have been thoroughly investigated, the elastic response of fully lamellar two-phase materials has not received the same amount of attention. Limited data are available [34,35] on the longitudinal modulus as a function of lamellar orientation based on tests conducted using PST (polysynthetically-twinned) specimens. The relative lack of information on the elastic behavior of two-phase, lamellar titanium aluminides is contrasted by the extensive work reporting the deformation and fracture behavior of this material system [36-39].

Most of the available properties, for single and dual phase γ-TiAl are based only on longitudinal deformation data. Boehlert et al. [33] and Zupan et al. [31] adapted the microsample tensile testing designed by Sharpe [40] to measure the elastic and plastic deformation behavior of

Ti-46Al (at%) [33], Ti-51Al [33] PST and Ti-55Al [31] single-phase γ materials. This testing employed an interferometric strain/displacement measurement system to measure the longitudinal strains. Parthasarathy and Dimiduk [34] used strain gages to measure the longitudinal deformation in the Ti-48Al PST material. The development of a consistent set of orthotropic properties requires longitudinal and transverse deformation measurements in PST or within grains. Hence, a program was initiated to characterize the elastic-plastic deformation and fracture behavior of individual grains in a γ-TiAl. This paper describes an integrated experimental and analytical approach to deduce the orthotropic elastic grain properties in a γ-TiAl. Unique tensile specimens with gage sections composed of single lamellar grains were tested in tension to determine the elastic behavior of this two-phase structure. The selection of a polycrystalline material in lieu of a polysynthetically-twinned (PST) variant was motivated by: (1) subsequent investigations that will focus on grain-to-grain interactions and the role of grain boundaries, (2) the ability to easily heat treat the material of interest to achieve large grain sizes suitable for measurements, and (3) PST crystals of complex chemistries are difficult to obtain. Extensive 3D finite element modeling analysis was used to deduce the orthotropic elastic constants from the measured longitudinal and transverse deformation data. The application of these results to predict the polycrystal properties and stresses in a sub-element is also discussed.

2. Material and Experimental Procedure

The alloy used in this study, nominally Ti-46.5Al-3Nb-2Cr-0.2W (at%), was developed by Kim [41] and designated as K5. The nominal grain size of this alloy is ~ 300 μm. To obtain the large grain microstructure required for this testing, the forged material (approximately 100 x 200 x 20 mm) was heat treated in air at 1400°C for 24 hours and homogenized at 900°C for 24 hours prior to cooling in air [19]. The heat treatment temperature is in the single-phase alpha field for the composition. The alpha-transus temperature for this alloy is 1340°C. As discussed later, the specimens were machined from the central portion of the 20 mm thick forging. This region experienced the slowest cooling rates. The microstructure in this region was near-fully lamellar with an average grain size of ~ 7 mm. A representative view of the lamellar spacing in this alloy is shown in Fig. 1. This image was obtained using a scanning electron microscope (SEM) in the backscattered-electron (BSE) mode. In this photo, the dark contrast phase is gamma and the light contrast phase is alpha-2. The material's chemistry was analyzed before and after heat treatment and the results are shown in Table 1. Except for the increase in the oxygen level, the material's chemistry did not change during the heat treatment.

The surfaces of the forging were ground to remove the heavy oxide that formed during heat treatment. Thin plates, ~ 2.6 mm thick (shown in Fig. 2), were electro-discharge machined (EDM) from the center region of the forging. The plates were taken from the center of the forging in an effort to obtain material that was minimally affected by oxygen pick-up during the air heat treatment. The plates were ground to remove the EDM recast layer and polished to a 600 μm finish and then etched to reveal the large grain microstructure. Dogbone tensile specimens were

EDM'd from the plates such that a single grain encompassed the gage section, Figs. 2 and 3. The gage section grains were chosen to provide various surface grain orientations, nominally 0, 45, 67 and 90°, with respect to the tensile loading direction. After the tensile specimens were EDM'd, the recast layer on the edges of the sample was removed by grinding and the sample was polished on all sides to a 1 μm finish. Finally, the specimens were immersion etched in Krolls reagent to reveal the microstructure of the entire specimen, Fig. 3.

The surface and edge (where possible) orientations of all grains in the specimens were determined through metallography. The surface and edge orientations of the gage section grain, as well as the calculated through-thickness orientation of this grain, are shown in Table 2. Figure 4 also shows the definition of the angles used to define the complete grain orientation. The angle ξ is defined as the angle between the normal to the lamellae projected onto the x-y plane and the loading axis. For the 7 specimens tested during this study, ξ ranged from 61° to 121°. Note that ξ = 90° corresponds to the lath orientation parallel to the loading direction. We were unable to obtain specimens with $\xi < 61°$ or $\xi > 121°$ probably because of the directionality or microstructural texture associated with the forging process.

Strain gages with a grid size of 0.381 x 0.508 mm were used to measure average longitudinal and transverse strains within the central grain. Gages were placed on the top and bottom surfaces and were located as near the center of the gage section as possible. All testing was done at room temperature using a servohydraulic machine in load control mode. The specimens were loaded to maximum stress levels of either 25 or 50 MPa, depending on the surface

orientation, thus ensuring that deformation was restricted to the elastic region. At least 100 data points were collected during the loading and unloading.

3. Experimental Results

Since the experiments were to be conducted on mini-specimens, the test system was verified using a fine-grained (~ 10 μm) Ti-6Al-4V specimen. This specimen was instrumented identically to the γ-TiAl specimens and loaded to similar stress levels, as shown in Fig. 5. Only about 20 to 30% of the data points are shown in this figure. The stress-strain responses from the top and bottom surface gages were nearly identical, with the corresponding moduli = 113.6 and 114.1 GPa, respectively. These tests confirmed the excellent alignment of the test system. The verification load-unload tests were also devoid of hysterisis.

The measured longitudinal and transverse stress-strain responses from specimens with $\xi =$ 88, 76 and 61° are shown in Figs. 6, 7 and 8, respectively. Only 10-20% of the data points collected are shown in these plots. As expected, all the specimens exhibited linear response. The apparent longitudinal modulus (= stress / surface strain) ranged from 145 to 183 GPa and the apparent Poisson's ratio ranged from 0.19 to 0.33. The modulus values are consistent with values reported in the literature for polycrystalline and PST (TiAl + Ti$_3$Al) lamellar materials [33-35,41]. This estimation of Young's modulus assumes isotropic material behavior and does not account for through-thickness orientation of the laths within the grain (see Table 2). Several investigations [28-30,32,33-35,42] have shown that the elastic properties of the grain are orthotropic. Hence, we

conducted a detailed 3-dimensional finite element (FE) analysis to deduce the orthotropic properties of the grains.

Some of the specimens exhibited a slight separation between the top and bottom strain gages. This separation of data was investigated by rotating the specimen about its longitudinal and transverse axes, and retesting. The difference between the top and bottom strain data was determined to be intrinsic to the test specimen after similar results were found for each test before and after specimen rotation.

4. Finite Element Analysis

Detailed 3D finite element (FE) models, containing ~ 60,000 to 70,000 degrees-of-freedom, were constructed for each specimen. The models comprised the entire gage section and shoulder region of each sample plus 2.5 mm into each grip section. Individual grains in each specimen were represented in the FE models based on grain mapping and orientations from SEM observations and metallography. The FE model for specimen 02-000 is shown in Fig. 9. One end of the specimen was held in a fixed position while the other was allowed axial, but planar (i.e. twist-free) movement, simulating clamped end conditions during loading. The elastic FE analyses were conducted using ABAQUS with orthotropic material properties used for the individual grains.

Properties were assigned to each grain based on the orientation of that grain in the specimen. The orthotropic properties of the constituents, gamma and alpha-2 phases (TiAl and

Ti$_3$Al, respectively) were selected from the measurements reported by Yoo and Fu [42]. Assuming an alpha-2 to gamma ratio of 1:9 and using the method developed for laminated orthotropic materials by Pagano [43], the initial set of orthotropic elastic constants were derived for lamellar K5 grains. Frank et al. [22] provide a detailed discussion of the derivation of this initial set of properties. This initial set of elastic properties, as shown in Table 3, was used in the first round of FE analyses of all the specimens. The corresponding predictions of stress-strain response are compared with the data in Figs. 6-8 and Table 4. This comparison showed that the average difference between the data and the initial FE strain predictions were ≈ -9.2% and -9.7% in the longitudinal and transverse directions respectively. Hence, an iterative process was used to modify the elastic properties to better correlate the data and the predictions. After about 8 iterations, we developed the final set of properties as reported in Table 3. The corresponding stress-strain predictions are compared with the data in Figs. 6-8 and Table 4. Figures 6-8 show that the current predictions (solid lines) are generaly closer to the data. The average difference between the data and the final FE strain predictions were ≈ -0.6% and –5.5% in the longitudinal and transverse directions, respectively. The difference between the moduli in the initial and final set of properties ranged from +7 to –15%. The deduced final set of properties are compared to the available data from PST and polycrystal γ-TiAl as discussed next.

5. Prediction of PST and Polycrystalline Properties

Most of the reported data regarding Young's modulus for lamellar gamma titanium aluminides were determined using PST material. PST material allows for specimens to be prepared with all lamellar orientations controlled by the experimenter. The technique presented in this study allows the experimenter to control, in a practical sense, only the surface angle (θ) when machining specimens. Therefore, to determine the validity of the elastic constants deduced during this study, the properties reported in Table 3 were used to calculate the response of a K5 equivalent PST material at various orientations. Figure 10 shows a comparison of reported Young's modulus as a function of lamellar orientation for a variety of binary PST materials and the predictions for a K5 equivalent PST based on the initial and final properties reported in Table 3. The predictions from the initial property set are higher than all the reported data consistent with the underestimation of longitudinal strain as shown in Table 4. Figure 10 shows that the prediction from the final properties is close to the data reported by Parthasarathy and Dimiduk [34] for the Ti-48Al PST alloy. Data reported by Boehlert et al. [33] are lower than the current predictions and the limited data from Ref. [34]. The difference between the current predictions and the data from Boehlert et al. [33] is only ~ 18%, except for one test. As discussed earlier, very limited data are available for Young's moduli as a function of orientation for PST materials. No PST data were available for the material (K5 γ-TiAl) investigated in this study. In addition, as shown in Fig. 10, the lamellar spacing was different for the various materials. Hence, the comparison shown in Fig. 10 only indicates that the properties deduced during this study are most likely in the right range.

In Figure 10, the elastic moduli for the K5 equivalent PST ranges from ~165 to ~185 GPa. This range corresponds to approximately 175 GPa ±5%. Hence, the use of average isotropic value of 175 GPa is sufficient for most elastic analyses.

The next step was to verify the application of the deduced K5 γ-TiAl grain properties for prediction of the isotropic polycrystalline K5 properties. The baseline 3D model developed by Frank et al. [22], shown in Fig. 11, was used to predict the polycrystalline properties. The equiaxed γ grains were represented as cubes and the lamellar grains were represented by truncated rhombic dodecahedra. The 3D cube consisted of 256 lamellar grains and 256 γ grains, with the orientation of each grain being randomly generated. The uniform lamellar and γ grain sizes were 145 and 20 μm, respectively. The volume fraction of γ grains was 4%. Additional FE details can be found in Ref. [22]. Nine tensile loading simulations were conducted using the final set of orthotropic properties from Table 3 for the lamellar grains and the properties from Ref. [22] for the γ grains. The 3D cube analyses yielded Young's modulus values in the range 168.7 – 170.6 GPa and Poisson's ratios in the range 0.209-0.221 for the polycrystalline K5 γ-TiAl alloy. The predicted Young's moduli correlate well with the values reported by Kim [41] for all γ-TiAl (=160-180 GPa) and Dolley [44] for the K5 alloy (=166-181 GPa).

6. Prediction of Average Grain Stresses in a Component

To demonstrate the application of grain-level modeling, 3D finite element analyses were performed on a subelement representative of the leading edge of a γ-TiAl blade. The radius of the leading edge was assumed to be 0.38 mm. A global model of the subelement, shown in Figure 12(a), was constructed and contained ~ 158,000 degrees-of-freedom. Isotropic elastic properties, with a Young's modulus of 170 GPa and a Poisson's ratio of 0.215, were used for the global model. Results from the global model were used to define the loading for a smaller sub-model. The sub-model, shown in Fig. 12(b), consisted of 82 randomly oriented grains with an average grain diameter of 300 μm, and contained ~ 390,000 degrees-of-freedom. The orthotropic material properties listed as Modified Properties in Table 3 were used for the sub-model analyses.

The leading edge model was subjected to an axial stress of 100 MPa. Initial sub-model results from the analyses are shown in Figs. 13(a) and 13(b) corresponding to predicted global and local stresses, respectively, averaged by grain. The global stresses, in the direction of the loading, exhibit a variation of approximately 10%, which is consistent with the mild orthotropy indicated by the properties from Table 3. The local stresses shown in Fig. 13(b) correspond to stresses normal to the lamellae of each grain. Cracks can be expected to initiate in those grains which have high stresses normal to the lamellae. There is significant variation in these local normal stresses consistent with the random orientation of the grains. Similar detailed grain-level analyses using elastic-plastic properties are in progress to analyze and predict crack initiation and growth in γ-TiAl.

7. Summary and Conclusions

An integrated experimental and analytical technique was developed to deduce the orthotropic elastic properties of grains in a gamma titanium aluminide alloy. Microstructurally-based 3-dimensional finite elelment analyses were conducted to successfully determine a consistent set of orthotropic elastic properties for the individual grains. The orthotropic elastic properties determined in this study are consistent with the available PST and polycrystalline results. The application of these properties to model a component sub-element at the mircrostructural level was demonstrated. Determination of the elastic-plastic behavior of the grains and detailed elastic-plastic 3-dimensional analyses are in progress.

References

1. Larsen JM, Worth B, Balsone S, Jones J. In: Kim YW et al, editors. Gamma Titanium Aluminides, Warrendale, USA: TMS, 1995, p. 821.

2. Bartolotta PA, Krasue DL. In: Kim YW et al, editors. Gamma Titanium Aluminides, Warrendale, USA: TMS, 1999, p. 3.

3. Rugg D. In: Kim YW et al, editors. Gamma Titanium Aluminides, Warrendale, USA: TMS, 1999, p. 11.

4. LeHolm R, Clemens H, Kestler H. In: Kim YW et al, editors. Gamma Titanium Aluminides, Warrendale, USA: TMS, 1999, p. 25.

5. Kim YW, Dimiduk DM, Loretto MH, editors. Gamma Titanium Aluminides, Warrendale, USA: TMS, 1999.

6. Dimiduk DM, Materials Science & Engineering A, 1999; A263:281.

7. Wright K. In: Darolia R et al, editors. Structural Intermetallics, Warrendale, USA: TMS, 1993, p. 879.

8. Biery N, De Graef MD, Pollock TM. In: Kim YW et al, editors. Gamma Titanium Aluminides, Warrendale, USA: TMS, 1999, p. 557.

9. Knaul D, Beuth J, Milke JL. Metallurgical and Materials Transacations 1999; 30A: 949.

10. Pollock TM, Mumm D, Muraleedharan K, Martin P. Scripta Metallurgica 1996; 35: 1311.

11. Larsen JM, Worth BD. Air Force Research Laboratory, AFRL/MLLM, Wright-Patterson AFB, OH, U.S.A., Unpublished results 1997.

12. Li K, Rosenberger AH, Worth BD, Larsen JM, and Porter WJ. Fatigue and Fracture of Engineering Materials and Structures 2002. Submitted.

13. Chan KS, Shih DS. Metallurgical and Materials Transaction 1997; 28A: 79.

14. Arata JJM, Kumar KS, Curtin WA, Needleman A. Interntl J of Fracture 2001; 111: 163.

15. Campbell JP, Kruzic JJ, Lillibridge S, Venkateswara Rao KT, Ritchie RO. Scripta Materialia 1997; 37: 707.

16. Bowen P, Chave RA, Jones AW. Materials Science and Engineering, 1995; 192/193A: 443.

17. Mercer C, Soboyejo WO, Acta Materialia 1997; 46: 4385.

18. Rosenberger AH. In: Blom AF, editor. Fatigue 2002, Engineering Materials and Advisory Services Ltd, West Midlands, UK, 2002, p. 3023.

19. John R, Rosenberger AH, DeLuca D, Porter WJ, Li K. In: Kim YW et al, editors. Gamma Titanium Aluminides, Warrendale, USA: TMS, 1999, p. 535.

20. Schlögel SM, Fischer FD. Comp Mat Sci 1996; 7:34.

21. Kad BK, Dao M, Asaro RJ. Mat Sci Engng 1995; 192/193A: 97.

22. Frank GJ, Olson SE, Brockman RA. Intermetallics 2001. Submitted.

23. Brockman RA, Frank GJ, Olson SE. In: Hemker KJ et al, editors. Structural Intermetallics 2001 (ISSI 3), Warrendale, USA,: TMS, 2001, p. 339.

24. Marketz WT, Fischer FD, Clemens H. In: Kim YW et al, editors. Gamma Titanium Aluminides, Warrendale, USA: TMS, 1999, p. 579.

25. Dimiduk DM, Parthasarathy TP, Hazzledine PM. Intermetallics 2001; 9; 875.

26. Lipsitt HA, Schechtman D, Schafrik RE. Metall Trans 1975; 6A: 1991.

27. Schafrik RE. Metall Trans 1977; 8A: 1003.

28. He Y, Schwarz RB, Migliori A, Whang SH. Journal of Mater Res 1995; 10: 1187.

29. Tanaka K, Ichitsubo T, Inui H, Yamaguchi M, Koiwa M. Phil. Mag. Lett 1996; 73: 71.

30. Yoo MH, Zou J, Fu CL. Mater Sci Eng 1995; 192/193A: 14.

31. Zupan M, Hemker KJ. Material Sci Engng 2001; A319-321: 810.

32. Lipsitt HA, Schechtman D, Schafrik RE. Metall Trans 1980; 11A: 1369.

33. Tanaka K, Okamoto K, Inui H, Minonishi Y, Yamaguchi M, Koiwa M. Phil. Mag. A 1996: 73: 1475.

34. Boehlert CJ, Zupan M, Dimiduk DM, Hemker KJ., In: Kim YW et al, editors. Gamma Titanium Aluminides, Warrendale, USA: TMS, 1999, p. 669.

35. Parthasarathy TA, Dimiduk DM. Air Force Research Laboratory, AFRL/MLLM, Wright-Patterson AFB, OH, 1998, Unpublished research.

36. Inui H, Oh MH, Nakamura A, Yamaguchi M. Acta Metall Mater 1992; 40: 3095.

37. Yokoshima S, Yamaguchi M. Acta Materialia 1996; 44: 873..

38. Yamaguchi M, Inui H, Yokoshima S, Kishida K, Johnson DR, Mater Sci Eng 1996; A213: 25.

39. Parthasarathy TA, Mendiratta MG, Dimiduk DM. Acta Mater 1998; 46: 4005.

40. Sharpe WN, Fowler RO. In: Corwin WR et al., editors. ASTM STP 1204 , 1993, p. 386.

41. Kim YW. JOM 1994; 46: 30.

42. Yoo MH, Fu CL. Met. Trans A, 1998; 29A: 49.

43. Pagano NJ, Mechanics of Composite Materials, V. 2, Academic Press, New York, USA; 1974. p. 23.

44. Dolley EJ. Isothermal High-frequency High-cycle Fatigue of the Ti-47Al-3Nb-2Cr-0.2W (at%) Gamma Titanium Aluminide Alloy. MS Thesis. University of Dayton, Dayton, USA. 1995.

Table 1: Effect of Heat Treatment on Composition K5 γ TiAl alloy

Element	Pre-HT (a%) As-cast	Post-HT (a%) Forged+HT
Al	46.38	46.46
Nb	3.00	2.98
Cr	2.17	2.05
W	0.20	0.21
Nb	0.10	0.12
Cr	0.05	0.05
Fe	0.05	0.05
O (in wppm)	1112	3050
Ti	(bal)	(bal)

Table 2: Dimensional and Microstructural Orientation Information of Test Specimens.
(Angles are defined in Figure 4)

| Specimen Number | Specimen Gage Section Thickness B (mm) | Specimen Gage Section Width W (mm) | Lamellar Orientation of Grain in Gage Section (°) | | | Loading Angle (°) |
			Surface (θ)	Edge Front (φ_F)	Through-thickness (ψ)	(ξ)
00-690	2.19	3.50	-3.0	1.0	-18.5	88
02-000	2.65	3.68	3.0	1.0	18.5	88
00-692	2.31	3.38	42.0	-10.0	-11.0	100
01-909	2.10	3.67	-88.5	14.0	-0.5	76
01-254	2.40	3.65	84.5	20.0	2.0	70
01-911	2.44	3.32	-45.5	29.0	-28.5	61
01-910	2.39	3.68	-67.0	-31.0	14.5	121

Table 3: Properties Used in Finite Element Analysis
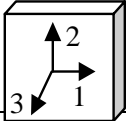
Property	Initial Properties	Modified Properties	
$E_1 = E_2$ (GPa)	186.2	164.0	Assumes 90% γ + 10% α_2
E_3 (GPa)	218.6	186.0	and lamellar structure
G_{12} (GPa)	72.5	63.1	
$G_{13} = G_{23}$ (GPa)	66.9	72.0	
ν_{12}	0.29	0.30	
$\nu_{13} = \nu_{23}$	0.15	0.15	

Table 4: Comparison of finite element results with measured stress-strain response.

Spec. No.	ξ (°)	Surface Longitudinal Strain at 50 MPa (μstrain) *			Difference Between Data and FE - Longitudinal (%)		Surface Transverse Strain at 50 MPa (-) (μstrain) *			Difference Between Data and FE - Transverse (%)	
		Data	FE -Initial Properties	FE - Final Properties	FE -Initial Properties	FE - Final Properties	Data	FE -Initial Properties	FE - Final Properties	FE -Initial Properties	FE - Final Properties
00-690	88	287	269	305	-6.44	6.10	75	73	87	-2.83	15.93
02-000	88	307	269	305	-12.68	-0.81	90	70	84	-22.50	-7.00
00-692	100	321	272	304	-15.18	-5.20	91	71	85	-21.66	-6.21
01-909	76	311	276	305	-11.45	-1.97	80	73	86	-9.74	6.44
01-254	70	313	282	304	-10.11	-3.09	92	70	83	-24.78	-10.71
01-911	61	316	288	303	-8.79	-4.20	65	66	72	0.92	10.09
01-910	121	289	291	303	0.59	4.73	57	65	75	12.40	29.82
				Average =	-9.15	-0.63			Average =	-9.74	5.48

* Average of top and bottom surfaces
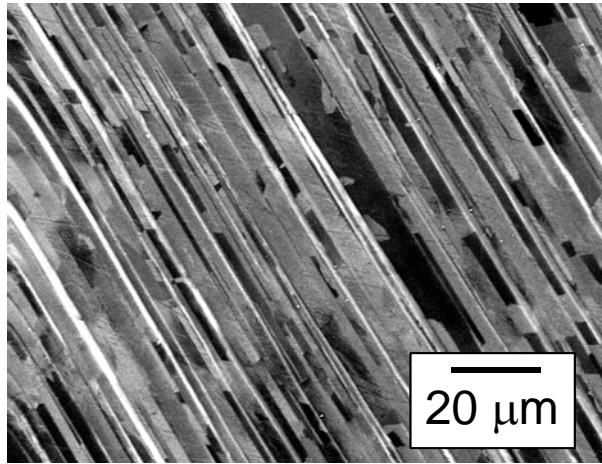
Figure 1: Microstructure of Ti-46.5Al-3Nb-2Cr-0.2W (a%) after 1400°C/24hr heat treatment (SEM backscattered-electron mode).

Figure 2:   Rectangular blanks machined out of heat-treated forgings. The specimens were machined such that the grain size in the gage section was 7 to 10 mm.

5mm
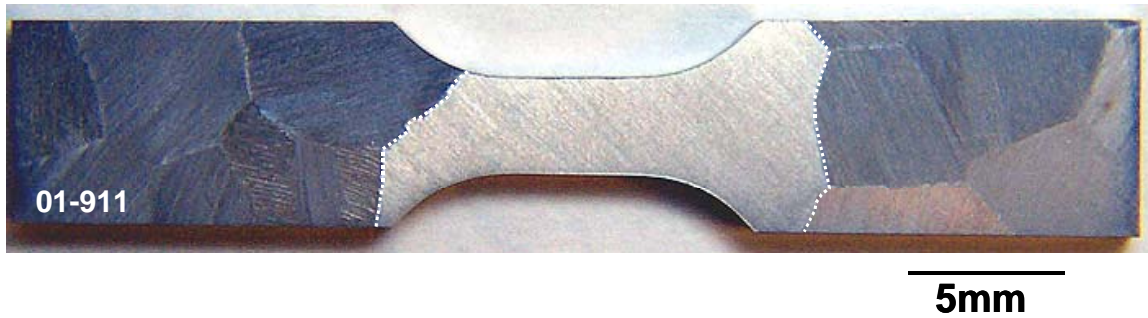
Figure 3: Tensile specimen (01-911) containing a single grain in the gage section. The dashed lines indicate the boundary of the primary grain in the gage section.
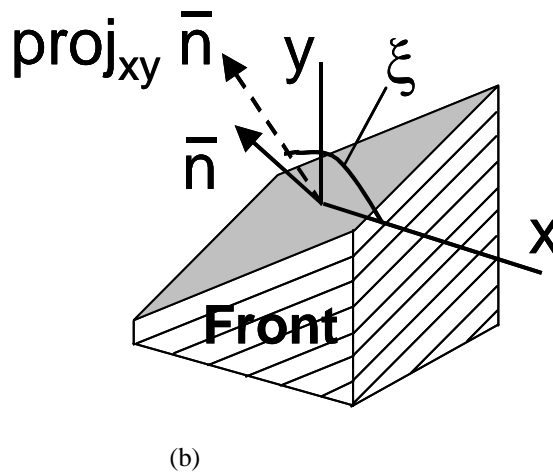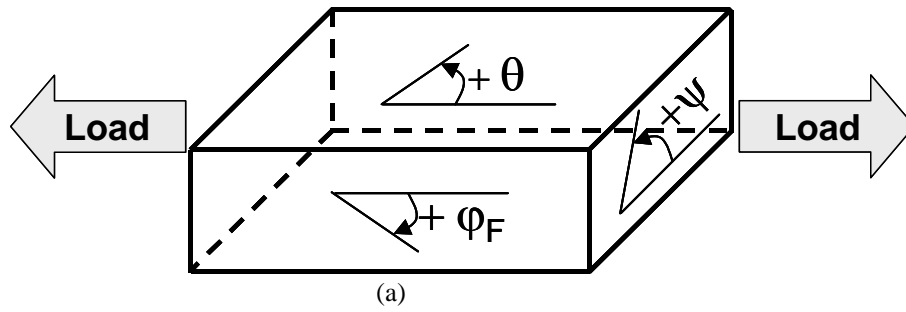
Figure 4:   (a) Schematic of lamellar orientation in the primary grain in the gage section.
(b) Definition of orientation of laths with respect to the loading axis.

ξ = 90° corresponds to the lath parallel to the loading axis.
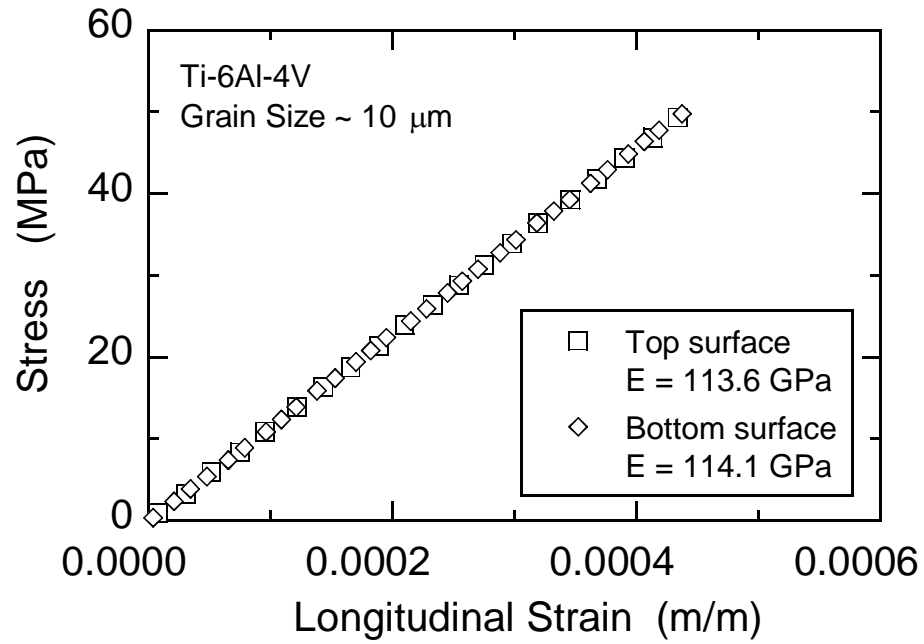
Figure 5: Verification of test system using fine-grained (~10 μm) Ti-6Al-4V specimen. Only about 20-30% of the data points are shown.
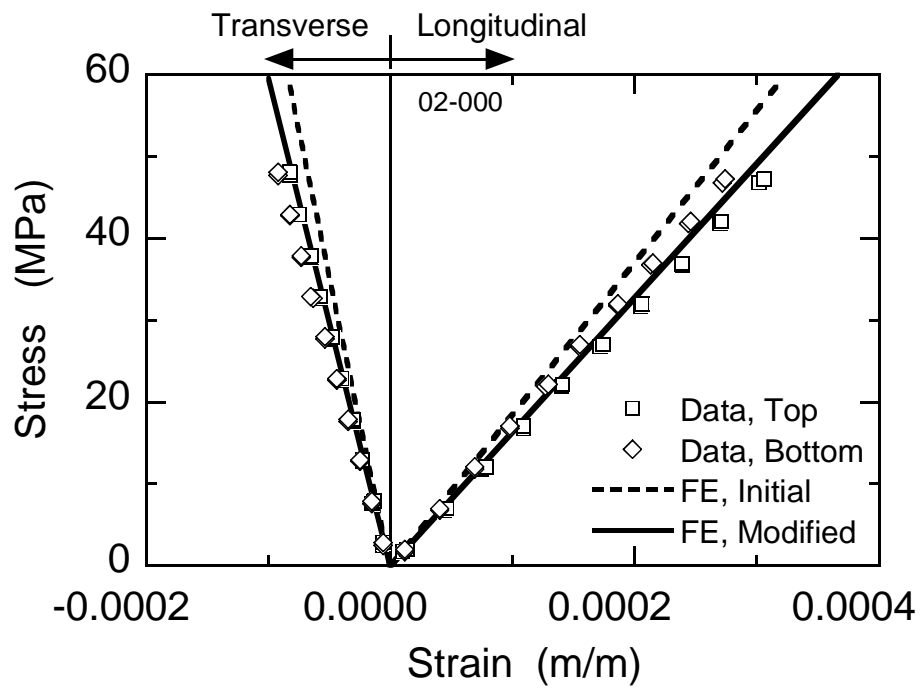
Figure 6:   Comparison of measured and predicted stress-strain response from specimen 02-000 with $\xi = 88°$.
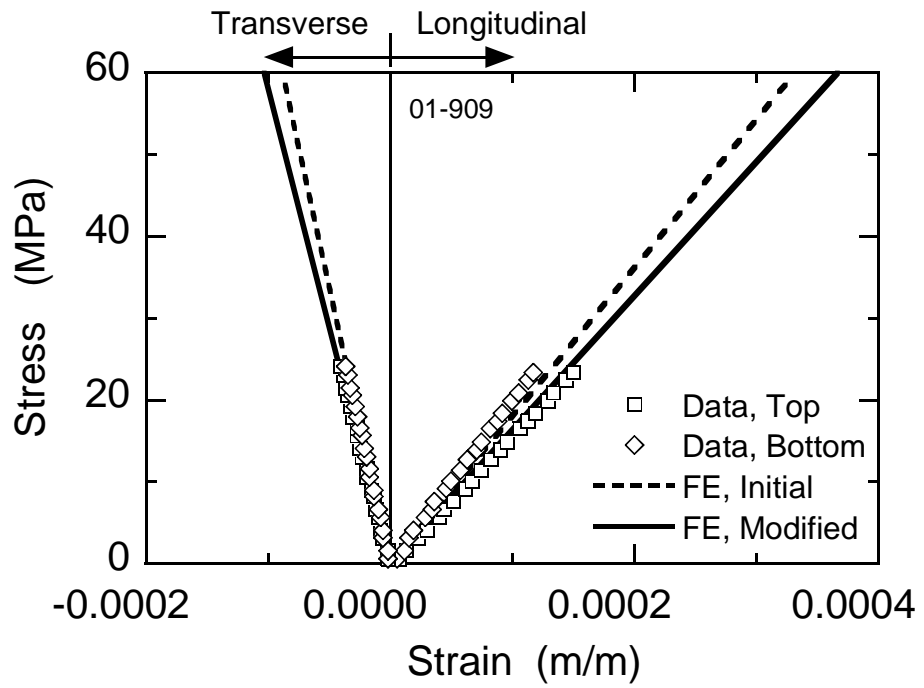
Figure 7: Comparison of measured and predicted stress-strain response from
specimen 01-909 with $\xi = 76°$.
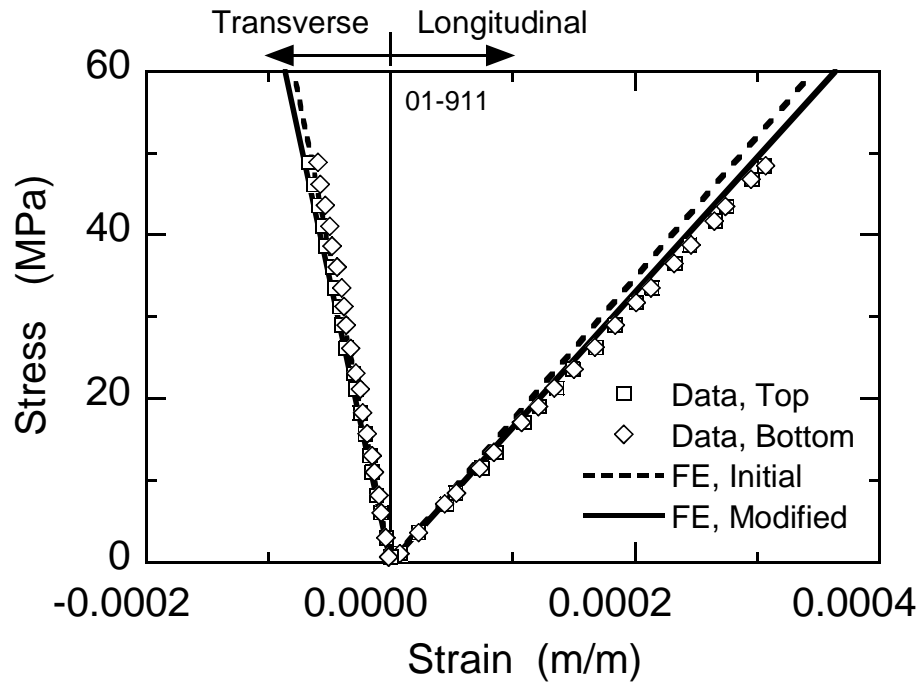
Figure 8:   Comparison of measured and predicted stress-strain response from specimen 01-911 with $\xi = 61°$.
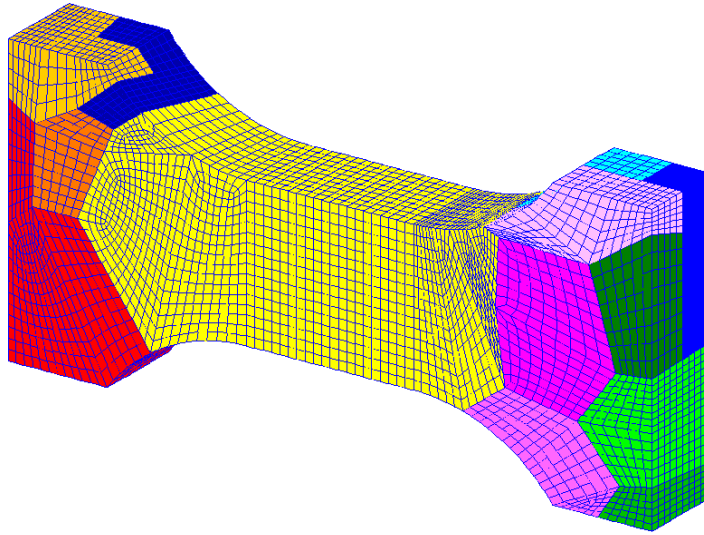
Figure 9: Finite element (FE) model of specimen 02-000 consisting of 23,859 nodes and 20,510 elements. Each grain was assigned specific properties based upon its metallographically-determined orientation. Shades of gray represent the grains in the specimen.
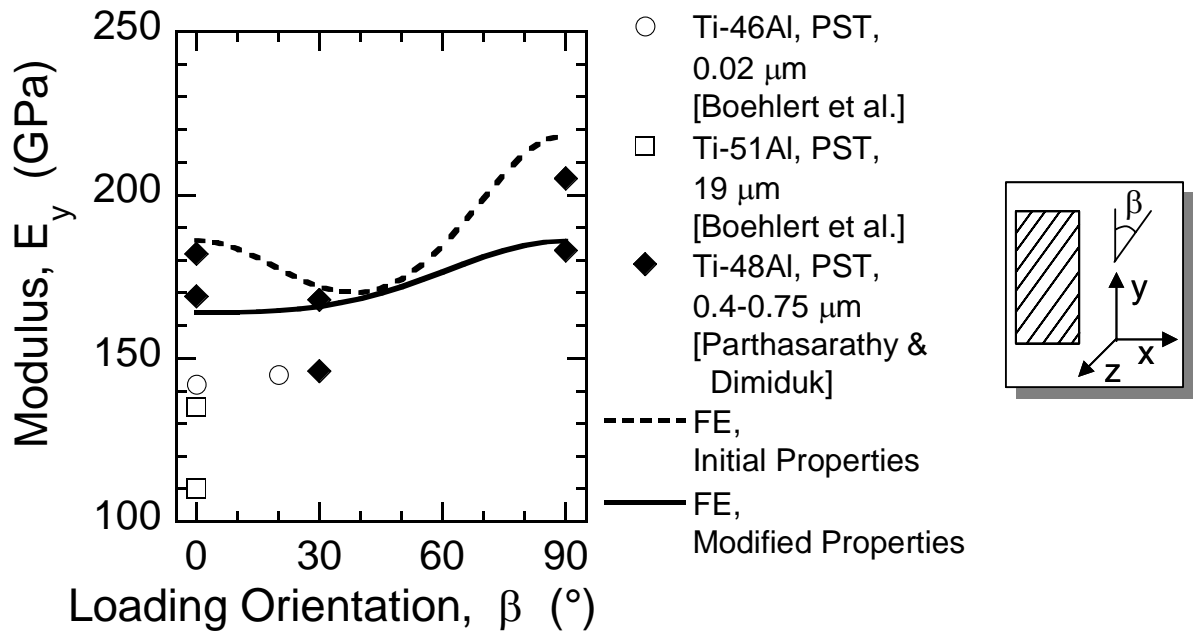
Figure 10: Comparison of predicted effective modulus of K5 equivalent PST with the data reported for other binary PST material. Note: $\beta = \xi - 90°$.
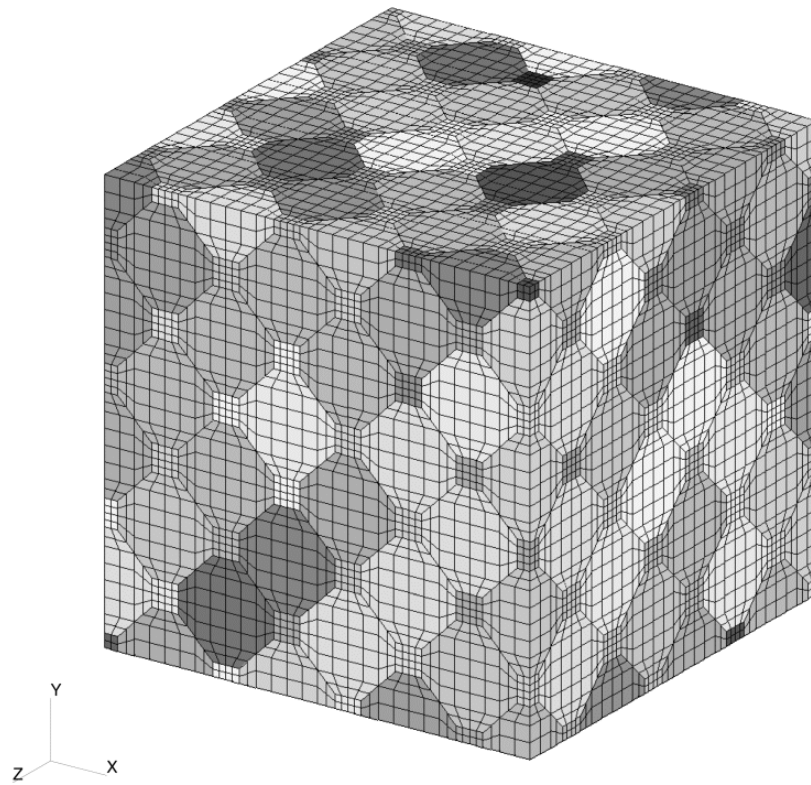
Figure 11: Baseline 3-dimensional polycrystalline model using cubic packing scheme for the grains. Gray shades indicate different grain orientations.
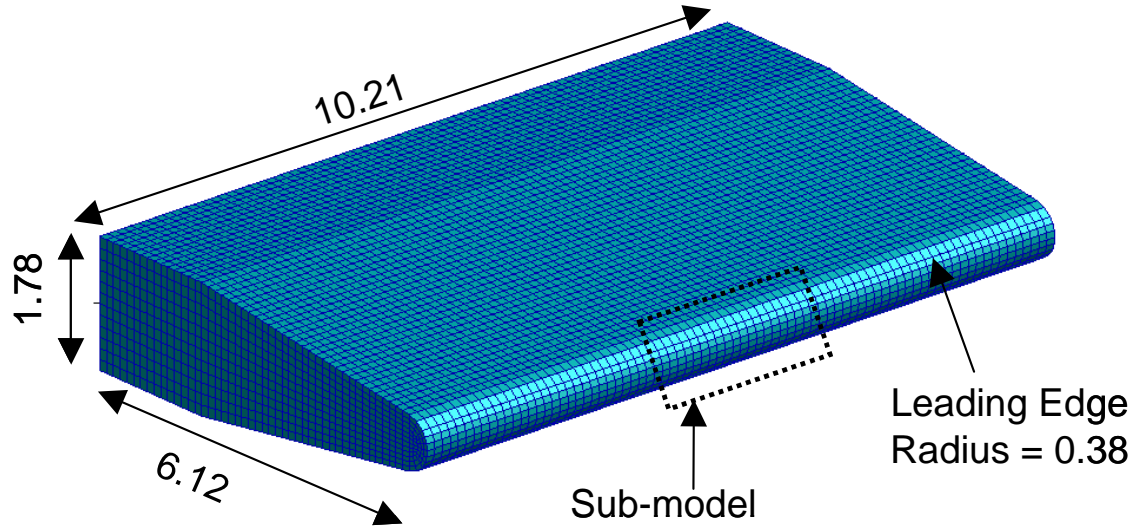
(a) Isotropic global model (Dimensions in mm)
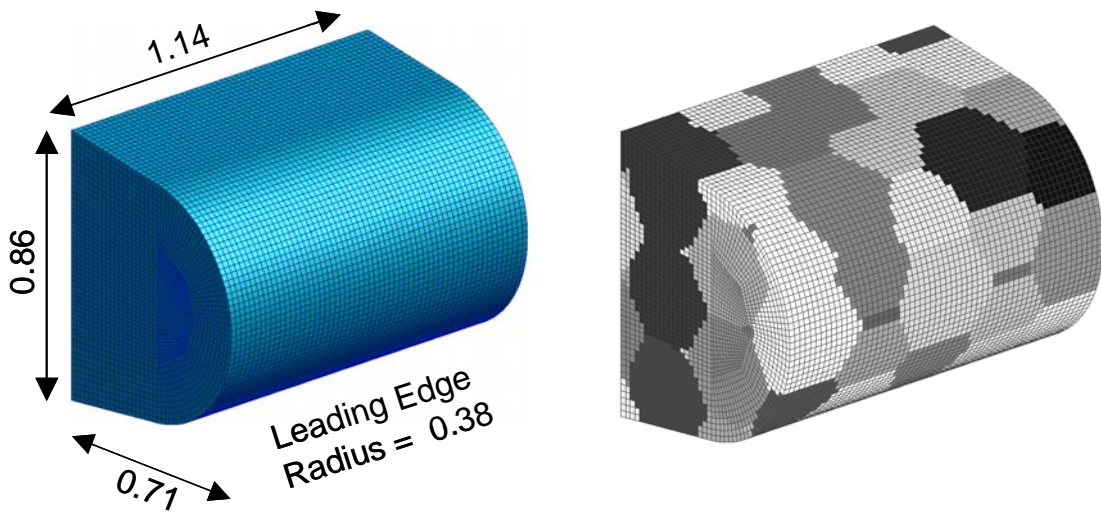
(b) Sub-model with random grain orientation (Dimensions in mm)

Figure 12:   Finite element model of the leading edge of a blade. (a) Isotropic global model. (b) Sub-model with random grain orientation. Gray shades indicate different grain orientations.
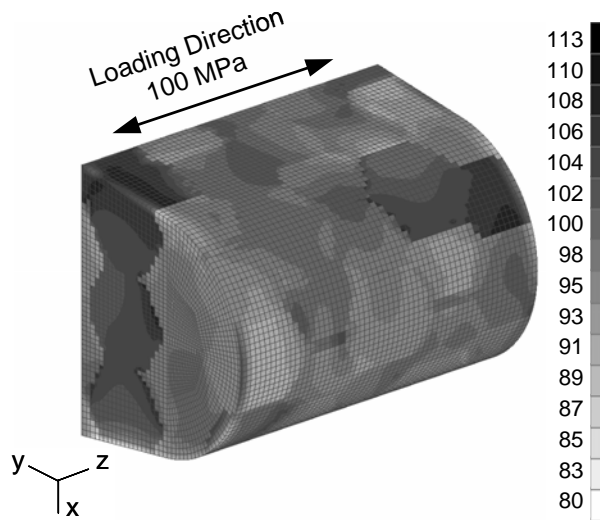
(a) Global σ_z stresses averaged by grain.
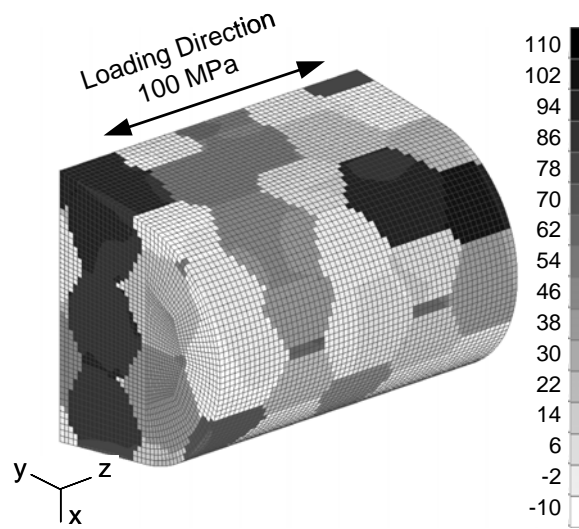
(b) Local σ_z stresses normal to lamellae averaged by grain.

Figure 13: Predicted global and local stresses at the leading edge averaged by grain.

Numerical Models of Orthotropic and Lamellar Grain Structures

G.J. Frank, S.E. Olson*, R.A. Brockman

University of Dayton Research Institute, 300 College Park, Dayton, OH 45469-0110 USA

Work Conducted and Supported by: Air Force Research Laboratory, Materials and Manufacturing

Directorate, Wright-Patterson AFB, OH 45433.

Abstract

In this paper, a method for numerically estimating localized stress concentrations that arise in materials with anisotropic crystalline grains is described. This method is used to quantify stress variations within polycrystals of $\gamma-$TiAl, a material system composed of two phases of orthotropic material - lamellar colonies of TiAl/Ti$_3$Al interspersed with small grains of pure TiAl. Effective elastic properties for the lamellar colonies are calculated from the constituent properties using a procedure developed for laminated orthotropic materials. It is postulated that the local anisotropy and differing orientations of adjacent grains of material can lead to microyielding at stresses below the mean yield strength of the material. The effects of local elastic anisotropy on stresses are presented as statistical variations in the stress distributions under simple states of loading. Three-dimensional and two-dimensional models are investigated.

Keywords: A. titanium aluminides based on TiAl, B. anisotropy, B. elastic properties, B. mechanical properties at ambient temperature, E. mechanical properties theory

1. Introduction

Considerable interest exists in the development of titanium aluminide (TiAl) alloys for use in high-temperature structural applications, due to their low density, strength retention at high temperature, and potential for excellent fatigue resistance. The best combination of mechanical properties is obtained with a duplex or small-grained nearly lamellar microstructure, in which a large fraction of the material exists in the form of lamellar colonies consisting of thin parallel layers of the γ (TiAl) and α_2 (Ti$_3$Al) phases. The lamellar microstructure exhibits some distinctive and complicated mechanical behavior. The

277

survey by Appel and Wagner [1] is recommended for a thorough presentation of microstructural details, processing issues, and microstructural behavior.

Our interest in the current investigation is to quantify the stress variations within polycrystals of γ–TiAl to better understand the influence of anisotropy and relative orientation of neighboring grains. The length scale represented in a typical model is a millimeter or more in each direction. As such, it is impractical to model the lamellae explicitly since their thickness, which is controlled by the cooling rate during processing, is between ten nanometers and a few micrometers. However, a representation of the localized response within individual lamellar colonies is needed to obtain a meaningful picture of the variations in stress throughout the polycrystal.

Much of the detailed numerical modeling of γ–TiAl that has been performed to date focuses on the individual phases (particularly the γ phase, which represents most of the material volume), or on the study of localized response within a single lamellar colony. Fischer, Schlögl, and co-workers have developed finite element-based micromechanical models of unit cells within a lamellar colony in both two [2] and three dimensions [3-5]. These and similar models use crystal plasticity models that represent the relevant slip systems explicitly, to capture anisotropic yielding, flow, and hardening characteristics accurately. Lebensohn, et al. [6] have developed a simple model of a two-lamellae structure which represents the most important deformation mechanisms of a γ–TiAl polysynthetically twinned crystal.

Polycrystals of materials with a simpler structure at the grain level have been analyzed in two and three dimensions by numerous researchers. Early investigations such as the classical work of Taylor [7] and Bishop and Hill [8] used relatively simple kinematic constraints between adjacent grains. Most recent developments employ finite element-based models, in which fewer kinematic assumptions are required. γ–TiAl polycrystals have been analyzed in two dimensions by Kad, Dao, Asaro and co-workers in a series of pioneering papers [9-12]. Planar projections of the three-dimensional crystallography are used in these works to investigate characteristics of the localized stress field while controlling the size of the numerical system to be solved. Even in two dimensions, analyzing the individual lamellae is impractical, and the authors employ effective properties which define the plastic flow behavior of a lamellar colony as a homogeneous entity.

278

All of the finite element-based models of polycrystals cited above focus on the effects of plastic anisotropy. These works predict the orientation sensitivity of yielding in individual lamellar colonies, predict the overall macroscopic response at deformation states well above yield, or predict the stress state at large plastic deformation. However, γ−TiAl materials also have elastic anisotropy that induces stress variations at the grain level under elastic loading. Analytical studies by Kozaczek, et al. [13] on a random polycrystalline material have shown that grain size, shape, and orientation can create stress concentration factors high enough to cause localized plastic microdeformation even when the polycrystalline aggregate is in the macroscopic elastic regime (i.e. when the loads on the material are such that one might expect fully elastic mechanical behavior).

Finite element modeling of lamellar γ−TiAl grain structures utilizes continuum models in which there are abrupt changes in the properties of the continuum at the grain boundaries. Thus, the models include singularities at intersections between the grains. In all of the finite element models that simulate polycrystalline response, these singularities are neglected. In this work, we attempt to minimize the impact of the singularities by presenting our results as volume-weighted distributions of stress, rather than as stress at specific locations. Convergence studies confirm that this method of presentation provides reliable data that is unaffected by the presence of singularities at the material interfaces. The rigorous treatment of these interface singularities remains an open questions of some significance.

This paper is strongly oriented towards a mechanical analysis of the material and, as such, seeks to predict differences in stress from the resting state. As a result, the effects of coherency stresses and mismatch structures at the material interfaces are not considered. The inclusion of such effects in future investigations into the fatigue and/or creep behavior of γ−TiAl is desirable, but would require coupling the conventional stress analysis with additional model for process simulation.

In what follows, effective elastic properties for the lamellar colonies are calculated from the constituent properties using a procedure developed for laminated orthotropic materials. Localized stress concentrations arising within polycrystals of γ−TiAl due to grain size, shape, and orientation are investigated using finite element models comprising several hundred grains. The effects of local elastic anisotropy on stresses are presented as statistical distributions of stress data throughout the sample for a given nominal strain or applied stress. Three-dimensional and two-dimensional models are investigated.

279

2. Elastic Properties Identification

Our modeling approach represents individual γ grains and lamellar γ+α$_2$ colonies, and their orientations, explicitly. However, our main interest lies in characterizing the stress variations among grains, and the stress or strain concentrations caused by changes in stiffness and orientation from grain to grain. Models with a sufficient number of grains to eliminate boundary effects typically consist of several hundred two-dimensional or three-dimensional grains or lamellar colonies. In this setting it is impractical to model discrete lamellae, and we resort to the use of effective properties and strengths for the lamellar γ–TiAl microstructure.

Elastic properties for the γ phase are based upon measurements reported by Yoo and Fu [14] for a composition of roughly Ti-56Al. Values of the room-temperature orthotropic elastic constants are listed in Table 1, in which directions (1,2,3) correspond to the [100], [010], and [001] crystal directions, respectively.

Table 1. Elastic Constants for γ (TiAl)

$E_1 = 140$ GPa	$\nu_{12} = 0.284$	$G_{12} = 78$ GPa
$E_2 = 140$ GPa	$\nu_{13} = 0.298$	$G_{13} = 105$ GPa
$E_3 = 135$ GPa	$\nu_{23} = 0.298$	$G_{23} = 105$ GPa

For the α$_2$ phase, the elastic constants again are based on measurements reported by Yoo and Fu [14]. Values of the orthotropic elastic constants are listed in Table 2. The α$_2$ crystal structure is hexagonal (DO$_{19}$); the '3' axis of the model is aligned with the 'c' crystal axis [0001], and the '1' axis is parallel to [11$\bar{2}$0].

Table 2. Elastic Constants for α$_2$ (Ti$_3$Al)

$E_1 = 125$ GPa	$\nu_{12} = 0.454$	$G_{12} = 43$ GPa
$E_2 = 125$ GPa	$\nu_{13} = 0.154$	$G_{13} = 62$ GPa
$E_3 = 191$ GPa	$\nu_{23} = 0.154$	$G_{23} = 62$ GPa

Effective room temperature elastic constants for lamellar γ–TiAl have been computed using the preceding elastic constants for each of the constituent materials. Constants for the lamellar material have been computed using a method developed for laminated orthotropic materials by Pagano [15]. A summary of effective orthotropic constants (in GPa) calculated for various proportions of α_2 and γ phases appears in Table 3. Orientation definitions for the elastic constants in Table 3 are aligned with the α_2 crystal structure.

Table 3. Effective Elastic Properties of Lamellar Colonies

Property	α_2:γ Ratio					
	1:1	**1:2**	**1:4**	**1:5**	**1:10**	**1:20**
E_1	160.2	171.4	179.7	182.0	187.0	189.6
E_2	160.2	171.4	179.7	182.0	187.0	189.6
E_3	206.4	211.5	215.5	216.6	218.9	220.2
G_{23}	64.6	65.5	66.3	66.5	66.9	67.1
G_{13}	64.6	65.5	66.3	66.5	66.9	67.1
G_{12}	59.4	64.7	69.3	70.3	72.6	74.1
ν_{23}	0.155	0.152	0.149	0.148	0.146	0.144
ν_{13}	0.155	0.152	0.149	0.148	0.146	0.144
ν_{12}	0.351	0.322	0.303	0.297	0.284	0.279

For the two-phase lamellar γ–TiAl, the crystallographic alignment at the γ-α_2 interfaces are $(111)_\gamma \| (0001)_{\alpha2}$ and $[1\bar{1}0]_\gamma \| [11\bar{2}0]_{\alpha2}$. To utilize the method described by Pagano, lamellar configurations have been simulated using alternating layers of α_2 and γ. Although actual lamellar γ–TiAl has multiple layers of γ phase for each layer of α_2 [16], numeric simulations show that models with single alternating layers provide results that are statistically indistinguishable from models with multiple layers of γ phase for each layer of α_2. Within each configuration, orientations for individual layers are assigned randomly from the range of possible orientations, and the elastic constants of the constituent materials are transformed into the appropriate orientations.

Values listed in Table 3 for each proportion of α_2:γ are the averages of results from three lamellar configurations containing 500 layers per configuration. The large number of layers is used to approximate the effective properties of a typical lamellar colony consisting of multiple layers. Even with this large number of layers, computed values among the three configurations for any given α_2:γ ratio deviate by up to 2.2% from the average for that α_2:γ ratio. Comparisons with tensile tests on dogbone specimens dominated by a single lamellar colony (having an α_2:γ ratio of 1:9) in the gage section indicate that the method used to calculate the elastic constants provides a good approximation to the measured constants for lamellar TiAl [17].

3. Modeling

The primary purpose of this paper is to examine stress distributions that can occur in polycrystalline structures and to investigate the capability of models, utilizing different degrees of refinement or using a two-dimensional representation for the microstructure, to accurately predict the stress variations. The structures considered here consist of both lamellar colonies and equiaxed γ (TiAl) grains, with an assumed volume fraction of lamellar $\gamma+\alpha_2$ colonies of 0.96 (with the remaining volume consisting of individual γ grains). All of the analyses are confined to the elastic regime. Results for similar three-dimensional models in which plasticity is considered are reported in a paper by Brockman [18].

For all of the models described here, elastic constants for the γ grains are those listed in Table 1. The constants selected for the lamellar colonies are those listed in Table 3 for a α_2:γ ratio of 1:10. Although our estimates for the effective properties include data from several sources and involve some level of approximation, these values are thought to be representative of the level of anisotropy present in the lamellar colonies. The results, presented as a deviation from the volumetric distribution of stress that would occur for an isotropic material, can be considered representative of the level of stress variation that occurs for material composed of mostly lamellar γ–TiAl.

Three-dimensional models

Filling three-dimensional space with a regular pattern of two grain types significantly restricts the number of possible geometric configurations available. The selected geometric configuration consists of

282

cubes, which represent the γ grains, alternating with truncated rhombic dodecahedra, which represent the lamellar colonies. This configuration was selected based on the meshing capabilities of the pre-processing software used to create the finite element model and the ability to efficiently assign elements to a specific lamellar colony or gamma grain. Fig. 1 shows a finite element model of a polycrystal composed of an equal number of lamellar colonies and equiaxed γ grains. The model contains 256 colonies and 256 grains, with the orientation of each grain being randomly generated. Fringe values in Fig. 1 depict the orientation of each grain with respect to the loading direction, which is parallel to the global 'x' axis for the case shown. Symmetry conditions are applied on the three rearward facing surfaces of the model (i.e. these faces are assumed to have a mirror plane at the boundary). The remaining three faces are constrained to remain planar, but may expand or contract in response to a tensile loading on any one of the faces. These constraints represent generalized plane strain conditions.
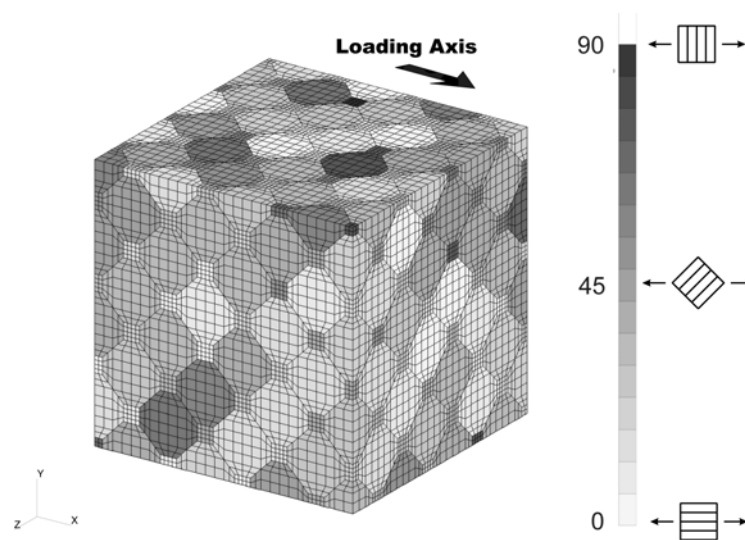
Fig. 1. Baseline 3D model using cubic packing scheme for the lamellae.

For the purpose of evaluating the effects of variations in model refinement, stress distributions have been computed for the various stresses of interest. The stress distributions indicate the volume of material above a specific fraction of the applied tensile stress, $\sigma_{applied}$. For comparing models, we look at three stress components: σ_{axial}, which is the global stress in the direction of the applied tensile loading;

σ_{norm}, which is the stress normal to the lamellae within each colony; and, τ_{rs}, which is the resolved shear on lamellar planes.

In the limit, as the elastic constants of the material approach those of an isotropic material and the number of grains becomes large, the volume of material V for which the stress ratio is above a specific value ϕ can be specified by explicit relations. For the uniaxial loading state defined above, we derived these relations as:

$$V\Big|_{\frac{\sigma_{axial}}{\sigma_{applied}}>\phi} = \begin{cases} 1 \text{ if } \phi < 1 \\ 0 \text{ if } \phi > 1 \end{cases} \tag{1}$$

$$V\Big|_{\frac{\sigma_{norm}}{\sigma_{applied}}>\phi} = 1 - \cos\left[\frac{1}{2}\cos^{-1}(2\phi - 1)\right] \tag{2}$$

$$V\Big|_{\frac{\tau_{rs}}{\sigma_{applied}}>\phi} = \cos\left[\frac{1}{2}\sin^{-1}(2\phi)\right] - \sin\left[\frac{1}{2}\sin^{-1}(2\phi)\right] \tag{3}$$

In all of the following comparisons, stress distributions computed using the preceding relations are overlaid on the results from the polycrystal models, thus allowing the stress variation that is due to the orthotropy of the material to be discerned from the distribution that is simply due to the orientation of the grain relative to the direction of loading.

Finite element analyses of the three-dimensional (3D) models have been performed with the ABAQUS code using 8-node hexahedral elements. The "baseline 3D model" shown in Fig. 1 has approximately 181,000 degrees of freedom (DOFs) and is of a size for which plastic deformation simulations can be analyzed in a practical time using the current generation of computers. To determine the effects of boundary conditions on the stress distributions, a model using more than five times as many colonies as that of the baseline 3D model has been developed, as shown in Fig. 2. Also, for evaluating the effects of mesh refinement, a model with eight times as many elements (2x refinement in all directions) but the same number of colonies as the baseline 3D model has been developed, as shown in Fig. 3. The number of DOFs in these models (1.1 and 1.4 million DOFs for Figs. 2 and 3, respectively) and the lack of sparsity in the stiffness matrices used for the finite element calculations make the models shown in Figs. 2 and 3 rather impractical for plasticity calculations at the present time.
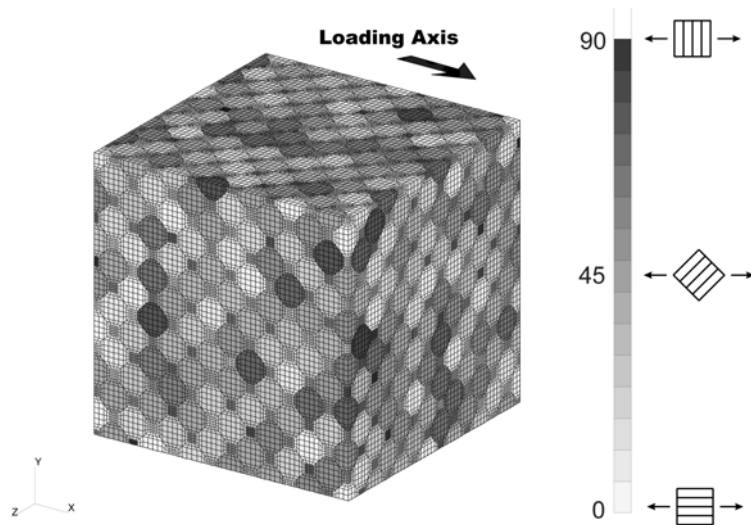
Fig. 2. 3D model with significantly larger number of grains.
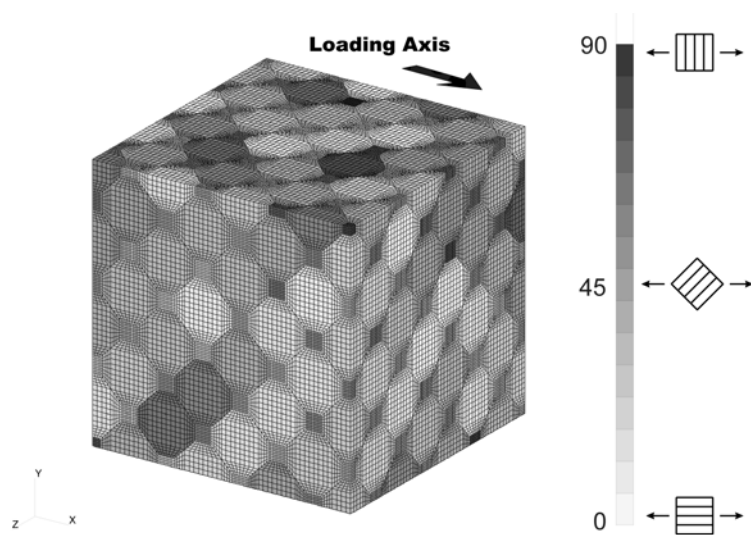

Fig. 3. 3D model with significant mesh refinement.

The response to axial loading has been used to determine effective elastic constants for the material. For all of the models shown in Figs. 1 through 3, the computed effective elastic constants are: E=178 GPa, G=72 GPa, and ν=0.23. These values have been repeatedly computed within 1.5% by all of the cases evaluated.

Distributions of axial stress for the baseline 3D model are shown in Fig. 4, where the curves are average distributions from nine cases. The nine cases have been generated using three models with randomly defined crystal orientation, with each of the three models loaded in each of three orthogonal directions. The γ grains show a larger variation from the mean stress, and also have net mean stress that is higher than the average axial stress (as indicated by the fact that more than 50% of the γ grain volume is above an axial stress ratio of 1.0). The larger variation occurs for the γ grains because their moduli are stiffer than the moduli of the lamellar colonies and some load is shed from the lamellar colonies to the γ grains.

Singularities exist at the grain boundaries due to the abrupt change in properties. However, these singularities only affect the mechanical behavior in a very localized region around the boundary. The impact of the singularities can be evaluated by investigating models of larger size or higher refinement. Analyses have been run on a model with over five times as many grains as were used in the baseline 3D model and on a model with eight times as many elements as were used in the baseline 3D model.

Fig. 5 compares the distribution of stress normal to the lamellae in the lamellar colonies for the baseline 3D model (256 colonies) with the distribution for a 1,372-colony model (shown in Fig. 2). The two stress distribution curves generated from the finite element results represent the average of the analyses for multiple cases. Error bars, which show ±1 standard deviation from the mean, indicate the variation between cases at discrete locations on the curves. Results from the baseline 3D model and the 1,372-colony model are very similar with greater variability seen in the results from the baseline 3D model. Results from the modeled orthotropic cases are similar to the isotropic material curve, but with stresses normal to the lamellae outside the range calculated for an isotropic material.
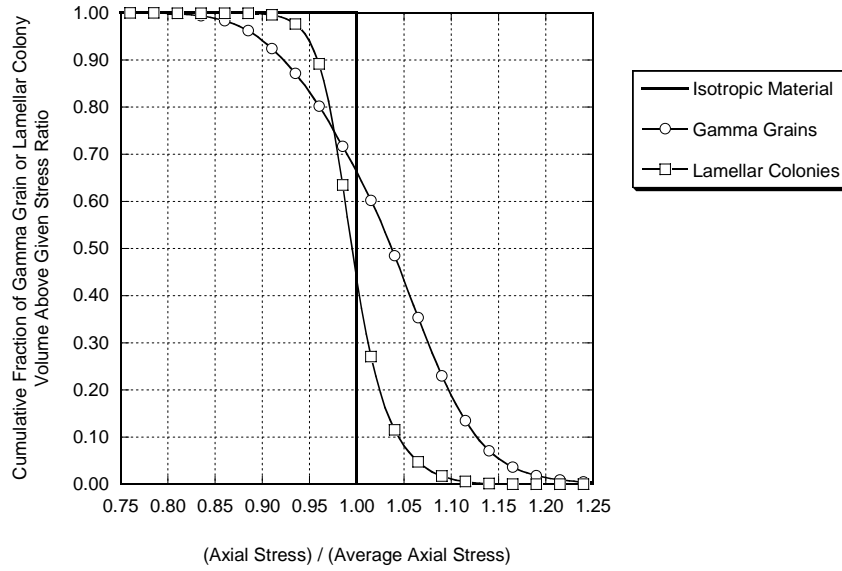
Fig. 4. Representative distribution of the stresses, aligned with the loading axis, as predicted by all three dimensional models.
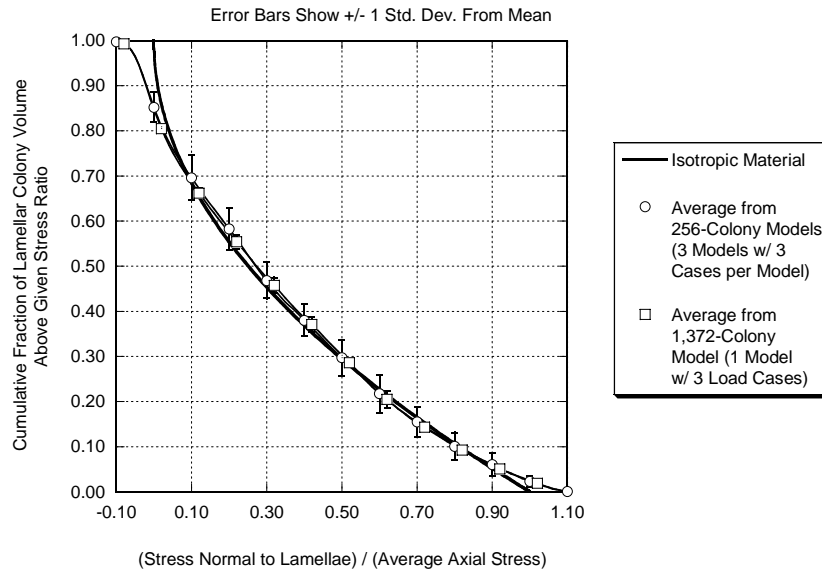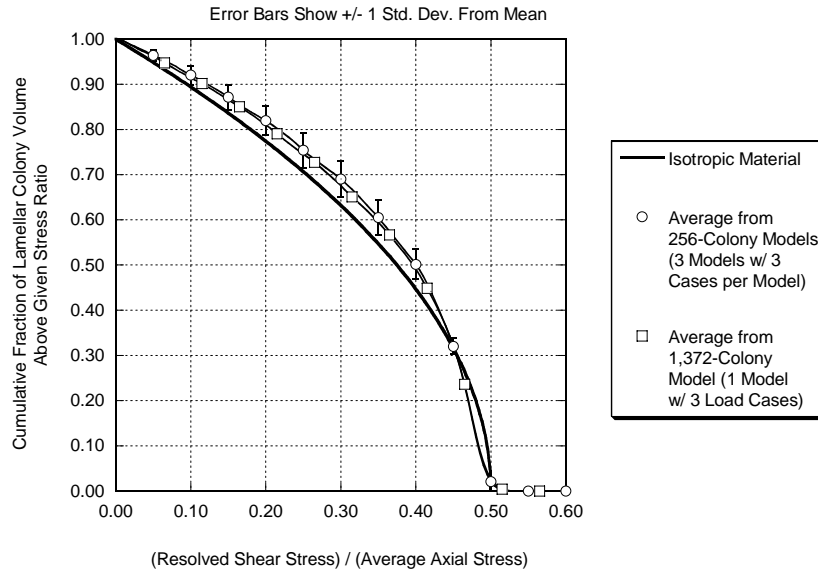

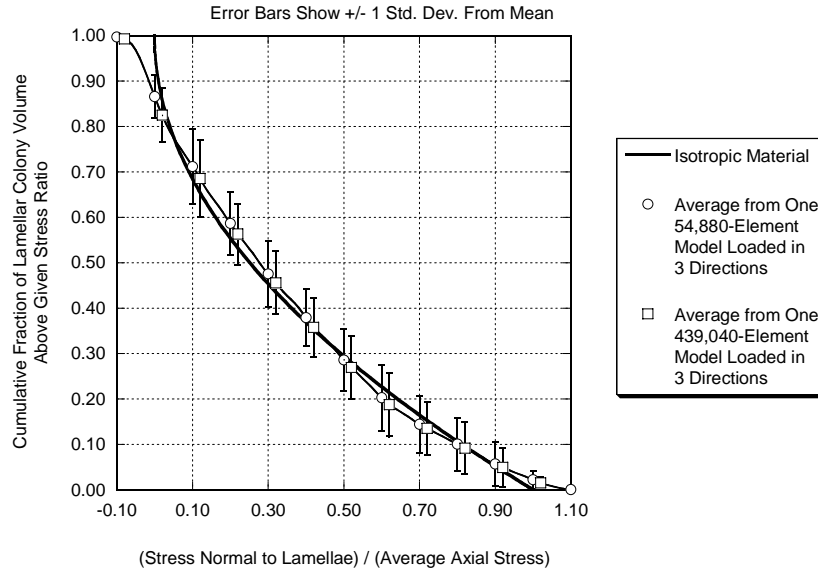Fig. 5. Distribution of the stresses, normal to the lamellae, in the lamellar colonies for the baseline 3D model and model with a significantly larger number of grains.

Fig. 6 shows similar data for the resolved shear stresses on the lamella. Again, results from the baseline 3D model and the 1,372-colony model are similar, with greater variability seen in the results from the baseline 3D model. Results from the modeled orthotropic cases are similar to the isotropic material

curve, but typically have a slightly larger fraction of lamellar colony volume at intermediate resolved shear stresses.

Fig. 6. Distribution of the resolved shear stresses in the lamellar colonies for the baseline 3D model and model with a significantly larger number of grains.

To assess the impact of element refinement on the stress distributions, analyses have been run on a model with eight times as many elements as were used in the baseline 3D model. For this comparison, the grain sizes and orientations are the same between the models, and only the element refinement is changed. Figs. 7 and 8 show data similar to that shown in Figs. 5 and 6, except that the comparison is for the baseline 3D model with the highly refined model shown in Fig. 3. High variability, as signified by relatively broad error bars, is due to the limited number of cases analyzed.

The key point demonstrated by these three-dimensional models is that averaging the results from relatively coarse finite element models with limited numbers of grains results in stress distributions that are very similar to those developed by models with far more grains or element refinement. Further studies are necessary to determine if similar coarse models can be used for analyses of problems in which plastic deformation is to be considered.

Fig. 7. Distribution of the stresses, normal to the lamellae, in the lamellar colonies for the baseline 3D model and model with significant mesh refinement.
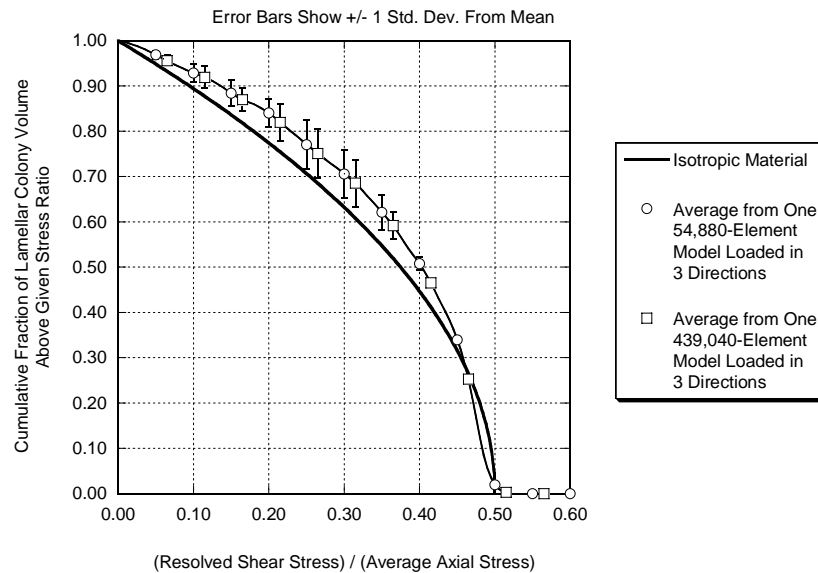
Fig. 8. Distribution of the resolved shear stresses in the lamellar colonies for the baseline 3D model and model with significant mesh refinement.

Two-dimensional models

Two-dimensional models have been analyzed to determine if simpler models can accurately capture the stress variation effects seen in the 3D models and to evaluate the effects of variations in grain size and shape. Filling two-dimensional space with a regular pattern of two grain types offers additional geometric configurations not possible in the 3D models. One possible geometric configuration represents

289

the lamellar colonies with squares and uses smaller squares, inset and rotated by 45°, to represent the γ grains. This configuration is illustrated in Fig. 9. Another configuration represents the lamellar colonies with hexagons, with small inset triangles representing the γ grains. This latter configuration, illustrated in Fig. 10, is similar to that used by Kad, Dao, and Asaro [9], albeit with triangles used here in place of their squares and diamonds. Fringe values in Figs. 9 and 10 depict the orientation of each grain with respect to the loading direction, which is parallel to the global 'x' axis for the cases shown. Symmetry conditions are applied on two adjacent edges of the model (i.e. these edges are assumed to have a mirror plane at the boundary). The remaining two edges are constrained to remain planar, but may expand or contract in response to a tensile loading on either of the faces. These constraints represent generalized plane strain conditions. Plane strain conditions (i.e. no out-of-plane strain) are assumed for the direction normal to the plane of the model.
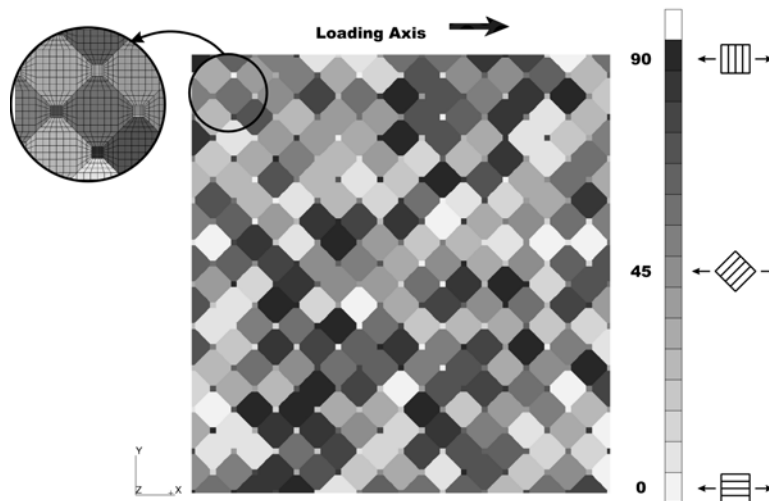
Fig. 9. Two dimensional finite element model using cubic packing scheme for the lamellae.
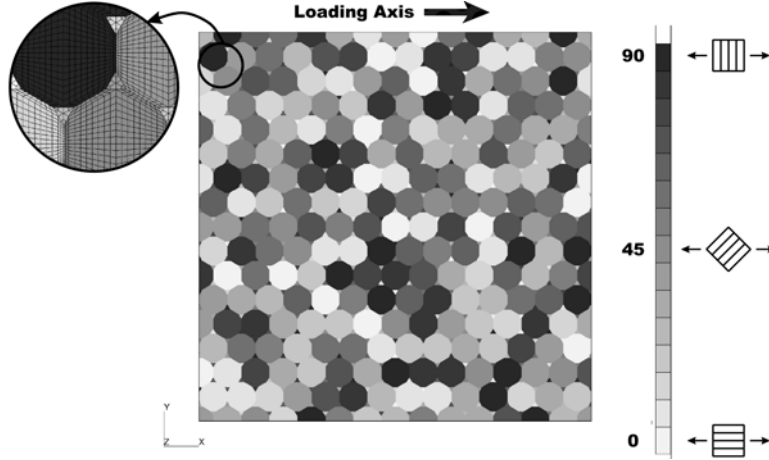
Fig. 10. Two dimensional finite element model using hexagonal packing scheme for the lamellae.

As was done for the three-dimensional models, the stress distributions are compared with the corresponding distributions for an isotropic material. In the limit, as the elastic constants of the material approach those of an isotropic material and the number of grains becomes large, the volume of material V for which the stress ratio is above a specific value ϕ can be specified by explicit relations. For an isotropic material with the plane strain loading condition defined above, we derived these relations as:

$$V\Big|_{\frac{\sigma_{axial}}{\sigma_{applied}}>\phi} = \begin{cases} 1 \text{ if } \phi < 1 \\ 0 \text{ if } \phi > 1 \end{cases} \tag{4}$$

$$V\Big|_{\frac{\sigma_{norm}}{\sigma_{applied}}>\phi} = \frac{1}{\pi}\cos^{-1}(2\phi - 1) \tag{5}$$

$$V\Big|_{\frac{\tau_{rs}}{\sigma_{applied}}>\phi} = 1 - \frac{2}{\pi}\sin^{-1}(2\phi) \tag{6}$$

To evaluate the effects of variability in colony size, finite element models have been developed that reproduce some of the size variability observed in nearly-lamellar γ–TiAl structures. Figs. 11 and 12 show two such models. Fig. 11 shows a model with no variation in grain size, while Fig. 12 shows a model in which the variation in grain size is specified as a random value with a standard deviation of 50% of the mean grain radius. These models are initially gridded with a uniform mesh of quadrilateral elements. Specific locations of lamellar colony region centroids are prescribed along with a radius value for each lamellar colony region. A sorting algorithm is used to assign elements to the region for which the distance

between the element centroid and the region's centroid, normalized by the region's radius, is a minimum. γ grains, with varying radii, are seeded at the boundaries of the lamellar colony regions and the sorting algorithm is applied a second time to assign elements to the lamellar colonies or the γ grains. Quadrilateral elements are split into triangles in selected areas to minimize the jaggedness of the mesh. Although this scheme for model generation does not mimic the process by which grains are formed, it does result in a model that simulates two phases of material with randomly distributed crystalline size and shape.

Analyses of the two-dimensional (2D) models have been performed with the ABAQUS code using four-node quadrilateral elements, assuming plain strain conditions. Three-node triangular elements are also used in the γ phase for the model based on hexagonal-shaped lamellar colony regions (Fig. 10) and along some grain boundaries in the random grain size meshes (Figs. 11 and 12). The properties are specified such that the '3' direction of the grains lay in the X-Y plane of Figs. 9 through 12, with a random angular rotation assigned for each grain's orientation. As discussed in the following paragraphs, this restriction has a limited effect on the elastic analyses. However, this restriction may become far more significant for plasticity analyses, where the stress distributions for the orthotropic crystals deviate far more significantly from the stress distributions for an isotropic material. For each of the 2D models, six cases have been analyzed. The six cases use three models with randomly defined crystal orientation (and possibly size), with each of the three models loaded in each of two orthogonal directions.
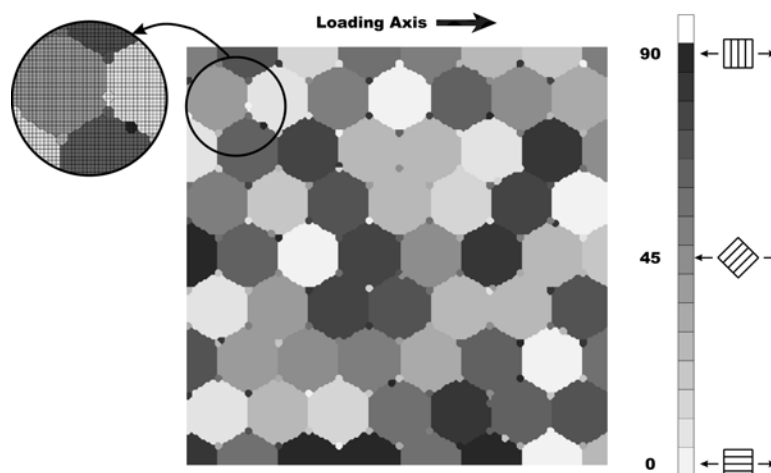

Fig. 11. Two dimensional finite element model using random grain generation with no variation in grain size.
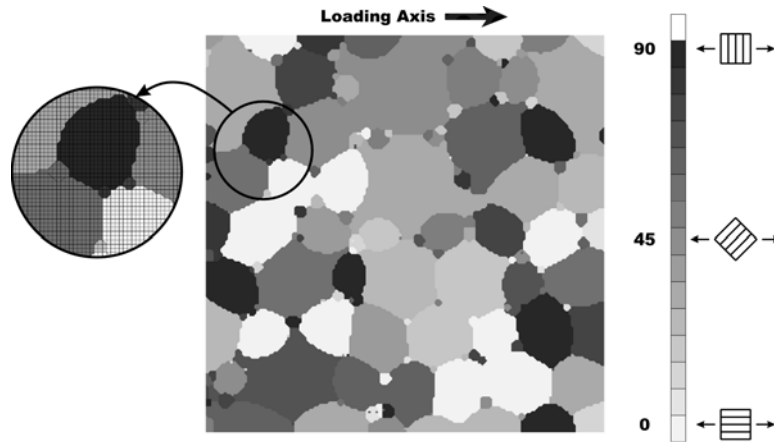
Fig. 12. Two dimensional finite element model using random grain generation with a 50% standard deviation in grain size.

Distributions of axial stress for the cubic 2D model are shown in Fig. 13. Nearly identical axial stress distributions are computed for all of the models shown in Figs. 9 through 12. The γ grains show a larger variation from the mean stress than do the lamellar colony regions. The larger variation occurs for the γ grains because their moduli deviate more from the average values of the polycrystalline system than do those of the lamellar colonies. Unlike the results for the 3D models, the γ grains have a net mean stress that is very close to the average axial stress. This difference between the two- and three-dimensional models is most likely due to the fact that the local '3' direction for all of the crystals is constrained to lie in the X-Y plane for the 2D models.
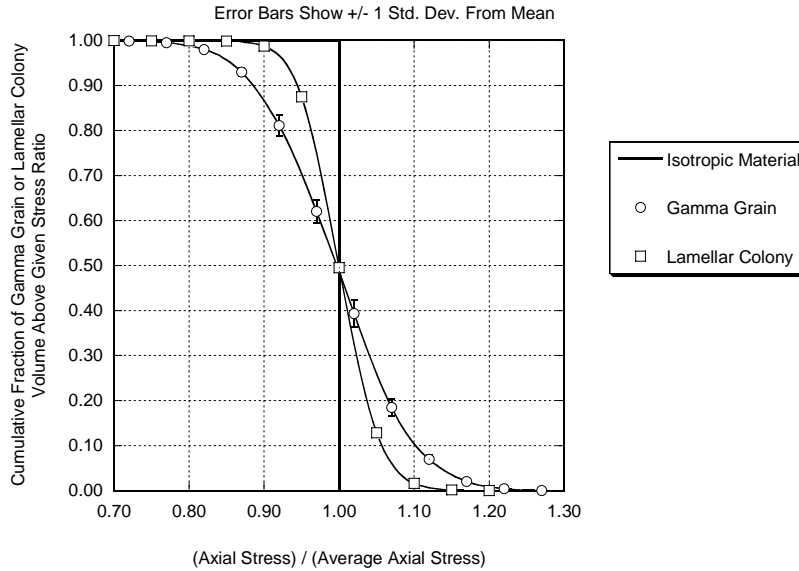
Fig. 13. Representative distribution of the stresses, aligned with the loading axis, as predicted by all two dimensional models.

The effect of variations in grain geometry has been assessed by comparing stress distributions from the cubic 2D model with results from the hexagonal 2D model. Fig. 14 compares the distribution of stress normal to the lamellae in the lamellar colonies for these two cases. The two stress distribution curves generated from the finite element results represent the average of the analyses for six cases. Error bars, which show ±1 standard deviation from the mean stress, indicate the variation between cases at discrete locations on the curves. As in the 3D models, results from the modeled orthotropic cases are similar to the isotropic material curve, but with stresses normal to the lamellae outside the range calculated for an isotropic material. Fig. 15 shows the distributions for the maximum resolved shear stresses on the lamella. Results from the modeled orthotropic cases are similar to the isotropic material curve but, unlike the results from the 3D model, typically have a slightly smaller fraction of lamellar colony volume at intermediate resolved shear stresses. This difference in resolved shear stresses between the two- and three-dimensional models again is most likely due to the fact that the local '3' direction for all of the crystals is constrained to lie in the X-Y plane for the 2D models.
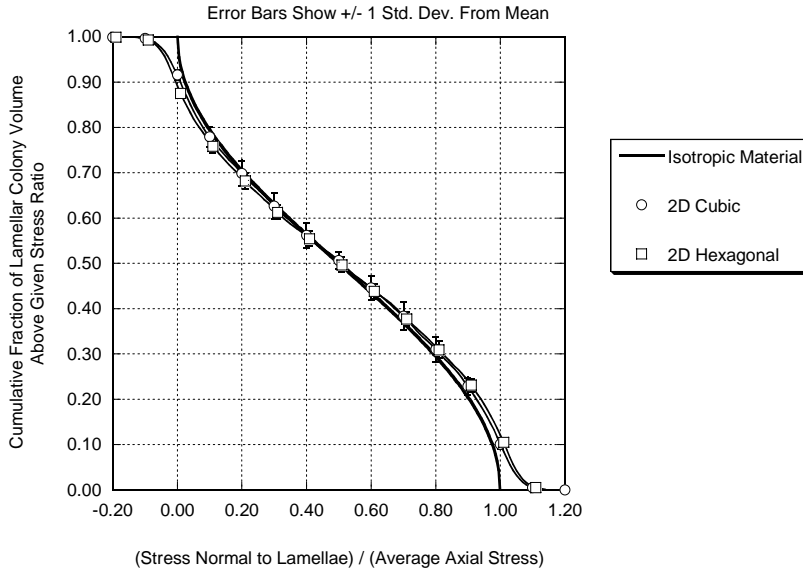
Fig. 14. Distribution of stresses, normal to the lamellae, in the lamellar colonies for 2D models with cubic and hexagonal packing schemes for the lamellae.
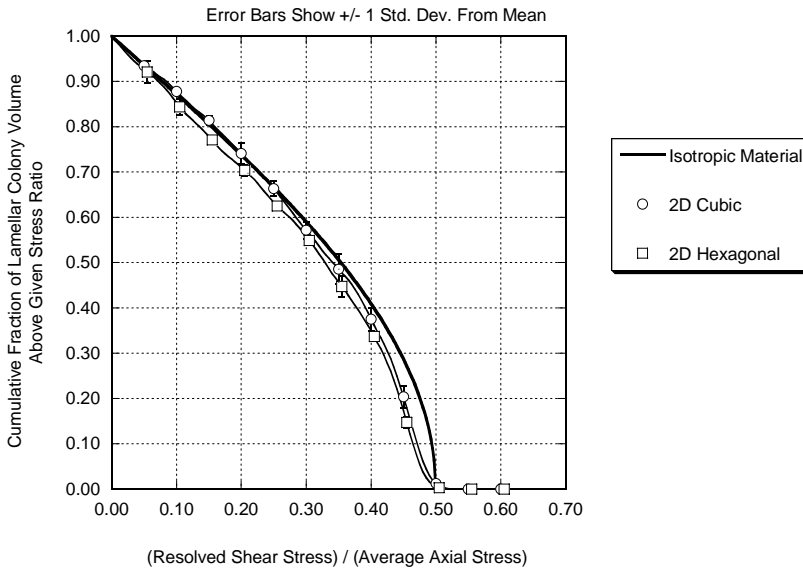

Fig. 15. Distribution of resolved shear stresses in the lamellar colonies for 2D models with cubic and hexagonal packing schemes for the lamellae.

The effect of variations in grain size on stress levels has been assessed by comparing stress distributions from random models (shown in Figs. 11 and 12) having size distributions with standard deviations of 0% and 50% of the mean size. Fig. 16 compares the distribution of stress normal to the lamellae in the lamellar colonies for these two cases, while Fig. 17 compares the distribution of the

maximum resolved shear stresses on the lamella. The stresses normal to the lamellae and the maximum resolved shear stresses on the lamella are similar for both models, with greater variability seen in the random model having size distributions with a standard deviation of 50% of the mean size. This result suggests that the variation in stresses due to size variability alone is relatively insignificant.
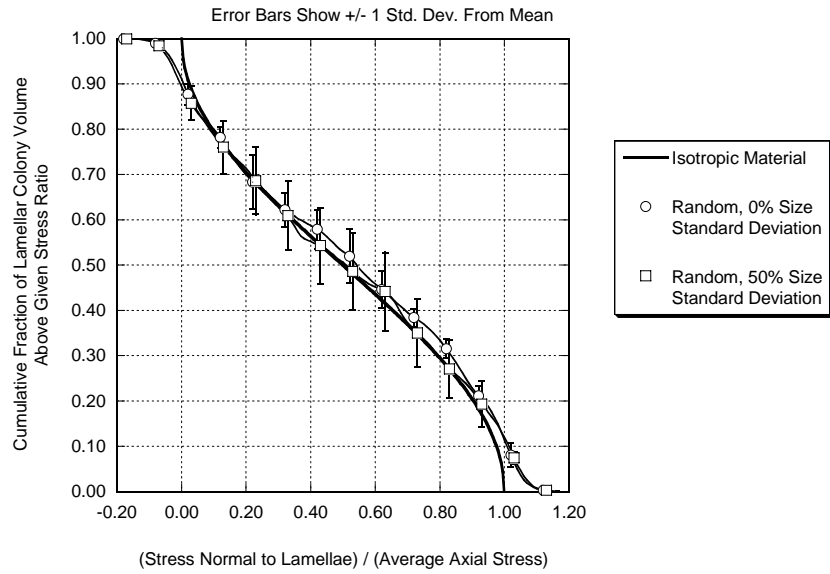

Fig. 16. Distribution of stresses, normal to the lamellae, in the lamellar colonies for 2D models with no variation in grain size and 50% standard deviation variation in grain size.
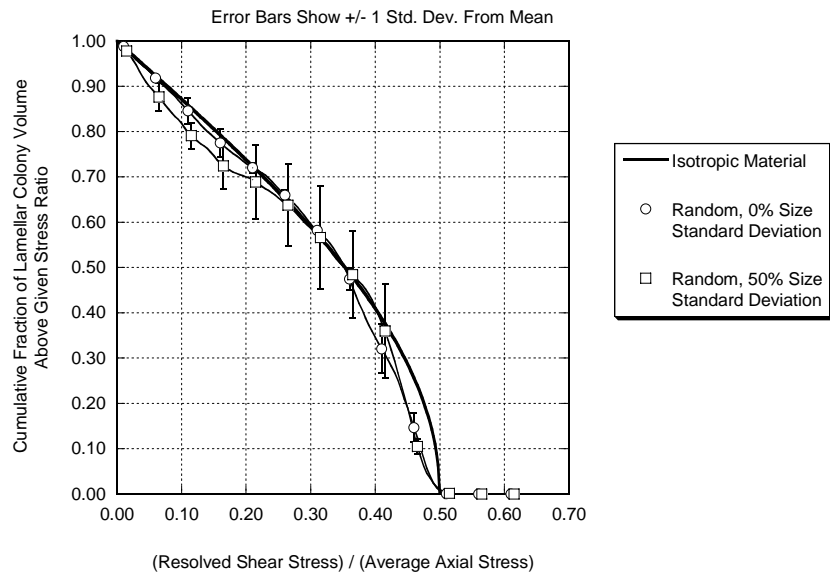
Fig. 17. Distribution of resolved shear stresses in the lamellar colonies for 2D models with no variation in grain size and with 50% standard deviation variation in grain size.

4. Conclusions

A method for evaluating the effects of stress concentrations that occur at the grain level in polycrystalline materials composed of anisotropic crystals has been presented. The method is based on comparisons of the volumetric distributions of specific components of stress. The method has been applied in the elastic regime for a γ–TiAl material system composed of two phases of orthotropic material, lamellar colonies of TiAl/Ti$_3$Al interspersed with small grains of pure TiAl. Requirements on model size and refinement necessary to produce reasonable statistical information have been investigated. The method has been applied using finite element representations of crystalline structures in two and three dimensions. The results indicate that three-dimensional models of only moderate size and refinement, for which analyses in the plastic regime may be performed in a reasonable time with the current generation of supercomputers, can sufficiently capture the stress distributions as well as models of much larger size or higher refinement. Two-dimensional models using a random size variation of the crystals show that size variation does not significantly affect the stress distribution within the material. Stress distributions predicted by two-dimensional models using various geometric representations for shape of the lamellar colony phase compare well with each other, but show less deviation from the distributions of an isotropic material than do the stress distributions generated by the three-dimensional models.

References

[1] Appel F Wagner R. Mat Sci Eng 1998;R22:187.

[2] Parteder E Siegmund T Fischer FD Schlögl S. Mat Sci Eng 1996;A192-193:149.

[3] Schlögl SM Fischer FD. Comp Mat Sci 1996;7:34.

[4] Schlögl SM Fischer FD. Phil Mag A 1997;75:621.

[5] Schlögl SM Fischer FD. Mat Sci Eng 1997;239-240:790.

[6] Lebensohn R Uhlenhut H Hartig C Mecking H. Acta Mater 1998;46:4701.

[7] Taylor GI. J Inst Metals 1938;62:307.

[8] Bishop JFW Hill R. Phil Mag 1951;42:1298.

[9] Kad BK Dao M Asaro RJ. Phil Mag A 1995;71:567.

[10] Kad BK Dao M Asaro RJ. Mat Sci Eng 1995;192-193:97.

[11] Kad BK Asaro RJ. Phil Mag A 1997;75:87.

[12] Dao M Kad BK Asaro RJ. Phil Mag A 1996;74:569.

[13] Kozaczek KJ Petrovic BG Ruud CO McIlree AR. Modeling of stress distributions on the microstructural level in Alloy 600. In: PVP-Vol. 306, Fatigue and Crack Growth: Environmental Effects, Modeling Studies, and Design Considerations, ASME, 1995;223.

[14] Yoo MH Fu CL. Met Mat Trans 1998;29A:49.

[15] Pagano NJ. Exact moduli of anisotropic laminates. In: G. P. Sendeckyj, editor. Mechanics of Composite Materials, Academic Press, New York, 1974.

[16] Parthasarathy TA Mendiratta MG Dimiduk DM. Acta Mater 1998;46:4005.

[17] Porter WJ. Private Communication. University of Dayton Research Institute, 2000.

[18] Brockman RA. Submitted to Int J Plasticity, 2000.

Creep Rupture Behavior of ±45° Oxide/Oxide Nextel™720/AS Composite

Dennis J. Buchanan*, Reji John and Larry P. Zawada
Materials and Manufacturing Directorate, Air Force Research Laboratory (AFRL/MLLN),
Wright-Patterson Air Force Base, OH 45433-7817
* University of Dayton Research Institute, Dayton, OH 45419

Abstract

Oxide/Oxide Ceramic Matrix Composites (CMC) are currently being demonstrated in high-temperature aerospace applications where their beneficial resistance to oxidation are critical to a successful design. Many applications are engine components that are axis-symmetric in shape and are subjected to axis-symmetric thermal and mechanical loadings. Traditional woven CMC materials used in these components are typically made from 0°/90° fiber architectures. In many cases the highest loads are not always coincident with the orientation of the reinforcing fibers. Hence, these components could produce stress states that approach the off-axis tensile and creep strengths. The CMC investigated was Nextel™720/AS. Nextel™720/AS is composed of an Alumina-Silica matrix reinforced with an eight-harness satin weave (8HSW) of Nextel™720 fibers. Tensile and creeps tests on ±45° Nextel™720/AS were performed to characterize the off-axis material behavior. All elevated temperature tests were performed at 1100°C. The data show that the ultimate strength and the 100 hour creep strength ratio of ±45° to 0°/90° are 0.6 and 0.3, respectively. The creep rupture behavior of the ±45° orientation was compared to the 0°/90° orientation.

Introduction

Damage tolerant ceramic matrix composites (CMC) that exhibit relatively little degradation in mechanical properties at elevated temperature are being evaluated for high temperature aerospace applications. Many of the applications require that the material properties be maintained at elevated temperature and under combustion environment conditions. Oxide/oxide CMC have an inherent resistance to oxidation and therefore exhibit little or no degradation in mechanical properties at expected service temperatures.—Several authors [1-7] have reported that oxide/oxide CMC exhibit excellent tensile and fatigue properties at room and elevated temperatures. Monotonic tensile behavior at room and elevated temperature (1100°C) on ±45° Nextel™720/AS [10,11] have shown that the failure strength and strain to failure are a function of test temperature which is in contrast to the 0°/90° behavior. This investigation focuses on the sustained load (creep) behavior of the ±45° orientation at 1100°C.

Material

The Nextel^{TM}720/AS oxide/oxide CMC was manufactured by COI Ceramics, Inc, of San Diego, CA. The Nextel^{TM}720 fibers, which are produced by the 3M Company of St. Paul, MN [15], are $\approx$ 12 μm in diameter. Approximately 400 fibers are bundled together in tows and woven into a balanced eight-harness-satin weave (8HSW) cloth. The matrix consists of a porous alumina-silica (AS) that is weakly bonded to the fibers without an engineered interphase. The panels used in this study contained 12 plies. Section samples of panels used in this study showed that the fiber volume fraction range was 42 - 50%. Figure 1 shows microcracks distributed throughout the matrix rich regions of the composite as a result of panel shrinkage that occurred during processing. Additional details about the manufacture of the CMC can be found in Ref. [12].
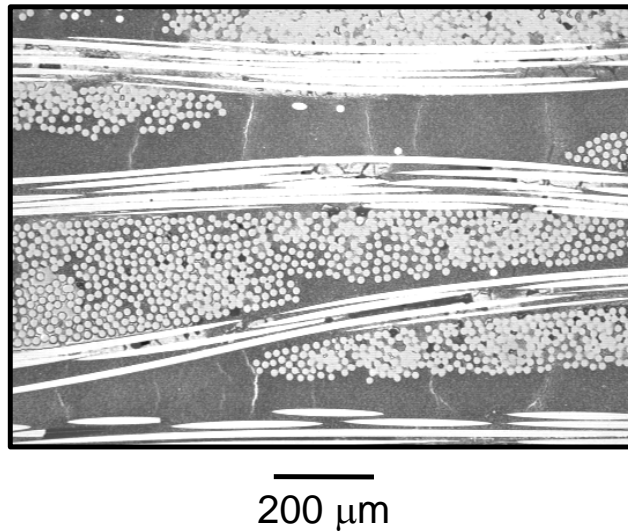

200 μm

Figure 1.   Microstructure of (0°/90°) 8HSW Nextel^{TM}720/AS microstructure highlighting the matrix cracks due to processing.

Experimental Procedure

Shown in Fig. 2 are the specimen geometries that were used for this study. The top figure, a dogbone specimen, was used for unnotched tensile and creep rupture tests. The two notched specimens, semi-circular and sharp notch, were used for creep rupture behavior. The nominal dimensions of the specimens were, thickness $\approx$ 2.5 mm and length $\approx$ 150 mm. The net-section width of the both dogbone geometry and the notched geometries was greater then the repeating cell size of the 8HSW cloth $\approx$ 9 mm.
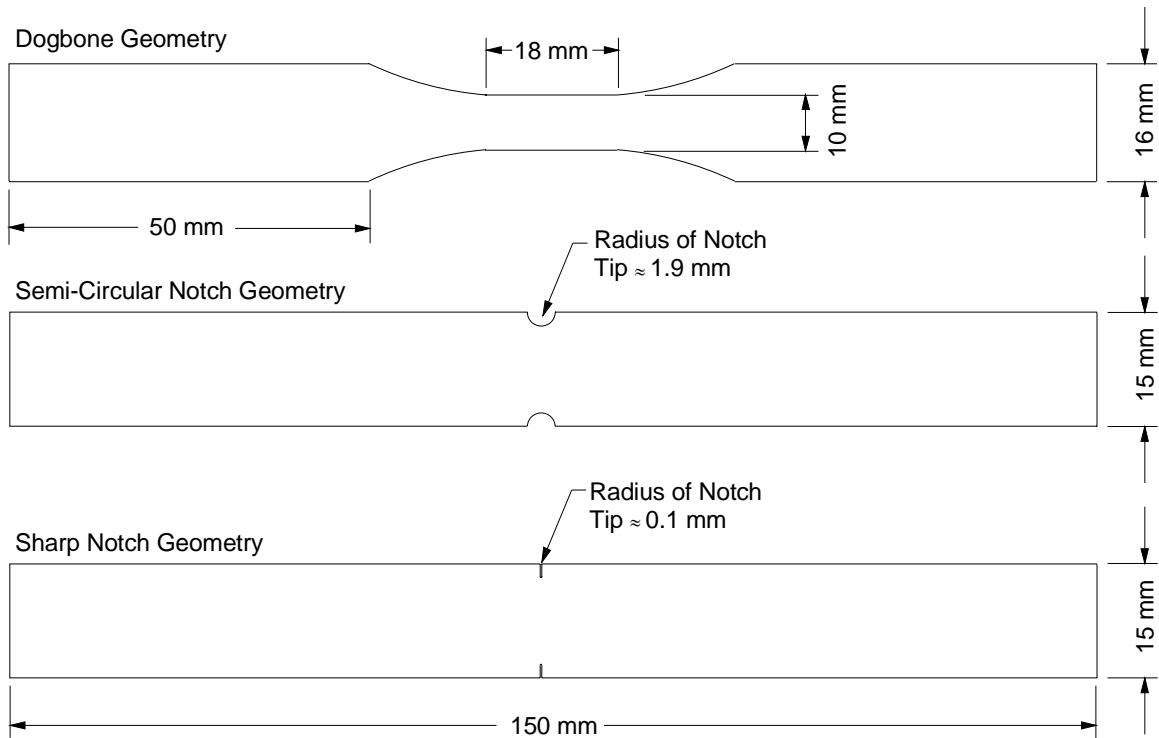
Figure 2. Dogbone and Notched Specimen test geometries.

The specimens were measured and photographed to document the condition of the gage section and notches prior to testing. The specimen ends were tabbed with fiberglass tabs to provide a flat uniform surface for the smooth grip surfaces and to minimize the possibility of grip failure. The specimens were mounted in a precisely aligned, rigid grip system that minimized specimen bending and rotation. A clamshell furnace with silicon-carbide heating elements and four-zone control were used for the elevated temperature creep tests. Thermal profile maps on the specimen showed that the specimen was uniformly heated, $\pm$ 0.6%, over the entire gage section of the specimen. All creep tests were performed in a closed loop servo-hydraulic horizontal test machine. A loading rate of 20 MPa/s was used for all the creep tests. Applied load, temperature and extensometry data were collected during the test.

The cross-sectional area used to calculate the net-section stress was based on the minimum cross-section of a plane perpendicular to the loading axis. The net-section stresses were based on cross-sectional area only and did not include the effects of stress risers due to the stress concentration factor of the geometry. The elastic stress concentration factor, $K_t = \sigma_{tip}/\sigma_{net}$, for the semi-circular and sharp notch were approximately, $K_t \approx 2.3$ & 7.1, respectively.

Experimental Results

Monotonic tensile tests were conducted on dogbone specimens with woven fibers mats aligned in the 0°/90° and ±45° orientations. The applied uniaxial loading direction was 0°. The axial stress versus axial strain response for the Nextel720/AS-0 0°/90° and ±45° orientations are shown in Fig. 3 at 1100°C. The elastic modulus for both orientations are similar, approximately

62 GPa. These modulus values are consistent with results reported by Zawada et al. [1] on 0°/90° Nextel720/AS-0 and by Kramb et al. [11] on ±45° Nextel610/AS at elevated temperatures. Above ≈ 50 MPa, the ±45° orientation has a large decrease in stiffness while the 0°/90° orientation maintains initial stiffness to failure. In contrast, the ultimate strength and strain to failure are very different for the two orientations.
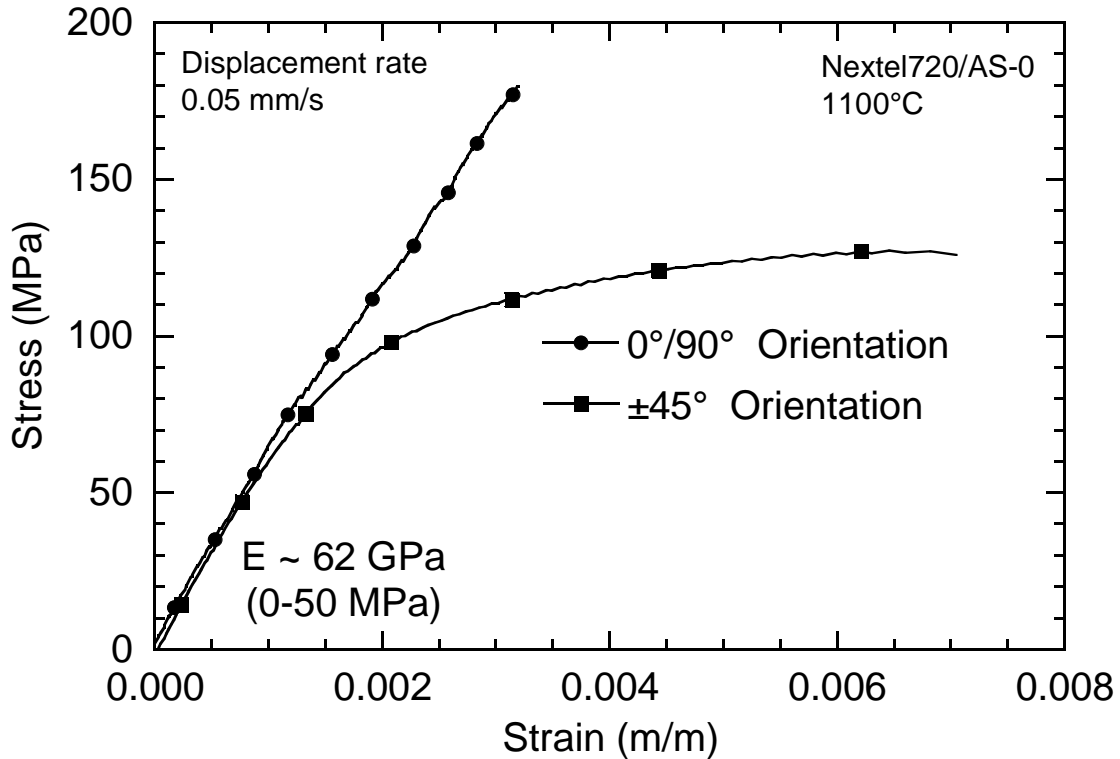

Figure 3. Stress versus strain for 2D fiber weaves oriented in the 0°/90° and ±45° at 1100°C.

Figure 4 shows the total strain versus time for creep tests of ±45° Nextel720/AS-0 at 1100°C at four different stress levels. The data show there is a strong influence of applied stress on the secondary strain rate. For a 60% increase in stress, 50 to 80 MPa, a 25X increase in strain rate is observed. These are stress levels that correspond to a range of 40-65% of the ultimate tensile strength.
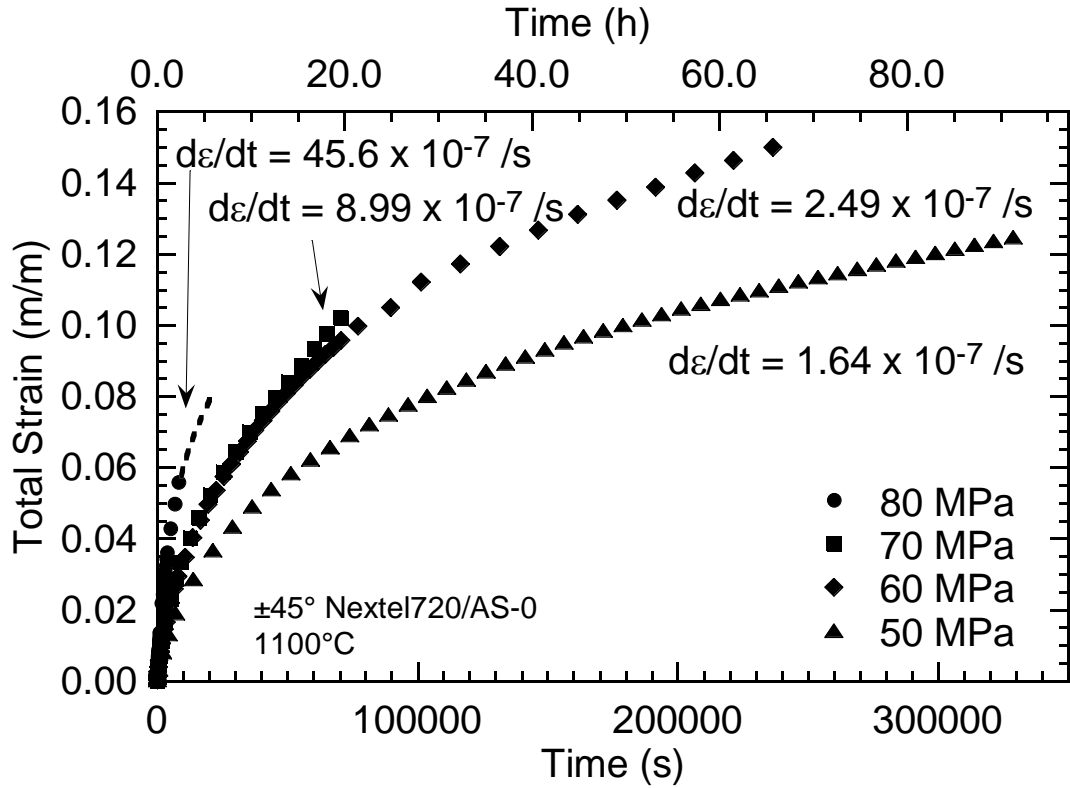
Figure 4. Total strain versus time for ±45° Nextel720/AS-0 at 1100°C.

Figure 5 is a comparison of strain rate versus applied stress for the 0°/90° and ±45° orientations. Creep results from Zawada et al. [2] and Lara-Curzio and More [14] on 0°/90° Nextel720/AS-0 at 1100°C and 1200°C, respectively, show a much lower strain rate compared to the ±45° data at 1100°C. For a creep stress, $\sigma \approx 90MPa$, the 0°/90° strain rate is over 5000X slower than ±45° at 1100°C. Even at 1200°C, which is above the usage temperature for the Nextel720 fiber, the 0°/90° strain rate is two orders of magnitude lower than the ±45° orientation.
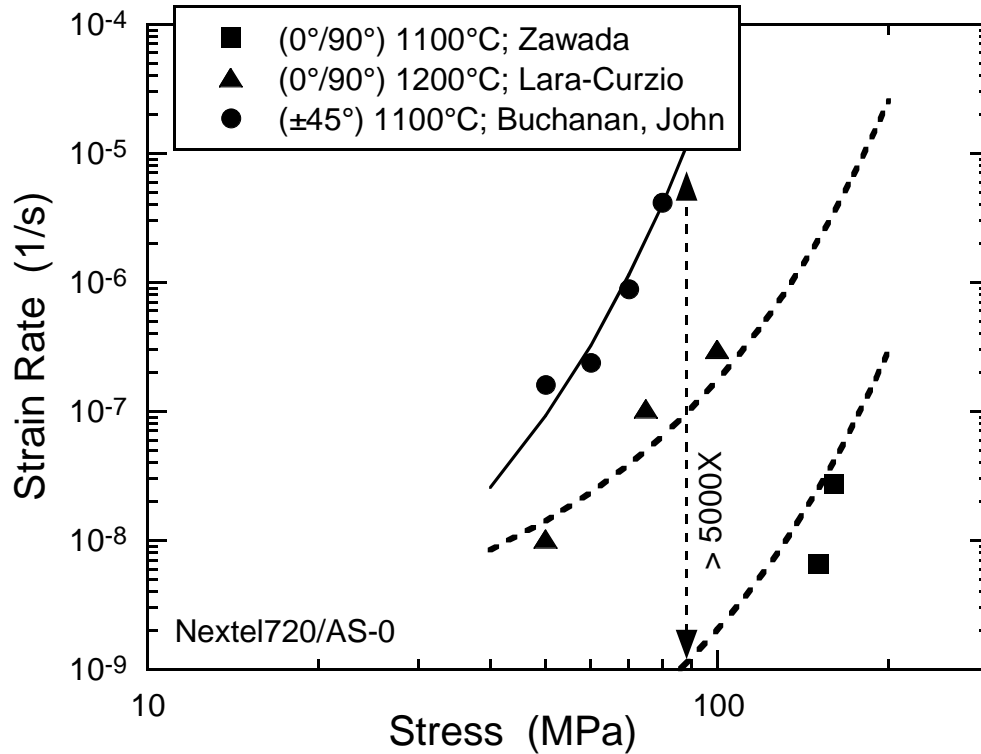
Figure 5. Strain rate versus time for creep of 0°/90° and ±45° Nextel720/AS-0.

Figure 6 shows the applied net section stress versus creep rupture time for unnotched and double edge notch 0°/90° and unnotched ±45° Nextel720/AS-0 at 1100°C. Previous studies [13,14] on the 0°/90° orientation have shown the double notched geometries show a reduction in creep rupture life when compared to the unnotched geometry. The unnotched ±45° orientation data in Fig. 6 show a further reduction in creep rupture life from the notched 0°/90° data. To achieve a rupture life of 100 hours at 1100°C the net section stress for the unnotched 0°/90°, notched 0°/90° and unnotched ±45° should be less than 155, 95 and 55 MPa, respectively. Clearly, this knockdown in the rupture life of the ±45° compared to the 0°/90° orientation at 1100°C limits the applicability of this material for components subjected to multiaxial states of stress.
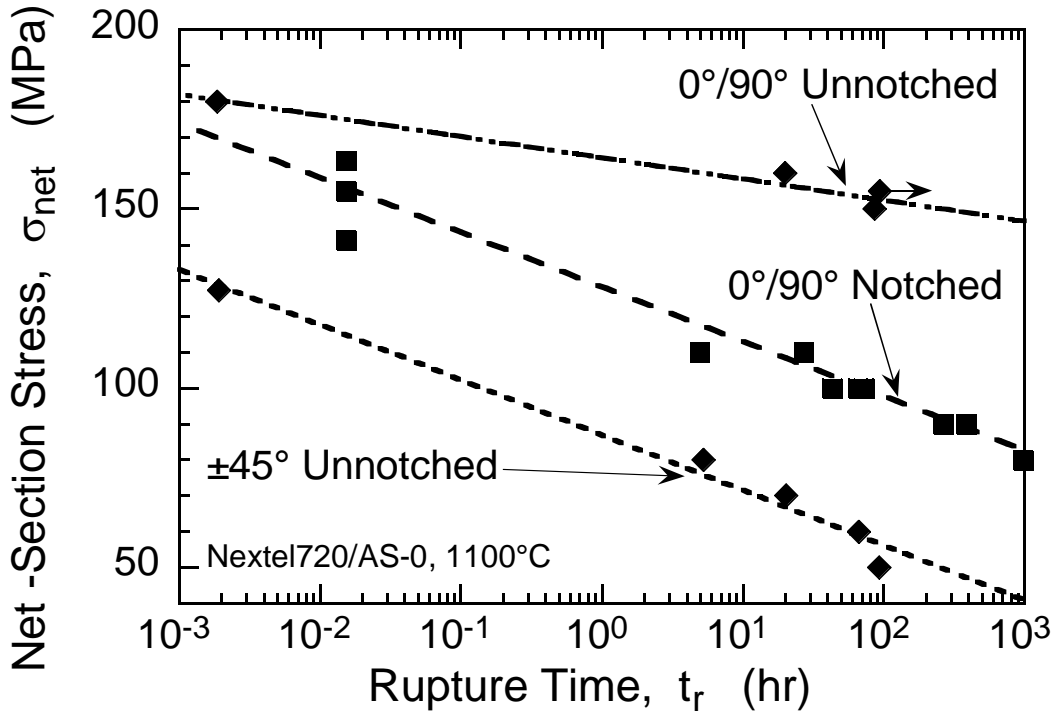
Figure 6. Creep rupture behavior of 0°/90° and ±45° Nextel720/AS-0 at 1100°C.

Summary

The creep rupture behavior of oxide/oxide Nextel[TM]720/AS CMC with 2D fiber mat orientations 0°/90° and ±45° were investigated. Tensile tests on 0°/90° and ±45° orientations at 1100°C show similar elastic moduli, however they have different ultimate strengths and failure strains. Results of creep tests show that the secondary creep strain rate of the ±45° orientation can be as high as 5000X that of the 0°/90° orientation at 1100°C. The ratio of the creep rupture strength at 100 hours and 1100°C of ±45° to 0°/90° is 0.3 for unnotched specimens.

Acknowledgments

References

1   Zawada, L. P. and Lee, S. S., "Mechanical Behavior of CMCs For Flaps and Seals," *Proceedings of Advanced Research Projects Agency (ARPA) Advanced Ceramics Technology Insertion Program (ACTIP) Annual Review*, W.S. Coblenz, Ed., Washington, DC, August 1995.

2   Zawada, L. P. and Lee, S. S., "Evaluation of Four CMCs For Aerospace Turbine Engine Divergent Flaps and Seals," *Ceramic Engineering and Science Proceedings*, Vol. 16, No. 4, 1995, pp. 337-339.

3   Mouchon, E. and Colomban, Ph., "Oxide Ceramic Matrix/Oxide Fiber Woven Fabric Composites Exhibiting Dissipative Fracture Behavior," *Composites*, Vol. 26, 1995, pp. 175-182.

4   Lange, F. F., Tu, W. C, and Evans, A. G., "Processing of Damage-Tolerant, Oxidation- Resistant Ceramic Matrix Composites by a Precursor Infiltration and Pyrolysis Method," *Materials Science and Engineering*, Vol. A195, 1995, pp. 145-150.

5   Zawada, L. P., Hay, R. S., Lee, S. S., and Staehler, J., "Characterization and High Temperature Mechanical Behavior of an Oxide/Oxide Composite," *Journal of the American Ceramic Society*, Submitted for publication, January 2001.

6   Levi, C. G., Yang, J. Y., Dalgleish, B. J., Zok, F. W. and Evans, A. G., "Processing and Performance of an All-Oxide Ceramic Composite," *Journal of the American Ceramic Society*, Vol 81, No. 8, 1998, pp. 2077-2086.

7   Heathcote, J. A, Gong, X. -Y, Yang, J., Ramamurty, U., and Zok, F. W., "In-Plane Mechanical Properties of an All-Oxide Ceramic Composite," *Journal of the American Ceramic Society*, Vol. 82, No. 10, 1999, pp. 2721-2730.

8   Wilson, D. M., Lieder, S. L., and Lueneburg, D.C., "Microstructure and High Temperature Properties of Nextel 720 Fibers," *Ceramic Engineering Science Proceedings*, Vol. 16, No. 5, 1995, pp. 1005-1014.

9   Yun, H. M. and DiCarlo, J. A., "Time/Temperature Dependent Tensile Strength of SiC and Al_2O_3-Based Fibers," *NASA Technical Memorandum 107370*, NASA Glenn Research Center, Cleveland, OH, USA, 1996.

10   Antti, M-L., and Lara-Curzio, E., "Effect of Notches, Specimen Size, and Fiber Orientation on the Monotonic Tensile Behavior of Composites at Ambient and Elevated Temperatures," The 25th Annual Cocoa Beach Conference and Exposition, The American Ceramic Society, January 2001.

11   Kramb, V. A., Buchanan, D. J., John, R., and Zawada, L. P., "In-Plane Shear Behavior in Oxide/Oxide Ceramic Matrix Composites at Room and Elevated Temperature," *submitted for publication to: Composites Science and Technology*, Nov., 2002.

12   Buchanan, D. J., John, R., and Zawada, L. P., "Notched Fracture Behavior of Oxide/Oxide Nextel™720/AS Composite," The 24th Annual Cocoa Beach Conference and Exposition, The American Ceramic Society, January 2000.

13   John, R., Buchanan, D. J. and Zawada, L. P., "Creep Deformation and Rupture Behavior of a Notched Oxide/Oxide Nextel™720/AS Composite," The 24th Annual Cocoa Beach Conference and Exposition, The American Ceramic Society, January 2000.

14   Lara-Curzio, E., and More, K. L., "Stress-Rupture Behavior of Nextel™720/AS fiber-reinforced Aluminosilicate CFCCs at 1200°C," The 24th Annual Cocoa Beach Conference and Exposition, The American Ceramic Society, January 2000.

15   3M Company Product Data Sheet, 3M Ceramic Fiber Products, 3M Center-Building 207-1W-11, St. Paul, MN 55144-1000.